WIND DRIVEN CIRCULATION IN TRINITY AND CONCEPTION BAYS

FRASER DAVIDSON

INFORMATION TO USERS

This manuscript has been reproduced from the microfilm master. UMI films the text directly from the original or copy submitted. Thus, some thesis and dissertation copies are in typewriter face, while others may be from any type of computer printer.

The quality of this reproduction is dependent upon the quality of the copy submitted. Broken or indistinct print, colored or poor quality illustrations and photographs, print bleedthrough, substandard margins, and improper alignment can adversely affect reproduction.

In the unlikely event that the author did not send UMI a complete manuscript and there are missing pages, these will be noted. Also, if unauthorized copyright material had to be removed, a note will indicate the deletion.

Oversize materials (e.g., maps, drawings, charts) are reproduced by sectioning the original, beginning at the upper left-hand corner and continuing from left to right in equal sections with small overlaps.

Photographs included in the original manuscript have been reproduced xerographically in this copy. Higher quality 6" x 9" black and white photographic prints are available for any photographs or illustrations appearing in this copy for an additional charge. Contact UMI directly to order.

Bell & Howell Information and Learning
300 North Zeeb Road, Ann Arbor, MI 48106-1346 USA
800-521-0600

Wind driven circulation in Trinity and Conception Bays

by

© Fraser Davidson

M.Sc. (Memorial University, St. John's, Canada) 1994
B.Sc.(Hon) (University of Ottawa, Ottawa, Canada) 1992

A thesis submitted to the
School of Graduate Studies
in partial fulfilment of the
requirements for the degree of
Doctor of Philosophy

Department of Physics and Physical Oceanography
Memorial University of Newfoundland

(October, 1999)

St. John's Newfoundland

Abstract

In this thesis the wind driven circulation of Trinity and Conception Bays is described. I make use of three numerical models, ranging from a linear, single-layer, reduced-gravity model to the 3-D eddy resolving CANDIE model. The CANDIE model is verified by applying it to a lake initially at rest with horizontally uniform stratification, a parabolic bottom profile, adiabatic boundary conditions and no external forcing of any kind. Over time, vertical mixing of the thermocline gives rise to horizontal density gradients and cyclonic circulation in the lake. The models are then applied to investigate mechanisms that lead to observed asymmetry in the response of Trinity and Conception Bays to steady wind forcing directed out of the bay. I investigate the influence of factors such as continuous stratification, vertical mixing, nonlinearity and realistic bottom topography. Adding non-linearity allows for significant cross-bay transport of upwelled water and leads to an along-bay pattern of the surface isotherms evident in observations, and can also lead to the separation of the coastal jet from the upwelling favourable shore. The response to variable wind is also investigated and the modelling effort is compared to available oceanographic observations of the two bays including ADCP, current meter moorings, thermistor chains, SST and CODAR data. Overall I find reasonable to good agreement with the data. Adding the non-linear terms to the CANDIE model improves the reproduction of observed thermocline movement. An application to particle advection is undertaken, which suggests that there may be little exchange of fish larvae between Trinity and

Conception Bays.

DEDICATED

TO THE MEMORY

OF MY GRANDMOTHER

CLARA ELEANOR MOORE (1906-1997)

IN APPRECIATION OF HER LOVE OF LEARNING

AND ENCOURAGEMENT TO ALL HER

GRANDCHILDREN

IN THEIR PURSUIT OF KNOWLEDGE

Contents

List of Tables

List of Figures

Acknowledgements

I would like to take this opportunity to thank all those who have made contributions to this dissertation. The hospitality of the Department of Physics and Physical Oceanography at Memorial University is gratefully acknowledged.

I wish to thank first and foremost my thesis supervisor, Professor Brad de Young for mentoring me through all these years despite adversity. He and Professor Richard Greatbatch, who was co-supervisor for part of these studies, contributed substantially to my knowledge and understanding of oceanography.

I am grateful to Drs. Pierre Pepin, Dr. Yakov Afanasayev, Jim Helbig and Jinyu Sheng for discussions and interactions. I thank Drs. David Schwab, William O'Connor and George Mellor for their helpfull comments on Chapter 3. I thank Dr. David Dietrich for providing the original source code as a starting point for the model used in this study.

I gratefully acknowledge the financial assistance by the School of Graduate Studies, the Department of Physics and Physical Oceanography, the Department of Fisheries and Oceans and the Maritime Award Society of Canada which have contributed to my education in the form of fellowships and scholarships.

Brenda Burke is thanked for relaying numerous correspondence and faxes. Len and Liz Zedel are thanked for their friendship and moral support. I would also thank my fellow students Youyu Lu, Mark Pepin, Anne Paradis and Hughes Benoit for their sharing of ideas as well as their friendship. I would also praise the positive

benefits of the Gordon Research Conference in Coastal Oceanography in providing an opportunity to discuss science in an informal and constructive setting.

Finally, special thanks go to my parents and family, who have always been a source of support for me. Their love and encouragement is greatly appreciated. I thank my father, Dr. Walter F. Davidson, for a critical review of this thesis.

Chapter 1

Introduction

1.1 Location

A lasting impression for visitors to St. John's, Newfoundland (Figure 1.1), is the variability in the weather stemming from the city's location on the Avalon Peninsula in the Northwest Atlantic.

The Avalon Peninsula lies off the western edge of the Grand Banks, south of which lie the eastward flowing warm waters of the Gulf Stream. Waters to the south of the Avalon peninsula are relatively warm in the summer (Figure 1.2) with surface temperatures above 16 °C in August. To the north-east of the peninsula is the southward flowing Labrador Current which is responsible for carrying sea-ice closer to the equator than anywhere else on the planet. Each spring, sea-ice appears off the east coast of Newfoundland, sometimes extending well south of the island to latitudes of 44°N. By late summer, the surface temperatures on the Newfoundland Shelf reach roughly 8-12 °C (Figure 1.2), cooler than on the Grand Banks to the south.

Winds in St. John's, particularly in the early summer, are noticeably cooler when the winds blow from the ocean because of the presence of the Labrador Current (Prinsenberg et al., 1997). Warm south-westerly winds influenced by warm continental air masses, are often a pleasant change after the Arctic winds from the north-east. This oscillation of wind contributes to the wide range of temperatures observed in any given month at St. John's where the two dominant wind directions are from the northeast (cool) and the southwest(warm). The Labrador Current thus has a strong indirect influence on the East Coast of Newfoundland and the Newfoundland Shelf. The cold waters of the shelf have been spawning grounds for generations of North Atlantic cod, precipitating many fishing endeavours and settlement from Europe since the late 15*th* century.

The source waters of the Labrador Current are outflow from Hudson Bay, Davis Strait, and the warmer ($\sim$ 4 °C) West Greenland Current (Smith et al. (1937); Kollmeyer et al. (1967); Chapman and Beardsley (1989); and Mertz et al. (1993)). The Labrador Current is composed of three branches at Hamilton Bank. The inshore branch carries approximately 1.6 Sv (1 Sv = 10^6 m^3 s^{-1}), the offshore branch situated over the shelf break carries roughly 9 Sv and the deep circulation (> 1000 m) of the Labrador Sea transports an estimated 40 Sv as part of the North Atlantic Subpolar gyre (Lazier and Wright, 1993). The inshore and offshore branches are baroclinic in nature while the deep offshore branch is primarily barotropic and associated with the large scale circulation in the North Atlantic. Colbourne et al. (1996) show that

along the Bonavista Transect (Figure 1.1) currents are spread out over the shelf with 5-10 cm s^{-1} southeastward flows inshore, increasing towards the shelf break. They (Colbourne et al., 1996) measured the total transport at 6 Sv with 3 Sv accounted for by geostrophy (i.e. thermal wind equations) along this transect. Adjacent to Trinity and Conception Bays, the flow splits (Figure 1.3) with a southward flow through the Avalon Channel (Petrie and Anderson, 1983) and an eastward flow along the northern edge of the Grand Banks.

The seasonal stratification of the water column on the east coast of Newfoundland can be described as follows. During the winter, surface cooling ensures that the water column is well mixed with temperatures around 0 °C. Analysis of data from Station 27 (cf. Figure 1.1) shows that during this time the first baroclinic mode phase speed has a value of 0.3 m s^{-1}. The seasonal temperature and salinity cycles influence the formation of ice along the Labrador Coast in January and February, and its subsequent advection down the Newfoundland Shelf (Myers and Akenhead, 1990). Over the course of the summer, once the pack ice has been blown offshore or has melted (Prinsenberg et al., 1997), the convectively mixed water column slowly gains stratification from April untill late August at which time surface waters are at their warmest, with water up to 14 °C measured at Station 27 (Petrie et al., 1992a). Station 27 is located just a few kilometres from St. John's (Figure 1.1) and is assumed to be a good proxy for the seasonal variations of temperature stratification in Conception and Trinity Bays (de Young and Sanderson, 1995). Stratification influences the wind

forced circulation by modifying the phase speed of internal gravity waves (Kundu, 1990).

While winds do influence the activities of the residents of St. John's, the question arises how wind influences circulation and temperature distribution in the nearby Trinity and Conception Bays. In this thesis, I explore the wind driven circulation and temperature distribution in Trinity and Conception Bays (Figure 1.1). While the effect of the Labrador Current is always present, I focus on the wind forced component of the current. An important feature near the coast is the occurrence of upwelling of cold deep water and downwelling of surface water, due to wind forcing and the subsequent propagation of this local response as waves.

As an introduction, I shall first review the theory of coastal trapped waves (Section 1.2). I then describe the local oceanography and observations in Conception and Trinity Bays (Section 1.3) and present results from previous modelling studies (Section 1.4) in this region. In Section 1.5, I touch briefly on larval fish abundance work and the importance of physical advection to larval fish distributions. Finally I formulate the thesis objectives in Section 1.6 and describe the thesis outline in Section 1.7.

1.2 Coastal Trapped Waves

In Trinity and Conception Bays, wind forcing appears to be the dominant contributor to the circulation and thermocline displacement (de Young et al., 1993b). Over

time, on an f-plane (i.e. the Coriolis force is constant in space), classic Ekman theory shows that, for wind parallel to an infinite shore line, the wind pushes the surface of the water to the right of the wind towards (or away) from the coast (Gill, 1982). This creates an upwelling (or downwelling) of the isotherms in stratified water (or the free surface in the barotropic case) and is a local effect of wind forcing.

Wind can also affect circulation near the coast or on the shelf from some distance away. This is achieved by one of two mechanisms (or both): the Kelvin wave (Lord Kelvin, 1871) and the Continental Shelf Wave (Robinson, 1964).

Kelvin waves occur in a rotating fluid in the presence of a vertical boundary which does not allow water to flow through it. When the wind pushes water towards or away from a coast with some alongshore variation, it creates an alongshore pressure gradient that propagates as a gravity wave with the coast to the right in the northern hemisphere. This wave is called a Kelvin wave. Internal Kelvin waves can occur whenever isopycnals intersect a coastline with a vertical wall despite the presence of variable topography (Wang and Mooers, 1976). The restoring force for Kelvin waves is gravity while the geostrophic balance produces a free-surface slope (or surface pressure gradient in the rigid lid case) to balance the Coriolis acceleration. In this thesis, I concentrate on the effect of the internal Kelvin wave whose phase speed is usually less than 1 m s^{-1}, but depends on stratification.

Over a variable bottom slope, however, Continental Shelf Waves occur whose restoring force is the conservation of planetary vorticity. Water moving on or off

the shelf becomes compressed or stretched, respectively, forcing it to spin slower or faster to conserve planetary vorticity. The vortices interact with each other making a horizontal oscillatory motion that is termed a Shelf Wave.

Numerical studies of coastal trapped waves over variable topography in the presence of continuous stratification were first carried out by Wang and Mooers (1976), and subsequently by Huthnance (1976). They showed that for continuous stratification over variable topography coastal trapped waves behave essentially as a combination of the two wave-types. For weak stratification and steep topography, the coastal ocean responds like continental shelf waves while for strong stratification the response is dominated by internal Kelvin waves.

A measure of the strength of stratification relative to the bottom slope, in order to determine which wave limit applies, is the stratification parameter S (Huthnance, 1976):

$$S = \frac{N^2 H^2}{f^2 L^2} \tag{1.1}$$

where N is the representative buoyancy frequency, H is the maximum depth, f is the Coriolis parameter and L is the width of the topographical variations. For $S << 1$, the shelf wave solution applies and for $S >> 1$, the Kelvin wave solution applies. In between, for S close to unity, hybrid waves occur. For Conception Bay in the summer, the typical value of S is 10 (de Young et al., 1993b). Thus, for Conception Bay, I expect that bottom topography will exert little influence on wave propagation characteristics around the bay during the summer months.

The presence of variable bottom topography near a coast also gives rise to edge waves. Edge waves are surface gravity waves with frequency higher than the inertial frequency f and are not affected by the Coriolis force. These waves may propagate with the coast either to the left or right. Edge waves are trapped close to shore by the effects of variable bottom depth and can readily be observed at beaches. In this study, however, I shall apply the rigid lid approximation and therefore surface gravity waves are filtered out of the model solution (Mysak, 1980). As will be explained in Chapter 2, the rigid lid approximation forces the barotropic component of the ocean to respond instantly to forcing.

1.3 Local Oceanography of Trinity and Conception Bays

In the study of de Young and Sanderson (1995), it was observed that the standard deviation of flow in Conception Bay is five times greater than the magnitude of observed mean flow, which is < 2 cm s^{-1} at 20 m depth. Thus I may infer that the intrusion of the Inshore Branch of the Labrador Current into Conception and Trinity Bays is probably sporadic. Tides are weak with current amplitudes between 1 and 2 cm s^{-1} for the M_2 and K_1 tidal components (de Young and Sanderson, 1995). Spatial correlation scales are roughly 4-8 km, approximately equivalent to the Rossby radius of the first baroclinic mode for summer stratification. Decorrelation time scales from current moorings vary between 2 and 5 days. Horizontal diffusion estimates from Lagrangian drifters are roughly $70 - 100$ m^2 s^{-1} (de Young and Sanderson, 1995).

Such diffusion includes effects of eddies which may be resolved in high resolution non-linear models and is probably an upper estimate for the diffusivity.

Several physical observation studies in Conception Bay have taken place in the spring and summer months. Drifter observations have shown cyclonic eddies (de Young and Sanderson, 1995). An anticyclonic eddy features in the diagnostic output of de Young et al. (1993a) based on density observations. The appearance of anticyclonic and cyclonic motion further illustrates the variability of the circulation pattern in the Bay. At a fixed point in time, ADCP (Acoustic Current Doppler Profiler) transects across the mouth of the bay show that the surface flow reverses direction two or three times between outflow and inflow (Pepin et al., 1995). Surface drifter observations of circulation patterns further indicate the presence of strong spatial variability in the centre of the bay, where drifters released close together (2 km) pursue different paths. de Young and Sanderson (1995) also noted that near bottom currents (100 m) showed some tidal effects as well as indications of a seiche movement at a period between 3-5 days. At the surface, however, tides are negligible compared to wind driven current variability. Flow at depth near the mouth is usually opposite in direction to that near the surface (de Young and Sanderson, 1995).

1.4 Previous Modeling Work

Previous physical oceanography modeling studies for Trinity and Conception Bay have focused on the wind driven response using linear reduced-gravity shallow water

models (Yao (1986). Otterson (1992) and de Young et al. (1993b)). These models have a light layer of water of a given depth (40 m for example) overlying a much deeper layer considered to be infinitely deep and at rest. The rigid lid approximation is made where displacement at the air-sea interface is assumed to be much smaller than the displacement of the interface between two water layers of differing density (Gill. 1982).

The imposition of a coastal boundary implies divergence or convergence of wind driven horizontal surface flow. This drives the interface between the two layers up or down generating alongshore pressure gradients (at discontinuities in the coastline) that propagate as internal Kelvin waves. There are no edge waves or shelf waves since bottom topography is absent from the model. Since the models are linear. they do not allow for horizontal transport of water properties (i.e. temperature. salinity or density).

The strength of a 2 layer reduced gravity model when comparing with observations lies in the displacement of the pycnocline. The 2 layer model is solved for the displacement of the interface between the upper and lower layers. This procedure is similar to the displacement of the observed pycnocline which is directly attributed to the divergence of the vertical integrated horizontal currents above the thermocline.

Otterson (1992) applied a wind-forced. single-layer. reduced-gravity, shallow water model to Conception Bay alone. Agreement of modeled thermocline displacement with mooring data at the head of the bay was found in the 2 to 5 day time scale with

a coherence squared of around 0.9 for 6 degrees of freedom. However, agreement with observed thermocline displacement at the mouth of the bay was poor. At the mouth circulation may be strongly influenced by mean currents on the Newfoundland Shelf as measured at Station 27 (?). Shelf currents are probably baroclinically unstable (Anderson, 1986) which may drive variable flow in and out of Trinity and Conception Bays. Such forcing would be most noticeable at the mouth of the bays. The model reproduced 4 major upwelling events observed in the bay during a 60 day period in 1989. The model domain included only Conception Bay with model boundaries extending 20 km beyond the mouth of the bay. Shallow water model comparisons with observations show that these models do not reproduce velocities as well (Yao (1986).de Young et al. (1993b)) as comparisons with thermocline observations.

de Young *et al.* (1993b) then applied the same model as Otterson (1992) to Trinity and Conception Bays. Including Trinity Bay in the model domain increased the explained variance between the model's interface displacement and the observed thermocline displacement in Conception Bay. The model reproduced thermocline displacement best at the head of the bay. Adding Trinity Bay to the model domain increased the amplitude of the modeled interface displacement in Conception Bay, such that it better matched the amplitude of the observed thermocline displacement, particularly near the mouth on the western shore (de Young et al., 1993b). These findings support the idea that upstream wind forcing directly influences circulation in Conception Bay.

For time-dependent wind-driven models, boundary conditions need to be implemented carefully. Model generated effects should occur due to wind forcing within the model domain boundaries (Greatbatch and Otterson, 1991) and not by spurious effects arising from the open boundary conditions. Kelvin waves should be generated only due to the presence of land and wind inside the domain. One could include generation of Kelvin waves at the boundary if additional information were available. Greatbatch and Otterson (1991) chose the boundary of their model domain so that the upstream open boundary (in the sense of Kelvin wave propagation) is a continuation of the coast. They also used a boundary condition of no normal gradient (Neumann) at the inflow boundary on both velocities and interface displacement. This ensures no spurious upwelling generated at the upstream boundary occurs. The boundary treatment of Greatbatch and Otterson (1991) was also used in Otterson (1992) and de Young et al. (1993b).

A diagnostic model has also been applied to Conception Bay (de Young et al., 1993a). Diagnostic calculations assess the currents for a given fixed density field usually prescribed from observations. Effects of wind forcing and wave propagation are implicit in the prescribed density field. The resulting velocity fields show one or two gyres present in Conception Bay, albeit with some meandering currents. However, evident in the modelled velocity fields is the absence of a coastal jet (there are no time dependent terms in this model) consistent with linear time dependent theory. It is noteworthy that in the surface layer, at 2 m depth, velocity distributions are

primarily affected by wind forcing and geostrophy, rather than from the density field; resulting in a strong horizontally homogeneous velocity field relative to that at 20 m or 50 m of depth (de Young et al., 1993a).

A linear reduced-gravity model and a diagnostic model constitute useful and versatile tools as first approaches to modeling currents in a bay. There are, however, limitations to such overly simplified approaches. The reduced-gravity model does not produce a 3D structure for the bay, its wave propagation characteristics remain fixed, and it does not include the non-linear terms of the Navier-Stokes equations. Furthermore, this model ignores bottom topography. On the other hand, the diagnostic model gives a 3D picture of the circulation field which is a "snap shot", geostrophically frozen in time, of the circulation field. Circulation in the ocean, on the shelf and in the bays is dynamic and three dimensional. Due to the variable nature of the circulation and water density distribution in Conception and Trinity Bays, a 3 dimensional prognostic eddy-resolving model is a sensible approach.

1.5 Biological Applications

The influence of physical circulation and temperature distribution on biological organisms is undeniable and a knowledge of the oceanographic environment can be useful in understanding biological observations such as those of fish egg and larval abundances (Helbig and Pepin, 1998b).

Studies have been conducted previously on larval advection in this region. In

particular Davidson and de Young (1995) demonstrated that it is unlikely that eggs spawned on the shelf break (200 km offshore) will drift into the bays of Newfoundland as larvae. This conclusion is corroborated by genetic differences found between cod fish wintering offshore and those wintering inshore in the Newfoundland Bays (Ruzzante et al., 1996).

With respect to Conception Bay, many studies have been carried out on factors influencing larval abundance observations. In particular (to name a few), effects of size dependence of predator and prey (Paradis et al., 1996), larval growth with temperature (Pepin, 1991), advective influences of larvae into and out of the bay (Pepin et al., 1995) and turbulence (Dower et al., 1998) have been investigated.

The importance of advective effects on observed larval abundance varies as the square root of the study area (Pepin et al., 1995). However, even in the theoretical limit when physical variability is well determined, current biological sampling protocols cannot adequately resolve larval abundance variability (i.e. mortality and growth) (Helbig and Pepin, 1998a,b).

The diagnostic circulation fields of de Young et al. (1993a) were applied to modeling the dispersion of capelin larvae (*Mallottus villosus*) in Conception Bay (de Young et al., 1994). They concluded that larval capelin residence time was reduced on the eastern shore of the bay where larvae were carried out into the Avalon Channel. Not surprisingly, they found that residence time was highest at the head of the bay.

While advection and temperature affect fish at the larval stage, they may also

influence adult fish. Templeman (1966) surmised that cod fish responded to near-shore upwelling events by moving into shallower waters where they can be caught by the trap fishery. This was observed by Rose and Leggett (1988) who noted higher catch rates of cod under favourable upwelling conditions on the Québec shore of the Gulf of St. Lawrence.

Whether cod fish respond to coastal upwelling events by moving to shallower locations closer to shore has not yet been decisively determined. Schneider (1994), Schneider and Methven (1988), and Ings et al. (1997) propose a modification of Templeman's (1966) idea, suggesting that cod respond only to extreme upwelling events (where surface temperatures decrease by more than 4 °C), and, move inshore only after upwelling subsides. The observations of Rose and Leggett (1988) of increased catches of cod by traps on the north shore of the St. Lawrence estuary may have been due to such extreme upwelling events.

Capelin distributions with respect to upwelling events in this region have also been considered by Schneider (1994), Schneider and Methven (1988) and Ings et al. (1997). Unlike cod, the near-shore presence of capelin increases during as well as preceding strong upwelling events.

The biological goal of this work centres on providing a realistic time dependent description of surface currents and surface temperature distribution in response to wind forcing for Trinity and Conception Bays. Knowledge of these current fields can then be applied to determine mean residence times and trajectories, to improve

the design of sampling schemes for larval abundance in the bay (Helbig and Pepin, 1998b) and to provide insights as to where (and why) upwelling is most prevalent in the region.

1.6 Research Objectives

This work has several objectives, all of which rely on the creation and implementation of a prognostic eddy resolving model based on the CANDIE model (Sheng et al., 1998) (based on the DieCAST model (Dietrich et al., 1987)). The work can be divided into technical and scientific objectives. The technical objectives of this thesis, are the assessment of the validity of the CANDIE model version created at Memorial University as well as the applied boundary conditions. This objective is achieved by applying the model to a succession of problems of increasing complexity and comparing the model solution with published studies as well as linear shallow water model solutions.

The scientific objectives include an understanding of the role of vertical diffusion in generating mean circulation in a coastal environment. The primary objective is to understand the wind driven response of Trinity and Conception Bays under steady and variable wind conditions. The approach taken here is to build up gradually an understanding of the wind forced circulation through the application of simple, shallow-water models to simplified embayment topographies before adding physical complexity one step at a time.

This thesis pulls together a multitude of published and unpublished data in describing the response of these bays to wind forcing. One specific objective is the comparison of model results with a variety of synoptic observation data sets such as remotely sensed observations (see Chapter 2). This objective includes an understanding of observed temperature distributions as well as the thermocline displacement. The influence of the non-linear terms on these model solutions is explored.

To date, there have been only a handful of physical oceanographic research publications devoted to Conception Bay, and even fewer to Trinity Bay. Recent observations of cod spawning and aggregations in Trinity Bay (e.g. Smedbol and Wroblewski (1997)) may serve to encourage future physical and biological work in Trinity Bay. This thesis provides new understanding of wind driven circulation in Trinity Bay.

The biological objective of this study is to describe particle retention patterns in Trinity and Conception Bays. A question I particularly wish to answer is whether the larval drift between Trinity and Conception Bay is significant. A secondary objective relates to the mapping of the retention patterns of larvae in both bays.

1.7 Outline

This work is presented as follows. In Chapter 2, I present the numerical models used and discuss their implementation. Furthermore, I describe a variety of observational data to which model results shall be compared in Chapter 5. In Chapter 3, the CANDIE model is applied to a parabolic stratified lake with adiabatic boundary

conditions in the absence of any wind forcing. In Chapter 4, the response of bays to a steady out of the bay wind stress is presented. In Chapter 5, the response of the bays to time dependent wind forcing is studied. In Chapter 6, modeled velocities are used in a tracking model for analysis of particle advection in Trinity and Conception Bays. Finally in Chapter 7, a brief summary and discussion on the important results of this thesis are given.

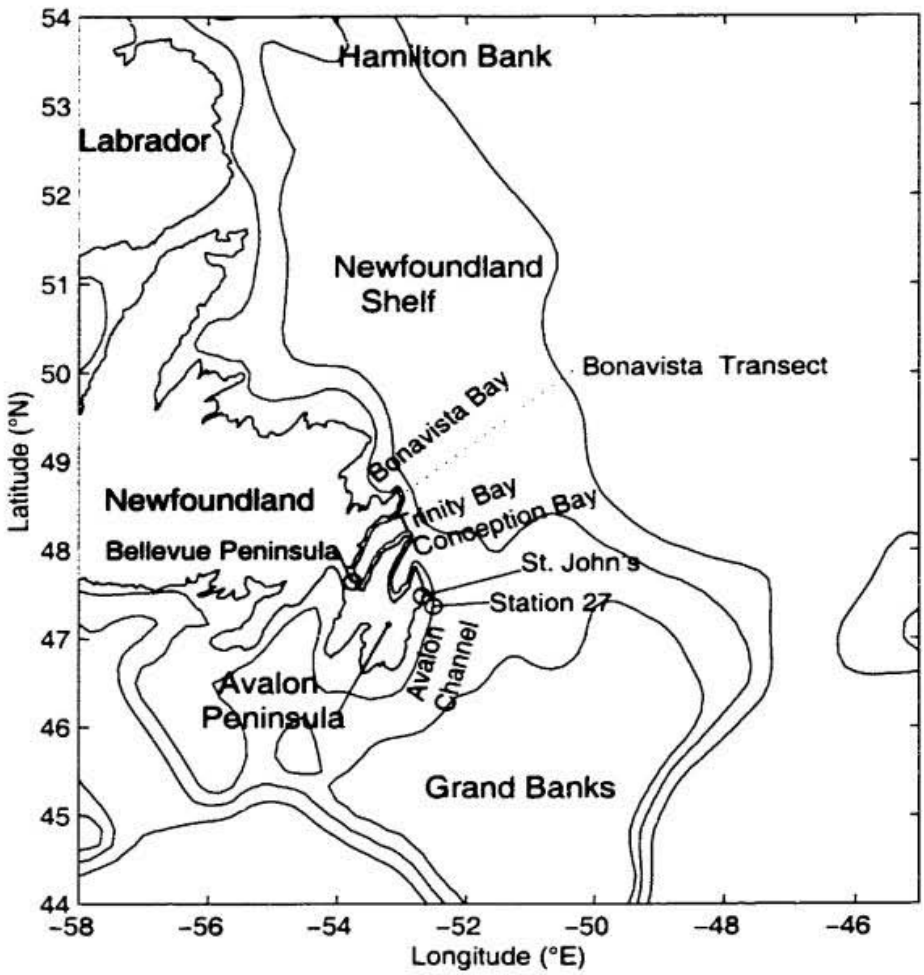

Figure 1.1: The region of interest for this study includes Trinity and Conception Bays, Newfoundland. Regular oceanographic observations have been made over the past 50 years at station 27, just a few kilometers offshore from St. John's.

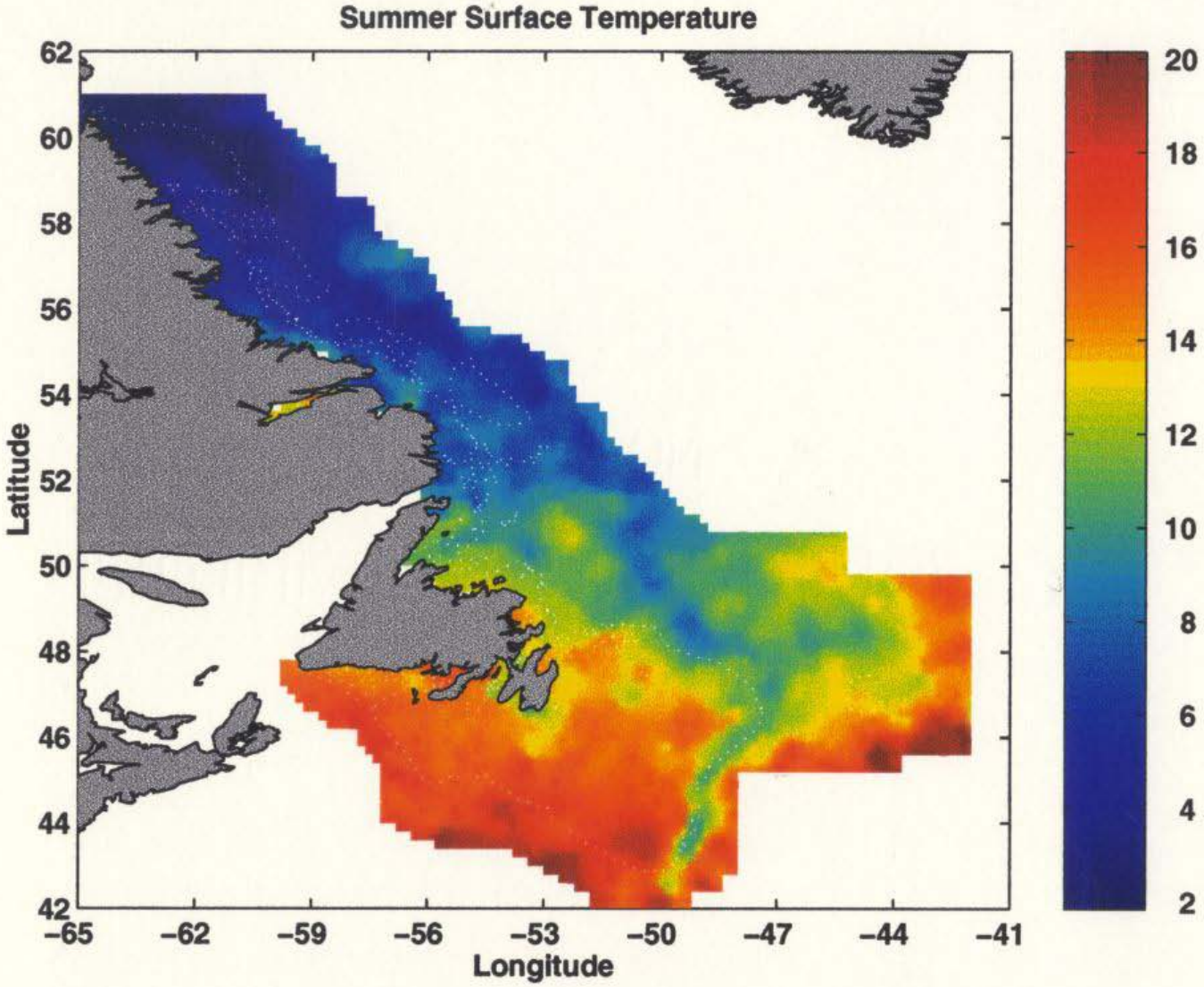

Figure 1.2: Sea Surface Temperature (SST) image from an optimal estimation of a climate database of all available temperature data taken in August for the east coast (roughly 15 million individual observations). The image is courtesy of Doug Gregory (Head, Data Management and Services) at the Department of Fisheries and Oceans, Bedford Institute of Oceanography.

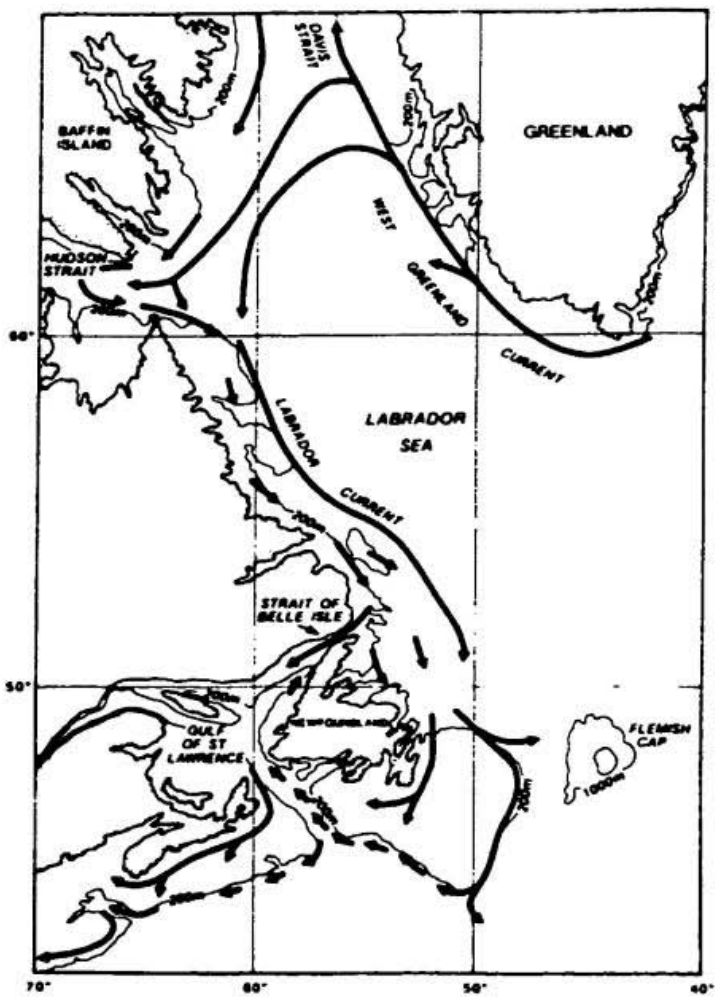

Figure 1.3: Figure reproduced from Mertz et al. (1993) showing the location of the Labrador Current. Note the inshore branch of the Labrador Current near the Newfoundland Coast and the offshore branch along the shelf break. Flow is split around the Grand Banks with little flow over the banks (Greenberg and Petrie, 1988).

Chapter 2

Model Approach and Observations

2.1 Introductory Remarks

In this chapter I describe the modeling approach for Trinity and Conception Bays and the data used to verify model results. I describe a hierarchy of models ranging from fairly simple 2-D linear models to a sophisticated 3-D eddy resolving model. The primary goal is to model the wind driven circulation in Trinity and Conception Bays. I focus on the effect of local wind forcing in the absence of explicit external forcing at the modelled open boundaries. Thus, there is no explicit influence of the Labrador Current in the model domain. Implicitly, however, some influence is present in the initial conditions for density stratification. The only explicit forcing in the model is local wind forcing over the model domain.

Three standard oceanographic approximations to the equations of motion are applied here. The first is the rigid lid approximation, in which the vertical displacement of the air-sea surface interface is ignored, assuming that it is much smaller than the

vertical internal interface displacement between two layers of water of differing density. The rigid lid approximation implies that pressure varies at the surface ($z = 0$) instead of allowing the surface to move up and down (Gill, 1982). In the rigid lid approximation, the barotropic mode solution is distorted since the phase speed is higher than that in the free surface case. This distortion of the barotropic wave speed is due to the short pressure adjustment timescale of the rigid lid compared to that of the free surface. The free surface takes a finite amount of time to move up and down and the pressure adjusts accordingly. In the rigid lid approximation however, pressure builds up nearly instantaneously at the surface, since by definition there are no vertical velocities at the rigid lid surface. The rigid lid approximation would not be appropriate for surface tides where sea surface height varies over time, and would overestimate by a factor of 100 (or more) the barotropic mode phase speed.

The second assumption is the Boussinesq approximation (Spiegel and Veronis, 1960): here spatial density variations are ignored in the conservation of momentum equations with the exception of the gravitational terms. The Boussinesq approximation is valid when relative density variations $\frac{\delta\rho}{\rho}$ are small. Furthermore, under the Boussinesq approximation, the continuity equation simplifies to zero divergence in velocity ($\nabla \cdot \vec{u} = 0$) as for an incompressible fluid.

The third simplification is the hydrostatic approximation in which the vertical momentum equation is taken as a balance between pressure and gravity and the water column is approximated to be at rest in the vertical axis. The hydrostatic approxima-

tion is valid when horizontal scales of motion are much bigger than vertical scales of motion (Gill, 1982). Vertical velocities are present, but calculated from the continuity equation. The relative error in vertical velocities is large since vertical velocities are derived from the horizontal gradients of horizontal velocities have relatively small values and consequently large errors (compared to the errors for u and v). The vertical velocity fields are therefore expected to be inherently noisy.

2.2 Density Stratification

In this section, I describe how the initial density stratification for model runs of Trinity and Conception Bays is derived. The most frequented oceanographic station in this region is Station 27 (Figure 1.1), which has been sampled over the last 50 years roughly twice a month (Petrie et al., 1992a), with higher sampling rates in the summer and fall. Station 27 is situated about 20 km to the south of the mouth of Conception Bay, and is considered a reasonable proxy for density stratification in Conception and Trinity Bays (de Young and Sanderson, 1995). The density profile at Station 27 is obtained from density observations at standard depths 0, 10, 20, 30, 50, 75, 100, 125, 150 and 175 m (Petrie et al., 1992a). All density observations taken in the month of June over a 40 year observation period are used to extract an average June density profile (Figure 2.1a). I then calculate a representative vertical profile of the square of the Brunt Väisälä frequency N^2 (Figure 2.1b) which is a measure of the

stability of the water column.

$$N^2 = \frac{g}{\rho_o}\frac{d\rho}{dz} \tag{2.1}$$

Here g is gravitational acceleration in m s^{-2}. ρ_o is the representative fluid density, and ρ is the fluid density. The linear density equation can be approximated by

$$\rho_t + w\rho_z = 0. \tag{2.2}$$

where the subscripts t and z represent partial differentiation with respect to time and the vertical coordinate z; w is the vertical velocity. I have neglected horizontal density transport terms and diffusivity. The only factor affecting density is advection in the vertical axis. Substituting for ρ_z in equation 2.2 one gets:

$$\rho_t - \frac{\rho_o N^2}{g} w = 0 \tag{2.3}$$

Separating the above equation using standard separation of variables

$$\begin{aligned}\left(u, v, \frac{p}{\rho_o}\right) &= \sum_{n=0}^{\infty} \left(u_n(x,y,t), v_n(x,y,t), p_n(x,y,t)\right) \upsilon_n(z) \\ w &= \sum_{n=0}^{\infty} \int_{-H}^{z} \upsilon_n(z) dz \\ \rho &= \sum_{n=0}^{\infty} \rho_n \frac{d\upsilon_n(z)}{dz}\end{aligned} \tag{2.4}$$

yields an equation in Sturm-Liouville form whose solutions are orthogonal (Kundu, 1990).

$$\frac{d}{dz}\left(\frac{1}{N^2}\frac{d\upsilon_n}{dz}\right) + \frac{1}{c_n^2}\upsilon_n = 0. \tag{2.5}$$

Here c_n is the phase speed of a wave associated with the vertical mode function ψ_n. Equation 2.5 is solved for a flat bottom ocean with 200 m depth and a vertical resolution of 1 m using matrix inversion. This vertical resolution of 1 m yields 200 modes. I specify a rigid lid and no flux condition at the surface and bottom of the water column ($\frac{d\psi_n}{dz} = 0$ at $z = 0$ and $z = -H$). There is one barotropic mode for which the vertical structure function is uniform at all depths (i.e. $\psi_0 = 1$) and the phase speed is large ($\sim$4000 m s^{-1}) as a consequence of the rigid lid approximation.

Using the N^2 profile given in Figure 2.1b, I solve for the vertical mode functions and their respective phase speeds (Figure 2.2). The wave speed of the first baroclinic mode for the month of June is 0.51 m s^{-1}, giving an internal Rossby radius of deformation of 5 km. For the rest of the year, similarly calculated monthly phase speeds vary between $c_1 = 0.3$ m s^{-1} in March and $c_1 = 0.8$ m s^{-1} in September for the first baroclinic mode. The above calculation of normal mode phase speeds provides useful insight into the single layer reduced gravity shallow water model described next.

2.3 Model Description

Three different numerical models are applied in this work: (1) A single-layer, reduced-gravity model in which the wave speed is specified; (2) a flat bottom, continuously stratified, linear shallow water model with several modes; and (3) the 3-D, Z-coordinate CANDIE model in linearized and non-linearized form.

2.3.1 Single-layer, Reduced Gravity Model

I take a vertical average of the equations of motion for a uniform layer of water of undisturbed depth H and density ρ_1 overlying an infinitely deep quiescent bottom layer of density ρ_2. The rigid lid approximation is made.

The corresponding momentum equations for the top layer are

$$u_t - fv = -g'\eta_x + \frac{\tau^x}{\rho_1 H} - \epsilon u, \tag{2.6}$$
$$v_t + fu = -g'\eta_y + \frac{\tau^y}{\rho_1 H} - \epsilon v.$$

and the corresponding continuity equation is

$$\eta_t + H(u_x + v_y) = -\gamma\eta. \tag{2.7}$$

Here, g' is the reduced gravity, defined as $\left(\frac{\rho_2-\rho_1}{\rho_2}\right) g$. f is the Coriolis parameter set at 10^{-4} s^{-1}. u and v are the velocity components of the upper layer in the x and y directions and τ^x and τ^y are the x and y components of wind stress.

We set the undisturbed depth of the upper layer at 40 m. to approximate the vertical profile of the first baroclinic mode for the month of June (Figure 2.2). Furthermore, the wave propagation speed $c = \sqrt{g'H}$ is set at 0.53 cm s^{-1} to represent the wave speed of the first baroclinic mode (Figure 2.2). Damping in this model is linear and done using constant Rayleigh friction and Newtonian cooling parameters ϵ and γ. The damping parameterization is an approximation for the vertical integrated diffusion terms. Instead of diffusing away sharp gradients, variables are damped according to their insitu magnitude. The Prandtl (Pr) number given by $\frac{\epsilon}{\gamma}$. In most

cases ϵ and γ are set to 0, but I experiment with runs including various values of ϵ and γ to study the effects of damping and of the Prandtl Number.

The model equations are finite differenced on an Arakawa C-grid (Figure 2.3) using the method of Heaps (1971). The finite difference equations are computed in the following order: (1) First the interface displacement via the continuity equation is updated

$$\eta^{n+1} = \left[\eta^n - H\Delta t\left(\frac{u^n_{i,j} - u^n_{i-1,j}}{\Delta x} + \frac{v^n_{i,j} - v^n_{i,j-1}}{\Delta y}\right)\right]\frac{1}{1+\gamma\Delta t}; \tag{2.8}$$

(2) Then the boundary conditions are applied to η; (3) After this, I update the u and v components of velocity.

$$u^{n+1} = \left[u^n + \Delta t\left(f\frac{v^n_{i,j} + v^n_{i,j-1} + v^n_{i+1,j} + v^n_{i+1,j}}{4} - g'\frac{\eta^n_{i+1,j} - \eta^n_{i,j}}{\Delta x} + \frac{\tau^x}{\rho_1 H}\right)\right]\frac{1}{1+\epsilon\Delta t} \tag{2.9}$$

$$v^{n+1} = \left[v^n + \Delta t\left(-f\frac{u^n_{i,j} + u^n_{i-1,j} + u^n_{i-1,j+1} + u^n_{i,j+1}}{4} - g'\frac{\eta^n_{i,j-1} - \eta^n_{i,j}}{\Delta y} + \frac{\tau^y}{\rho_1 H}\right)\right]\frac{1}{1+\epsilon\Delta t} \tag{2.10}$$

In the above equations, the damping terms (i.e. γ and u) are differenced backwards in time for unconditional numerical stability (of these terms). All other terms are differenced forwards in time. The stability criterion for the forward differencing in time is $\Delta x/\Delta t > c$. Since the phase speed c is fixed, it is necessary to ensure that $\Delta t < \Delta x/c$ where $c = \sqrt{g'H}$. Thus the maximum time step for a stable solution with a phase speed of 0.5 m $s^{-1}$and a grid spacing of 500 m is 1000 s.

2.3.2 Stratified Model (Normal Modes)

Here the three dimensional linear equations of motion are solved by separation into standard vertical normal modes (section 2.2) for a flat bottomed coastal ocean following McCreary (1981). The product of vertical viscosity (or diffusivity) times the square of the Brunt Väisälä frequency (N^2) is assumed constant. This simplification allows for easy separation of variables: ($\nu \times N^2 = \Lambda_M$) and ($\kappa \times N^2 = \Lambda_\rho$). The constants of proportionality Λ_M and Λ_ρ can be equal or different (i.e. Pr $\neq$ 1).

We first separate the equations of motion into vertical normal modes and then solve the equations for the horizontal structure of each mode, given below, using the finite difference method of Heaps (1971), as for the reduced-gravity model.

$$\begin{aligned}
\frac{\partial u_n}{\partial t} - f v_n &= -\frac{\partial p_n}{\partial x} + F_n - \left(\frac{\Lambda_M}{c_n^2}\right) u_n \\
\frac{\partial v_n}{\partial t} + f u_n &= -\frac{\partial p_n}{\partial y} + G_n - \left(\frac{\Lambda_M}{c_n^2}\right) v_n \\
\frac{\partial p}{\partial t} + c_n^2 \left(\frac{\partial u_n}{\partial x} + \frac{\partial v}{\partial y}\right) &= -\left(\frac{\Lambda_\rho}{c_n^2}\right) p_n
\end{aligned} \tag{2.11}$$

The variables u_n, v_n, p_n, are the velocity components and pressure for each mode. In this model, the continuity/density equation is expressed in terms of pressure, as opposed to interface displacement for the single layer model. With $\nu = \Lambda_M/N^2$ and $\kappa = \Lambda_\rho/N^2$, viscosity and diffusivity are expressed as Newtonian cooling and Rayleigh friction in the above shallow water equations; ρ_o is the reference density for the model; F_n and G_n are the projections of the x and y components of wind stress

on each mode (discussed below). The density and the vertical momentum equations are easily derived (cf. Kundu (1990)). The phase speeds c_n are determined from the normal mode equations and depend on the N^2 profile selected.

It should be noted that Rayleigh friction and Newtonian damping depend on $1/c_n^2$. Since higher modes have slower phase speeds, they are damped at a greater rate and propagate shorter distances before they decay.

Wind stress is applied at the ocean-atmosphere interface. Wind stress may be imparted to the water column either as (1) a body force over a depth H_w, or (2) as the surface boundary condition, allowing momentum to spread downward through the water column by vertical diffusion. For wind stress applied as the surface boundary condition, Λ_M and Λ_ρ must be non-zero for the model to have physical meaning.

For the body force implementation, wind stress projections F_n and G_n are:

$$(F_n, G_n) = \frac{(\tau^x, \tau^y)}{\rho_o H_w} \frac{\int_{-H_w}^{0} \upsilon_n dz}{\int_{-D}^{0} \upsilon_n^2 dz} \tag{2.12}$$

Here, τ^x and τ^y are the horizontal components of wind stress. H_w is the depth over which wind forcing is applied as a body force. D is the total water depth and υ_n is the vertical structure function for the n^{th} mode.

For wind stress applied as a surface boundary condition, the projections onto the normal modes are given by:

$$(F_n, G_n) = \frac{(\tau^x, \tau^y)}{\rho_o \int_{-D}^{0} \upsilon_n^2 dz} \tag{2.13}$$

The model solution is obtained by summing the modal solutions (u_n, v_n, p_n) with

the vertical structure for each mode. The amplitude of each mode is dependent on the strength of the wind stress projection (i.e. the magnitudes of the F_n and G_n functions) and the damping coefficients Λ_M/c_n^2 and Λ_ρ/c_n^2. The wind stress projections on the vertical structure e_n of each mode (F_n and G_n) depend on the wind stress application method (see Figure 2.4). Lower baroclinic modes are the least influenced by the wind stress projection method. For the first and second baroclinic modes, only the 50 m bulk layer wind stress projection method yields different results from the other methods, particularly for the second baroclinic mode (Figure 2.4). Applying wind stress over a bulk layer of 50 m reduces the importance of all higher modes to negligible contributions. For the first 10 modes, the wind stress projection for the 10 m bulk layer method and surface boundary condition method give almost identical results.

2.3.3 CANDIE Model

The third model I use, and the primary model of this study, is the CANDIE model (Sheng et al., 1998) based on the DieCAST model of Dietrich et al. (1987). This model solves the 3-D non-linear Navier Stokes equations on an f-plane using the hydrostatic, Boussinesq and rigid-lid approximations. Density is used as the model tracer instead of temperature and salinity for computational feasibility. The x, y, and z momentum equations as well as the density and continuity equations are:

$$\frac{\partial u}{\partial t} + \mathcal{L}u - fv = -\frac{1}{\rho_0}\frac{\partial p}{\partial x} + \mathcal{D}_m u + \frac{\partial}{\partial z}K_z\frac{\partial u}{\partial z} \tag{2.14}$$

$$\frac{\partial v}{\partial t} + \mathcal{L}v + fu = -\frac{1}{\rho_0}\frac{\partial p}{\partial y} + \mathcal{D}_m v + \frac{\partial}{\partial z}K_z\frac{\partial v}{\partial z} \tag{2.15}$$

$$0 = -\frac{\partial p}{\partial z} - \rho g \tag{2.16}$$

$$\frac{\partial \rho}{\partial t} + \mathcal{L}\rho = \mathcal{D}_\rho \rho + \frac{\partial}{\partial z}A_z\frac{\partial \rho}{\partial z} \tag{2.17}$$

$$u_x + v_y + w_z = 0 \tag{2.18}$$

$$\tag{2.19}$$

Here $\mathcal{L}$ is the advection operator. $\mathcal{D}_m$, and $\mathcal{D}_\rho$ are the horizontal momentum operator and density diffusion operator respectively. These operators are defined as:

$$\mathcal{D}_{(m,\rho)}q = A_{(m,\rho)}\left(\frac{\partial^2 q}{\partial x^2} + \frac{\partial^2 q}{\partial y^2}\right) \tag{2.20}$$

$$\mathcal{L}q = u\frac{\partial q}{\partial x} + v\frac{\partial q}{\partial y} + w\frac{\partial q}{\partial z} \tag{2.21}$$

for a given variable q. A_m and A_ρ are respectively the horizontal viscosity and diffusivity coefficients. A_z and K_z are the vertical diffusivity and viscosity coefficients respectively.

The above equations are solved on a 3-D. Arakawa C-grid (Figure 2.5) with a time step of 5 minutes for a 1 km horizontal resolution run and 100 seconds for a 500 m horizontal resolution model run. I use quadratic bottom friction where the frictional drag on velocity is proportional to the square of the magnitude of the velocity in the bottom layer.

A free-slip or a no-slip condition is applied on the lateral land boundaries. In the free-slip boundary condition, the gradient of the shore parrallel current is set to 0 over all land boundaries. In the no-slip boundary condition, the shore parrallel velocities are set to 0 at the land boundary. In all cases there is no flux of momentum or density through the land boundaries. The sensitivity to free-slip and no-slip boundary conditions is tested in chapter 4. For all runs, apart from those in chapter 3 (the lake domain) and where indicated in chapter 4, a free slip boundary condition is used. In this thesis the use of the free-slip or the no-slip boundary condition does not change the model results significantly as will be shown in chapter 4.

Vertical and horizontal viscosity and diffusivity are set constant. The vertical resolution is 10 m throughout the water column. For an eddy viscosity of 10^{-4} m^2 s^{-1}, the upper model layer contains all of the Ekman transport.

The model solves for vertical velocity at the interface between model layers (Figure 2.5). At the model surface ($z = 0$), w is zero under the rigid lid approximation. At the bottom boundary, w is also zero in order to eliminate momentum flux through the bottom.

The surface boundary condition for wind stress is:

$$(\tau^x, \tau^y) = \rho_0 K_z \frac{\partial(u, v)}{\partial z} \tag{2.22}$$

where τ^x and τ^y are the x and y components of wind stress, K_z is vertical diffusivity and ρ_0 is a representative value for the density of water. Wind stress is applied to the top model layer at every time step. The redistribution of this imparted momentum

to deeper layers takes place by vertical mixing.

The open boundary conditions of the model are applied following Greatbatch and Otterson (1991) for a shallow water model. The upstream open boundary (in the sense of Kelvin wave propagation) is an extension of the coastline (Figure 2.6). The baroclinic and barotropic components of the velocity normal to the open boundary are treated separately. In the first instance, I set the normal gradient to zero across all boundary points for velocity (both u and v components), density and pressure. Subsequently, I remove the vertically averaged velocity normal to the boundary from local velocity at each boundary grid point. In the vertical average, there is no flow normal to the boundary. This creates divergence at the boundary and imposes small vertical velocities at the boundary from the continuity equation. The zero vertical average velocity on the boundary is consistent with the zero vertical average baroclinic mode structures (i.e. $\int_{-D}^{0} v_n dz = 0$). The Neumann boundary condition (i.e.no normal pressure gradient) proved to be sufficient in allowing propagation of disturbances out of the domain.

For non-linear runs that cover long periods of time (i.e. 10-20 days or more), I modify the vertical diffusion terms in the CANDIE model. In this case, vertical diffusion of density is applied only to departures from the initial density field. This permits background stratification to be modified by the advection terms, but not the diffusion terms. This approach is also a form of nudging the model solution to maintain the initial stratification. This avoids the necessity of including surface

heating to maintain summer stratification.

2.3.4 Boundary Conditions

All three model topographies possess three open boundaries (Figures 2.6. 2.7 and 2.8) At the northern and eastern open boundaries I apply a Neumann (no normal gradient) boundary condition on pressure (or surface elevation). On the southern boundary. a Sommerfeld radiation condition is set for the shallow water models to allow Kelvin waves to leave the domain. In the 3-D. CANDIE model. a Neumann condition is applied at all open boundaries. With the shallow water models I solve for the baroclinic modes which implies zero vertically averaged velocity. In the 3-D z-coordinate model. for comparison to the normal mode model results. I set the vertically averaged velocity at the open boundaries to zero at each model time step.

In general. open boundaries present a challenge in oceanographic numerical modeling. The problem is ill posed (Bennett and Kloeden. 1978) and all boundary conditions require simplifications of the model dynamics at the boundary of the model domain. Open boundary conditions constitute a source of inaccuracies in almost any model (Chapman. 1985). The boundary conditions applied here are passive (i.e. there is no forcing applied at the boundary) save for zeroing the vertical averaged velocity normal to the boundary in the CANDIE model. The choice of boundaries works reasonably well here. Test cases with a radiation condition on the southern open boundary showed no noticeable improvement.

2.4 Model Setup

2.4.1 Model Domain

In this thesis I apply three different model geometries. an idealized flat bottomed square embayment (Figure 2.6). an idealized flat bottomed rectangular embayment (Figure 2.7). and the realistic geometry of Trinity and Conception Bays (Figure 2.8). In the latter. realistic geometry case. I use either realistic bottom topography or a flat bottomed version that retains the realistic coastline geometry. For those model runs that use a flat bottom. the depth is 200 m. The average depth of Conception Bay is about 200 m although the maximum depth is roughly 290 m. The realistic bottom topography (Figure 2.8) is applied for some of the runs using the 3-D CANDIE model. In all cases. the model's upstream open boundary (in the sense of Kelvin wave propagation) is an extension of the northern coastline. as in Greatbatch and Otterson (1991).

Hsieh et al. (1983) show that if the model horizontal grid spacing exceeds the Rossby radius of deformation. spurious spatial oscillations start to occur. The use of 500 m grid spacing ensures proper resolution of the radius of deformation for the first 10 baroclinic modes (from 5 km to 500 m) (see Figure 2.2). Modes greater than 10 are assumed to have a negligible contribution to the overall solution.

2.4.2 Wind Forcing

Wind forcing in the model is either specified for idealized studies or computed from observed wind speed. I ignore orographic effects and assume that the wind is spatially homogeneous over Trinity and Conception Bays as in de Young et al. (1993b). While the Rossby radius of deformation in the atmosphere is around 1000 km, orographic effects do affect wind locally on smaller scales (Smith and MacPherson, 1987). However, in the absence of any spatial coverage of wind observations, I make use of the most comprehensive data set for wind speed and direction in this region. Hourly wind observations are made by Environment Canada at St. John's airport, which is situated 10 km to the east of Conception Bay (Figure 1).

Wind stress calculations require winds velocities to be specified 10 m above the ocean-air surface, which I determine in the following manner. Observed wind speed data at St. John's are multiplied by a correction factor of 1.25 to account for the difference in wind speed over the ocean relative to land (Smith and MacPherson, 1987). Wind speed is then converted to wind stress according to the quadratic formulation of Large and Pond (1981). I low-pass filter wind stress to remove signals at periods shorter than 32 hours. The filter is run forward and backward over the data to remove any effects of phase distortion by the filter. The last modification involves the application of a smooth ramping function over the first two days of the computed wind stress data. This procedure avoids exciting Poincaré waves of near-inertial frequency when the wind stress time series is initially applied to the model (Pollard and Millard,

1970).

Wind stress calculated following the above approach is shown in Figure 2.9 for the year 1990 and 1994. The y-axis points 30° east of north so that it is aligned with the axis of the bay. The time period shown covers roughly 60 days starting at Julian day 145 (May 24th). This time period coincides with mooring deployments during June and July of these two years.

Winds show similar characteristics over both observation periods Wind blows out of the bay for periods of 3-6 days with weak winds in between. In both years there are a few short episodes (1-3 days) of light winds blowing into the bay with magnitudes of less than 0.1 Pa. Throughout the two periods of observations, peak wind strength subsides from 0.4 Pa in early June to 0.2 Pa towards the end of July (Figure 2.9).

Analysis of the historical records of wind speed at St.John's airport from 1953-1992 shows that during the summer the frequency of southwesterly wind increases while the frequency of northeasterly winds decreases. Monthly binned wind speeds over the 40 year record show a drop in maximum wind speeds from 40 m s^{-1} in February to a minimum 20 m s^{-1} in August. Mean, monthly binned wind speeds also show a minimum in the summer of 6 m s^{-1}, compared to 8 m s^{-1}speeds in the winter.

Most of the wind energy occurs at periods of 2 to 5 days. Figure 2.10 shows the power spectrum for the unfiltered wind stress for the 50-60 day period of interest (June and July) in 1990 and 1994. In both cases, there is a broad peak in energy at roughly 5 days (0.2 cpd). Also noticeable is a small peak at roughly 1 cycle per day.

I surmise that this approximately diel peak is due to the daily cycle of sea breeze brought on by the differential heating rates of air above land and above the ocean. In this study, however, I am interested in the effect of wind driven circulation at the dominant frequency band 0.2-0.5 cycles per day (cpd) as seen in Figure 2.10. I therefore use filtered wind stress to remove energy below the 32 hr time period.

2.4.3 Model Initialization

All model runs are initialized at rest (i.e. no motion) with horizontally uniform stratification. In the reduced-gravity model this means that the initial upper layer depth is uniform at 40 m. For the normal mode model, the pressure anomaly for each mode is initially zero. In the 3-D model, the initial density stratification is specified.

The model is run with spatially uniform wind stress, which may be time dependent (based on observations at St. John's Airport), or fixed. In all cases, wind stress is introduced over 2 days using a hyperbolic tangent ramping function. This smoothed application of wind stress avoids exciting near-inertial oscillations (Pollard and Millard, 1970). We start measuring time when wind reaches 50% strength (i.e. after 1 day).

2.5 Observations in Conception and Trinity Bays

In this section, I present the observational data from Conception Bay with which model results are compared. Four types of data are used and are presented in the

following order: Mooring results, ADCP transects across the bay, HF coastal radar (CODAR) survey of surface velocities, and satellite based SST image observations for the Avalon Peninsula including Trinity and Conception Bay.

2.5.1 Current Moorings

I use observations from current moorings deployed in 1990 and 1994 in Conception Bay at the head of the bay (Figure 2.11a) and nearer to the mouth (Figure 2.11b). The moorings deployed in 1990 were part of the Cold Ocean Productivity Experiment (COPE). The 1994 data were collected as part of a joint project with the Department of Fisheries and Oceans and have not been previously published.

A discussion of the 1990 data set is given by Otterson (1992). Figure 2.12 shows the vertical temperature structure from Julian day 150 to 200 (June and July) at 3 mooring locations: H2 on the west side of the bay, H4 at the head of the bay, and H6 on the eastern side of the bay near Bell Island. Bottom depths at the mooring locations are 148 m, 151 m and 100 m for moorings H2, H4 and H6, respectively. These moorings are roughly 16 km (H2-H4) and 18 km (H4-H6) apart. While the moorings were deployed from Julian day 110 to 203 in 1990, the analysis presented here is limited to the summer months when the water column is well stratified.

Thermocline

Throughout June and July, the increasing stratification trend is clearly visible in Figure 2.12. Over the 50 days, several strong downwelling events are apparent (i.e. days 148, 158, 173 and 188) on the west side of the bay (H2), and at the head of the bay (H4). These same downwelling events are also present at H6 on the east side of the bay, but with lower amplitudes, particularly near the surface at 25 m depth.

A common trend among the three moorings in Figure 2.12 is that thermocline variability at depth (60 m) may lead, by up to 2 days, the near-surface signal at 25 m. For example, at H2 around day 174, the 2 °C isotherm reaches a local maximum depth about one day before the 5 °C isotherm reaches a maximum depth.

On the eastern side of the bay (H6), isotherm displacements are relatively small on the 5 day time scale (compared to the west side). However, short term oscillations with periods less than 2 days are more visible here than at H2 and H4 (e.g. compare the 2 °C isotherm).

The 1990 contour plots exhibit larger vertical deflections of the isotherms at depth which reflects the decline in water column stability with depth, as shown by the N^2 profile in Figure 2.1.

The response of the thermocline at the head of the bay to wind forcing is expected to be amplified (Yao, 1986). This is a linear effect due to the length of the upstream coastline along which upwelling continues to develop until a Kelvin wave arrests it. Such events have been commented on by Otterson (1992) and are related to wind-

driven upwelling. The reduced-gravity model of Otterson (1992) reproduces the major upwelling and downwelling events from day 170 onwards at H4 (20 m depth 1990).

In 1994, moorings were deployed along the north-west shore of Conception Bay. Temperature at depths ranging between 12 m to 80 m were recorded. Figure 2.13 shows the vertical isotherm distribution over time for 3 moorings (W1,W4 and W7 in Figure 2.11) placed following the 100 m isobath from near the mouth (W1) towards the head of the bay (W7). The horizontal along-shore spacing between the moorings is roughly 18 km.

At W1 near the mouth of the bay, thermal stratification is stronger than at W7 near the head (Figure 2.13). Furthermore the -1 °C isotherm is shallower by roughly 20 m at W1 than observed at W7, suggesting that at a depth of 50 m, the temperatures decrease towards the mouth of the bay. Mean temperature profiles from day 180-212 at W1 and W4 show similar structure (Figure 2.14), with a strong temperature gradient (3.4 °C per 10 m) down to 40 m, and a weaker gradient (0.3 °C per 10 m) below this. At W7, temperature is more weakly stratified with a vertical temperature gradient hovering around 1.8 °C per 10 m throughout the water column. Thus the vertical mean temperature structure (day 180-212) at W7 (inside the bay) is less stratified than at W1 (at the mouth). Prior to day 180, mean vertical temperature structures are similar except that W7 is warmer by 1 °C at all depths.

There is a significant difference in the variability of the thermocline structure between moorings located along the axis of the bay. At W1, the amplitude of the

vertical isotherm displacements seem relatively depth invariant (Figure 2.13). The variability of the -1 °C isotherm is similar to that of isotherms near the surface around day 185. In contrast, at W7 the amplitude of the thermocline displacement increases appreciably with depth.

At W7, the amplitude of isotherm vertical displacements is larger by roughly a factor of 2 than near the mouth at W1. For example, at day 205 there is the strongest and most sudden downwelling event on record at W7 with the 2 °C isotherm dropping 33 m in depth, whereas at W1 the event is not as strong with the 2 °C isotherm dropping by 14 m (Figure 2.13). Two factors may contribute to the along-bay variability of the amplitude of the isotherm vertical displacements. These are, an increase of upwelling intensity with distance into the bay (i.e. longer upwelling favourable coastline) and an along-bay variability of water column stability (inferred from Figure 2.14) with increased stability towards the mouth of the bay due to advective influence of cold sub-surface water by the Labrador Current.

In the last part of the record, shown near day 209 there is an interesting downwelling event near the mouth of the bay (W1 Figure 2.13), when the near surface response leads by 1.5 days the response at depth. Furthermore the increased amplitude of isotherm displacement with depth, contrasts with the events observed prior to day 209 at this location. At W7, further into the bay, the same downwelling event, shows no lag in the response with increased depth.

Surface density decreases over the summer period (Petrie et al., 1992a). Surface

stratification sets in throughout June and July. I thus expect the buoyancy frequency in the surface layers to increase with time, increasing wave propagation speed and the Rossby radius of deformation. With increased stratification, the magnitude of thermocline displacement will decrease.

From the current moorings, near-surface (14 m) salinity is observed to decrease over the summer (not shown) in agreement with Myers and Akenhead (1990) who show that spring ice melt of the Labrador Shelf drives a surge of fresh water moving down the coast of Labrador towards Newfoundland. At Station 27, a salinity minimum near the surface is observed in early fall, and 5 months later at depth (Petrie *et al.*, 1992). Thus while salinity is not properly resolved in the mooring arrays for incorporation into a density profile, salinity does play a role in the stratification of Conception Bay, particularly at the mouth which is most susceptible to the influence of the Labrador Current's inshore branch.

Velocities

Figure 2.15 shows mean currents and the principal axis of standard deviation of the 6 moorings deployed around the head of the bay in 1990. At 20 m depth (Figure 2.15a), mean currents exhibit a clockwise circulation pattern at the head of Conception Bay. These mean currents of up to 3 cm s^{-1} are strongest near the head and on the eastern side of the bay. At the outermost moorings, H1 and H6, mean currents are roughly 1 and 0.4 cm s^{-1}.

At 80 m depth, the mean circulation pattern consists of relatively strong outflow parallel to the topography in the middle of the bay with mean speeds greater than that observed at the surface (20 m) (Figure 2.15b). At this depth, the strongest mean currents are found at the outermost moorings in the middle of the bay. Although mean currents generally weaken with depth, they increase at H2 from 2.4 to 3.6 cm s^{-1} and at H6 from 0.4 to 1.3 cm s^{-1} respectively. Except at these two moorings, other mean currents at 80 m depth range from 0.2 cm s^{-1} to 0.7 cm s^{-1}.

There is a conspicuous trend in current variability in the 1990 moorings observations (Figure 2.15a). On the west side of the bay (Moorings H1-H3), currents are steered by topography with the eccentricity of the principal axis (minimum/maximum axis of standard deviation) varying between 0.55 and 0.3. On the eastern side and at the head (H4-H6), currents are less directional with principal axis eccentricities ranging from 0.7 to 1. On the west side of the bay, away from the head (moorings H1 and H2), maximum flow variation crosses slightly the isobaths, while further in the bay (H3), maximum current variability is parallel to the topography. Standard deviations of velocity are greatest on the west side of the bay with values 6-11 cm s^{-1}. They are weakest at the head and on the eastern side, with values ranging from 4.3 to 4.5 cm s^{-1}.

At 80 m depth, the principal axis of standard deviation is lined up with bottom topography with weak cross-shore variability. Standard deviations are generally 2-10 times weaker (i.e. less than 1 cm s^{-1}) than at the surface. The exception is H6 where

the standard deviation is comparable to the surface value of 4.5 cm s^{-1}. At the head of the bay (H4), the standard deviation of currents is less than 1 cm s^{-1} with a principal axis eccentricity of 1. Generally at 80 m, standard deviations are comparable or less than the mean with the exception of H2 that has a mean of 3.6 cm s^{-1} and a standard deviation of 2.2 cm s^{-1}.

The 1994 data set on the western side of the bay provides a description of the cross-shore and along-shore variability in velocity. Figure 2.16a shows the means and principal axis for velocity observed at 13 m depth from days 150 to 210. Figure 2.16b features a simplified vertical cross-section of the mooring line W2-W6 seen in Figure 2.16b.

Mean velocities at a depth of 13 m vary with weak into the bay flow of 0.9 cm s^{-1} within 3 km of the shore. From 4 to 9 km away from shore, mean velocities are directed out of the bay with magnitudes between 1 and 4 cm s^{-1}. Eleven kilometres from shore (W6) the mean current is directed away from the coast at 2 cm s^{-1}.

The most variable currents are found near-shore within 5 km of the coast with standard deviations from 10 to 14 cm s^{-1}(H2, H3, H4 and H7). Here maximum velocities are found at H3 and H7 with standard deviations of roughly 14 cm s^{-1}. A clockwise shift of the principal axis direction is evident with offshore distance. The eccentricity of the principal axis varies from 0.2 to 0.6 with offshore distance due to the presence of the shoreline.

The observations at W1 do not match those elsewhere in the bay (and discussed

above). Here the standard deviation of currents is weak (5 cm s^{-1}) although the mooring is within 5 km of the shore. The differences at W1 are probably due to its position at the mouth of the bay where it is subject to forcings from outside the bay.

The data reveal a strong depth dependence to the mean currents (Figure 2.16b). Within 4 km of the coastline. mean currents at 33 m depth are directed into the bay with maximum velocities of 1.6 cm s^{-1}. This is roughly twice the surface values of 0.9 cm s^{-1}.

There is a general trend of current direction shifting to the right with depth over the entire mooring array. Mean currents above the bottom at W3. W4 and W5 increase in magnitude from 1 to 3 cm s^{-1} with offshore distance (and depth). These bottom currents are directed straight into the bay. The largest mean currents (about 3 cm s^{-1}) are observed just above the bottom at a depth of 160 m.

Near the surface, beyond 3 km offshore (at W4 and W5). mean surface currents (13 and 33 m) of 1.2 cm $s^{-1}$are directed out of the bay in the opposite direction of near bottom currents. At 80 m mean currents of 1.5 cm $s^{-1}$are directed into the bay and offshore (W5 and W6).

The magnitude of the principal axis of standard deviation decreases roughly 30-50% between 13 and 33 m depth with the greatest variation at W2 with a bottom depth of 41 m. The direction of the principal axis varies little with depth in contrast to the trend in mean current direction. The smallest magnitudes of standard deviations are at 80 m depth 8-11 km offshore.

In the cross-shore direction, the de-correlation length scale is roughly 5 km (i.e. cross-shore distance between two moorings for which the correlation coefficient of the two temperature time series drops by $1/e$). In the along-shore direction, the de-correlation length scale is greater than 10 km. Coherence in along-shore velocity and temperature is significant between the moorings at the head of the Bay (H1, H2, H3 and H4), as discussed in Otterson (1992) and de Young and Sanderson (1995).

In summary, summer-time mean currents in Conception Bay are weak with mean speeds less than 3 cm s^{-1} in all the available records. A clockwise mean circulation is observed around the head of the bay. On the western side of the bay, mean currents are directed out of bay except near-shore within 3 km where the flow is weak and directed into the bay.

Current variability is high with respect to the mean at the surface, but variability decreases with depth with the standard deviations becoming comparable in magnitude to the mean current (2-5 cm s^{-1}) near the bottom at 130 m to 160 m depth. Maximum mean current strengths of 3 cm s^{-1} appear in deep water within 25 m of the bottom. Current variability near the mouth seems to be influenced by forcing from outside the bay.

2.5.2 Acoustic Doppler Current Profiler Data

ADCP velocity transects across Conception Bay near the mouth in late July of 1994 provide data with high horizontal resolution of 250 m and a high vertical res-

olution of 4 m. These data (Figures 2.17 and 2.18) were obtained using a 150 kHz RDI ADCP system run in bottom tracking mode. Straight line transects were carried out along different lines several times during the 1994 mooring deployment. Comparisons of cross-bay structure with the time dependent CANDIE model are presented in Chapter 5.

In each of the plots (Figures 2.17 and 2.18) the corresponding wind stress time series is shown in the bottom left corner. On 18 July, wind has been blowing straight out of the bay for a day with a maximum wind stress of 0.2 Pa. The cross sections on July 19th (Figures 2.17b) reveal a strong jet of current into the bay on the eastern side of bay near the mouth with strong currents away from shore (Figure 2.17A). The jet is centered in the top 50 m roughly 2km off-shore. Substantial flow 1-2 km in width with an in the bay velocity of 10 cm s^{-1} extends down to the bottom at 120 m. The u-component of velocity indicates strong offshore currents greater than 15 cm s^{-1} within 4 km of shore, with small onshore flow (6 cm s^{-1}) beyond this point.

The structure of the cross-bay (u) velocity field on July 19^{th} is interesting (Figure 2.17A). Here, near-shore velocities are towards the coast, whereas beyond 5 km from the coast, flow is offshore with strongest flow near the bottom (15 cm s^{-1}). The flow pattern of the transects often show several reversals of current with depth indicating the possible importance of higher modes, or perhaps flow instability. Further evidence of higher modes is observed in Figures 2.17A and B on the east coast of the bay (x= 23 km) where the width of the jet decreases with depth.

On July 21st (Figures 2.17C and D), surface cross-bay currents are strong with westward flow up to 20 cm s^{-1} in the middle of the bay. Strong currents (> 15 cm s^{-1}) are confined to the top 30 m of the water column except on the east coast where there is a mid-bay ridge extending north from Bell Island. Here currents are outwards and westwards across the bay. This strong flow is confined to the ridge. In Figure 2.17 numerous small jets on the west side of the transects show maxima at 20-30 m in depth rather than at the surface (5 m).

Two transects were run across Conception Bay on July 22nd: one across the mouth, and the other 5 km inside the bay (Figure 2.18). For the cross-bay components of velocity both transects show similarities. There is strong eastward flow within 5 km of both shores. Near the centre of the bay, there is a divergence of the u-velocity component with west-ward and eastward flow from the center of the bay. There is very little vertical shear at 16 km off shore in Figure 2.18A and at 10 km in Figure 2.18C, perhaps indicating barotropic flow structure at these locations.

The v-components of velocity differ in structure in both transects taken on July 22nd (Figure 2.18). Particularly on the western side of the bay, near-shore velocities are into the bay at the mouth and are pointed out of the bay 5 km further in from the mouth (Figures 2.18d). Furthermore, along-bay velocities on the eastern side are stronger 5 km inside the bay then at the mouth and have substantial near shore velocities at depth

The differences in transects near and at the mouth of Conception Bay suggest

short spatial scale events such as eddies or separation of jets from the coast near the mouth. Both transects were completed consecutively with each transect taking about 2-3 hrs to complete. thus. the two transects are separated in time by roughly 2-3 hours.

The ADCP sections reveal velocities greater than 15 cm s^{-1} within 5 km of land, trapped above isolated topography (Figure 2.17d for example) or in the surface 40 m layer (Figure 2.17c). In summary, the ADCP observations show that currents are dynamic with vertical patterns over the entire water column changing from one day to the next (Figure 2.17) and between vertical transects 5 km apart taken the same day (Figure 2.18).

2.5.3 CODAR Data

Theory

Coastal Ocean Dynamics Applications Radar (CODAR) makes use of the backscatter of electromagnetic radiation from ocean surface waves to extract surface current information. Sea surface gravity waves can act as a diffraction grating for radio waves (Crombie. 1955), particularly for the 3-30 MHz radio band known as the HF band (Barrick et al.. 1985: Hickey et al.. 1994).

Surface gravity waves on the ocean with a wavelength λ_w will reflect back radio waves at grazing incidence of wave length λ_r if $\lambda_w = \lambda_r/2$. This is the Bragg condition for constructive interference of the reflected radio waves.

The scattering of radio waves satisfies

$$\vec{k}_s = \vec{k}_i \pm \vec{k}_w \tag{2.23}$$

where $\vec{k}_s$ is the scattered (radio) wave number, $\vec{k}_i$ is the incident (radio) wave number and $\vec{k}_w$ is the ocean surface gravity wave number. The Doppler frequency shift between the scattered and incident radio wave is $\Delta\omega_o$ with

$$\Delta\omega_o = \pm\omega_w = \omega_s - \omega_i \tag{2.24}$$

where ω_w is the frequency of the surface gravity wave.

For the data in this section, the CODAR system used had an incident radio frequency of 25.4 MHz for which the corresponding radio wave length is 11.8 m. The corresponding wavelength λ_w of the surface gravity wave is 5.9 m allowing the deep water approximation for surface gravity waves. The phase speed of the surface gravity wave satisfying the Bragg condition is

$$c_w = \sqrt{\frac{g\lambda_w}{2\pi}} = \sqrt{\frac{g\lambda_r}{4\pi}} \tag{2.25}$$

where g is the gravitational acceleration (9.81 m s^{-1}). The phase speed of the waves that scatter the 25.4 Mhz frequency is roughly 3 m s^{-1}.

The CODAR system measures the Doppler shift ($\Delta\omega_{obs}$) between the scattered and incident HF wave. This shift is due to the phase speed of the surface gravity wave and the component of surface current v parallel to the incident radio wave. This radial component of surface current can be measured by comparing the observed frequency shift $\Delta\omega_{obs}$ with the theoretical value for wave scattering $\Delta\omega_o$.

The surface velocity is given by

$$v = (c_{obs} - c_w) = k_w^{-1}(\omega_{obs} - \omega_w) = \Delta f \frac{\lambda_r}{2} \tag{2.26}$$

where c_{obs} and c_w are the observed phase speed by the radar array and the phase speed of a surface gravity wave of wavelength $\lambda_r/2$. Here Δf is the frequency shift between the observed and Bragg diffraction peaks. The measured "surface" velocity v is representative over a depth of thickness $\frac{\lambda_r}{4\pi}$ (Stewart and Joy, 1974) which is roughly the depth over which the amplitude of the horizontal velocities associated with surface gravity waves decay by 50% .

The CODAR data used in this thesis were provided courtesy of Dr. Jim Helbig (Department of Fisheries and Oceans). The observations for Conception Bay were made using two radar antenna arrays set up roughly 25 km apart on the western side of the bay (see solid dots in Figure 2.19). Each array collected range, bearing and wave speed. A robust least squares fit was used to fit data to a grid using the radial data from both radar sites to give estimates of horizontal currents. These grided data were linearly interpolated in time over data gaps. The two antenna arrays consisted of 4 antennae of length $\lambda_r/4$ arranged at the corners of a square $0.8\lambda_r/2$ in width (Jeans and Donnelly, 1986). Pulses were emitted in 8 μs bursts with the receiving antennas range gated into 8 μs bins providing a resolution of 1.2 km. Bearing of the backscattered signal was calculated by phase comparison among the array's 4 receiving antennae.

Velocity Fields

CODAR data were collected hourly, but were low-pass filtered (with a 5 weight Butterworth filer) and are plotted at mid-day (noon local time) for each day (Figures 2.19 and 2.20). The time in the wind feather plots indicates the day at 12 noon (Figures 2.19 and 2.20). Velocity patterns over the 17 day observation period show a strong correspondence to wind forcing magnitude and direction. CODAR derived surface velocities for Conception Bay appear to react within 6 hours hours to wind. Large peaks in wind stress magnitude preceded bay averaged peak velocity magnitudes by roughly 6 hrs (not shown). For days with strong winds directed out of the bay, currents inside the bay are directed outwards and veer to the right near the mouth. This circulation pattern is evident on July 11th and July 17th when winds of 0.12 Pa and 0.2 Pa are directed roughly 30° to the right from the positive (along-bay) y axis. Also during weaker wind periods (less than 0.05 Pa) gyre type features are visible in the bay. For instance, after July 11th, the strong out of the flow relaxes giving way to a gyre type flow in the bay that persists for another few days to July 14th. During weak wind conditions, undulating jets with currents of roughly 15 cm s^{-1}can also be seen in the bay. There is a coastal jet directed out of the bay that appears on days when winds are directed out of the bay (i.e. 18 July). In particular, on July 2nd (Figure 2.19) the coastal jet on the western side of the bay separates from the shore 10 km inside the mouth of the bay.

Length Scale of Velocity Fields

Figures 2.21 and 2.22 show the e-folding length scale ($L\sigma$) for the variance of the u and v components of velocity from the CODAR data with respect to the along-bay position. The y-axis represents $L\sigma$, the distance over which the variance between two points decreases to 1/e. The variance was used instead of the correlation coefficient r because the latter decayed too slowly with respect to the total length of the transect (40km). The x-axis represents the along-bay distance as seen in the location plot to the right of Figure 2.21.

For the u (cross-bay) component of velocity, the along-shore length scale $L\sigma$ is roughly 4-6 km up to 20 km from the head of the bay and beyond 35 km. Between 20-35 km the length scale is higher, approximately 10 km. For the along-bay component of velocity (v), the along-bay length scale is high with a value of 16 km near the center of the bay, dropping by half to 7 km near the mouth (beyond 40 km).

Two more transects were explored, one on the west, the other on the eastern side of the bay (Figure 2.22). On the west side of the bay, the e-folding length scale ($L\sigma$) for the u-component of velocity increases from 3 km near the head to 6-7 km towards the mouth. In contrast, the e-folding length scale of the v-component of velocity is around 22 km near the head, decreasing gradually towards the mouth to a value of 16 km, and dropping off suddenly at the mouth to a value of 7 km.

On the eastern side of the bay (Figure 2.22 solid line), the length scale of the u component is slightly greater than that for the v-component. The length scale $L\sigma$

varies around 10 km at the center of the bay, and decreases near the head and towards the mouth below to values ranging between 4 to 7 km.

2.5.4 Sea Surface Temperature over the Avalon

To provide the best synoptic picture of sea surface temperature in the region, I make use of Advanced Very High Resolution Radiometry (AVHRR) observations from NOAA satellites. AVHRR sensors (radiometers) measure the skin temperature of the ocean surface which is the temperature of the top millimeter (absorption length scale of IR radiation in the ocean) of the water column (Robinson, 1995). The wavelength band labeled as infrared covers the 1 μm to 1 mm wavelength range.

A radiometer measures the intensity of incoming radiation over a specific wave length interval within a near normal solid-angular incidence width of 1.3 mrad called the instantaneous field of view (IFOV) (Robinson, 1995). Usually the radiometer is fixed facing a rotating mirror that reflects incoming radiation. Over time, with the mirror's axis of rotation parallel to the satellite track, the mirror exposes the radiometer to a swath of width 2580 km at the surface of the earth perpendicular to the satellite's orbital track. The NOAA satellites offer a resolution on the ground of the instantaneous field of view of the sensor that is about 1 km at the surface of the earth directly below the satellite (i.e. at nadir) (Robinson, 1995).

An object emits radiation that depends on its temperature and its composition. For sea surface temperature observations, radiation at the 10.3-11.3 and 11.5-12.5

μm infrared wave band are used for several reasons. This band features the peak intensity of the emitted black body radiation spectrum for 300 K (i.e. 27 °C) water. The atmosphere is nearly transparent to radiation at this wavelength, and there is also little reflected radiation off the ocean from sun at this wavelength. Thus, the dominant source of radiation propagating upward from the earth in this wave band is "black body" radiation from the ocean.

Empirically tested algorithms have been tested to transfer the radiance measurements indicative of the ocean skin temperature into a value of sea surface temperature representing the top 1 m in the ocean (Cornillion et al., 1987). The atmosphere does play some role in modifying the observed ocean emitted IR radiation and algorithms are applied to account for atmospheric effects. Clouds in particular, can contaminate an SST image. Water vapour in clouds absorb ocean emitted IR radiation and re-emits the radiation at other frequencies. This phenomenon contributes to underestimating the sea surface temperature in cloudy locations (Robinson, 1964).

Distinguishing between cold surface water and cloud cover has evolved almost into an art form. I looked for cloud presence over land, which is easier to distinguish than cloud presence over water. If islands and coastline shape are clearly visible in the image, and no clouds appear over land, this is an indicator that the image is cloud free. Land appears as very warm temperatures (> 25 °C) on the image. Cloud cover stands out more clearly over land than water.

The AVHRR data used here come from the Graduate School of Oceanography

at the University of Rhode Island (URI) (courtesy of Dr. Peter Cornillion), who provide an AVHRR image archive in cooperation with RSMAS in Miami. Twenty seven relatively cloud free images (some taken on the same day) were collected for the region out of a total of roughly 100 images available for July and August of 1997 and 1998. The primary purpose of these data is to illustrate sea surface temperature patterns during the summer. I am not interested in absolute temperature readings, but am looking for good relative temperature detection in order to distinguish cold up-welled water from warmer surface water. Therefore an exact knowledge of atmospheric influence on the data is not necessary provided these influences are spatially uniform over the area of interest. A recent study shows that for NOAA AVHRR data, the IR radiometer can distinguish sensor temperature differences of 0.2 °C (Ullmann et al., 1998). In Conception Bay, in-situ temperature observations vary from -1 °C at depth to 14 °C near the surface providing a strong temperature contrast between up-welled water and warm surface water. Thus with a relative temperature accuracy of 0.2 °C, the SST imagery can clearly distinguish upwelling fronts in this region.

The SST image is affected by the time of day of the satellite pass over the Avalon Peninsula. Most images were taken between 3 pm and 6 pm local time. In the mid-afternoon images, islands are clearly visible, whereas in the evening land and warm ocean areas (~12 °C) are less easily distinguished. Islands are not apparent in the evening images. We surmise that the apparent temperature over land drops as the angle of the sun decreases towards the horizon.

As noted earlier, in the summer, the wind direction is primarily from the south-west with occasional winds from the north-east (see Figure 2.9). Wind from the south-west generally implies clear weather in this region, whereas winds from the north-east favour cold overcast weather on the Avalon Peninsula. I conjecture that cloud free images tend to be biased to conditions when winds blow from the south-west. In all of the 27 cloud free images, wind direction (from St. John's airport) is either from the west, southwest or from the south. Of these 27 cloud free images, 24 of them exhibit an upwelling pattern consistent with south-westerly winds (the most common wind direction). For the images in which cloud cover hinders the determination of SST, winds are blowing from the north-east 6 times out of 14.

In the images with south-west winds, upwelling occurs along coastlines parallel and to the left of the wind direction (Figure 2.23). There are three areas with consistent strong upwelling visible throughout the images. These areas are the north-west coast of Trinity Bay, Cape Race and the southern tip of the Burin Peninsula (Figure 2.23) with upwelling observed at these sites in 24, 21 and 18 images respectively (out of 27). Weaker upwelling is observed in St. Mary's Bay in 13 images and also in Conception Bay in 10 images. Figure 2.23 qualitatively shows that Trinity Bay features the largest area of cold upwelled water in the region. Figure 2.23A shows upwelling on the east coast of the Avalon from Cape St. Francis southwards. The 3 dark spots in this figure north-east of St. John's are probably isolated clouds. In Figure 2.24b pixel width is approximately 2 km, while all other images shown have full 1 km resolution data.

In this thesis. I concentrate on Trinity and Conception Bays, however SST images of coastal sea surface upwelling around the entire Avalon Peninsula are presented. Including Placentia and Cape Race into our SST observations both supports and validates that upwelling is indeed observed in Trinity Bay (and is not some artifact due to cloud distribution).

Figure 2.24 shows the sea surface temperature in Trinity and Conception Bays for 4 images taken in late July (23rd and 28th) and early August (2nd and 11th). The corresponding wind stress time series at the bottom of Figure 2.24 shows that winds blowing weakly out of the bay for the first 3 images with a magnitude of less than 0.02 Pa. In the 4th image on day 223. winds are stronger with magnitudes of 0.1 Pa. The extent of cold upwelled water is linked to wind strength (Figure 2.24.

In 26 of 27 images collected (not all are shown). the surface temperature of Trinity Bay is cooler than in Conception Bay as (Figure 2.24). In fact. upwelling in Trinity Bay. is the predominant pattern in all of the images except for one in which the two bays show equal and uniform temperature distribution.

The pattern observed in both bays is that of cold water on the northwestern side of the bays and warmer water on the south-eastern side of the bays. In particular. on the eastern side of Conception Bay. around Bell Island. warmer surface temperatures (greater than 15 °C) are observed. This happens to be a region of shallow topography with an average depth of 50 m. The pattern observed in both bays is consistent with winds blowing across the bays from the southwest. the dominant wind direction during

the summer.

The along-shore distribution of upwelled water ($T < 2$ °C with dark pink colour) in Trinity Bay, is patchy with a length scale varying between 5 and 25 km in length. Furthermore, the cross-shore extent of upwelled water accompanied by fingers of cold water (most visible in Figure 2.24c) extending almost across the entire bay (25-30 km).

2.6 Summary

In this chapter I have presented the models I will use in this thesis and presented available oceanographic observations for Trinity and Conception Bays. The data gathered here is extensive and comprises of current mooring observations, CODAR observations, ADCP transects and SST imagery. The data are further discussed in chapter 5 for comparisons with the time dependent model runs.

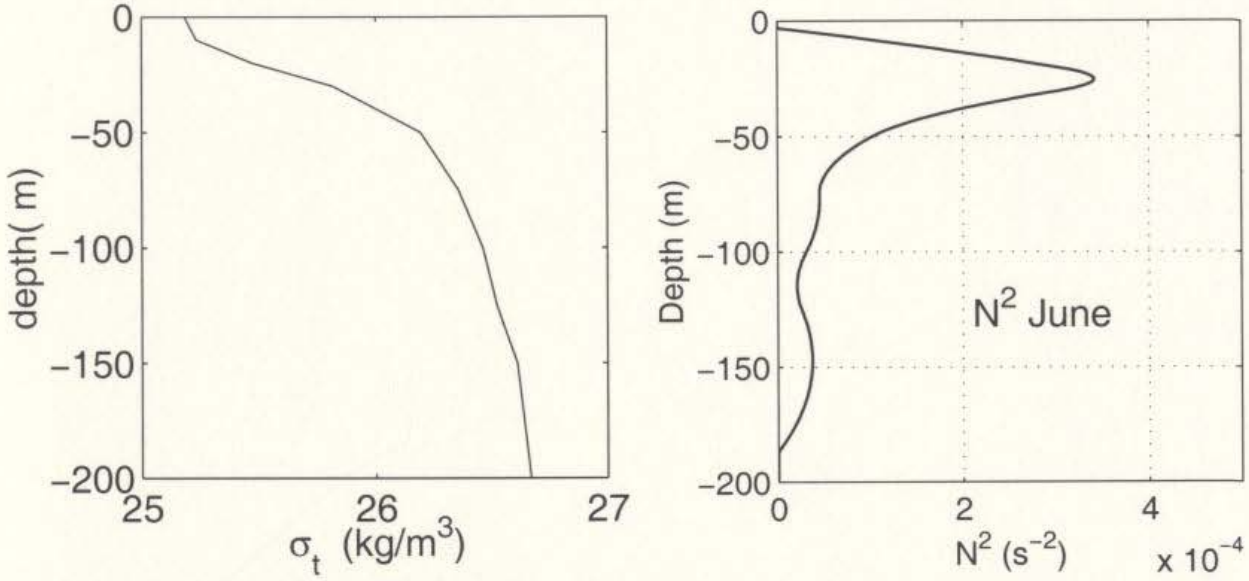

Figure 2.1: (a) The 40 year, average density for the month of June at Sta 27. (b) Corresponding N^2 profile for plot(a). Density was interpolated to 1 m and smoothed before calculating N^2.

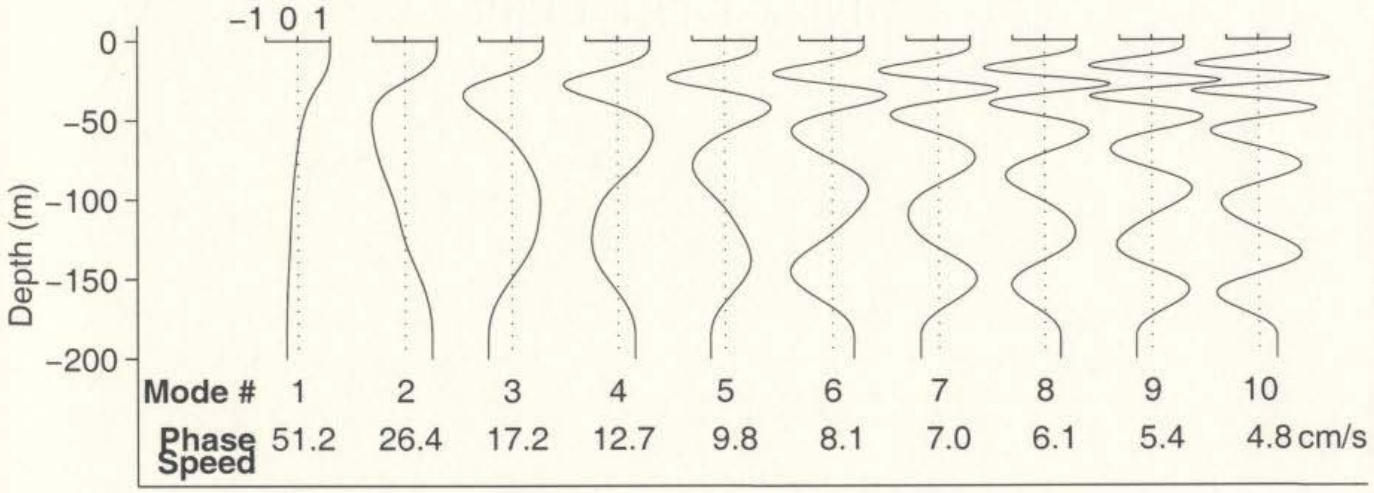

Figure 2.2: Normalized modal structure $\psi_n(z)$ of the first 10 baroclinic modes. The amplitude scale is shown at the top of each modal structure.

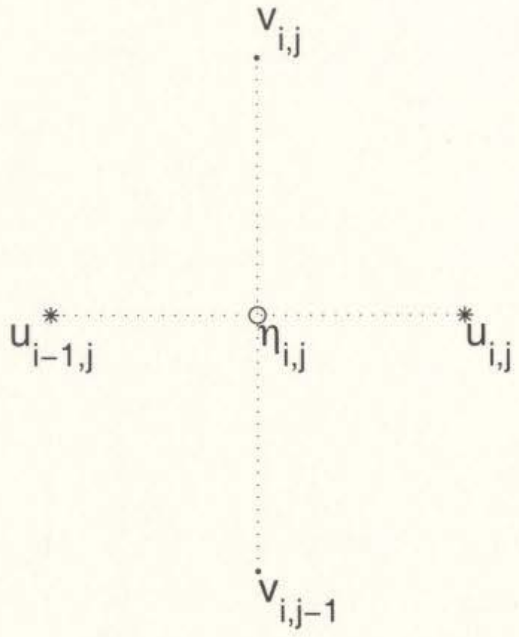

Figure 2.3: Grid sheme diagram for 2-D shallow water models (Arakawa C-grid).

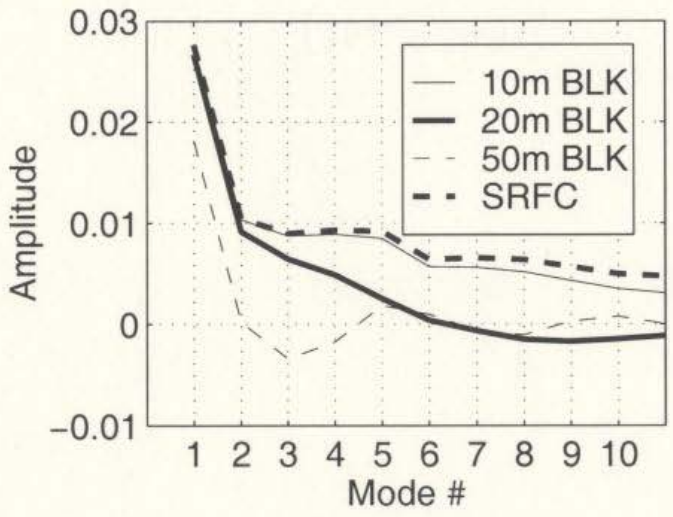

Figure 2.4: Projections of wind stress on the first 10 baroclinic normal modes. The amplitude of the projection determines the importance of each mode in the wind-driven response. The label BLK refers to treating the wind as a body force. SRFC specifies the wind stress as a surface boundary condition. The 10 m body force and the surface wind stress methods resemble each other the most. Applying the wind over a deeper layer reduces the influence of higher modes.

Figure 2.5: C-grid sheme for 3-D CANDIE MODEL.

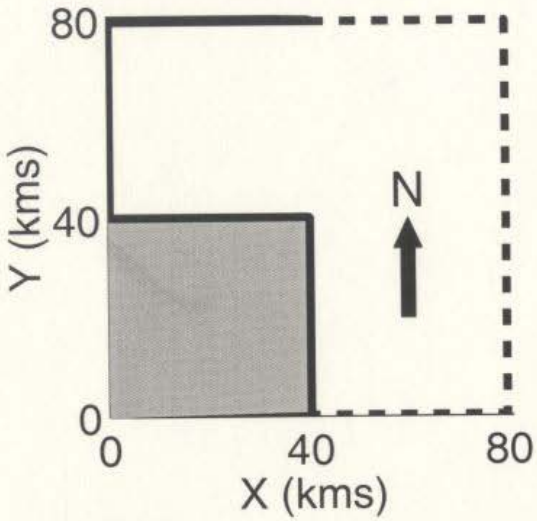

Figure 2.6: Idealized model topography of a square bay. Open boundaries of the domain are indicated by dashed lines. Solid lines indicate closed boundaries. Bottom depth is 200 m for the continuously stratified normal mode model.

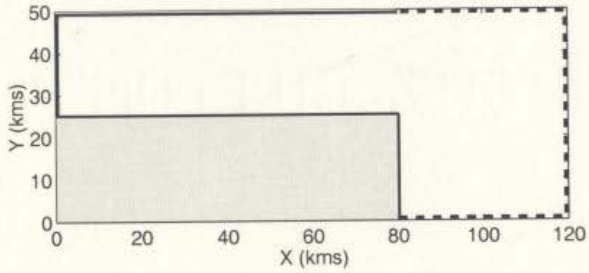

Figure 2.7: Idealized rectangular model topography of Trinity Bay. Open boundaries of the domain are indicated by dashed lines. Solid lines indicate closed boundaries. Bottom depth is 200 m. Model domain is 120 km by 50 km in the horizontal. The bay is 25 km wide and 80 km long.

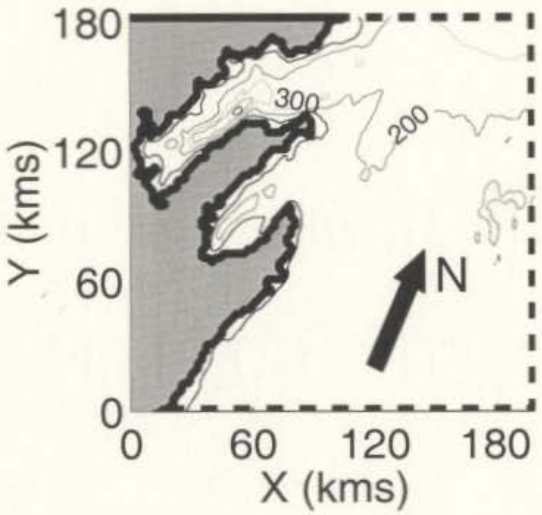

Figure 2.8: Model topography for Trinity and Conception Bays. Depth contours are every 100 m. Dashed lines indicate open boundaries.

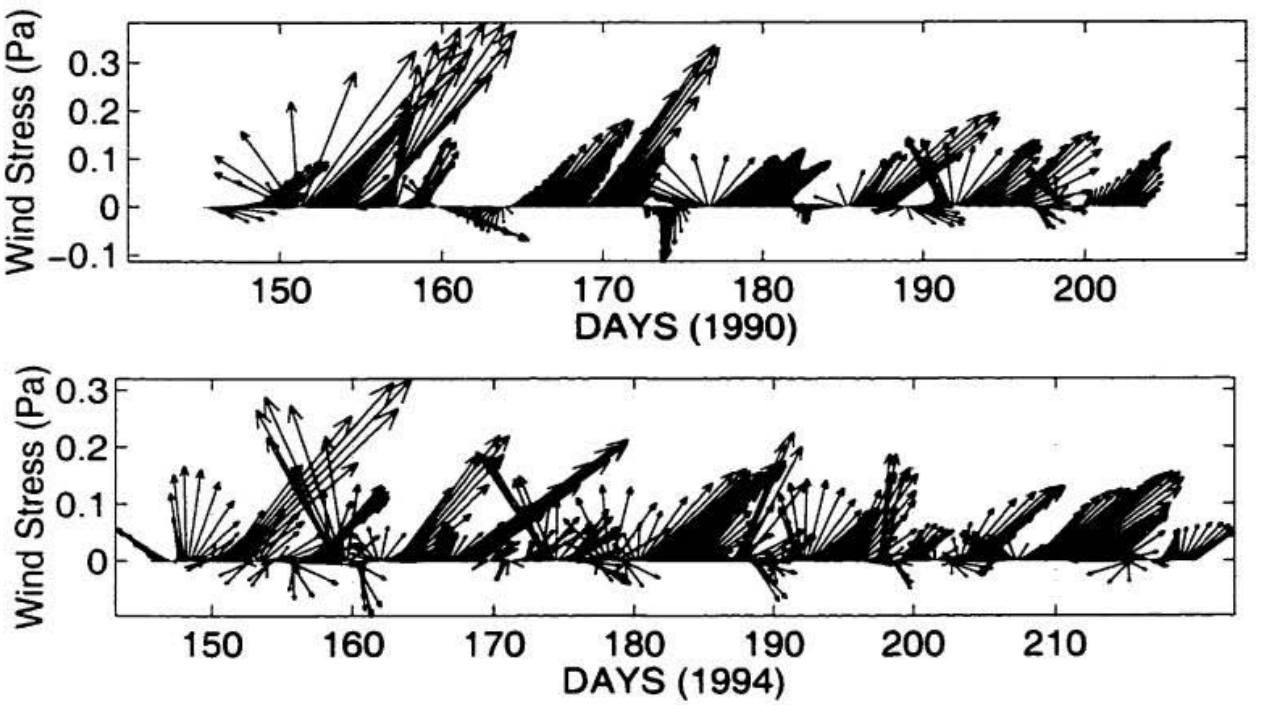

Figure 2.9: (a) Feather plot of winds measured at St. John's airport in 1990. Wind data have been filtered using low pass Butterworth filter to remove signals with timescale less than 32 hrs. Wind is plotted in bay coordinates such that the y axis points straight out of Conception Bay (30° east of north). (b) As in (a) for winds in 1994.

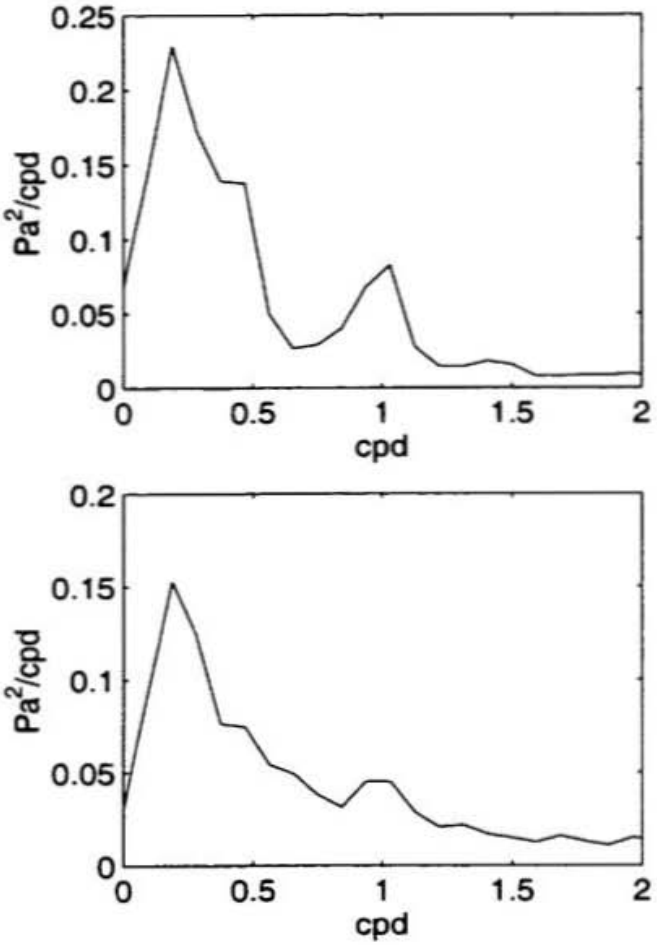

Figure 2.10: Power spectrum for wind stress magnitude in 1990 (a) and 1994 (b). Here the raw unfiltered wind stress data was used (note the small peak at 1 cpd, particularly in 1990).

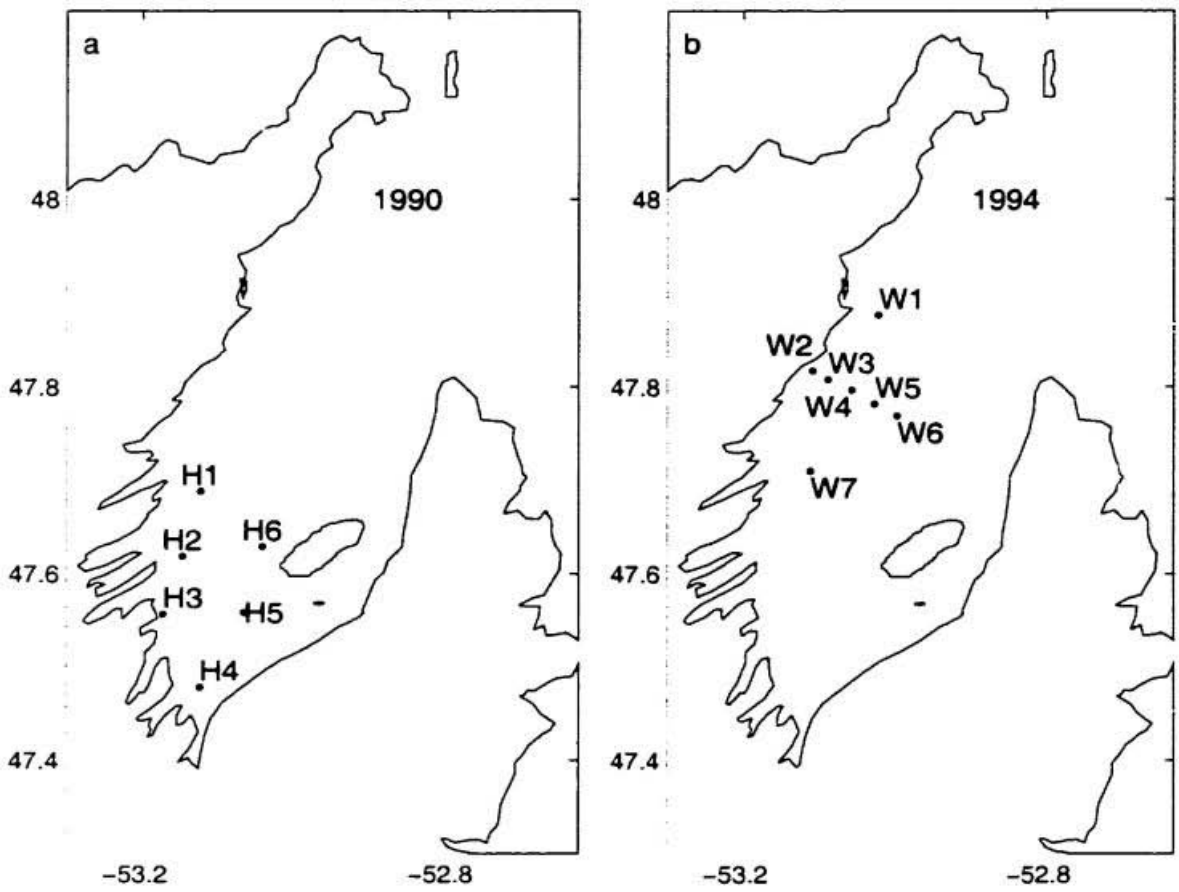

Figure 2.11: Mooring locations in (a) 1990 and (b) 1994.

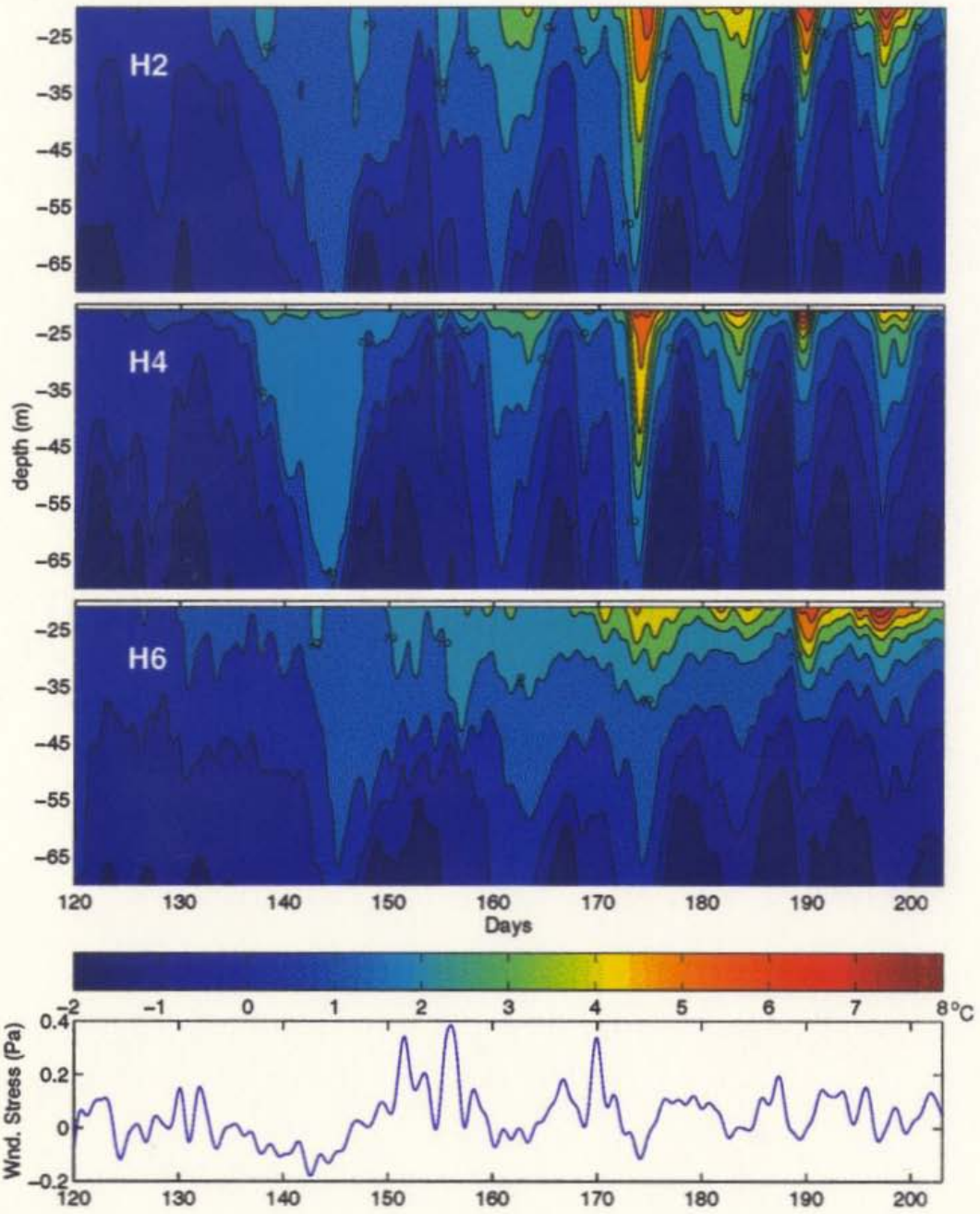

Figure 2.12: Contour of vertical temperature distribution over time at 3 mooring locations (H2,H4,H6) in 1990 with along-bay wind stress plotted at the bottom.

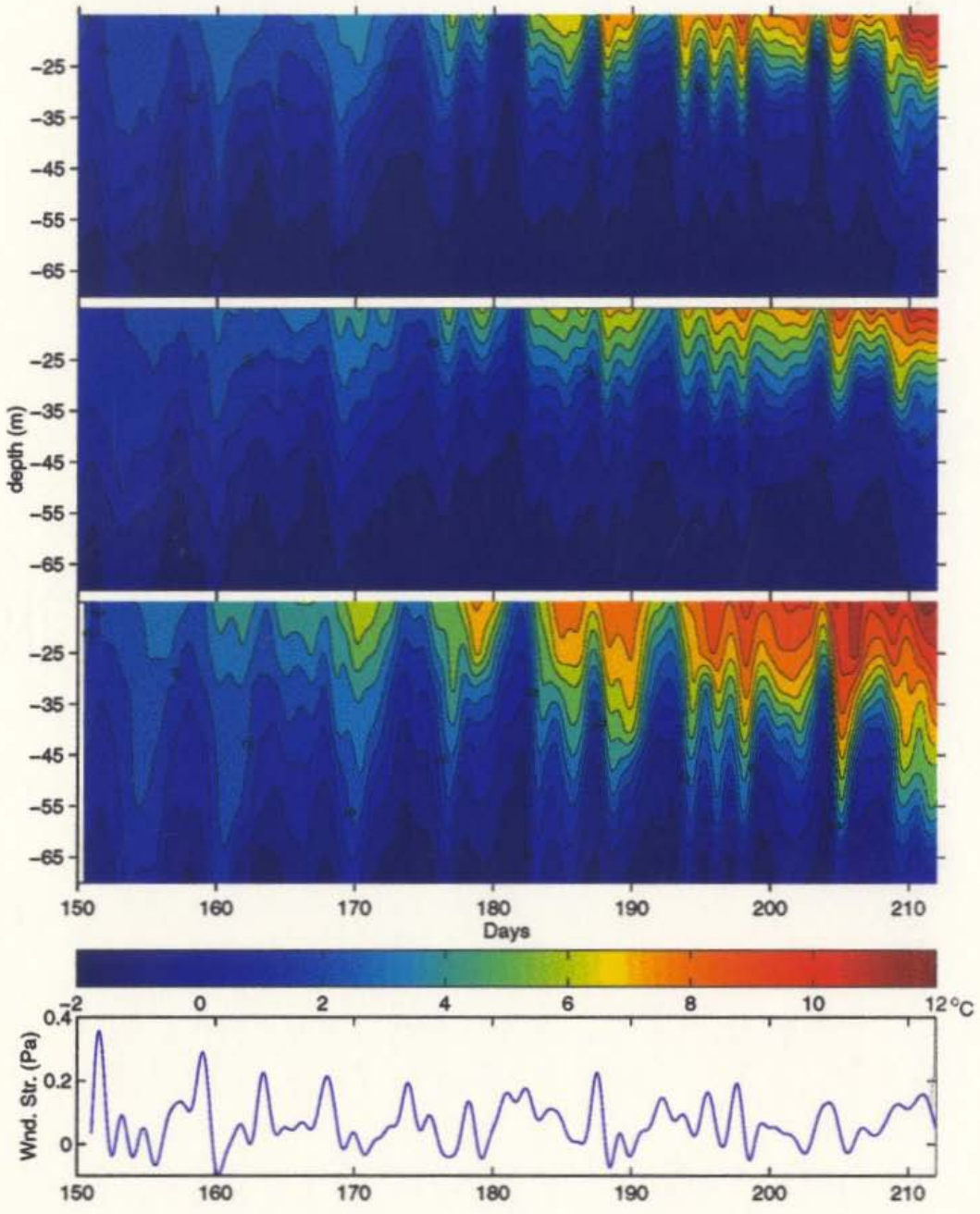

Figure 2.13: Contour of vertical temperature distribution over time at 3 mooring locations (W1,W4,W7) in 1994 with along-bay wind stress plotted at the bottom.

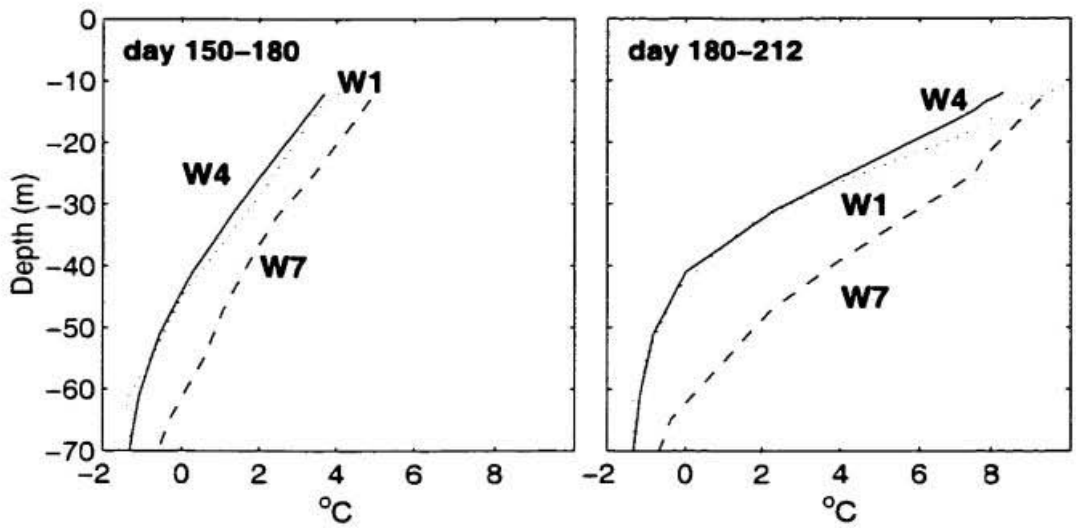

Figure 2.14: Time-mean vertical temperature profile at moorings W1, W4 and W7. Time intervals are indicated on the plots.

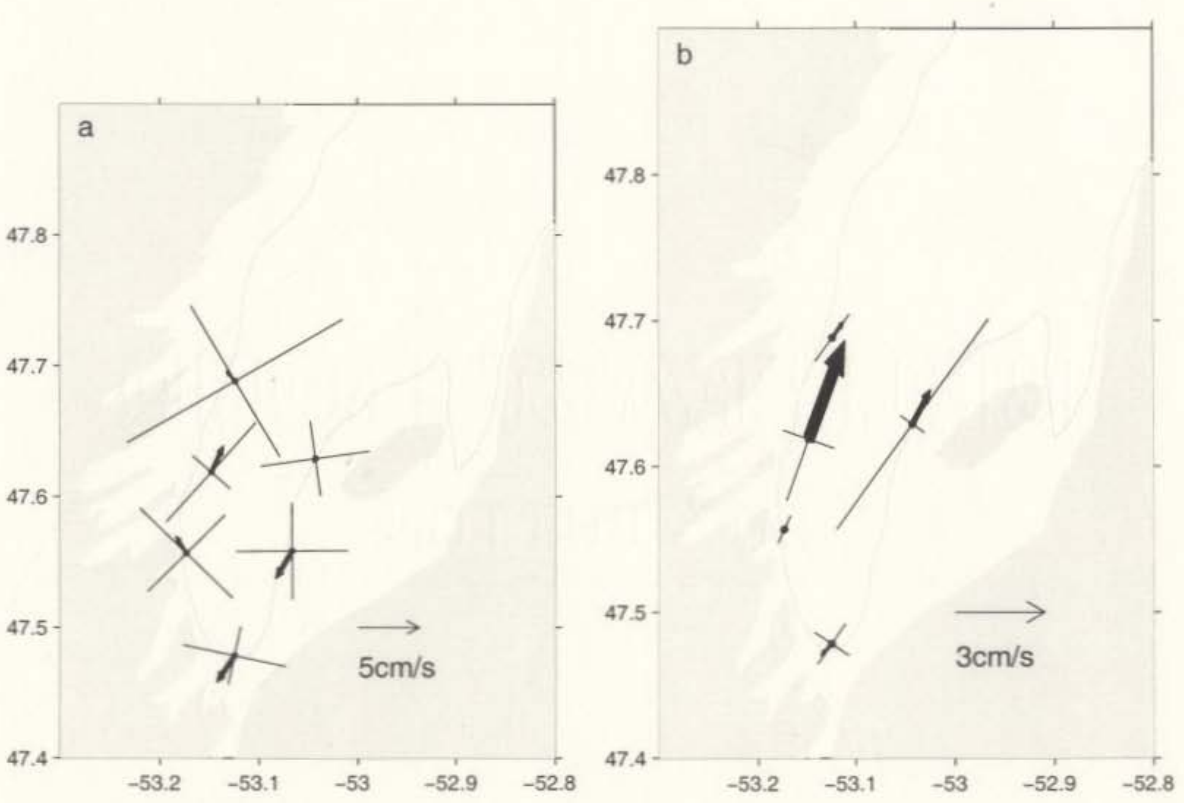

Figure 2.15: Mean velocities (solid arrows) and principal axis of standard deviation for 1990 velocity observations covering day 150 to 200 for (a) 20 m depth and (b) 80 m. The 100 m isobath is shown.

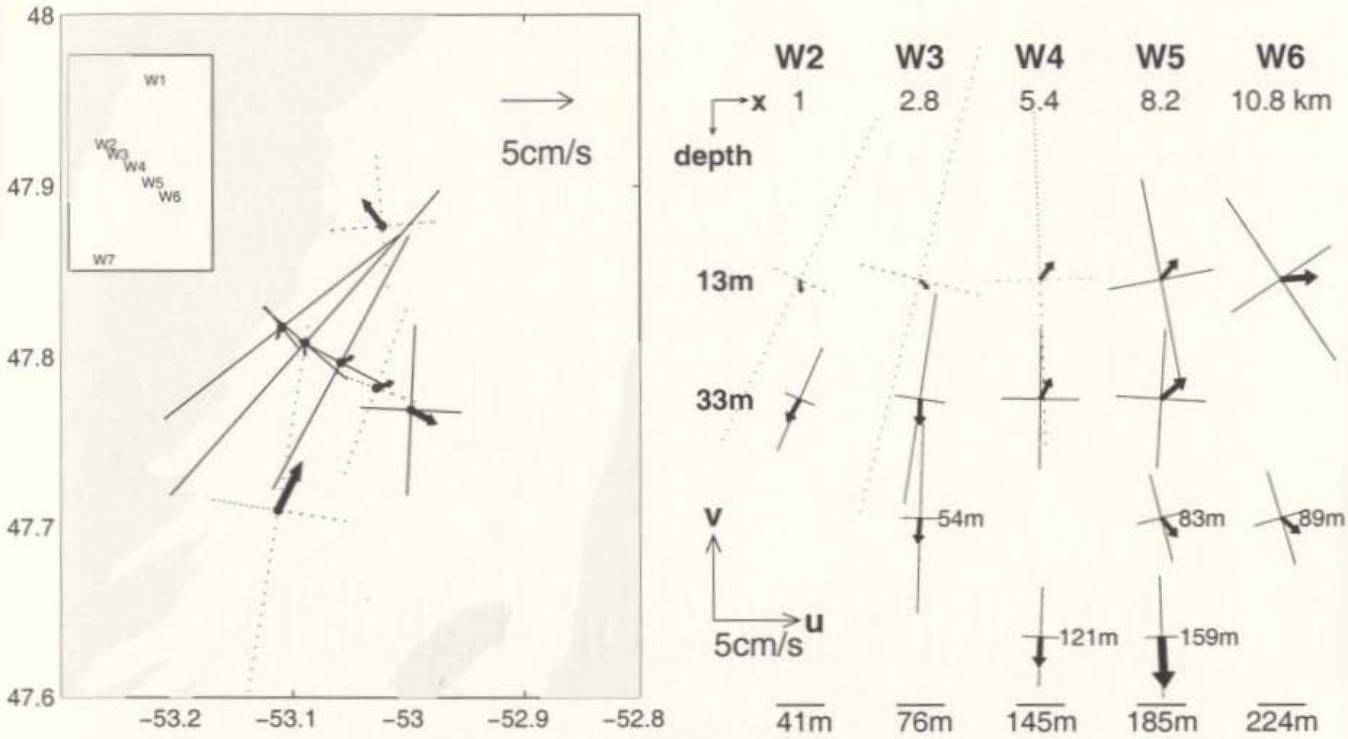

Figure 2.16: Mean velocities and principal axis of standard deviation for 1994 velocity observations from Julian day 150-210. Left panel: Velocities at a depth of 13 m. Right panel: Vertical cross-shore sections of mooring W2-W6. Columns correspond to individual moorings with cross-shore distance increasing to the right. The depth of the top two rows are 13 and 33 m respectively. Other depths are indicated to the right of the mean current vectors. Mooring distances from the coast for W2, W3, W4, W5 and W6 are 1, 2.8, 5.4, 8.2 and 10.8 km respectively.

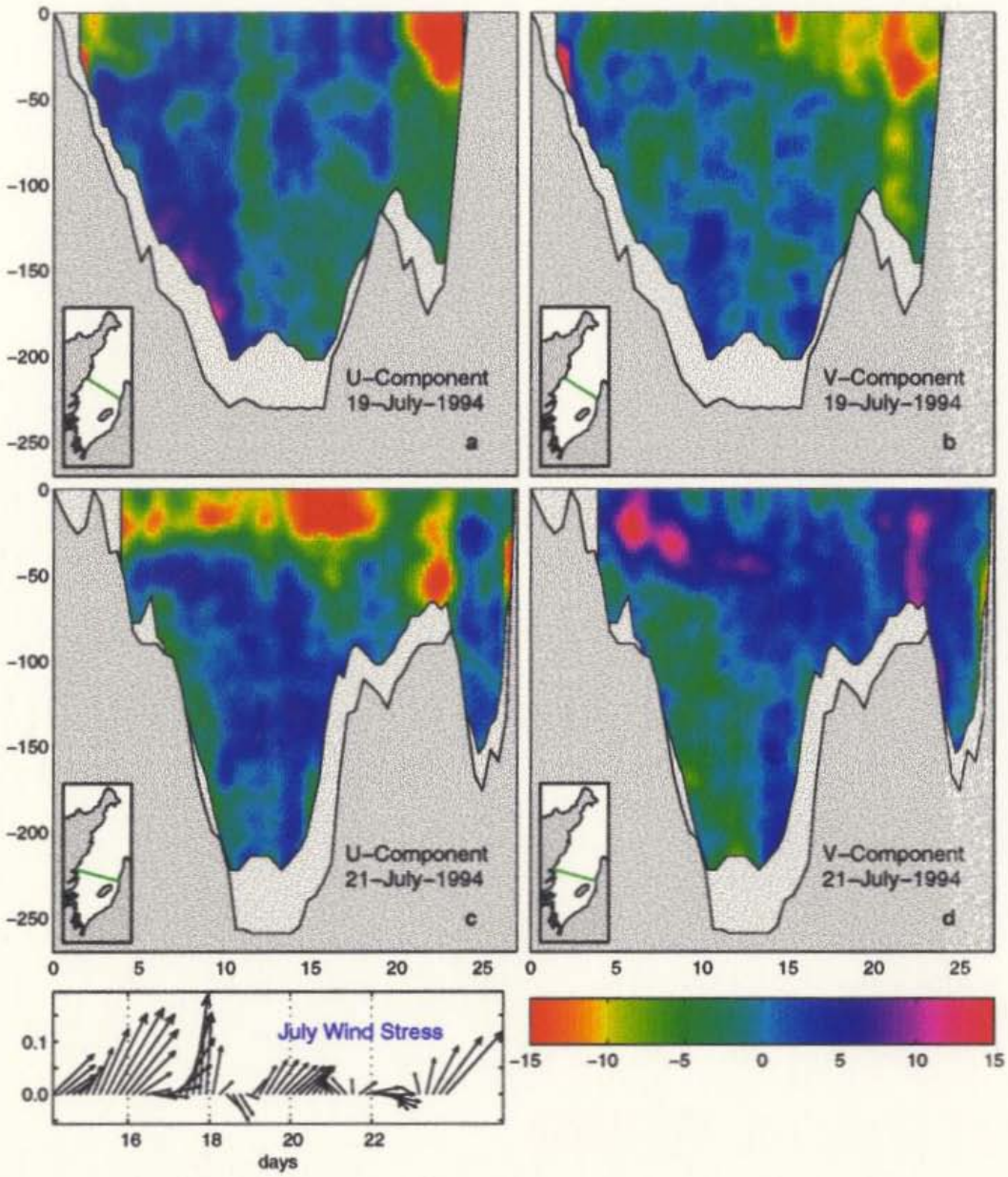

Figure 2.17: Observed velocities using an ADCP on July 19th and July 21st 1994. The inset maps of Conception Bay show the transect line across the bay. The U velocity component is parallel to the transect line and the V velocity is perpendicular to the transect line with the positive direction pointing out of the bay. The colour scale indicates speeds in cm s^{-1}, the y-axis represents depth (m) and the x-axis represents cross-bay distance (km). Wind stress (in Pa) during the time of observation is shown at the bottom. The x-axis are the days in 1994. Positive y-axis points straight out of the bay and perpendicular to the transect lines.

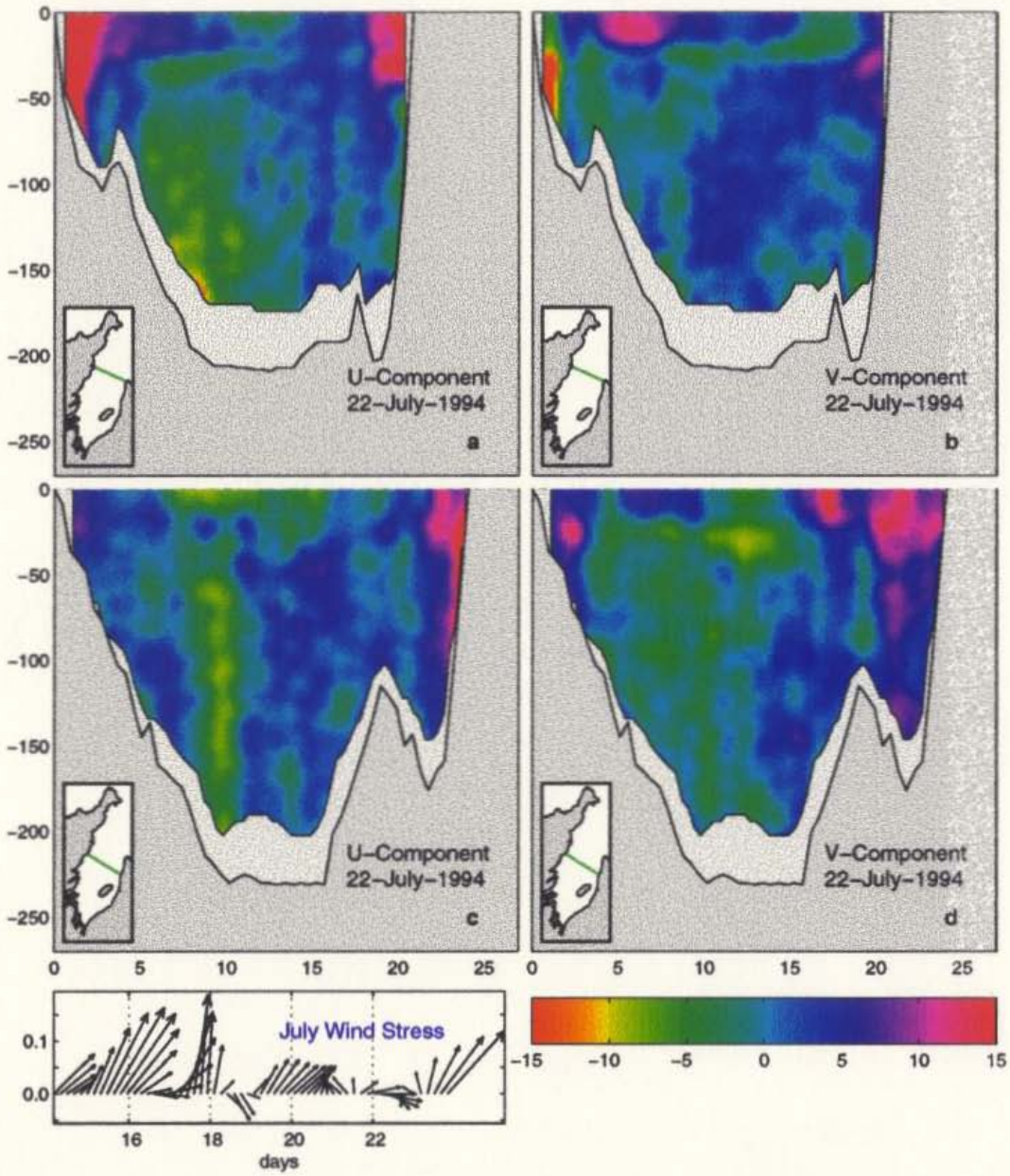

Figure 2.18: ADCP current observations as in Figure 2.17 but for 2 transects taken on July 22nd 1994.

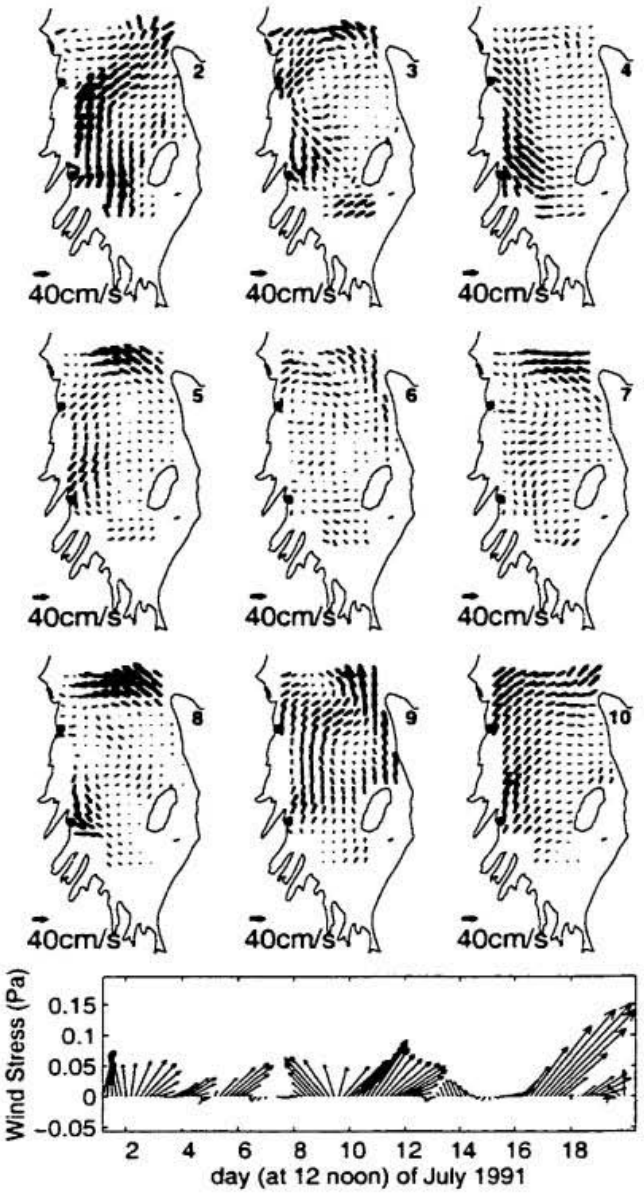

Figure 2.19: Surface velocities in Conception Bay observed by CODAR covering July 2nd to July 10th of 1991. Hourly velocity observations were filtered with a 32 hr low pass filter. Shown are the filtered velocities at noon on the days in July indicated beside each plot. A time series of wind stress for this period is shown below with the time in days of July indicated at 12 noon (See section 2.4.2 for detail on the wind stress time series). The CODAR data have been decimated from 1 km resolution in the original data to 2 km (distance between base of arrows) for clarity of presentation. The solid dots on the western side of the bay show the locations of the two antennae.

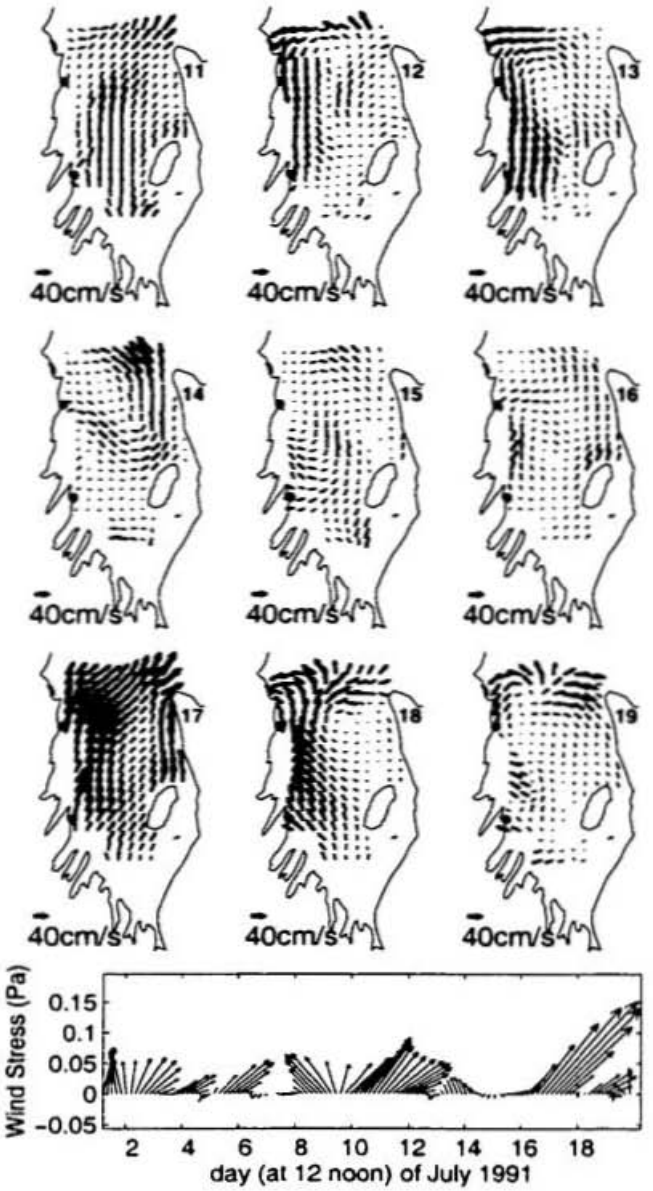

Figure 2.20: As in Figure 2.19, but for the period covering July 11th to July 19th.

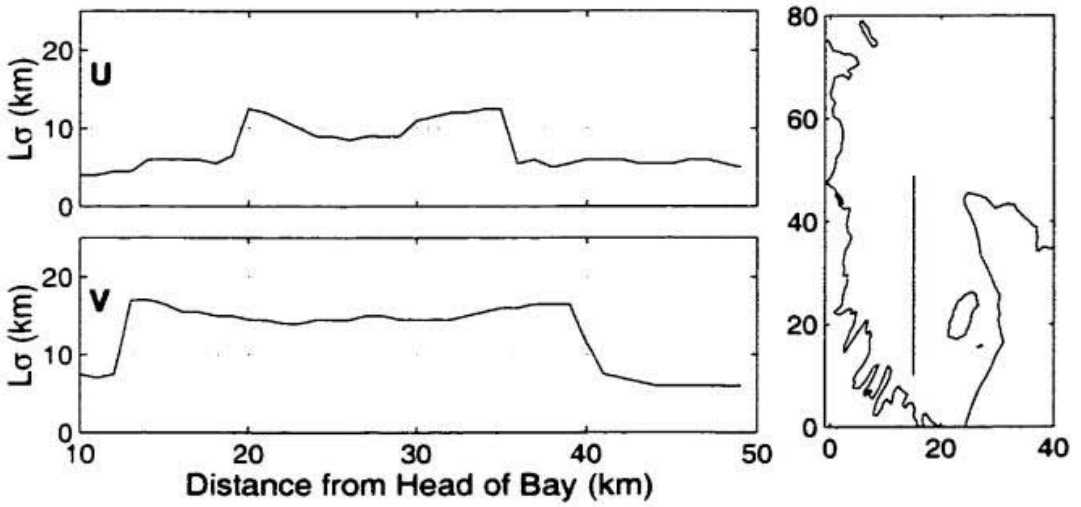

Figure 2.21: Decorrelation length scale $L\sigma$ for u and v with along-bay position as observed in CODAR data for Conception Bay. The v component is directed straight out of the bay. For the 2 panels on the left, the x-axis indicates position from the head of the bay. The y-axis represents the along-bay distance over which the variance r^2 drops by e^{-1}. The map on the right shows the position of the along-bay transects.

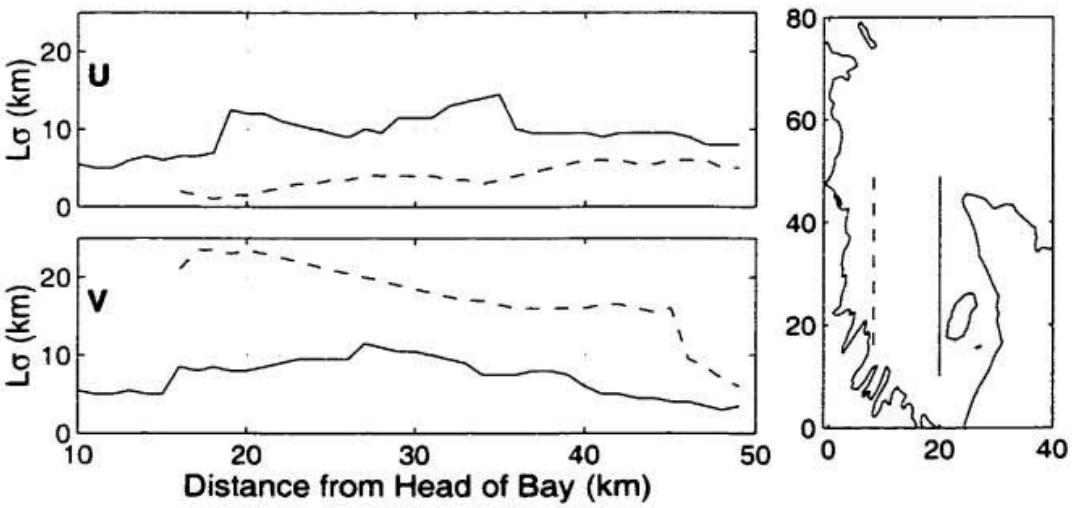

Figure 2.22: As in Figure 2.21, but for an along-bay transect on the western side of the bay (dashed line) and on the eastern side of the bay (solid line).

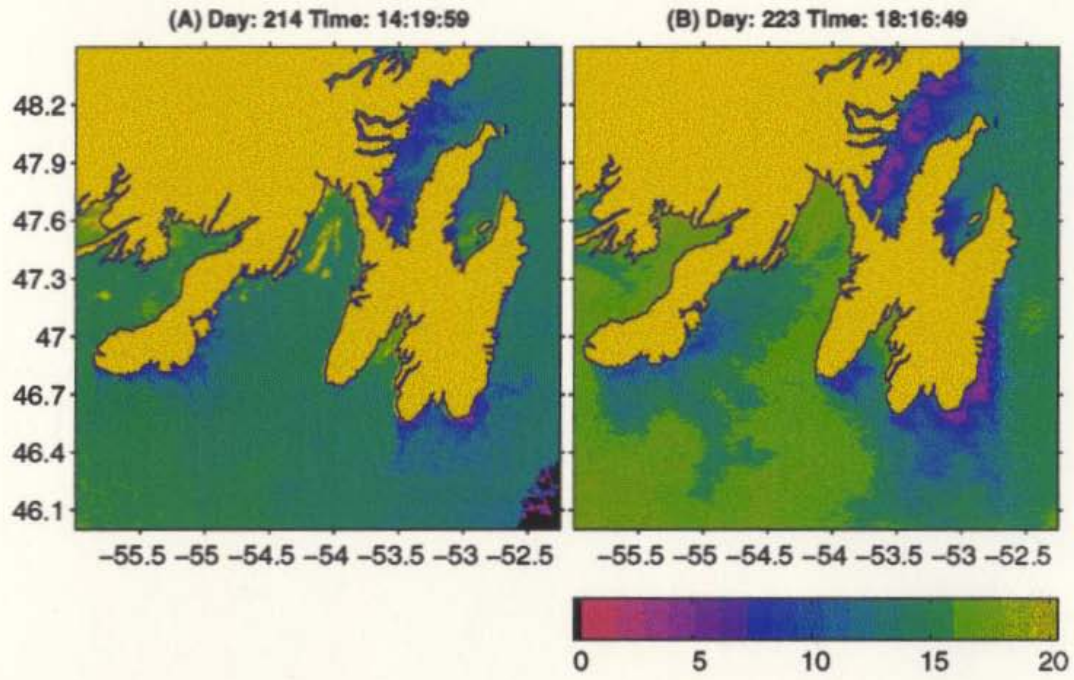

Figure 2.23: Typical images of observed sea surface temperature in the summer of 1998. Visible in both images are the upwelling of cold water (purple colour) in Trinity Bay, off Cape Race and the Burin Peninsula. To a lesser extent there is also upwelled water in Conception and St. Mary's Bay. The black spot in the bottom right hand corner of A is a cloud. Original images are courtesy of Peter Cornillion from the University of Rhode Island satellite image data base.

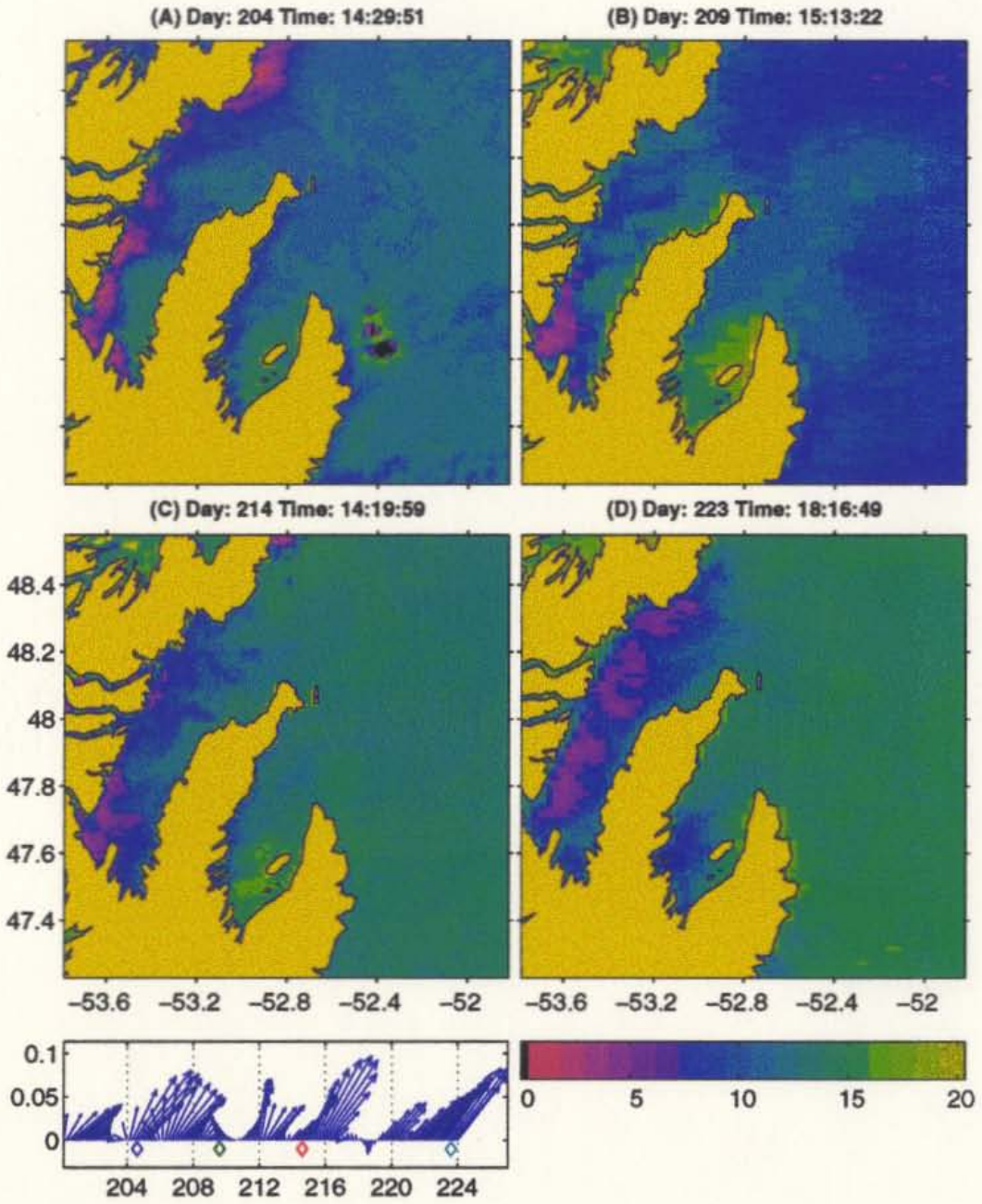

Figure 2.24: Observed sea surface temperature images of Trinity and Conception Bay on 4 different days in August and September. The extent of upwelled water is greater in Trinity Bay than in Conception Bay. Also noticeable in Trinity Bay is the the alongshore variability of upwelling. The original images for these plots are courtesy of Peter Cornillion from the University of Rhode Island satellite image data base. The corresponding wind stress time series for these images is shown at the bottom left. Diamond markers refer to the time when the images were taken. The y axis represents wind stress (Pa) and the x axis is Julian days in 1998. As before the positive y-axis points out of the bays.

Chapter 3

Mean Cyclonic Flow in Large Stratified Lakes

3.1 Introduction

In this chapter, the CANDIE model is tested with an application to a large (100 km radius) enclosed lake of parabolic bottom topography. The lake topography provides a means to validate and check the model in the absence of open boundary conditions and wind forcing, and to ensure the numerics of the code are correct. On the scientific level, it provides an insight into mean cyclonic circulation in a large stratified lake, a problem relevant to the circulation in coastal embayments.

Emery and Csanady (1973) have noted that many large stratified lakes and semi-enclosed seas and estuaries exhibit a mean cyclonic circulation during periods of stratification. Wunsch (1970) states that an adiabatic boundary condition for a stratified fluid over a sloping bottom implies that the fluid cannot remain in a state of rest, since isotherms must intersect the bottom at right angles. Wunsch's idea is illustrated by Schwab et al. (1995), who model a parabolic lake of depth 100 m and width 100 km.

with no external forcing. Initially the lake is at rest with a horizontally uniform thermocline between 10 m and 20 m of depth. An adiabatic condition is imposed on all boundaries of the lake implying that the isotherms intersect the bottom at right angles. From the initial state of horizontally uniform stratification, the isotherms tilt to intersect the bottom normally. The downward sloping isotherms at the edge of the lake imply a surface-intensified cyclonic circulation in the northern hemisphere with a maximum speed of a few cm s^{-1} close to shore.

The purpose of this chapter is to emphasise that it is the combination of vertical mixing, the associated surface and bottom boundary conditions and the variable depth that produces the cyclonic circulation. I suggest that vertical mixing of cold water to the surface over deeper regions of the lake produces the doming thermocline that generates cyclonic flow. Without vertical mixing, there would be no doming of the thermocline.

To understand the importance of variable depth in combination with adiabatic surface and bottom boundary conditions, I consider the vertically averaged temperature field. Initially the lowest values are found where the water is deepest (see Figure 3.1c for an example), indicating that if water were to be vertically mixed instantaneously, the resulting horizontal density gradients would produce a pressure gradient which by the thermal wind equations drives a surface intensified cyclonic circulation. The development of cyclonic circulation in the vertical average is the consequence of bottom friction, as will be explained.

In this chapter I repeat the Schwab et al. (1995) study using the non-linear CANDIE model. I include additional experiments using a different bottom topography and one experiment with seasonal heating at the surface. The model is described in Section 3.2 and the model results are presented in Section 3.3. Section 3.4 provides a summary and discussion for this chapter.

3.2 Model Setup for the Lake Problem

Changes in the implementation of the CANDIE model as described in Chapter 2 are outlined in this section along with the description of model runs. The model uses a step-like topography with 5 m vertical resolution and 2.5 km horizontal resolution. The model solves for velocities and temperature (as opposed to density). Salinity is set to a constant 0.2 ppt to represent fresh water (as in Schwab et al. (1995)). Vertical diffusion and viscosity coefficients were set to 3×10^{-5} and 2×10^{-5} $m^2\ s^{-1}$ respectively as in the uniform coefficient experiments of Schwab et al. (1995). Schwab et al. (1995) also use the (Mellor and Yamada, 1974) turbulent closure scheme, but obtain similar results using uniform coefficients. Sensitivity to horizontal diffusivities and viscosities of 0, 5 and 50 $m^2\ s^{-1}$ have been tested. Horizontal diffusivities and viscosities are set equal in all experiments giving a Prandtl number equal to one.

The boundary conditions applied to the temperature in the CANDIE model are that the vertical temperature gradient is set to zero at the bottom and the horizontal temperature gradient normal to the boundary is set to zero at the sides of the lake

(the latter only applies to model runs with non-zero horizontal diffusivity). Schwab et al. (1995) use the Princeton Ocean Model (POM; Blumberg and Mellor (1987)). As they point out, the correct boundary condition at the lake bottom is that the isotherms intersect the bottom orthogonally. POM uses a sigma coordinate in the vertical in which the vertical coordinate varies with bottom topography. The no-normal flux condition is applied by setting the derivative of temperature with respect to sigma equal to zero at the bottom, the derivative being taken at fixed horizontal coordinates (Mellor, 1992). This is equivalent to setting the vertical derivative of temperature equal to zero, and is a valid approximation since the slope of the lake is weak, the lake width being 10^3 times greater than its depth.

For momentum, a quadratic bottom friction parameterisation is employed with a drag coefficient equal to 0.002 as opposed to 0.003 in Chapter 2. In cases with non-zero horizontal viscosity, a no-slip boundary condition is applied at the horizontal walls, otherwise the boundary condition is one of no normal flow.

The model geometry considered in this chapter consists of a circular lake with a maximum depth of 100 m and a width of 100 km. The lake is centred at 45 °N. Two model topographies with cylindrical symmetry are used. The first is a parabolic lake (Figure 3.1a), and is the same model lake as used by Schwab et al. (1995). The second is a step shelf lake with two different depths (Figure 3.1b), the shallow part being of depth 30 m, the deep part of depth 100 m. The lake is initially at rest, with a horizontally uniform temperature field. Initially, a linear temperature

gradient between the depths of 10 m and 20 m separates a 15 °C surface layer from a 5 °C deeper layer (Figures 3.1a.b). The initial vertically-averaged temperature field has horizontal gradients (Figures 3.1c.d) in both cases implying that vertical mixing in combination with adiabatic surface and bottom boundary conditions can be expected to generate flow in both cases. Unless otherwise stated, there is no applied external forcing implying no heat transfer with the environment. The only mechanism for initiating any circulation is vertical mixing in combination with the surface and bottom boundary conditions.

A test run with a flat-bottom topography was carried out. No circulation was found using the flat bottom topography.

3.3 Results

3.3.1 Parabolic Lake

The model with the parabolic lake (Figure 3.1a) was run to repeat the original model run by Schwab et al. (1995). The horizontal eddy diffusivity and viscosity are both set to zero. After 60 days, a cyclonic circulation is observed in the model. Surface water at the centre of the lake is cooled by vertical diffusion more so than at the edges of the lake where the thickness of the initial 5 °C cold water layer is thin. This results in a sinking of the isotherms at the edges of the lake (Figure 3.2). The corresponding vertically averaged circulation (Figure 3.3) is cyclonic and reaches a

maximum azimuthal velocity of 3 cm s^{-1} (Figure 3.2c), comparable to Schwab et al. (1995). Figure 3.2b shows a vertical profile of azimuthal velocity. The circulation is cyclonic and surface intensified.

The surface intensification of the flow can be explained as follows. In the absence of bottom friction, and as long as the flow maintains cylindrical symmetry, the vertically-averaged flow remains zero. This can easily be demonstrated, assuming the non-linear momentum advection terms are negligible (as is the case in most of our model experiments). Based on the thermal wind equations, one then expects to find cyclonic flow near the surface and anticyclonic flow at depth. Adding bottom friction to this flow generates bottom Ekman transport up the slope, away from the centre of the lake, implying convergence of the vertically integrated transport towards the sides of the lake, and divergence away from the centre. As a consequence, the free surface rises at the sides of the lake, compared to the centre, and generates vertically-integrated cyclonic circulation that acts to reduce the anticyclonic flow at depth. Since our model makes the rigid-lid approximation, the barotropic adjustment associated with changing the free surface is filtered from our model equations, and is assumed to occur instantaneously. In fact, when the rigid-lid approximation is made, convergence towards the sides of the lake is inconsistent with the vertically integrated continuity equation, implying that the generation of anticyclonic circulation at the bottom of the lake is strongly inhibited throughout the model integration. The net result is a surface intensified cyclonic circulation, as can be seen in Figure 3.2b.

Figure 3.2c is a transect of vertically averaged azimuthal velocity across the lake. Maximum velocities are centred roughly 10 kms from the coast. This differs from Schwab et al. (1995) (their Figure 4) whose currents reach a maximum only a couple of kilometres from shore.

Model runs with non-zero horizontal diffusivity and viscosity coefficients were undertaken. Including horizontal mixing reduces overall current strength and spreads the current over a larger area. Maximum surface velocities after 60 days for model runs with horizontal diffusivity and viscosity coefficients of 0, 5 and 50 $m^2\ s^{-1}$, are 11. 6 and 1.4 cm s^{-1}respectively. Increased vertical diffusivity increases circulation strength as noted by Schwab et al. (1995).

We carried out model runs using parabolic topography, but with half the original depth, twice the original depth, and twice the original width of the lake. While the topography differs, the initial temperature structure, vertical resolution and horizontal resolution are the same in each case. The horizontal viscosity and diffusivity are set to zero. Two sets of experiments were carried out, one set using the full model, and a second set in which advection of the temperature field is withheld. Table 3.1 shows the maximum vertically-averaged azimuthal velocity after 60 days in each case that was run. Schwab et al. (1995) suggest that the maximum vertically-averaged azimuthal velocity depends inversely on the bottom slope. The 200 m and 100 m cases including advection of the temperature field are consistent with this dependence. The 50 m depth case is expected to have stronger circulation. However in this case, the

flow is baroclinically unstable reducing current strength (an example of baroclinic flow instability is shown when I consider the step shelf). For the run with a lake of double the width (100 m depth) and thus a weaker bottom slope, flow is weaker than the 100 m depth case contradicting the suggestion of by Schwab et al. (1995) that circulation strength is inversely proportional to the slope of the lake topography. Reasons for this are discussed later in this chapter.

With advection of the temperature field suppressed, model runs show the opposite dependence on bottom slope to that put forward by Schwab et al. (1995), with the strongest velocities being found when the bottom slope is greatest. It follows that advection of the temperature field has an important effect on the circulation. It should be noted that because of the cylindrical symmetry (at least until flow instability sets in), advection is by the radial component of velocity. The latter can be regarded as a secondary Ekman circulation, generated by the vertical mixing of momentum associated with the azimuthal flow. The effect of the secondary circulation is to flatten isotherms, reducing the geostrophic shear. (Since geostrophic balance is a good approximation for the azimuthal flow, reduced vertical shear implies a reduced radial gradient of density because of thermal wind, and a corresponding flattening of the isopycnals.) In the 200 m depth case, the flow is confined in a narrow jet near to shore when advection of the temperature field is suppressed. When advection of temperature is included, the radial velocity flattens out the radial density gradient, leading to a considerable reduction in the maximum velocity, as can be seen from

Table 3.1. On the other hand, when the bottom slope is less, the flow field without advection is much more radially spread out, with the result that advection by the radial velocity is less effective at flattening isopycnals, leading to much less of a reduction in maximum velocity when advection is included, as can be seen from Table 3.1.

3.3.2 Step Lake

In this section, the model is run with the step lake topography (Figure 3.1b). All side walls of the lake are vertical. Initially the isotherms are perpendicular to the lake walls and satisfy the side, bottom and surface boundary conditions exactly. With time, vertical mixing causes the isotherms to dome in the centre of the lake (Figure 3.4a), leading to a cyclonic circulation at the shelf break (Figure 3.5). In the absence of horizontal mixing, the circulation is baroclinically unstable (Figures 3.4 b,c and 3.5). Horizontal mixing of 5 $m^2\ s^{-1}$ is sufficient to suppress most of the flow instability in the step lake case. If horizontal mixing is set at 50 $m^2\ s^{-1}$, there is no flow instability and maximum azimuthal currents in the step lake are slightly stronger than in the parabolic lake. In the case with no horizontal mixing, maximum azimuthal velocity in the step shelf case is less than half that in the parabolic case on account of the unstable flow found in the former case but not the latter.

As a final application of this chapter, the model is run with the topography of Trinity and Conception Bays (Figure 2.8) in diffusion-only mode. Here vertical dif-

fusion is set to 10^{-4} m^2 $s^{-1}$with horizontal diffusion set at 10 m^2 s^{-1}. The results (Figure 3.6) show velocities of order 1 cm s^{-1} or less generated flowing as in the lake case, with the coastline to the right. After 10 days the flow is strongest on the eastern sides of the bay. The set up near the coast diffuses gradually. At 70 days the circulation is broader and considerably weaker (by a factor of 2) particularly on the western side of both bays. Also shown in Figure 3.6 is the density field departure from initial stratification. Density differences at the surface are only minute (0.02 kg m^{-3}) and located close to shore. Thus, while the effect of flow driven by vertical mixing is present, it is weak in the context of Trinity and Conception Bay, contributing a mean flow in the surface layer that is roughly 1 cm s^{-1}.

3.4 Discussion

In a lake with a step topography (Figure 3.1b), and for my choice of initial stratification, the adiabatic boundary conditions at the surface, walls and bottom are satisfied exactly in the initial state. Vertical mixing is required to diffuse the thermocline leading to a doming of the thermocline as the cold water in the deep part of the lake is mixed upwards. The step-shelf topography case emphasises the importance of vertical mixing for generating cyclonic circulation. As the thermocline diffuses, it eventually cannot satisfy the adiabatic boundary condition at the bottom without generating horizontal gradients and hence flow. This is despite the fact that in the initial state, the adiabatic boundary conditions are satisfied exactly.

However, adiabatic boundary conditions are not necessarily needed to produce the doming of the thermocline. For the step shelf if one were to uniformly heat the bottom of the lake and the bottom of the shelf, the shallow parts of the lake would heat up more quickly than the centre part of the lake due to the shallow depth of the water column (assuming no heat input at the surface). A cyclonic circulation would be generated even though there is no longer a zero normal gradient boundary condition being applied at the bottom. While the imposition of the adiabatic condition at the bottom does play a role in realistic problems (Schwab et al., 1995), it is only part of the story. What is important is the combination of vertical mixing, the associated boundary conditions at the surface and at the bottom and the presence of variable depth.

Advection by the radial velocity can have a major impact on the maximum azimuthal velocity, and is a key factor in determining the dependence of the maximum azimuthal velocity on the model parameters. Experiments show that azimuthal velocity is confined nearer to shore if advection of the temperature field is not included in the model. Advection of the temperature field is particularly important when the slope is steep and the horizontal mixing of momentum and temperature is zero. The offshore scale of the azimuthal flow is also determined by the location where the thermocline intersects bottom topography. The advective terms of the momentum equation are not important compared to the temperature advection terms, at least prior to the onset of flow instability. Basically, there is no change in circulation

strength and pattern when advection of momentum is suppressed, except that the gyre pattern is slightly smoother.

The equation for maximum azimuthal velocity given by Schwab et al. (1995) appears to apply to a parabolic lake of fixed width where depth is varied, provided advection of the temperature field is included. On the other hand if the width of the lake were increased by 1000 times, the slope of the lake would be almost flat. The equation in Schwab et al. (1995) would predict a very strong circulation since it relates current strength to the inverse of the bottom slope. However when the width of the lake is increased, the horizontal gradient of the vertically averaged temperature field is reduced, and consequently cyclonic circulation is reduced. In the limit, as the width of the lake increases to infinity, the parabolic lake becomes a flat bottomed lake, there is no horizontal gradient in the vertical averaged temperature field and consequently no circulation.

This chapter has considered a mechanism for producing cyclonic circulation in the absence of any kind of external forcing. To relate these results to observed long term circulation, two plots of velocity contours in Lake Ontario from Simons and Schertzer (1989) are shown. Figure 3.7 shows the north-south cross section of time-averaged eastward current from May to August 1982 in Lake Ontario. Similarly Figure 3.8 shows the time-averaged eastward current for the winter of 1983 (November 82 to March 83). The model results of current cross section (Figure 3.2b) compare well with the summer observations (Figure 3.7). The model reproduces the vertical distribution

of azimuthal current as well as the magnitude of the surface circulation which is around 6 cm s^{-1}. However for winter, observed mean flow is basically barotropic (Figure 3.8) and circulation is not just a simple cyclonic gyre. Thus for the summer months, vertical diffusion of the thermocline is likely to be important for generating the observed mean cyclonic flow.

A model run with uniform seasonal surface heating was run to investigate the effect of seasonal heating throughout the year. The lake was initially specified at a uniform temperature of 5^{o} to represent lake conditions at the end of winter. A sinusoidal shaped heat flux was applied. During the warming phase, a cyclonic circulation is generated near-shore (2 km) and progressively spreads further offshore as heat is diffused to greater depths. However, during the cooling phase, a complex barotropic circulation sets in. The circulation of the lake during the cooling phase is beyond the scope of this work and is not investigated further.

The model run with realistic topography for Trinity and Conception Bay, shows that diffusion may generate small mean currents of 1 cm s^{-1}or less. However this mechanism for mean current does not dominate, since observations in chapter 2 show anti-cyclonic flow around the head of Conception Bay, rather than the cyclonic pattern produced by diffusion of the thermocline over variable topography seen in this Chapter.

Table 3.1: Maximum vertical averaged azimuthal velocity (cm s^{-1}) after 60 days. 2 W refers to the case with twice the width. 200, 100 and 50 refer to the cases with 200 m, 100 m and 50 m depths respectively. "adv. off" means that the advection of the temperature field is suppressed. Note that the 50 m depth case with advection exhibits a meandering flow at 60 days.

	200	100	50	2 W
adv. on	2.39	4.12	3.69	3.91
adv. off	6.26	5.47	2.74	3.18

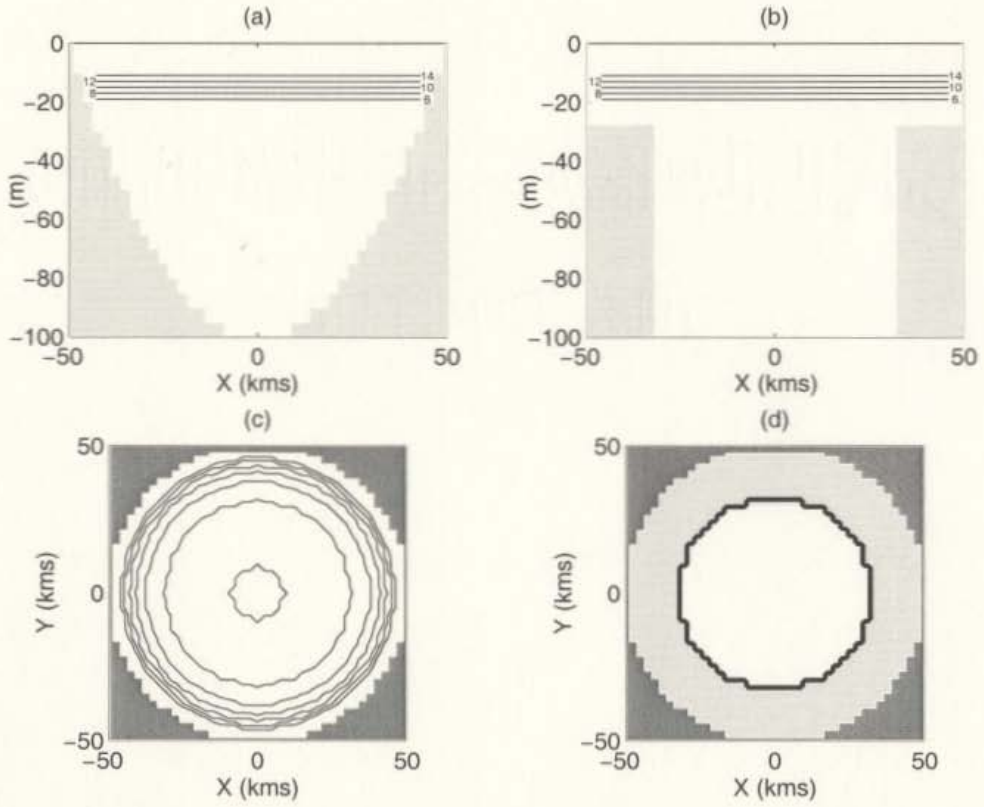

Figure 3.1: (a) Initial vertical temperature distribution and profile of the parabolic lake. (b) As (a) but for the step lake. (c) Initial vertically averaged temperature field for the parabolic lake. Contour intervals are 1 ^{o}C. The centre of the lake is at 7.9 ^{o}C. (d) As (c) but for the step lake. The shallow region of the lake is at 12 ^{o}C. The centre of the lake is at 7.9 ^{o}C.

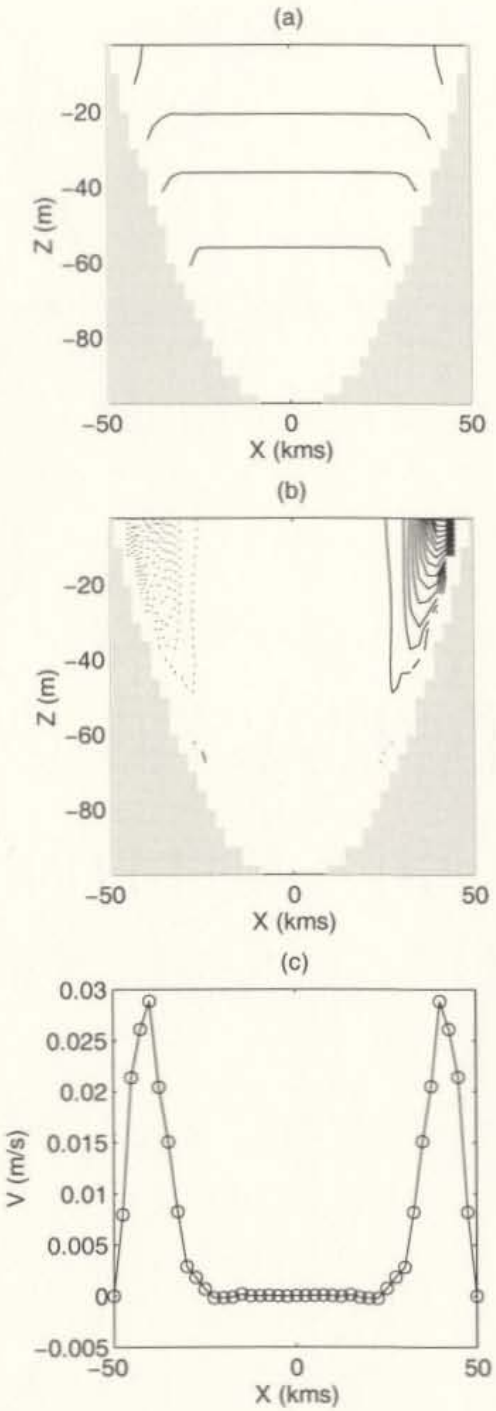

Figure 3.2: Vertical cross-sections at Y = 0 (see fig 1c), of the parabolic lake model run at 60 days. (a) Temperature field: Contour intervals are 2 ^{o}C and the deepest contour is 6 ^{o}C. (b) Contour of velocity normal to the section with intervals of 0.5 cm/s. Dotted lines represent out of the plane flow and solid lines represent flow into the plane. (c) Vertical average of the velocity in (b).

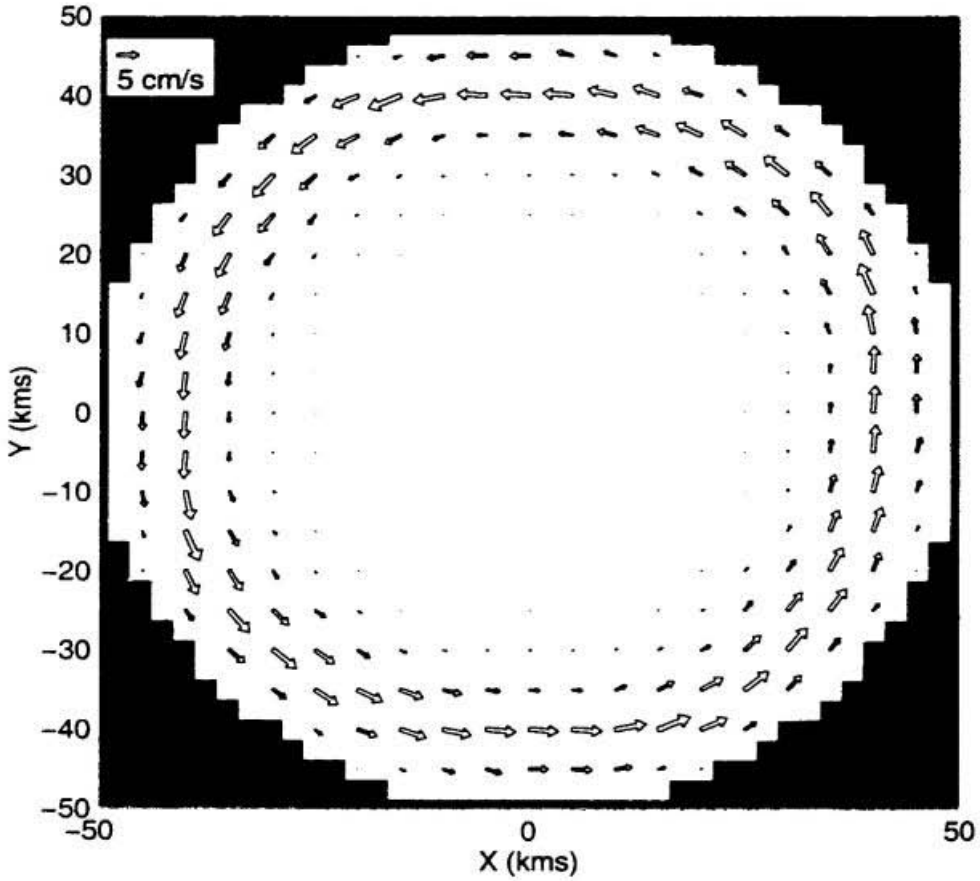

Figure 3.3: Vertically averaged circulation in parabolic lake model run at 60 days.

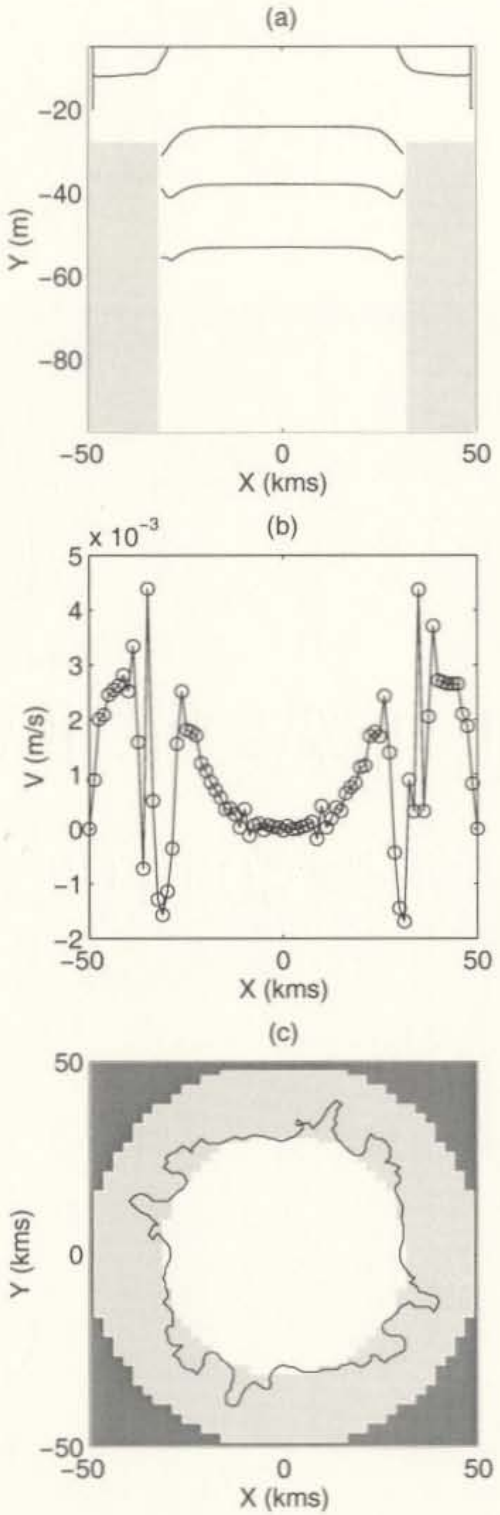

Figure 3.4: Cross-sections (Y = 0) of the step lake model run at 60 days: (a) Temperature field: Contour intervals are 2^o and the deepest contour is 6^o. (b) Vertically averaged azimuthal velocity. (c) Top view of vertically averaged temperature field. The one contour line is 11^o.

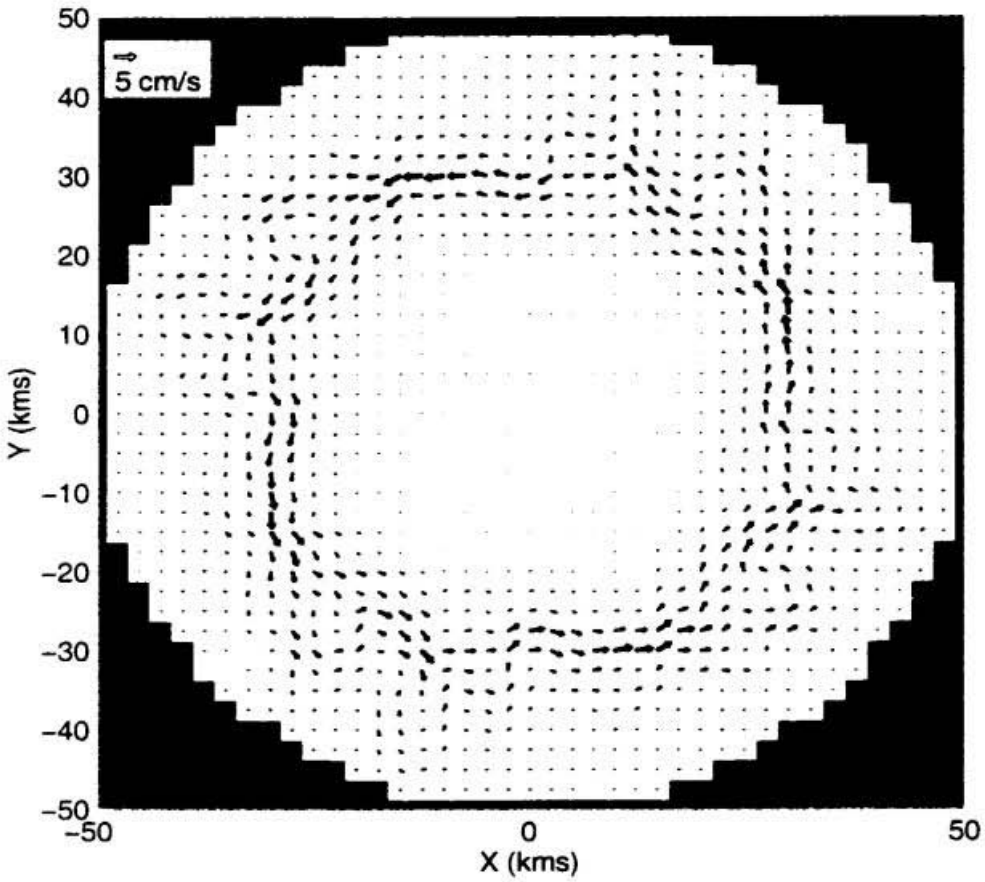

Figure 3.5: Step lake model run at 60 days: Surface circulation.

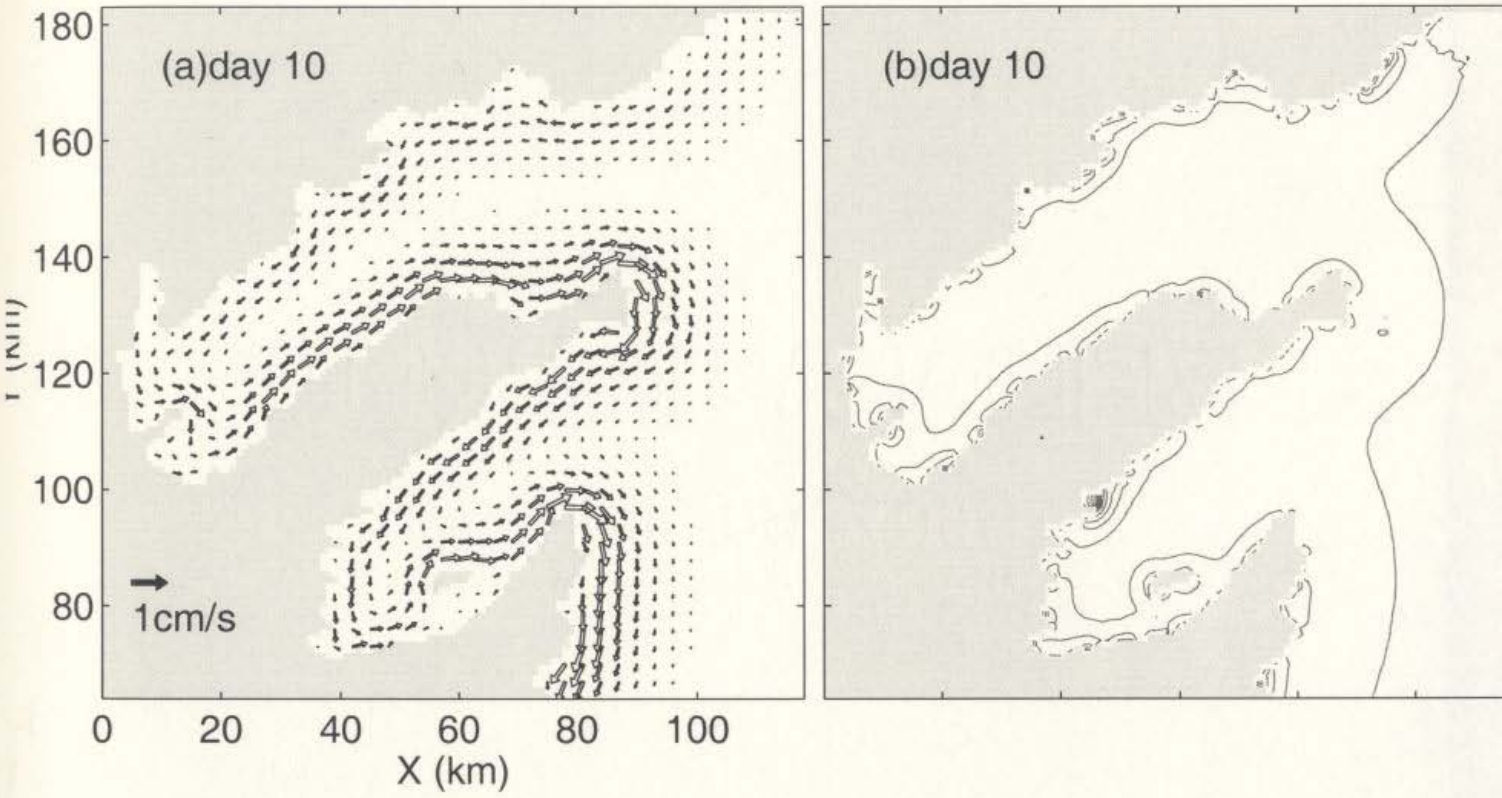

Figure 3.6: (a) Surface level velocities (top 10 m) from diffusion only CANDIE model after 10 days. (b) Corresponding surface density structure. Contour intervals are in 0.01 kg m^{-3}.

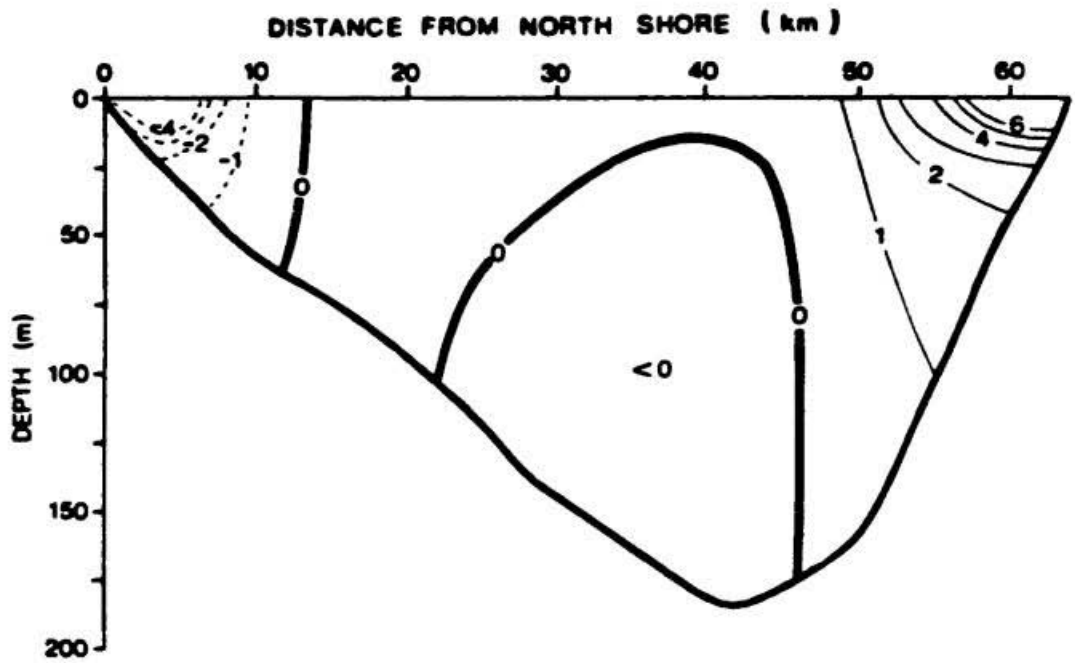

Figure 3.7: Time averaged eastward circulation in Lake Ontario for Summer of 1982. Reproduced from Simons and Schertzer (1989).

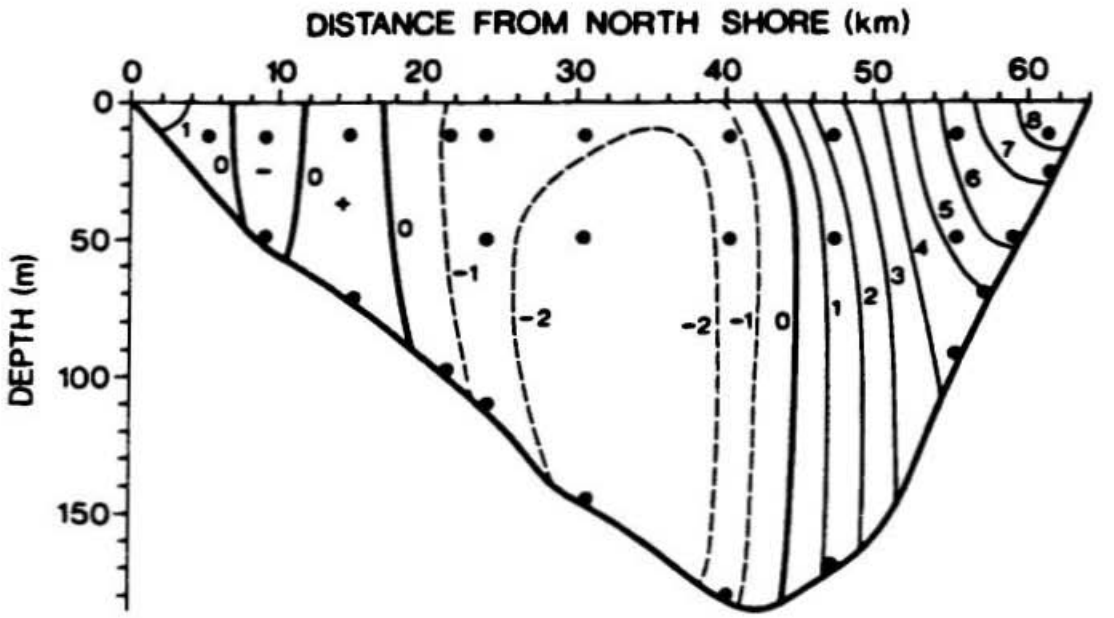

Figure 3.8: Time averaged eastward circulation in Lake Ontario for Winter of 1982/1983. Reproduced from Simons and Schertzer (1989).

Chapter 4

The Response To Steady Wind

4.1 Introductory Remarks

In this chapter I model the response of Trinity and Conception Bays to a steady spatially-uniform wind, blowing from the southwest along the axis of the bays. The response after 5 days of such a wind is investigated, along with a discussion of the response when the wind persists over longer time scales or relaxes to zero at day 5. This chapter starts by applying the simplest models using the simplest geometry, and proceeds to models of increasing complexity culminating with the CANDIE model using a realistic model geometry (i.e. observed coastlines and bottom topography). The main purpose of this chapter is to explain the asymmetry in the observed upwelling pattern in Trinity and Conception Bays as seen in satellite imagery (Figure 4.1).

This chapter is presented as follows. In section 4.2 results from the single mode, shallow water reduced-gravity model using an idealized square bay topography (Figure 2.6) are presented. Section 4.3 expands the discussion to continuous stratification

and solves the shallow water model with several modes. The effect of wind parameterization, the Prandtl number (Pr) and horizontal diffusion are examined. In sections 4.4 and 4.5, I apply the linearized and nonlinear versions (respectively) of the CANDIE code to the square bay topography (Figure 2.6). In 4.6 I focus on the response of a long thin rectangular bay (similar to the geometry of Trinity Bay) and discuss the effect of the relaxation of wind stress. In section 4.7 I apply the CANDIE model to realistic geometry of Conception and Trinity Bays in order to investigate the role of bottom topography and a realistic coastline on model results.

4.2 Single Layer Reduced Gravity Model

I begin by showing a result from the reduced-gravity, shallow water model with the wave speed chosen to correspond roughly to the first baroclinic mode in June (Figure 2.2). Velocities and interface displacement are shown in Figure 4.2, for a case with no friction or damping. For a wave speed of 0.5 m s^{-1}, Kelvin waves propagate roughly 60 km in a day. With a total coastline length of 160 km, the model reaches steady state by day 3, after which all Kelvin waves have left the domain and the interface displacement is symmetric about the axis of the bay.

The open boundary condition is designed so that no waves may enter the domain through the northern (upstream) boundary (Greatbatch and Otterson, 1991). The northern side of the bay reaches steady state first (Figure 4.2). Kelvin waves are generated at the mouth and propagate through this region in the first day. The last

region to reach steady state is the downstream side of the bay near the mouth, where Kelvin waves exit the bay.

4.3 Shallow Water Model Results: Continuous Stratification

Next I include continuous stratification with a finite bottom depth of 200 m. The solution procedure is described in section 2.3.2 but basically involves solving the finite difference shallow water equations for the first 10 baroclinic normal modes and then summing the modes to obtain the complete solution (summing over more than the first 10 modes does not significantly change the results to be presented). Higher mode waves have slower wave speeds and may not travel around the bay within 5 days. Adding the solution of these higher modes leads to an asymmetry in the cross-bay structure after 5 days that is not found in the solution for the 1st baroclinic mode in Figure 4.2. The importance of the higher modes depends on the extent to which the wind forcing projects onto each mode.

I consider two methods of applying the wind stress to the water column: (i) as a surface boundary condition or (ii) as a body force acting over a layer of depth H_M. Figure 2.4 shows the magnitude of the wind stress projection on the first 10 baroclinic modes for each of the two methods and for H_M = 10, 20 and 50 m. These projections determine the forcing function applied to the shallow water momentum equations associated with each mode. For a body force acting on a 10 m layer, the wind stress projection onto the first 10 modes is very similar to that obtained when

the wind stress is applied as a surface boundary condition (given by equation 2.13). Effective wind forcing of modes higher than 2 is reduced for a body force distributed over a depth of 20 m or 50 m.

4.3.1 Results

In the following runs, the model is run with the wind stress implemented as a body force acting over a depth of 10 m. As noted above, for the first ten modes, this gives a projection onto each mode very similar to that when the wind stress is implemented as a surface boundary condition. The model is first run with no friction or damping. I note that running the model with no vertical mixing of momentum, yet implementing the wind forcing as a surface boundary condition makes no physical sense, hence the adoption of the 10 m body force approach. This approach is consistent with the CANDIE model where wind stress is imparted to the top 10 m thick model level.

By day 5, the third mode and higher Kelvin wave modes have not exited the bay. This is apparent in the velocity and pressure field (Figure 4.3) along the south shore of the bay where there is outflow near the mouth. The anticyclonic gyre is now restricted to the inner half of the bay, whereas as observed in Figure 4.2 it fills the whole bay after only 3 days. The baroclinic flow structure of the coastal jet is clearly visible in the cross-sections of currents shown in Figure 4.3. On transect A, the northward coastal surface jet at the head of the bay exhibits reverse flow at depth, and extends away from the coast below the wind driven Ekman current. On transect B, there

is generally anticyclonic flow in the upper part of the water column, and cyclonic flow at depth, although the detailed vertical structure differs on the southern and northern boundaries due to the contributions from the various normal modes. It is clear from these results that taking account of the realistic density stratification in the bay, and the role played by the higher baroclinic normal modes, are sufficient to lead to a significant asymmetry in the cross-bay response to wind on the 5 day time scale typical of wind events in Conception and Trinity Bays.

I now investigate the effect of adding vertical mixing of momentum and density. For a Prandtl number of one, the addition of vertical mixing does not greatly affect the model response unless Λ_M, Λ_ρ in equations (3) have a value approaching 10^{-6} m^2 s^{-3}, corresponding to vertical eddy viscosity/diffusivity of 10^{-2} m^2 s^{-1}for $N^2 = 2\times10^{-4}$ s^{-2} (see Figure 2.1). For Prandtl numbers less than one, the model response after 5 days is not greatly different from that in Figure 4.3. A Prandtl number greater than one, implying stronger mixing of momentum than density, has a greater effect, particularly in increasing the horizontal scale associated with the model response (Yamagata and Philander, 1985). Figure 4.4 shows a case with a Prandtl number of 100 corresponding to choosing Λ_M and Λ_ρ equal to 2×10^{-6} m^2 s^{-3} and 2×10^{-8} m^2 s^{-3}, respectively and should be compared with Figure 4.3. The fields in Figure 4.4 are quite similar to those obtained with a Prandtl number of one when both Λ_M and Λ_ρ are equal to 10^{-6} m^2 s^{-3}, showing that on the 5 day time scale being considered here, it is the vertical mixing of momentum that has the greatest effect in modifying the response.

On longer time scales (e.g. 20 days), the dependence on Prandtl number is more like that predicted by Yamagata and Philander (1985): that is, the model response is broad and diffusive for Pr = 100, but is characterized by narrow jets, significantly narrower than the radius of deformation for the first baroclinic mode, when Pr = 0.01.

Implementing the wind stress as a body force acting over a depth of 20 m reduces the importance of the higher modes (as I expect from Figure 2.4). Figure 4.5 shows a case with Λ_M and Λ_p both set to zero and with H_M = 20 m. I note, in particular, that the eastward jet on the south side of the bay near the mouth is weaker than in Figure 4.3.

4.4 Linear CANDIE Model Results

In this section I study the response of a flat-bottomed, idealized square bay to wind forcing using the CANDIE model. I use the idealized model geometry shown in Figure 2.6 with a uniform depth of 200 m, vertical resolution of 10 m and horizontal resolution of 500 m. In most of the model runs, vertical viscosity and diffusivity are set at 10^{-4} $m^2\ s^{-1}$ and the horizontal mixing of momentum and density is zero unless otherwise stated. The density stratification is representative of June, as discussed in chapter 2, and identical to that used in the continuously stratified case runs described in section 4.3. The density equation is linearized about the (horizontally uniform) June density profile and the momentum equations are linearized about a state of rest,

although some fully non-linear runs are described later. The rigid lid, Boussinesq and hydrostatic approximations are used in the model. The open boundary conditions are described in Chapter 2 and are the same as those applied to the shallow water equation models. The model has been tested using vertical viscosity and diffusivity set inversely proportional to N^2, as in the normal mode model. The model results are almost identical to the normal mode solution obtained in section 4.3.

As previously described, a westward wind stress of 0.05 Pa is introduced gradually over 2 days. The zero in time is taken to be 1 day into the ramping. Given that the vertical grid spacing is 10 m, the wind stress is in effect implemented as a body force acting over the 10 m depth of the top model level. Figures 4.7 and 4.8 show plots of velocity and density 5 days into the model run. At the head of the bay, the characteristic northward surface jet with velocities 10-15 cm s^{-1}, broadens at 15 m depth (Figure 4.7) and is accompanied by reversal in flow at greater depth, very similar to what was obtained using the normal mode model (Figure 4.3). At level 2 (15 m depth), the horizontal flow and pressure fields (Figures 4.7 and 4.9) resemble those obtained using the first baroclinic mode alone. This is a consequence of the vertical structure of the higher modes which have zero crossings at roughly 15 m depth (Figure 2.2) and thus have little influence on flow at 15 m. At level 2 Ekman driven contribution to the flow is minimal. On the southern boundary at the mouth of the bay, the flow at 15 m depth is the reverse of that at the surface (this is also a feature of the normal mode model, see Figure 4.3). The importance of higher vertical

modes noted when discussing Figure 4.3 can also be observed in the cross-sections of the density field (see Figure 4.8). I note, for example, the vertical pinching of the isopycnals on the southern boundary near 20 m depth in Figure 4.8, and the fanning out of the isopycnals near 40 m depth on the western boundary.

4.5 Non-linear CANDIE Model Results

Next I apply the full non-linear equations of motion to the above problem employing the square bay topography found in Figure 2.6. I use the CANDIE model without any linearisation. Model resolution remains at 500 m in the horizontal and 10 m in the vertical and the model parameters are the same as for the linearized runs, apart from the inclusion of horizontal mixing of momentum and density with eddy mixing coefficient 10 $m^2\ s^{-1}$. The model also simulates convective overturning by increasing the vertical diffusivity to 10 $m^2\ s^{-1}$ whenever hydrostatic instability occurs to mix out unstable vertical density profiles. A free slip boundary condition is applied to the velocity field and the normal gradient of density is set to zero on the model boundaries.

Figures 4.10 and 4.11 show the results of the non-linear run at day 5. The cross-bay advection of upwelled water widens and strengthens the coastal jet on the upwelling favourable (northern) boundary while it narrows and subdues the coastal jet on the downwelling favourable (southern) boundary. The most striking difference from the linear case (Figure 4.7) is the separation from the coast of the jet on the north side of

the bay. The transport of surface water at the head of the bay towards the upwelling favourable coast creates an alongshore density and pressure gradient which drives flow away from the coast forcing the coastal jet to separate from it (Figure 4.12).

This separation is an effect due to density advection at the head of the bay in the north corner and is evident by comparing the surface density field in Figure 4.11 with that in the linear case (Figure 4.8). In the non linear case, upwelled water is spread cross shore in the interior of the bay, but this spreading is halted towards the head of the bay by the northward flowing coastal jet at the head of the bay.

On the south side of the bay (Figure 4.10, transect B), the along-shore component of flow is much weaker than in the linear case (Figure 4.7). The transport of density across the bay reduces the cross-shore density gradients, reducing the strength of the coastal jet set up by the passage of Kelvin waves. Flow in this area remains weaker at the surface and at depth. The surface coastal jet on the north side (transect B) penetrates deeper with the inclusion of the non-linear terms. Maximum flow strength is about 5 km off the coast in this cross-section.

At the head of the bay, transect A (Figure 4.10) shows weakening of the coastal jet near the coast, but a spreading into the interior at depth compared to the linear case (Figure 4.7). The velocity structure at 15 m depth shows evidence of this broad northward flow. In Figure 4.11, density decreases from the head of the bay towards the mouth along transect A. Just beyond the mouth of the bay, the isopycnals are tilted upwards away from the bay. The cross-bay jets at depth evident on transect A

(Figure 4.10) are associated with these features in the density field.

The surface density field in the non-linear case resembles qualitatively the observed surface temperature structure in Figure 4.1 with a predominantly cross-bay structure and evidence of broad upwelling on the north shore, with the upwelled water extending out into the interior of the bay.

4.6 Rectangular Idealized Bay Results

I apply the CANDIE model to an idealized flat bottom topography of Trinity Bay (Figure 2.7) with a width of 25 km and a length of roughly 80 km. As noted before, an out of the bay (positive x direction) steady wind stress is smoothly introduced over a 2 day period to the bay, which is initially at rest. As before, initial stratification is horizontally uniform and represents June stratification.

Our emphasis in this section is focussed on understanding the separation and evolution of the coastal jet on the upwelling side of the bay observed in section 4.5 (Figures 4.10, 4.11 and 4.12). Furthermore, I want to explore the effects of width and length of the bay on the model solution. I study several cases with wind varying from 0.05 to 0.1 Pa; linear cases, non-linear cases and a special case with non-linear advection of momentum but not density.

Model resolution is 500 m in the horizontal and 10 m in the vertical above 100 m. Below this depth, vertical resolution is 20 m.

4.6.1 Linearized Model Results

I start with a model run with 0.05 Pa wind using linear dynamics. Figure 4.13a shows the surface velocity field from the linearized model at day 5. The velocity field shows anti-cyclonic flow around the head of the bay, with a coastal jet on the north side and a coastal jet on the south side. While the first mode response would be symmetric at day 5 at the surface (noting that the total coastline length is 240 km), the effect of higher modes, cause a lingering of the eastward jet on the south side of the bay. This jet recedes slowly (5 cm s^{-1}) out of the bay.

The corresponding surface density field (not shown) has denser water on the north side and around the head. The south side of the bay near the coast features lighter water. One should note that in the linearisation of the density equation, when vertical velocities are negative, surface density diminishes to conserve mass.

In the linearized result, all the change in surface density and velocity occur within vicinity of the coast (i.e the first baroclinic Rossby radius). The longer the length of the bay, the stronger the upwelling and currents along the coast near the head will be.

Since realistic winds in this region are variable, I examine the linear response of a bay to the relaxation of the wind after 5 days of steady wind. I run the linear CANDIE model with a constant wind of 0.05 pa directed along the axis of the bay up to day 5 and then let wind stress relax over 2 days back to zero. Figure 4.13b shows the surface velocity at day 10. Kelvin waves progressively erase the initial

coastal setup. After 3 days, there are still significant currents and density gradients in the bays. The north shore relaxes first, with the south shore still having significant velocity 5 days after the onset of relaxation. From day 5 to day 10, currents on the southern shore of the bay reverse in direction due to the propagation of Kelvin waves from the north shore. Over time, velocities decay, and the bay returns to rest.

4.6.2 Non-linear CANDIE Results: Constant Wind

I now explore the non-linear response of the idealized Trinity Bay (see Figure 2.7). The model setup is identical to that in section 4.6.1 except I now include non-linear terms for the momentum and density equations.

At the surface, (Figure 4.14), the northern coastal jet (J1) separates from the coast roughly 25 km from the head of the bay (as in Figure 4.10 for the square bay topography case). The coastal jet (J1) extends only about 40 km from the head of the bay beyond which there is a broader diffuse eastward jet (J2) centered 8 km from shore.

Cross sections A, B and C in Figure 4.14 show the evolution of the Northern Jet (J1). From A to B the northern jet broadens, deepens and intensifies. In cross-section C, 40 km away from the head, the coastal jet is now weaker and centered roughly 8 km off shore.

At the second level (15 m depth) (Figure 4.14b), circulation around the head of the bay is anti-cyclonic and the coastal jet J1 does not appear to separate as in

the surface velocity field. Currents on the south coast of the bay are inward near the head of the bay, and outward near the mouth, with maximum flow strength of $\sim$10 cm s^{-1} in strength at level 2 and $\sim$20 cm s^{-1} at the surface.

A cyclonic gyre is present to the south of the mouth (G1 in Figure 4.14b). Gyre G1 is most visible at 15 m due to the imposition of wind stress at the surface. The gyre is caused by the combination of horizontal mixing, the coriolis force and the presence of the corner. The shape and strength of the gyre depends on the use of the slip or no-slip boundary condition which will be discussed later in this section. In the square bay topography case, the gyre observed at the mouth is much weaker with currents less than 2 cm s^{-1} and hardly noticeable in the surface layer (Figure 4.10).

Looking at the density field (Figure 4.15a), there is upwelled water distributed over the entire bay from the north side, except at the head. Similar to the square bay case, the northward coastal jet at the head of the bay transports upwelled water northward, resulting in the narrowing (pinching) of horizontal isopycnals near the head of the bay.

There is a wave-like structure in the density fields (W1) on the north shore of the bay, which is more noticeable here than in the short square bay case shown in Figure 4.11. This feature (W1) appears at the juncture between jets J1 and J2 in figure 4.14. The wave like structure grows and eventually forms gyre in the bay.

At the second level, isopycnals bulge out away from the corner, associate with the gyre identified in the velocity field (G1) (Figure 4.15). From vertical cross-sections

A through C. I observe that: (1) The top two levels are mixed more thoroughly further away from the head of the bay; (2) the pinching of isopycnals on the south side deepens with distance from the head.

Figure 4.16 shows a model result for the top 2 model levels for velocity and density. The only difference from the previous run is that the constant out of the bay wind now has a strength of 0.1 Pa (i.e. a two-fold increase) on the surface of the bay. The increased wind stress strengthens the coastal wave setup and associated velocities. This increases the strength of the non-linear terms, which is clearly observed in Figures 4.16 a, b, c and d.

For example, the jet J1 is evolved into a gyre even at the surface, despite the tendency for wind stress to mask out gyres at this level. The jet (J1) however still separates from the coast around 25 km from the head of the bay. In the corner C2, the northward jet at the head of the bay separates from the head and cuts diagonally across the corner to rejoin the north shore. The density field indicates upwelling in this corner.

The secondary jet J2, now broken up into 2 or 3 sections, appears unstable and is centered further off-shore. The density field shows horizontal wave like undulations coinciding with these crescent-moon shaped velocity patterns of J2. These undulations grow in amplitude, and move towards the mouth of the bay at an estimated speed of 0.56 ± 0.05 m s^{-1}which is roughly equal to the first baroclinic wave speed of the initial water column.

At the south-west corner of the bay (C4), the gyre G1 has increased in strength with speeds above 20 cm s^{-1}. The velocities from the top two levels at the coast near this region indicate upwelling.

With continued model integration under 0.1 Pa winds, the instabilities from J2 grow and move towards the mouth. Eventually they form gyres with warm water in the center as seen in Figure 4.17. The surface density pattern resembles fingers of cold water stretching southward from the north coast. This pattern is similar to that observed in satellite SST observations by Petrie et al. (1992b) on the Scotian Shelf.

There exists an obvious leakage of water from all the gyres in the bay G2, G3 and G4 near the coast, with the coastline to the right of the leaked current. This pattern of "leaky eddies" near the coast is in good agreement with the analytical work of Nof (1988) and the modelling work of Sheng (1999). I note that for gyre G2 the leaked current starts initially slightly off shore by 5 km. At day 10, the G1 gyre at the corner has developed with a strong current near the coast (see Figure 4.17).

The sensitivity of the model solution to the land boundary condition is tested by running the model with a no-slip boundary condition instead of the free-slip condition. The results at day 5 are shown in Figure 4.18. Overall the pattern does not change from that in the free-slip cases. However some minor differences are readily seen near the coast including the absence of "leakage current" from the gyres along the southern coastline, a reduction of the strength of the gyre G1 and slight differences in the coastal jet in the corner C2. The separation of the jet J1 from the north coast

occurs 2-3 kms further from the head of the bay then in the free-slip case. This is a consequence of the cyclonic vorticity imposed by the no-slip boundary condition along the northern shore.

4.6.3 Non-Linear Results: Relaxation of Wind

I now run the non-linear CANDIE model as in section 4.5 for the idealized Trinity Bay (Figure 2.7), however, as of day 5, I relax the 0.1 Pa wind to zero (over a 2 day period till day 7) and observe the non-linear response. As previously discussed, 5 days after the onset of heavy constant wind, a gyre is formed in the bay, a gyre is formed to the south of the bay's mouth and instability features exist inside the bay ahead of the coastal jet J1 (Figure 4.16).

When the wind is relaxed, the top model layer is no longer influenced by horizontally uniform wind stress. The horizontal patterns of velocity and density are almost identical in the top 2 layers. Upwelled water transported across the bay by Ekman transport is convectively mixed to stabilize the water column. This results in an upper homogenized mixed layer of 30 m depth with little vertical shear of density and horizontal velocity (Figure 4.19) over this depth.

As the wind dies down, the anti-cyclonic gyre at the mouth of the bay (G1), moves northward around the south corner, into the bay shedding a smaller anti-cyclonic eddy (G4) at the corner inside the bay. This corner eddy is weak, not enhanced by the Coriolis effect and is a result of the non-linear and horizontal mixing terms.

The coastal jet J1 has evolved into a sinusoidal jet flowing westward through a field of 2 small cyclonic eddies and 1 anti-cyclonic eddy. Part of the jet also contributes to an eddy near the head of the bay. On the south coast. there is an eastward jet that follows the shore line until roughly 20 km from the head where it separates from shore with flow splitting into eastward flow along the north shore and a cyclonic gyre in the south-west corner. The westward jet on the south shore is associated with the linear relaxation process (cf. Figure 4.13b) and appears to be stable.

4.6.4 Role of Density Advection

I run the non-linear CANDIE model. with advection of momentum suppressed forced by a steady 0.1 Pa out-of-the-bay wind stress. I seek to isolate the cause that precipitates the separation of the jet J1 from the coast.

Figures 4.20 and 4.21 show the velocity and density for the non-linear run with linearized momentum. The coastal jet J1 is present along the north coast as far as 25-30 km from the head of the bay. Outwards from this point towards the mouth. flow is across the bay at the surface and dense water is advected across the bay. I note the strong difference between vertical cross sections A and B with cross section C. The coastal jet visible in A and B. is not featured in panel C situated 40 km from the head.

The coastal jet J1 does not persist off shore. nor does it persist along the shore beyond 30 km from the head of the bay at day 5. While density transport creates an

along-shore density gradient, the separation from the coast of coastal jet J1 requires the non-linear momentum terms for the jet to persist off shore and for gyres to develop.

4.7 Realistic Coastline Geometry Results

In this section I use the CANDIE model to explore the influence of the realistic coastline and bottom topography of Trinity and Conception Bays (Figure 2.8). Coastal trapped waves travel with the coastline on the right in the northern hemisphere. Thus waves generated in Trinity Bay can exert an influence on Conception Bay. Indeed, the influence of Trinity Bay on upwelling events in Conception Bay was inferred by de Young et al. (1993b). Here I investigate the effects of a wind blowing along the axis of the bays (that is at 30 degrees from the x-axis of our model domain - see Figure 2.8). The wind stress has magnitude 0.05 Pa and, as before, it is introduced over a period of two days to reduce the excitation of inertial oscillations.

Four different model versions are considered: (a) a single mode for the shallow water normal mode model, (b) the linearized CANDIE model with a flat bottom, (c) the linear CANDIE model including realistic bottom topography and (d) the nonlinear CANDIE model using realistic bottom topography and a free slip lateral boundary condition. All models have a horizontal diffusivity of 10 $m^2\ s^{-1}$for momentum and density. For computational feasibility, the resolution of the models is 1 km instead of 500 m. A comparison with the 500 m case indicates good agreement.

Figure 4.22 shows the modeled velocity fields, respectively, for each of the 4 runs.

Panels e and f feature the density fields for cases c and d, respectively.

Let me consider the first case (a). The first baroclinic mode represents well the initial upward displacement of the pycnocline on the north shore of Trinity Bay. However, after 5 days, the circulation in Conception Bay weakens with almost zero pressure gradient across the bay. This lull in circulation in Conception Bay is a direct consequence of the downwelling Kelvin wave generated on the south side of Trinity Bay compensating for the upwelling wave generated on the north side of Conception Bay. One day later, the circulation builds up again, as the upwelling wave generated in Trinity Bay (on the north side) pushes into Conception Bay.

Moving to continuous stratification (case (b)), there is now significant flow in Conception Bay, indicative of the role being played by higher order baroclinic modes. There is also surface flow out of each bay along the southeastern boundary near the mouth, as in the idealized cases (Figure 4.7), as well as southward coastal jets around the capes at the head of the bays. As in the idealized experiments, the higher modes increase the response time of the bays to wind forcing.

Adding realistic bottom topography (case (c)) to the linear case, makes for only minor differences to the model solution on the time scale of 5 days being considered here. For example, there is a slight strengthening of the coastal jet on the north shore of Conception Bay using realistic topography. I can therefore conclude that in the model solutions realistic bottom topography is not critical in determining the baroclinic response at the surface to wind on a five day time scale in the linearized

case.

Turning to the nonlinear case (case (d)). I find that. as in the idealized case (Figure 4.10). there is cross-bay advection of upwelled water in association with the cross-bay Ekman transport. This leads to the predominantly along-bay structure of the surface isopycnals (panel f). similar to the pattern of isotherms in Figure 4.1. A coastal jet is featured on the north side of each bay. but contrary to the linear case (b). there is no coastal jet on the south side of the bays. suggesting that Kelvin waves are damped on the south side of the bays. This dampening is driven by the cross-bay Ekman transport of light water that confines wave action near the coast and inhibits upward movement of the pycnocline due to Kelvin waves.

Furthermore. the non-linear terms shift the coastal jet on the upwelling side of the bays away from the coast. bypassing coastal indentations (i.e such as on North Side of Trinity Bay). There is also a suggestion. particularly in Conception Bay. that the coastal jet along the north shore separates from the coast as indicated by Figure 4.10. While non-linear terms contribute greatly to the surface solution. they contribute little at 50 m depth (not shown) due to small velocities and density gradients at this depth.

After 10 days of wind forcing (Figure 4.23). a separated jet is found in both bays as well as wave-like features beyond the separated jet. In Figure 4.23 a and b). The separation of the north shore jet in Trinity Bay is caused by along shore density gradients due to the competing influence of northward transport by the coastal jet at the head of the bay opposing southward cross-bay Ekman transport. Model runs

undertaken with idealized rectangular bay topographies of different width and lengths (not shown), demonstrate that the separation point of the jet on the northern coast is independent of bay width and bay length (provided these are greater than 2 or 3 internal Rossby radii). The narrowing of the coastal jet near the head of Trinity Bay is also noticeable in the idealized case (Figure 4.11). Moreover as evidenced, in the satellite observations (Figure 4.1) there is a narrowing of the band of cold water near the head of the bay.

The instability features beyond the jet (Figure 4.23) propagate towards the mouth of the bay, with an estimated speed of $\sim 0.56 \pm 0.1$ m s^{-1}equivalent to the propagation speed for the first baroclinic mode (Figure 2.2). These wave like features grow until they form gyres and are likely due to be baroclinic instabilities. Analysis of time series output from the model suggests that when the horizontal amplitude of the waves reaches bay width, a gyre is formed. At later times (e.g. 16 days, not shown), the flow in both bays is dominated by gyre circulations associated with the separated jets, with two gyres occupying Trinity Bay, as against a single gyre in the shorter Conception Bay . These gyres are dynamic and progress slowly out of the bay, shedding short lived (1-2 days) smaller eddies.

The inclusion of non-linear terms leads to a distinct separation of the coastal jet and formation of gyres beyond 10 days of model integration. Comparison of model results indicates that while 500 m resolution resolves the instability features more cleanly, 1 km resolution permits for reasonable reproduction of all observed features

in the 500 m resolution runs.

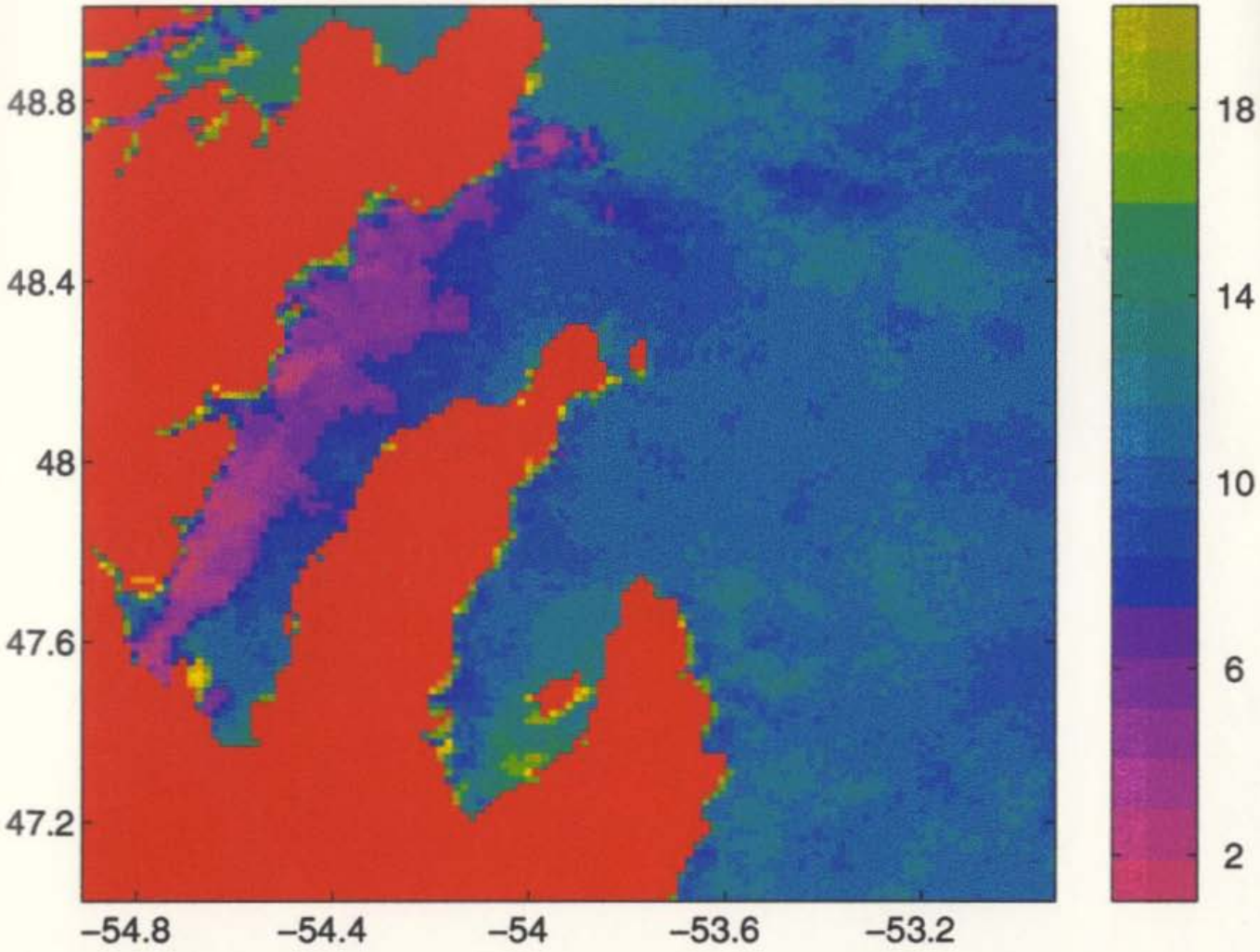

Figure 4.1: Observed sea surface temperature in Conception and Trinity Bays on Aug 4th 1997. Color scale is in °C. The north-west side of both bays are significantly cooler than the south-east side. Wind has been blowing from the south-west for the previous 3-4 days. The picture is based on an AVHRR satellite image (Courtesy of Peter Cornillion, University of Rhode Island) and processed using the RSMAS sea surface temperature algorithm.

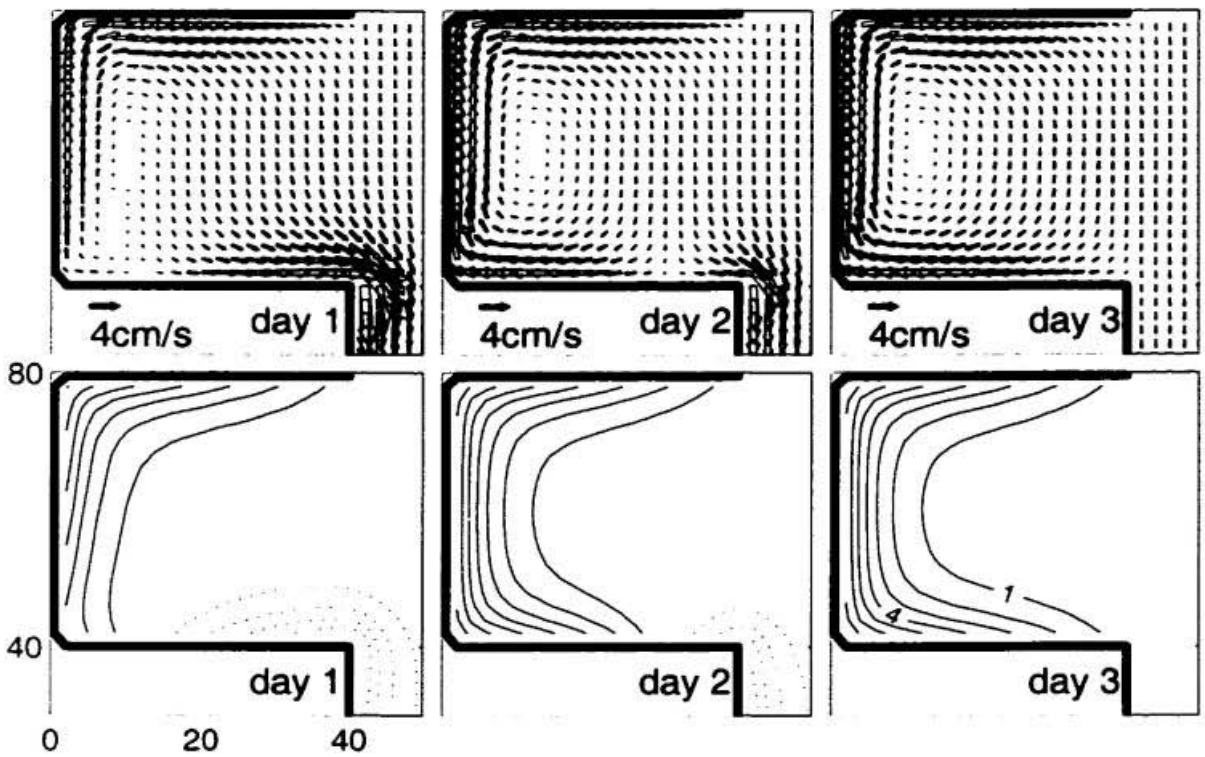

Figure 4.2: Upper Row: Upper layer velocity from the single-layer, reduced-gravity model run with a phase speed $c = 0.5$ m $s^{-1}$and no damping (i.e. inviscid) at days 1, 2 and 3. Lower Row: As in upper row, but for interface displacement. Solid lines represent upward interface displacement and dotted lines downward interface displacement.

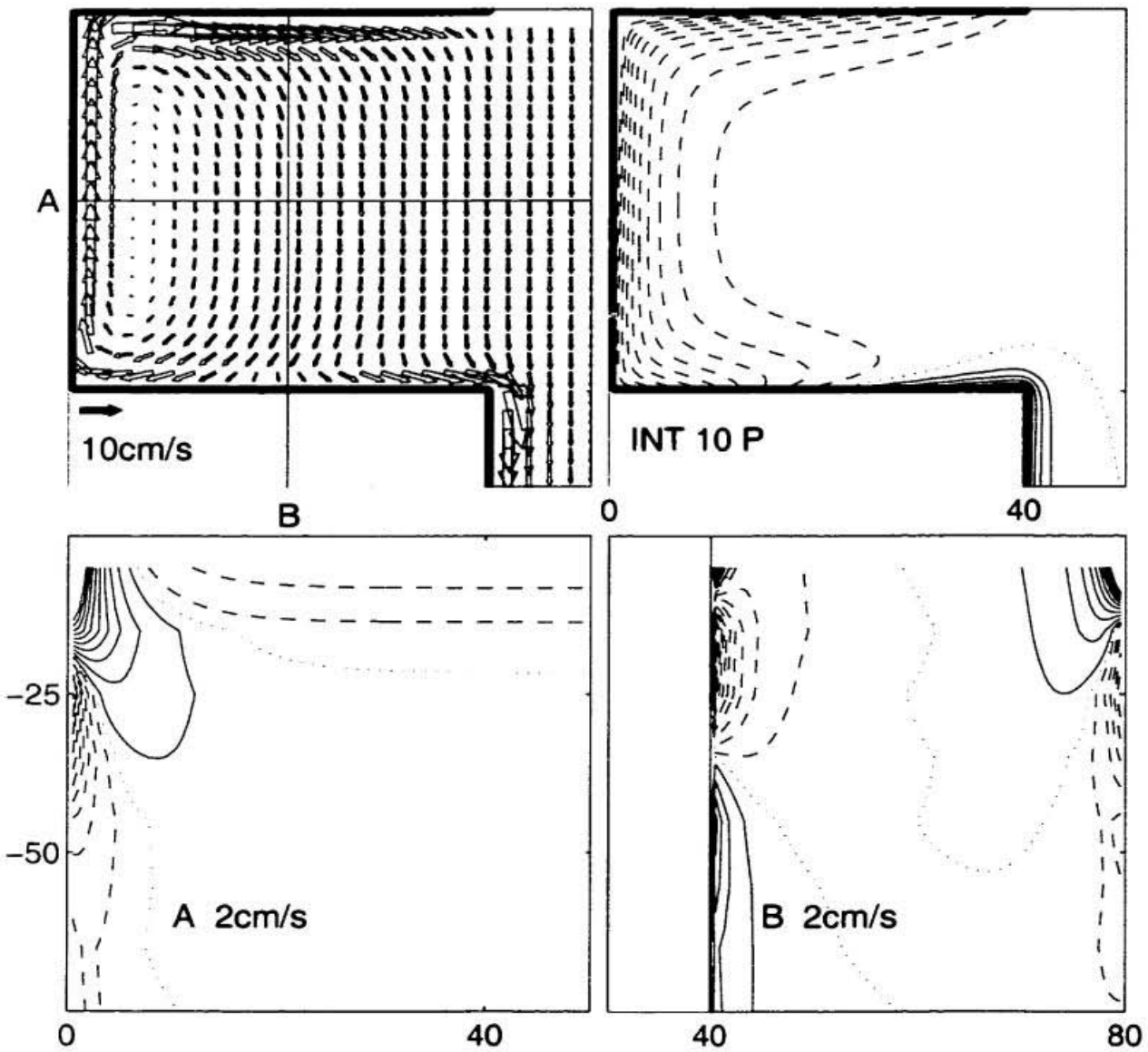

Figure 4.3: The normal mode model at day 5 with no friction or damping. Top left: Surface velocity field. Top right: Surface Pressure field. Dashed contours represent negative pressure anomaly and solid lines indicate a positive pressure anomaly. Bottom Left: Vertical profile of velocity normal to transect A. Bottom Right: Vertical profile of velocity normal to transect B. The maximum depth shown in the vertical transect plots is 75 m. Solid contours indicate flow into the page and dashed contours indicate flow out of the page. The zero contour is shown by a dotted line.

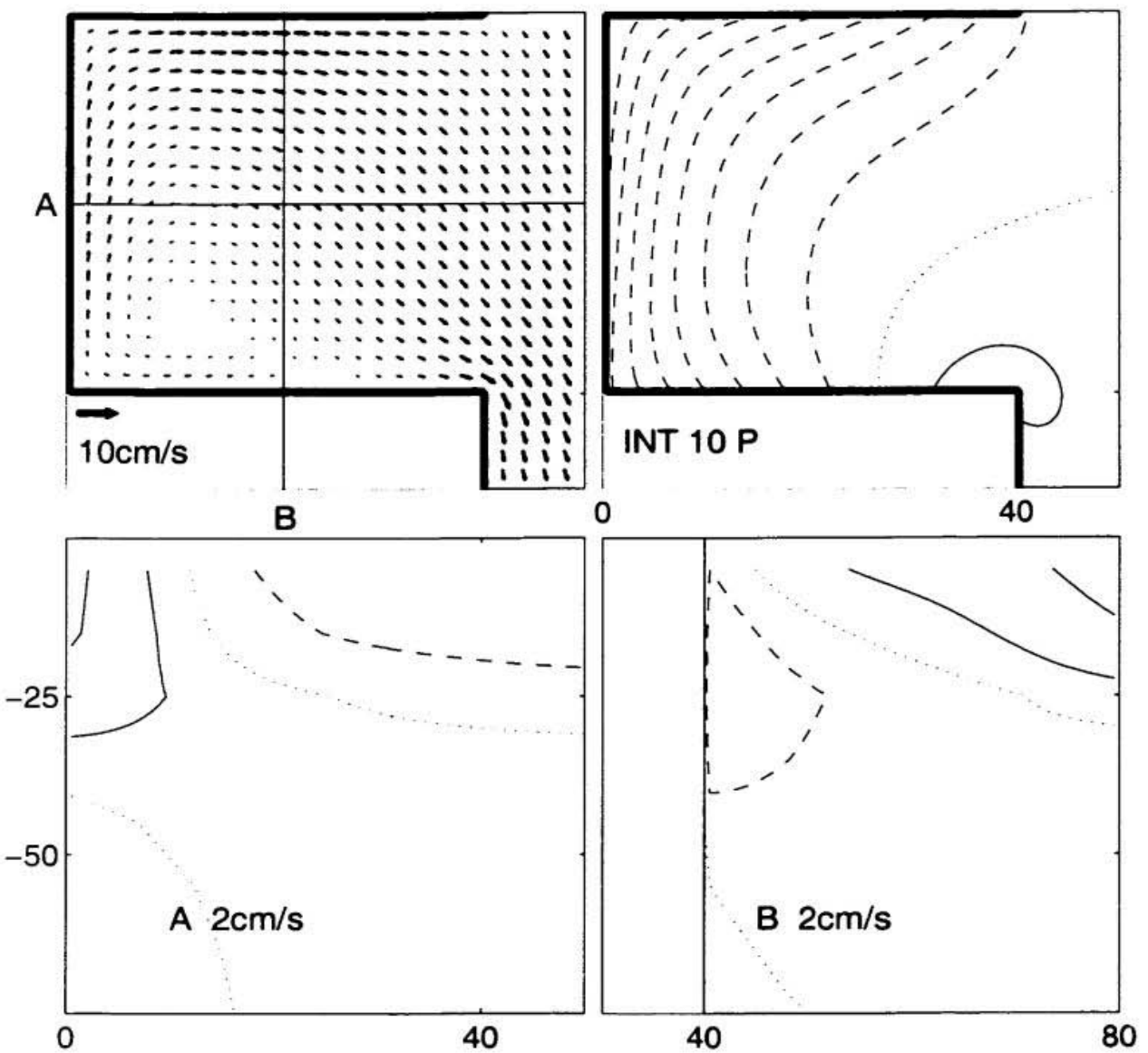

Figure 4.4: As in Figure 4.3 but with a Prandtl number (Pr) of 100. (i.e. now $A_m = 2 \times 10^{-8}$ m^2 s^{-3}).

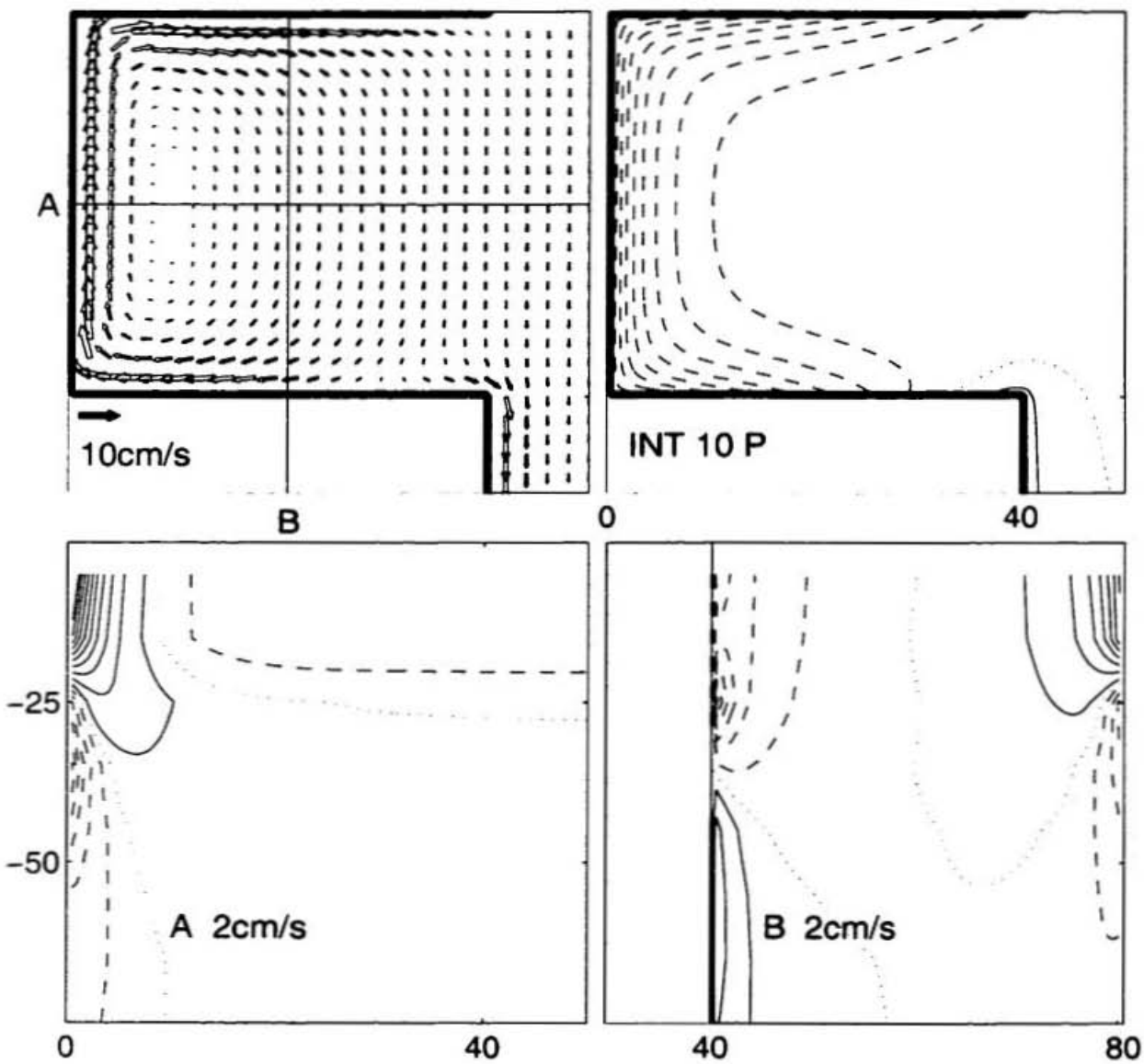

Figure 4.5: The normal mode model at day 5 as in 4.3, but with wind stress modeled as a body force acting over the top 20 m.

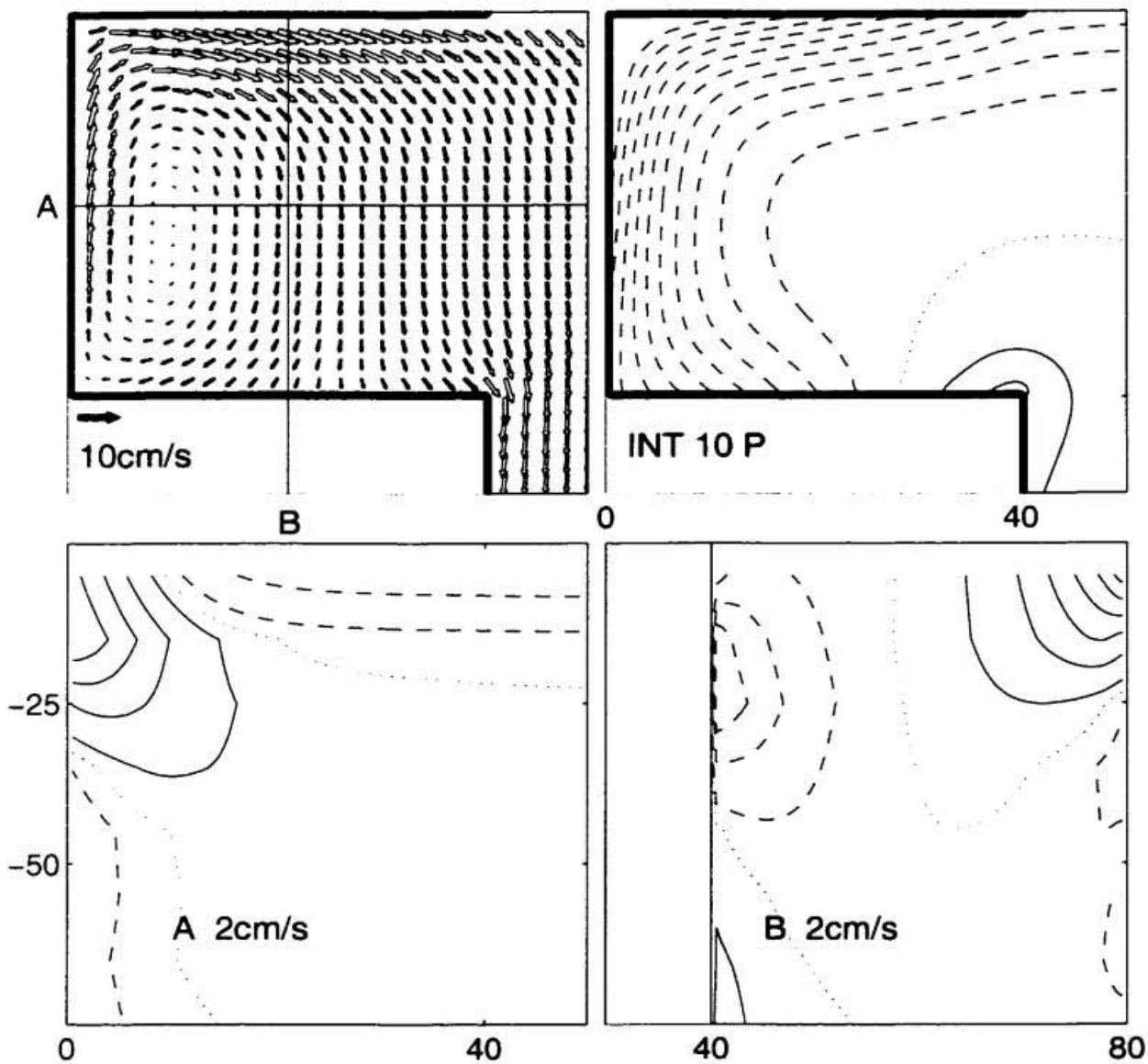

Figure 4.6: As in Figure 4.3 but with diffusivities for momentum and pressure of 50 $m^2\ s^{-1}$.

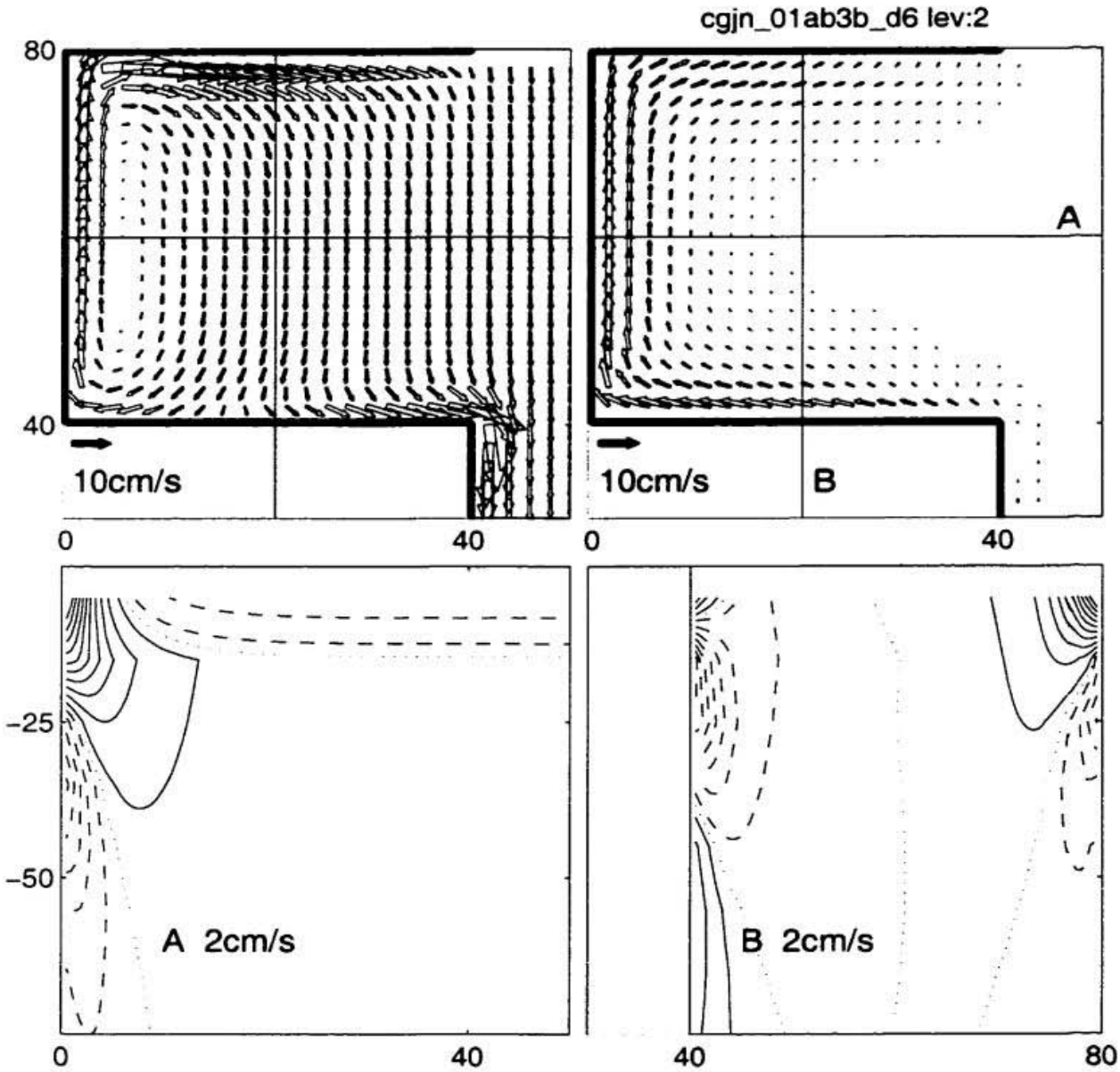

Figure 4.7: The linearized CANDIE model at day 5 with idealized geometry: Top left: surface level velocity. Top right: second level velocity. Bottom left: velocity normal to transect A. Bottom Right: Velocity normal to transect B. Solid lines indicate flow into the page and dashed lines indicate flow out of the page. The dotted lines are the zero contours.

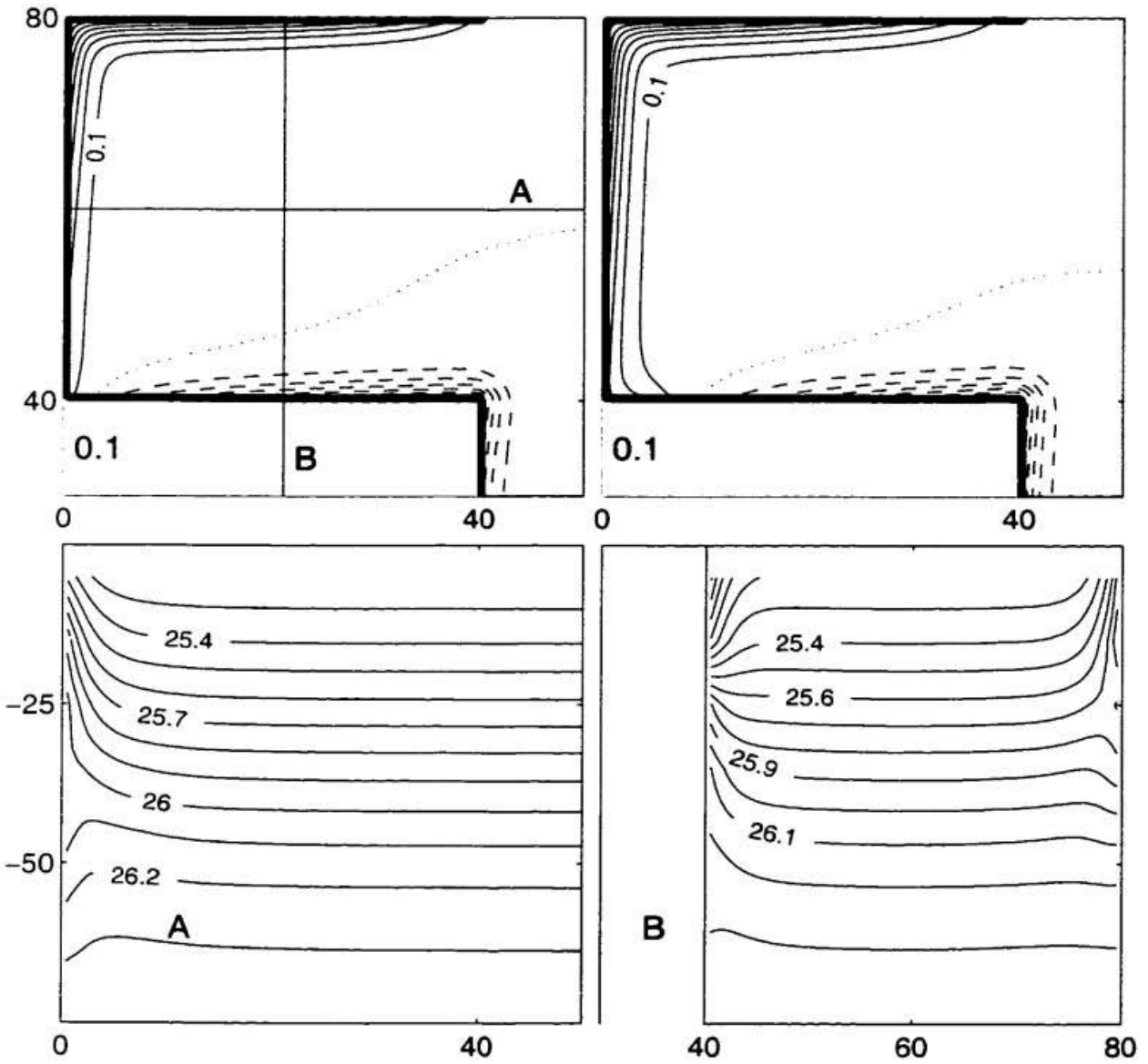

Figure 4.8: Density field for Figure 4.7.

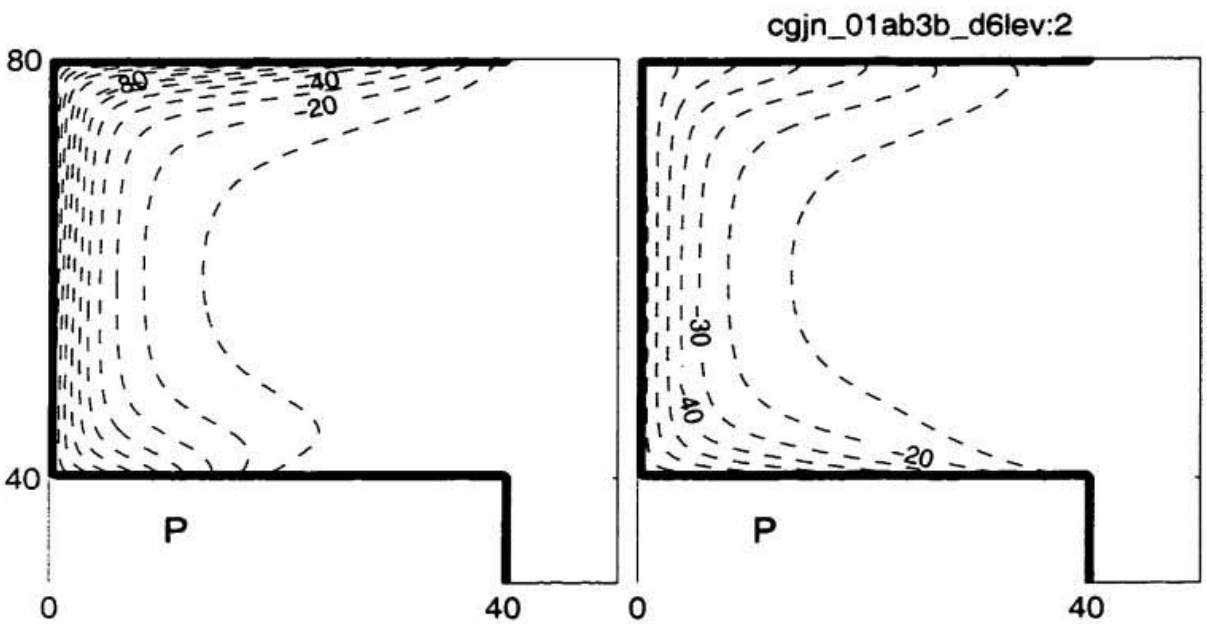

Figure 4.9: Surface (left) and second level (right) pressure field for the same run as Fig. 4.7. Contour intervals are in 10 Pa increments.

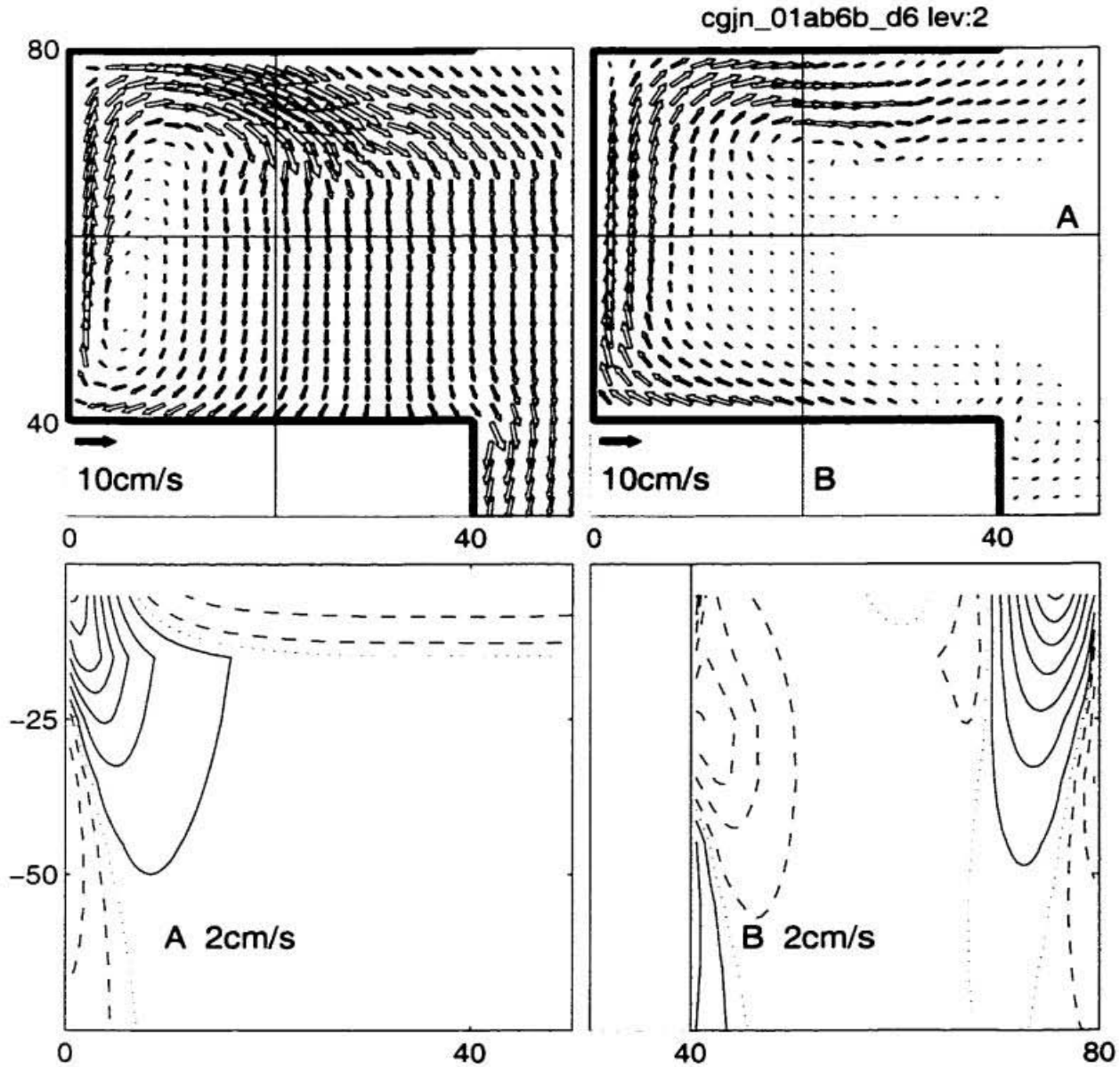

Figure 4.10: The non-linear CANDIE model at day 5 with idealized geometry. Top left: surface level velocity. Top right: second level velocity. Bottom left: velocity normal to transect A. Bottom Right: Velocity normal to transect B. Solid lines indicate flow into the page and dashed lines indicate flow out of the page. The dotted lines are the zero contours.

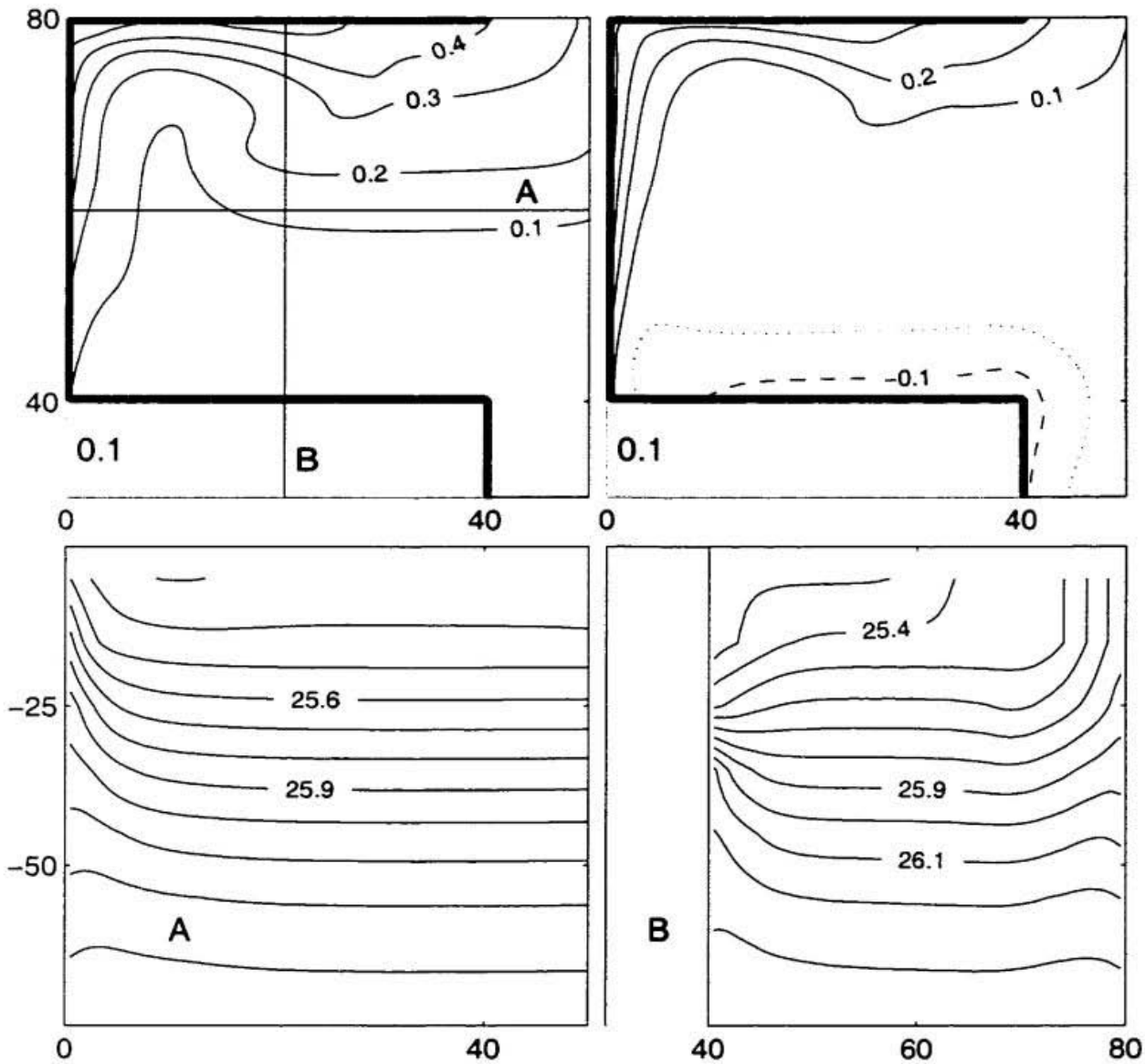

Figure 4.11: As in Figure 4.10 but for the density field.

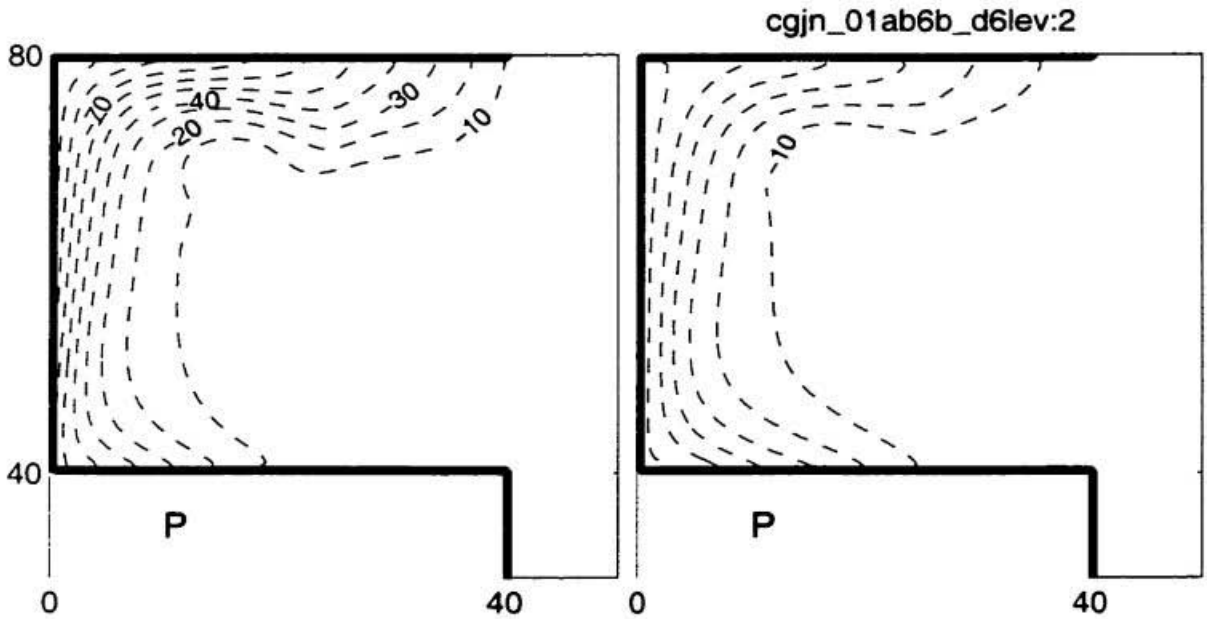

Figure 4.12: Non-linear CANDIE RUN: Surface and second level pressure field. Intervals are in 10 Pa increments.

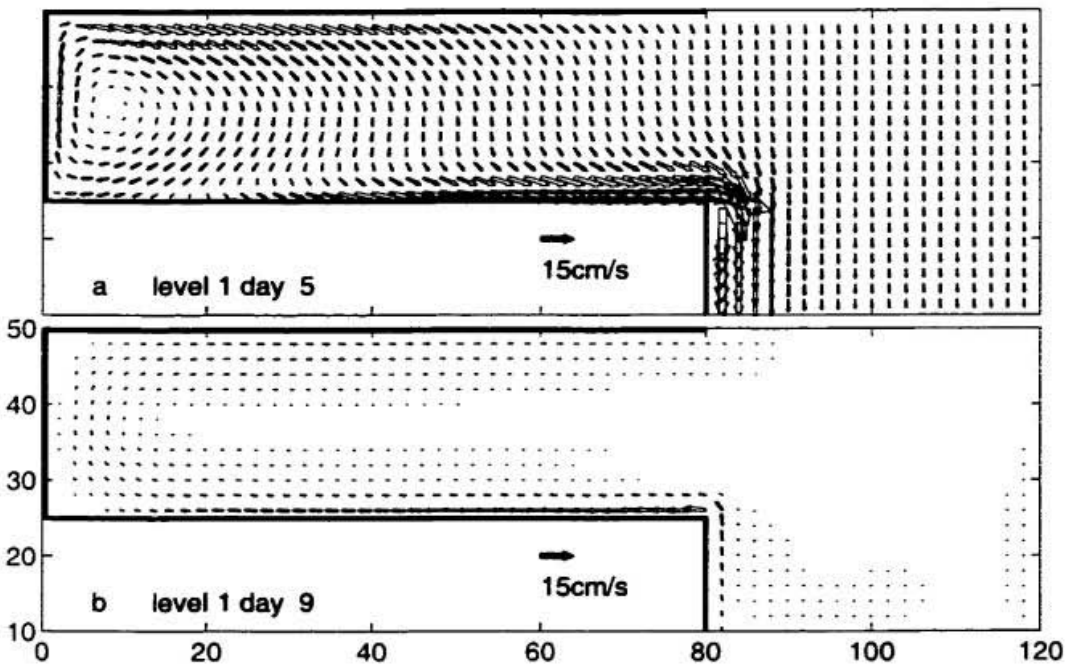

Figure 4.13: Surface velocity field (top 10 m) from linearized CANDIE run at (a) day 5 and (b) day 10 using idealized 200 m flat bottom Trinity Bay topography. Wind of 0.05 Pa is blowing along the x axis till day 5, relaxes to zero from day 5 to day 7 and remains off till day 10.

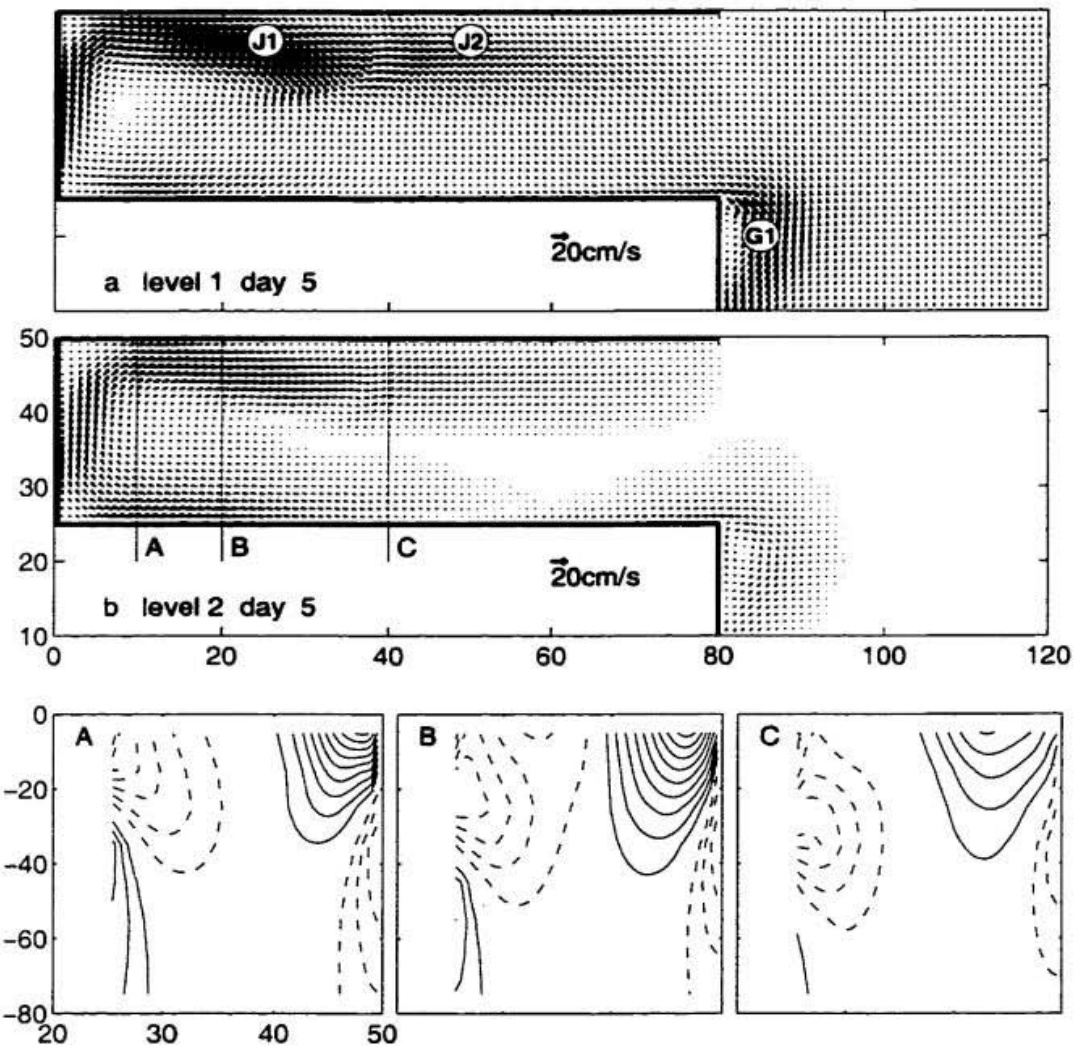

Figure 4.14: Non-linear CANDIE model with 0.05 Pa constant wind along the x-axis at day 5. (a) surface level. (b) second level. Vertical cross-sections A. B and C (see b) are contours of velocity normal to the plane. Contour intervals are 2 cm s^{-1} with solid lines representing flow out of the page. dashed contours indicating flow into the page. and the dotted line giving the zero contour.

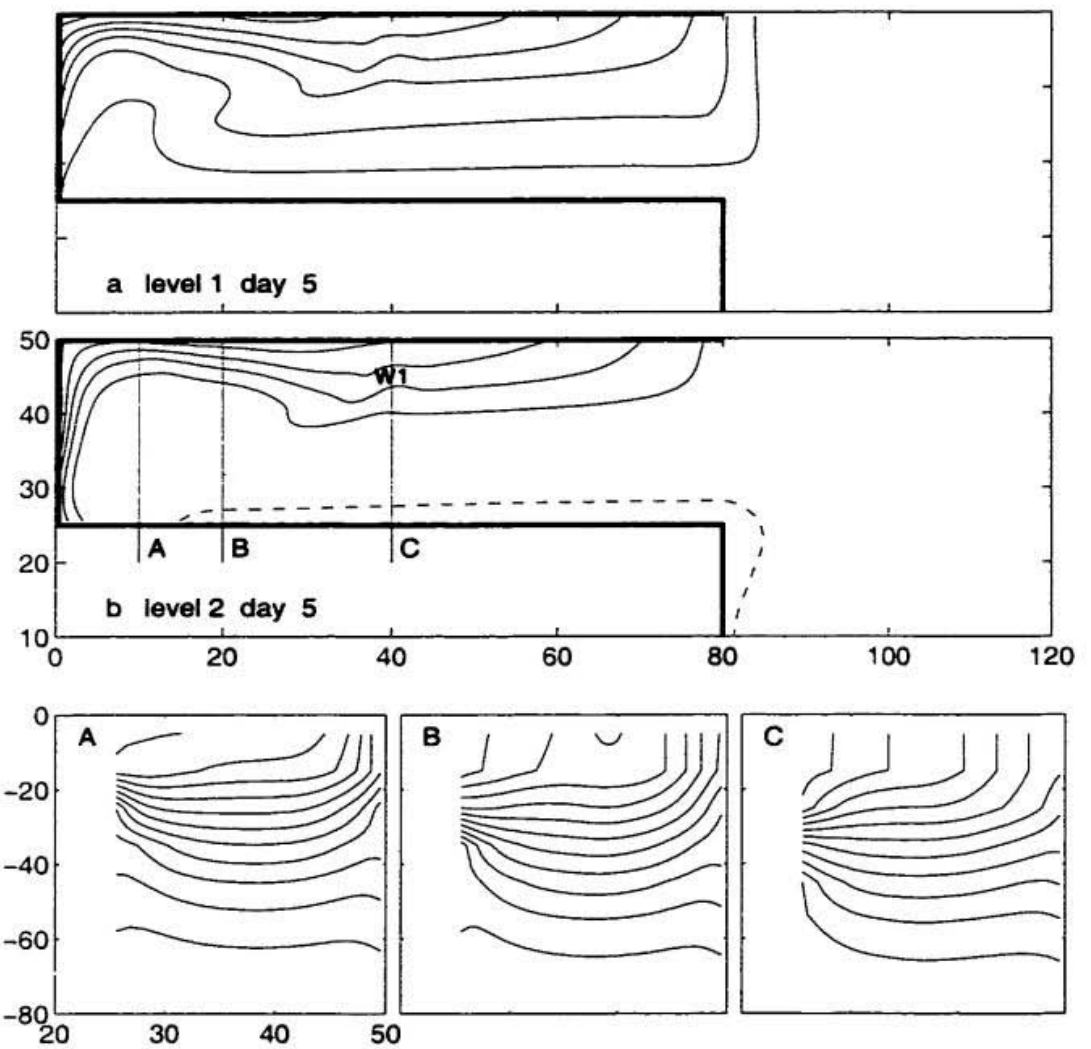

Figure 4.15: Density contours for Figure 4.14. All contour intervals are 0.1 kg m^{-3}. (a) and (b) show horizontal contours of density departure from initial stratification with solid lines representing a density increase and dashed lines a density decrease. Cross-sections A, B and C are contours of total density.

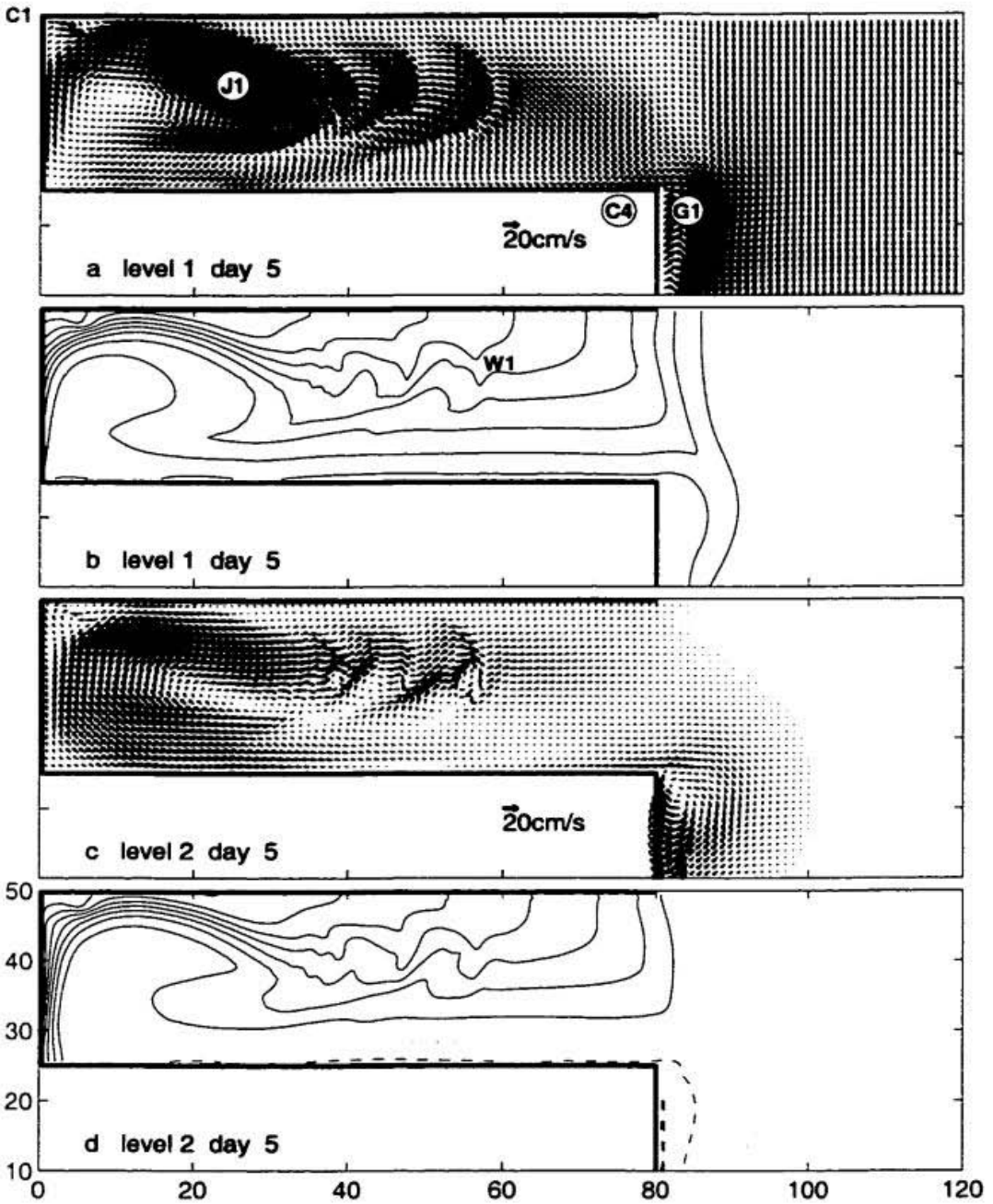

Figure 4.16: Non-linear CANDIE model run with constant 0.1 Pa wind blowing in the positive x-axis direction at day 5.

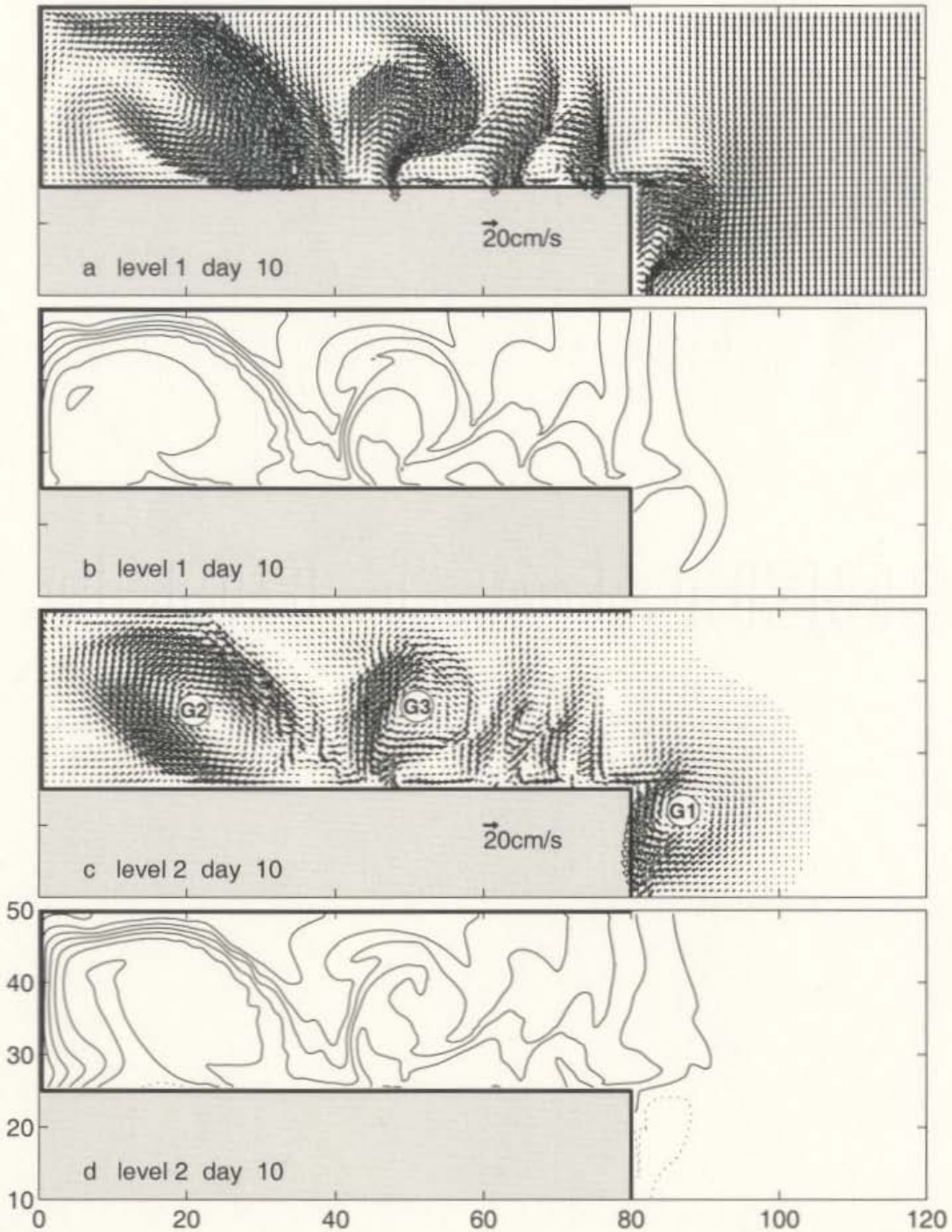

Figure 4.17: Same as figure 4.16, but results shown for day 10

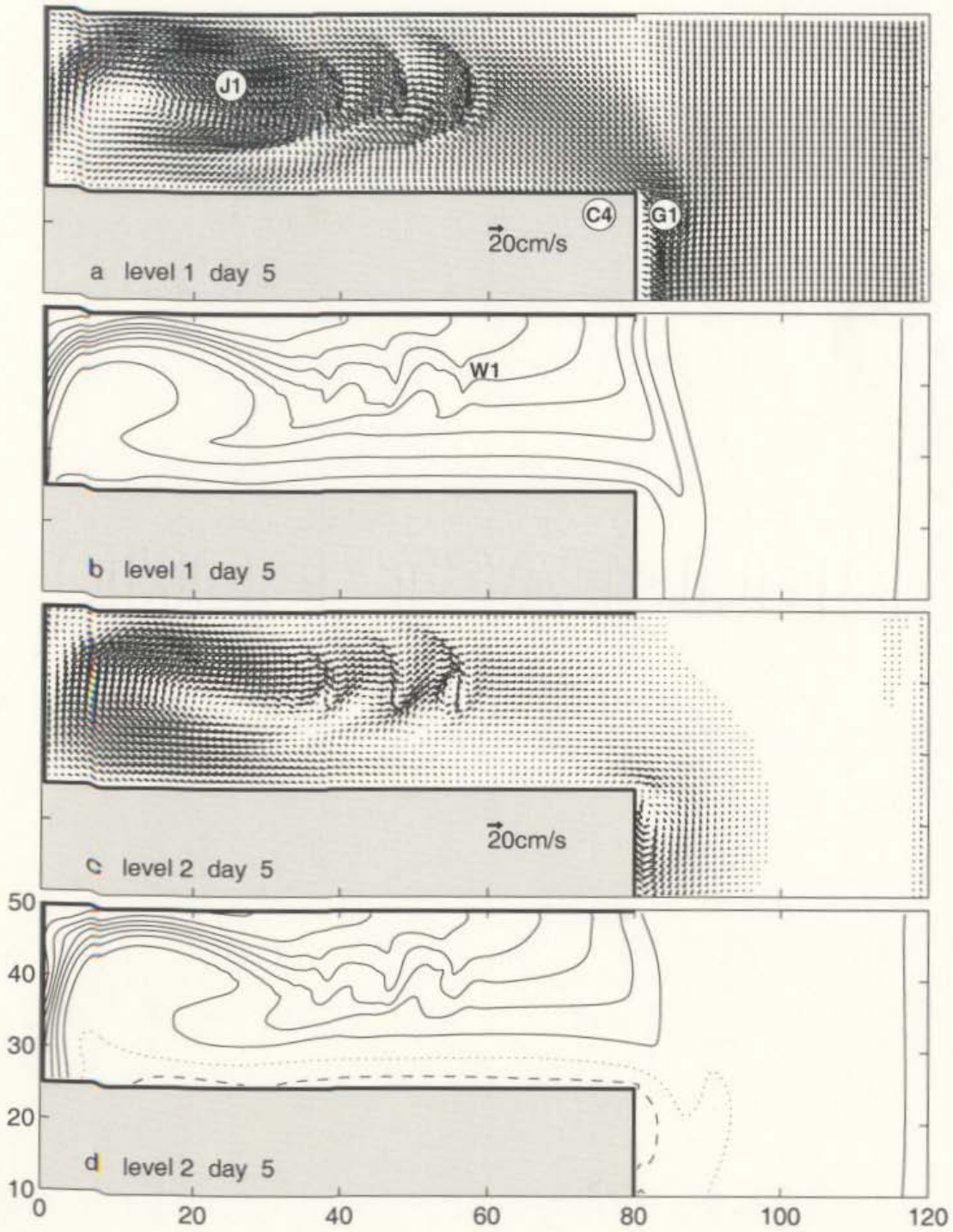

Figure 4.18: Same as figure 4.16, but with a no-slip boundary condition applied instead of a free-slip condition.

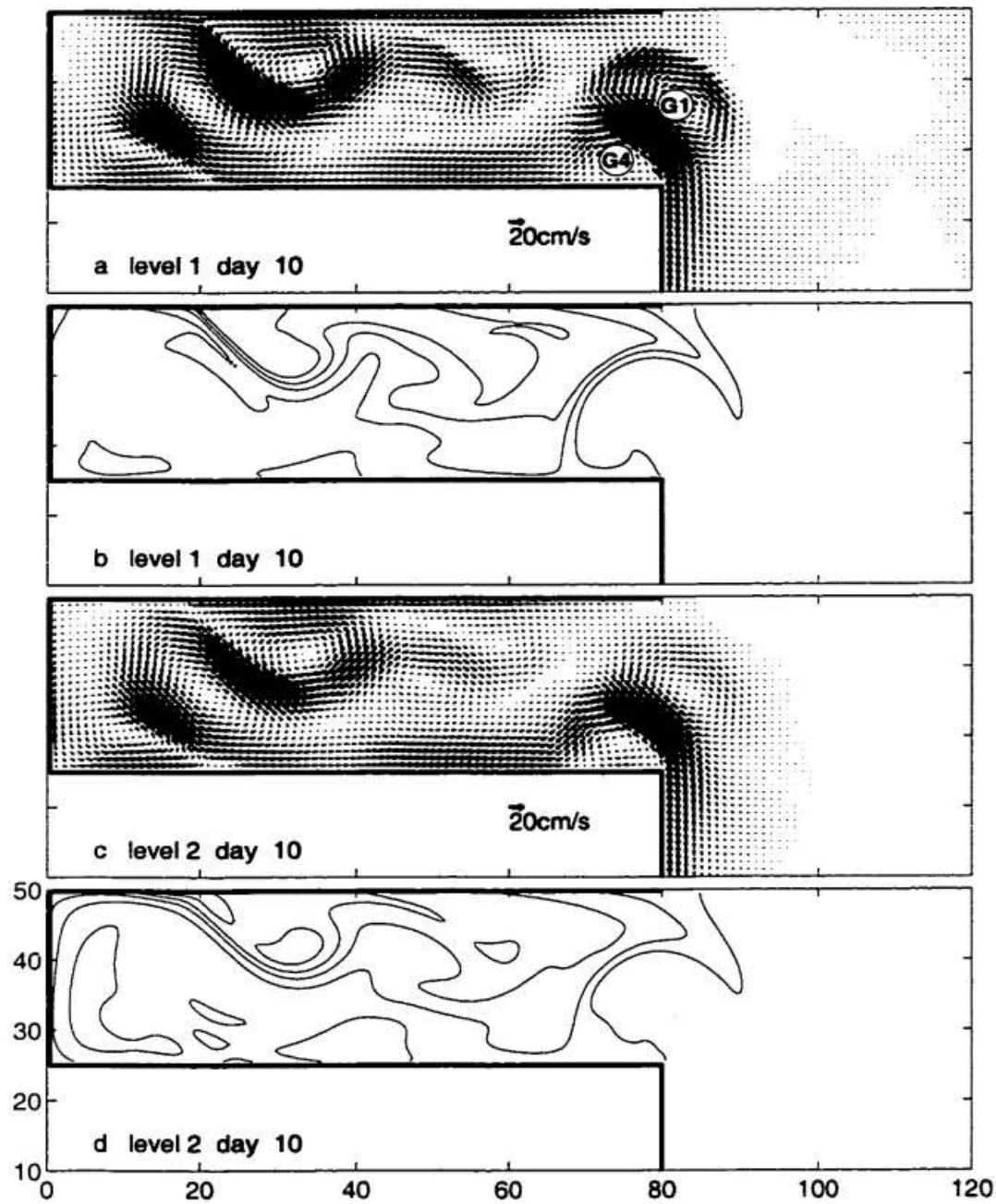

Figure 4.19: Same as figure 4.17 but wind is relaxed from 0.1 Pa to zero (over 2 days) as of day 5. Results are shown for day 10.

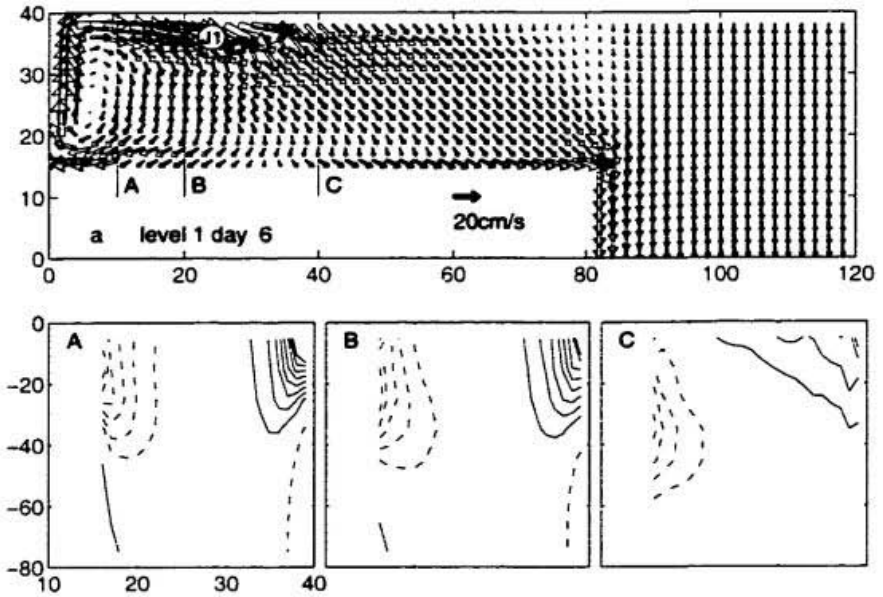

Figure 4.20: Velocity at day 5 of model run with linearized momentum, yet including density advection. Note: Model resolution is 1 km in the case.

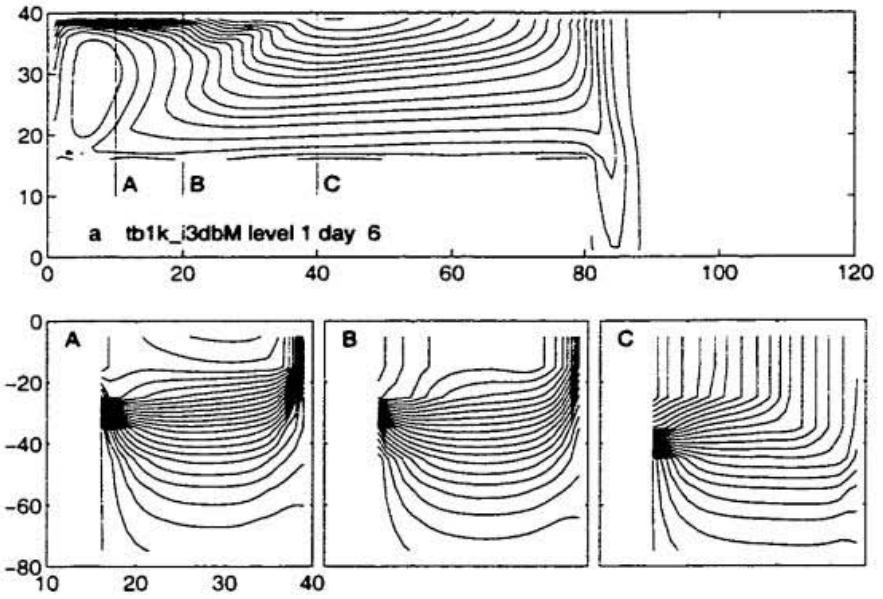

Figure 4.21: Same as Figures 4.20 but for density. Contour intervals are 0.05 ppt.

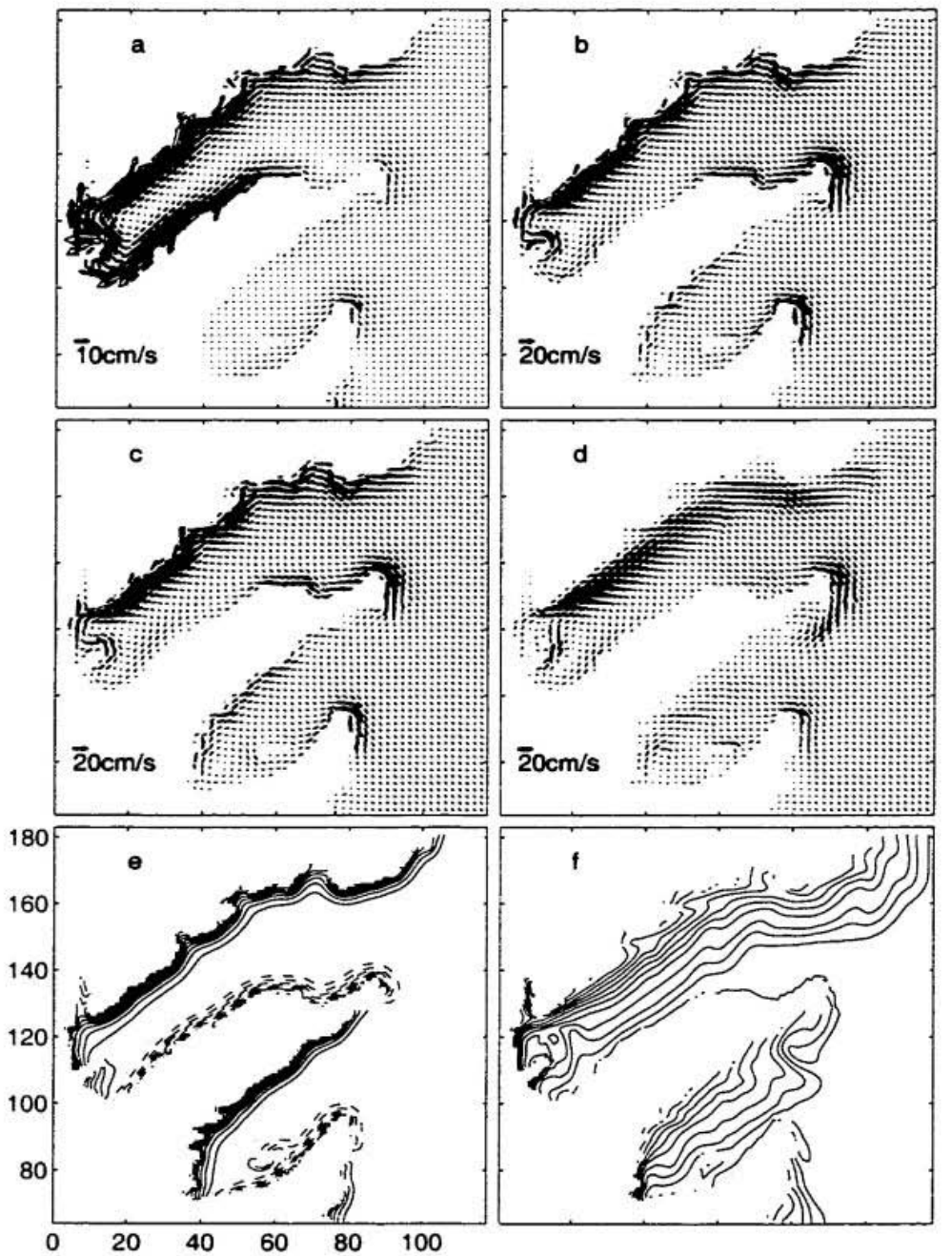

Figure 4.22: Surface velocities at day 5 from various models with realistic geometry: (a) the single layer, baroclinic model, (b) the linearized CANDIE model with a flat bottom, (c) the linearized CANDIE model with realistic bottom topography, (d) the non-linear CANDIE model with realistic bottom topography. The density departure from initial density for cases c and d are shown in panels e and f respectively. Solid contours indicate an increase in density, dashed contours a decrease and the dotted line is the zero contour. Contour intervals are 0.05 kg m^{-3}.

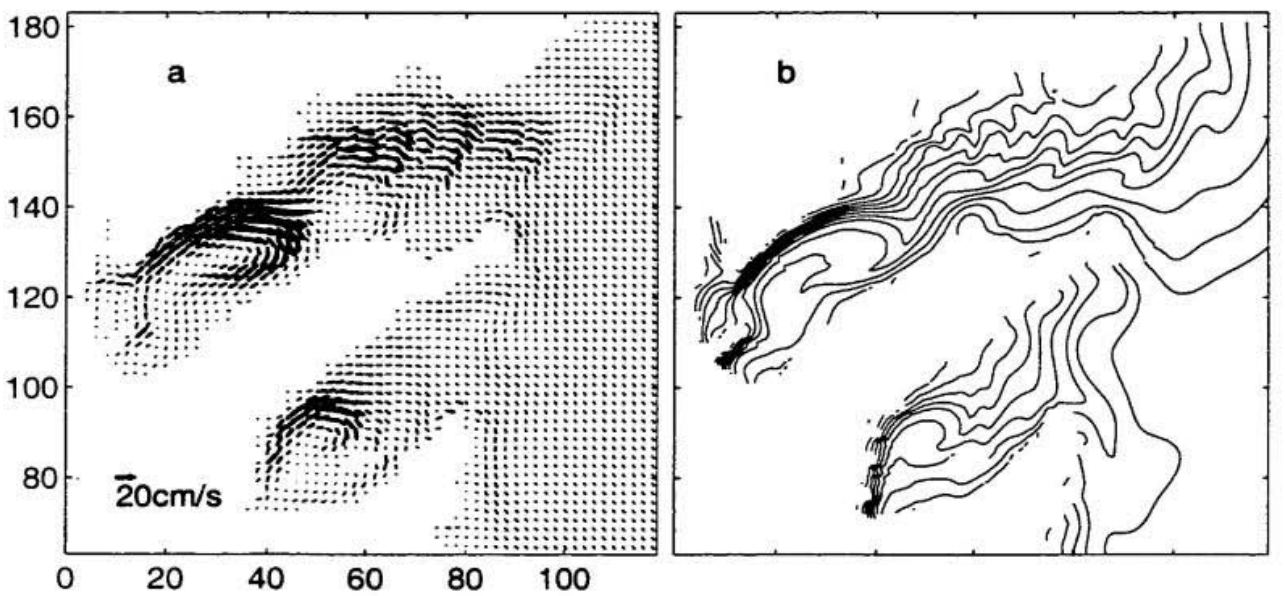

Figure 4.23: Surface fields at day 10 for the nonlinear CANDIE model: (a) Velocity (b) density departure from initial values with contours of 0.05 kg m^{-3}.

Chapter 5

Circulation Response to Variable Wind Forcing

5.1 Introduction

In this chapter, I explore the influence of time dependent winds on thermocline and current variability in Trinity and Conception Bays. The objective is to compare modeled results with observations: current data from moorings, ADCP transects and HF Coastal Radar (CODAR) observations from Conception Bay. There are also satellite SST images which cover both Trinity and Conception Bay. I use the linear and non-linear CANDIE model using realistic topography (Figure 2.8) to investigate the role of non-linearity and topography in the time dependent solution for wind driven flow.

This study focuses on two time periods for which moorings were deployed in Conception Bay in the summers of 1990 and 1994 (see Chapter 2). These two 50-60 day periods of interest start on Julian day 150 (May 30th) in 1990 and again in 1994. In addition, model simulations are run for July of 1991 to coincide with HF

Radar observations as well as for July and August of 1998 to overlap with the SST observations.

Chapter 4 demonstrates that the surface circulation in these coastal embayments is relatively unaffected by bottom topography during the summer, at time scales less then 10 days, for steady wind forcing. Over longer time periods and variable wind forcing, does topography make a difference to surface circulation, circulation at depth and the thermocline variability in the bay?

Comparisons are made using the data for Trinity and Conception Bays described in Chapter 2. In section 5.2, changes applied to the CANDIE code for application in this chapter are described. In sections 5.3 and 5.4, model runs are compared to current mooring observations (temperature and velocity) from 1990 and 1994 respectively. In section 5.5, vertical transects of modeled velocity are compared to ADCP transects. In section 5.6, the modeled surface currents are compared with the CODAR velocity observations in Conception Bay. In section 5.7, the modeled surface density structure is compared to observed SST images for this region. In section 5.8, the results of this chapter are discussed and summarized.

5.2 Changes in Model Setup

The major difference in the application of the non-linear model in this chapter is the application of the diffusion of density. Diffusion is applied only to departures from initial density. Since the initial density field is horizontally uniform for my

applications, only vertical diffusion is modified. It should be noted that this method is somewhat unrealistic in creating water that is lighter than initial density. However the advantage of this method is that the thermocline structure is preserved by not letting the background density field diffuse. The background phase speed for Kelvin waves is preserved and is not reduced by diffusion of the thermocline.

In the vertical, background density stratification is preserved over the model run period, since only departures from the initial density field are diffused. Were real diffusion allowed, after 50-60 days, a vertical diffusion coefficient of 10^{-4} m^2 s^{-1} mixes the thermocline over a length scale of 20-25 m (i.e. 2 grid levels). By disallowing this diffusion, the background stratification is kept constant. While the spreading of the thermocline in the non-linear case dampens density variations from local upwelling and downwelling, it also changes the propagation characteristics of Kelvin waves.

The model setup is as described in Chapter 2. Model runs start 5-10 days prior to the period in which results and observations are compared. The filtered wind stress time series is introduced at day 145 and smoothly ramps up over 2 days using a tanh function. As in chapter 4, model runs begin at rest with a horizontally uniform pycnocline representing June stratification. The first baroclinic mode wave speed is 0.53 m s^{-1}. The open boundary formulation is such that model solutions depend only on the forcing in the interior of the model: nothing is inferred about coastline geometry outside of the model domain.

5.3 Comparison with current mooring observations in 1990

In this section, CANDIE model results are compared to current mooring observations deployed around the head of Conception Bay. Tests are also carried out with the shallow water model used by de Young et al. (1993b). Sensitivity of the model to parameters is tested by reproducing the observed thermocline movements at 3 locations around the head of the bay.

The CANDIE model is applied with simple parameterizations including uniform vertical viscosity and initially horizontally uniform stratification. The main interest is in reproducing the wind driven upwelling observed in Conception Bay. A further objective is to explore the influence of the non linear terms and model sensitivity to realistic bottom topography.

As seen in Chapter 4, density advection plays a crucial role in modifying the horizontal density and velocity structure for wind forced coastal embayments. Furthermore, bottom topography has little effect on the surface circulation and density fields. A first mode baroclinic Kelvin wave generated on the south shore of Trinity Bay affects the circulation in Conception Bay roughly 5 days after its generation. For time dependent forcing, waves are continuously propagating from Trinity Bay to Conception Bay.

To match observational sampling, the full vertical profile of velocity and density in the CANDIE model is extracted at the horizontal grid point closest to the current-mooring locations every 4 hrs during the model run. The vertical profile of modeled

density can then be compared to the observed vertical temperature profile from from the current mooring thermistor chain measurements.

5.3.1 Modeled Pycnocline Response

Figure 5.1 shows the superposition of the modeled density profile for the non-linear CANDIE model onto the observed temperature profile. The model reproduces the major upwelling events, particularly in the latter period of observations from day 170 to 190 in 1990. The model reproduces the gradual 40 m rise of the 1 °C thermocline at H2 over a period of 3-5 days followed by a more rapid 40 m descent within a day (see days 167, 187 and 193). This asymmetry in upwelling and downwelling rates may stem from a difference in the rate of rise and descent of wind stress magnitude for a given wind stress episode (2-10 days). The asymmetry between the rate of rise and descent of the thermocline is noticeable to a lesser extent at the head of the bay (H4) and on the eastern side of the Bay (H6).

A further explanation of this asymmetry may be due to the combination of local wind forcing and the propagation of Kelvin waves from upstream locations. During the onset of an out of the bay wind stress, Chapter 4 shows it takes 5 days for a downwelling wave generated on the eastern side of Trinity Bay to propagate into Conception Bay. The arrival of this downwelling Kelvin wave, may lead to the rapid descent of the thermocline within a day.

Furthermore, the model reproduces the phase shift of up to 1-2 days between the

near surface response of the thermocline and that at depth (i.e 65 m). The response at depth may lead or follow the signal at the surface (Figure 5.1). This phase shift could be due to the relative importance of the different modes with depth.

The greatest variability in the vertical displacement of the observed isotherms and modeled isopycnals is found at H4 at the head of the bay (cf. Figure 5.1). At H6 thermocline variability increases significantly with depth, whereas at H2 and H4 the upwelling signal is relatively strong near the surface at 25 m depth and more uniform with depth.

A difficulty encountered in the model is that stratification varies over time in the observations, whereas in the model background stratification is fixed. Initially the response of the model is quicker than observed, then lags the data as summer stratification progresses.

Figure 5.2 shows the modeled isopycnals overlayed on the observed temperature field for the linearized CANDIE model. The modeled density field varies substantially in the vertical. This is in part due to the nature of the linearized density equation which allows for dense water or light water to form to balance vertical divergence or convergence of the vertical momentum field. In the linearized case, density can only be advected in the vertical axis.

5.3.2 Comparison of Vertical Velocities

The linearized 1-D vertical density and temperature equations with no diffusion or horizontal advection are used to extract an estimate of the vertical velocities from the modeled density and observed temperature field. This equation for density is

$$\rho_t + w_{app}\rho_z = 0. \tag{5.1}$$

and can be readily solved for temperature too. I define w_{app} as the apparent vertical velocity associated with the movement of temperature/density field. This gives a time series of a single scalar variable that represent. observed upwelling and downwelling in Figures 5.1 and 5.2. The sensitivity of w_{app} to the depth was verified and a depth of 40 m was chosen. Calculating w_{app} allows for an easy comparison of modeled results with observations for which a correlation coefficient is readily calculated.

Figures 5.3 and 5.4 show the comparison of apparent vertical velocities at 40 m depth between observations and the non-linearized and linearized CANDIE model. In the non linear case, correlations (r) with observations are 0.51, 0.56 and 0.36 for H2, H4 and H6 moorings sites. The model lags observations by 8 hrs at H2 and 20 hrs at H4. At H6, the model lags the data by 6 days. In the flat bottomed case, correlation with data increases slightly at H2 and H4 values of .57 and .57. At H6, the correlation decreases slightly to 0.34 in the flat bottomed run. Correlations are defined here by finding the maximum correlation in the lagged cross-correlation function of two time series.

In the linearized case run of Figure 5.4, the model overestimates the apparent vertical velocities. Correlations decrease to roughly 0.4 at both H2 and H4 mooring locations.

5.3.3 Comparison of Isopycnal and Isotherm Vertical Displacement

Another method for extracting a single variable from the vertical density and temperature structure is to track the position of an isopycnal/isotherm. While still permitting comparisons with observations, this method permits easier comparison with results from the single layer reduced gravity shallow water model. This enables one to compare the abilities of both CANDIE and the single layer reduced gravity model in reproducing thermocline movement.

Figure 5.5 shows the vertical position of the 1025.8 kg m^{-3} isopycnal and the 1 °C observed isotherm at mooring sites H2, H4 and H6. The correlation between the two times series is 0.5, 0.65 and 0.3 at H2, H4 and H6 respectively. The model performs best at the head of the bay (H4).

Figure 5.6 shows the comparison between the interface displacement and the observed 1 °C isotherm. The linear shallow water model overestimates the amplitude of the thermocline displacement at H4, but gives a reasonable amplitude at H2 and H6. The lagged correlations vary between 0.4 and 0.49 with lags from 3-4 days. The highest correlation is on the eastern side of the bay at H6.

The non-linear terms affect the relative rates of upwelling and downwelling. In particular, at day 188, the CANDIE model reproduces the sudden drop of the 1 °C thermocline (Figure 5.5). In the linear shallow water model, however, the rate of rising and descending of the interface is more symmetrical.

5.3.4 Sensitivity of Modeled Pycnocline Response

In this section, the sensitivity of the bottom topography and the Prandtl number for the non-linear CANDIE model is investigated. As touched upon briefly in Chapter 1, Conception Bay in the summer is a highly stratified environment with steep topography such that the stratification parameter S if much greater than one. This implies that coastal trapped waves will behave mostly like Kelvin waves and not be affected by topography. As seen in Chapter 4, the Prandtl number modifies the scale and intensity of the coastal circulation response to wind forcing. The reason for examining its effect in this model, is that some debate exists whether in the real ocean, the Prandtl number is different from unity.

Figure 5.7 shows the superposition of the vertical density structure contour time series output from the non-linear CANDIE model using a flat bottom topography overlayed over the non-linear CANDIE model with realistic topography.

The greatest influence of bottom topography occurs at H6 on the eastern side of Conception Bay. Here the variability of the isopycnals is damped between 45 and 65 m depth in the flat bottomed run case. Near the surface at H6, the influence of

bottom topography is less dramatic although differences between the two runs are clearly visible (Figure 5.7). At 40 m depth, a comparison of w_{app} between the two cases reveals a correlation of 0.73.

At the head of the bay (H4), bottom topography has relatively little influence (Figure 5.7). The correlation coefficient of the apparent vertical velocity w_{app} at 40m between the two cases (flat and realistic topography) has a value of 0.94. On the western side of the bay (H2), w_{app} also has a correlation of 0.94 between the flat bottom and realistic bottom topography cases. However, in Figure 5.7, the differences between the two model runs with flat and real topography are more readily visible at H2 and particularly H6, compared to H4 at the head of the bay.

Sensitivity of the model to the Prandtl number is tested with a vertical Prandtl number of 100 (Figure 5.8), with vertical viscosity increased from 10^{-4} m^2 s^{-1} to 10^{-2} m^2 s^{-1}. Again the biggest sensitivity to a change in the model parameter is at H6 on the eastern side of the bay. The correlation of w_{app} at 40 m with the base case (with Prandtl number 1) 0.76, 0.81 and 0.55 for mooring locations H2, H4 and H6 respectively. The effect of increasing the Prandtl number is to diffuse the stratification, which is readily noticeable as run time progresses beyond 25 days. The effect of increasing the Prandtl number is to reduce the response speed of isopycnals to wind forcing. The response of the isotherm displacement at H6 is delayed by 4 days when the Prandtl number is increased from 1 to 100.

This increased sensitivity at H6 to model parameters may result from the longer

propagation time of Kelvin waves before reaching H6, allowing more time for changes in parameterization to influence the propagating Kelvin wave.

For the modified Prandtl number, the effect does not appear initially, but develops over time (Chapter 4 and Yamagata and Philander (1985)).

5.3.5 Comparisons in the Frequency Domain

The power spectrum of the calculated apparent vertical velocities at mooring sites in the non-linear model reveals an interesting pattern around the head of the bay (Figure 5.9). The model reproduces the shape of the power spectrum best on the western side of the bay (H2) and poorest at the head of the bay. At the head of the bay (H4), observed peaks in the autospectrum are at 0.1, 0.4 and 0.6 cpd (cycles per day) while the model shows a peak between 0.1-0.2 cpd with nearly twice the observed intensity in this band. However the model does not reproduce the peaks at 0.4 and 0.6 cpd. The shape of the modeled power spectrum for apparent vertical velocity is similar at both H2 and H4 mooring locations.

The effect of bottom topography is to increase the energy of the 0.2 cpd peak by 40-50% (Figure 5.9). At H4, the small peak at 0.6 cpd is increased in amplitude for a flat bottomed topography run.

On the eastern side of the bay there is a substantial weakening of the energy of the apparent vertical velocities compared to H2 and H4. Here the model is more energetic than the observations. The observed spectrum is relatively flat from 0.1-0.6

cpd while the modeled spectrum is slightly domed with a peak around 0.3 cpd in the realistic bottomed case.

5.4 Comparison with current mooring observations in 1994

In 1994, 3 moorings were deployed in the along shelf direction 20 km apart on the western shore of Conception Bay over the 100 m isobath. The model was run for a 60 day period from Julian day 150 to 210 in 1994 spanning the deployment period of these moorings.

Each of these three moorings had thermistor chains. Figure 5.10 shows the modeled density contours of the non-linear CANDIE model layed over the observed temperature field at the mooring locations. The model shows good visual agreement with the temperature data. The model reproduces almost all of the 13 upwelling events observed during this period, only missing a couple of small observed upwelling events at day 184 at mooring W7.

The model shows a slight increase in the upwelling response as one travels further into the bay from W1 through to W7. This increase in the amplitude of the response is larger in the observed temperature field (Figure 2.13) than the model. This result suggests that stratification changes in the along-bay direction are significant and affect the wind driven response of the bay.

Figure 5.11 shows the displacement of the 1025.7 kg m^{-3} isopycnal from the non-linear model compared to that of the observed 1 ^{o}C isotherm. Due to the along-shore

temperature gradient, for W7 the 1026 kg m^{-3} isopycnal was chosen for comparison since the mean depth of the 1026 kg m^{-3} isopycnal more closely matched the mean position of the observed 1 °C isotherm. Correlations between the model output and observations are good along the western shore of Conception Bay with lagged correlation coefficients between 0.67 (W4) and 0.74 (W7) with the model trailing observations by 24 hours.

In the linear CANDIE model run (Figure 5.12), the model lags the data by only 8-12 hours, but agreement with data is not as good. Lagged correlation values are 0.48 (W4) and 0.57 (W7) for moorings W1, W4 and W7 respectively.

Comparing the linear and non-linear case shows that the non-linear terms contribute to a better match for individual upwelling responses. The non-linear terms tend to flatten the peaks of upwelling, while increasing the rate of downwelling and sharpening the downwelling peaks of the isopycnals.

The effect of bottom topography was verified by running the model with flat bottomed topography for both the non-linear and linear case runs. Adding topography makes only minor differences to the isopycnal displacement. In the non-linear case, including realistic bottom topography delays the model by 4hrs, whereas in the linear case, including bottom topography does not effect the phase of the pycnocline's response on the western side of the bay.

The correlation for the displacement of modeled isopycnals (seen in Figure 5.11) between the flat bottom and realistic bottom case are 0.92±0.01 for the non-linear

model and 0.97±0.01 for the linearized CANDIE model. Thus the model response suggests that bottom topography plays only a minor role in the response on the western side of Conception Bay. The non-linear terms increase slightly the influence of bottom topography.

A final check undertaken on the thermocline response for the 1994 data, is to look at the shallow water modeled result (Figure 5.13). Here the interface displacement between the two model layers is compared to the 1 °C thermocline (2 °C for W7). Modeled phase speed is 0.5 m s^{-1}, horizontal diffusion is set to 10 m^2 s^{-1} and the upper layer is 40 m thick. Once again, the lowest correlation is observed at W4 (0.56), the highest at W7 (0.67), and with a correlation of 0.6 at W1. Again the model lags the data by 12 hrs as in the linearized CANDIE model runs. Unlike the non-linear model and the data, the shape of the upwelling peaks are symmetric in similar fashion to the linearized CANDIE model.

5.5 Comparison of Currents in 1990 and 1994

5.5.1 Comparison with ADCP Transects

For the 1994 model simulations, two transects across the bay, one across the mouth, the other 10 km in from the mouth were sampled from the model (Figure 5.14 and Figure 5.15). These slices correspond to ADCP transects undertaken 19-22 July 1994 and are discussed in Chapter 2.

From 19-22 July the model exhibits anti-cyclonic surface circulation in Conception Bay as shown in Figure 5.14a. The extent, position and strength of the gyre in Conception Bay depends on the wind, but the modeled surface flow features mainly anti-cyclonic flow. On 22 July, the wind is weak with the wind stress magnitude less than 0.03 Pa. A gyre is situated between the mouth of the bay and Bell Island. Furthermore, surface flow in the model is directed into the bay on the eastern side and outwards on the western side. The position and strength of these gyres vary in time. The wave speed of the first baroclinic mode is around 1.8 km per hour (0.51 m s^{-1}) with a wave travelling roughly 10 km in less than 6 hours. Propagation of waves in the coastal wave guide, may change the observed velocity structure with in 3-6 hrs, reducing the comparison between the observations and the model. It is worth noting that comparisons with current meter data show that the model may lag the observations by up to one day.

At the mouth, on the western side of the bay, cross-bay flow (u) is directed away from the shore in both the model results (Figure 5.14d) and the ADCP data (Figure 5.14f). The vertical and horizontal structure of the cross-bay flow on the western side of the bay is also similar in the model results and in the observations. Modeled cross-shore velocities above 8 cm s^{-1} (dark blue to red colour) extend to a depth of 30 m and up to 10 km from shore. Observed ADCP data velocities above 8 cm s^{-1} extend to a depth reaching 75 m close to shore, extending offshore 8 km at the surface and extending offshore by 2 km at a depth of 75 m.

On the eastern side of the bay, at the mouth, the direction of modeled cross-bay flow is opposite to that of the ADCP data. The model shows flow away from the coast while the data show, out-of-the-bay and westward flow (Figure 5.14).

As with the cross-shelf flow at the mouth of Conception Bay, the alongshore flow agrees with data on the western side of the bay (Figure 5.14e and g). This is most noticeable near the surface where a narrow (5-8 km) jet of outflow greater than 10 cm s^{-1} is centered 5-8 km offshore in both the model results and the ADCP observations.

On the eastern side of mouth, the model exhibits strong along-shore inflow (into the bay) of 15 cm s^{-1} within 5 km of the coast down to a depth of 30 m. Below this depth, there is a weak outflow jet with speeds of 5 cm s^{-1}or less. The modeled inflow extends, deepens and weakens offshore half way across the bay's mouth (10 km) from the eastern shore. The ADCP data show somewhat similar characteristics to the model results on the eastern side of the bay with inflow into the bay with speeds of 5 cm s^{-1} or less, beyond 2 km from shore and extending away from shore with depth. In contrast to the model, however, very near the western shore, (within 1-2 km) the ADCP indicates outflow of 7-8 cm s^{-1}which broadens to an outflow 8 km wide at 30 to 60 m of depth. While this outflow feature on the eastern side of the bay is reproduced to some extent at depth by the model, it does not extend to the surface and is comparatively weak.

Wind driven flow in Conception Bay is dynamic, and the locations of the gyres in

the model vary extensively in time. Disagreement between the ADCP data and the model, may come from the misrepresentation of the position of the gyres and coastal jets in the bay at a given point in time.

Furthermore, the only forcing in the model is by the time filtered (32 hr) wind. The ADCP however, samples the water column in real time and observes the velocity due to all the forcing (e.g. near inertial currents driven by the wind, intrusions of the Labrador Current). An ADCP transect takes roughly 3 hrs to complete. During this time, a first mode baroclinic Kelvin wave with a speed of 0.51 cm s^{-1} may move by up to 6 km, and may influence the direction of near-shore velocities during this time.

As observed in the vertical transects of modeled velocity, the strongest currents are confined to the surface layer of depth 10-20 m. The observations, show that particularly near-shore, strong coastal jet currents reach depths of about 70 m or so.

An observed feature not reproduced by the model is the presence of bottom intensified currents. There is for example, strong westward flow (5-10 cm s^{-1}) up the sloping sides from 180 m depth to 100 m depth (Figure 5.14f).

The model does not simulate the columnar flow features 1 km in width as observed at $x \simeq 16$ km in the u component of velocity (Figure 5.14f). These columnar features have little vertical shear of horizontal currents are also observed on the cross-shore transect 10 km inside the bay in both the u and v components of velocity.

Inside the bay, (Figure 5.15d and e), modeled velocities do not agree as well as is the case near the mouth. Here the model shows broad inflow in contrast to a 5 km

narrow outflow jet on the eastern side of the bay. However on the western side of the bay, there is a surface outflow jet evident in both the model and the data in the top 10-20 m several kilometres from the shore. Again here, the vertical characteristics of these features differ between model results and ADCP observations. But the most salient difference is the small vertical shear in the coastal jets (within 2 km from shore) in the ADCP data.

The modeled cross-shelf flow pattern inside the bay (Figure 5.15d) exhibits qualitative agreement with the observations. From west to east across the transect, cross-shelf flow is first eastward (0-4 km from shore), then westward (4-14 km) and finally eastward (14-24 km). Below the surface layer (top 50 m), there is little current strength and structure in the model results. This stands in contradiction to the ADCP data, indicating that forcings other than wind stress affect the flow at depth.

5.5.2 Comparison of Mean Currents with Moorings

Figure 5.16 shows the mean currents at 15 m and 45 m for the non-linear model runs for 1990 and 1994. Both years feature very similar characteristics in the velocity pattern.

At 15 m depth (the second model level), these similarities include a large gyre inside the mouth of Trinity Bay and strong clockwise circulation near the head of the bay off the Bellevue Peninsula. Furthermore in Conception Bay, the mean flow in both years features a meandering coastal jet that starts on the eastern side of the bay

and flows clockwise around the head of the bay with flow split around Bell Island. The jet then increases in strength, and extends along the entire western bay coastline.

At a depth of 45 m, mean flow is directed towards the head in the inner half of the bays with strong flow coming from the south around the headland into Conception Bay. This flow splits with a portion of the flow moving northward across the bay and around the headland and Baccalieu Island into Trinity Bay, where an anti-cyclonic gyre with velocities around 10 cm s^{-1} is formed. In the inner half of Trinity Bay, circulation is weak and directed towards the head. On the western shore of Trinity Bay, a coastal jet of width 6 km meanders towards the head of the bay.

Differences in the mean circulation between years in the model is attributed to differences in wind forcing. At level 2, the most notable differences are the meandering of the jet in the inner half of Trinity Bay, which is seen in 1990 but not in 1994, and the presence of a gyre beyond the mouth of both bays that drives circulation northward across the mouth of both bays in 1990.

At model level 5 (45 m) the most notable features are an increase in gyre strength inside the mouth of Trinity Bay and a stronger coastal jet flowing towards the head on the western shore of Trinity Bay.

The mean velocity patterns from the model agree fairly well qualitatively with observations. The main observed features (Figures 2.15 and 2.16) reproduced by the model is the cyclonic flow around the head of the bay at a depth of 20 m. In addition weak mean currents on the western flank of Bell Island are accounted for both in the

model and the data.

At depth however, the agreement between model and data is not as strong. The data exhibit outward mean flow on both sides of the bay whereas the model shows inflow on the western side of the bay near the head.

Near the mouth of the bay, the 1994 surface current mooring data show agreement with the model. Most noticeable is the shoreward direction of mean current at W1 at the mouth, which corresponds to the northward cross-shore mean flow exhibited by the model at the mouth of Conception Bay.

Figure 5.17 shows a partial cross-shore transect from the western side of Conception Bay for mean flow and the corresponding major and minor axis of standard deviation. Mean flow increases away from shore and is comparable in size to the standard deviations of 10 cm s^{-1} at the surface. The mean flow near the shore is weak and standard deviations are high (15-20 cm s^{-1}).

At 35m depth, mean flow is directed into the bay. Further off-shore, mean flow is shoreward 4 km from shore. Beyond this point, flow is directed outwards of the bay parallel to surface flow. The mean current pattern is similar at 35 m and 75 m depth with smaller magnitudes.

At 135-170 m depth, the data show a strengthening of inflow into the bay with mean velocities up to 3 cm s^{-1}. This is not reproduced in the model. The comparison of model mean velocities and the data comes across best at 35 m depth. Here the patterns are similar for the data with inflow near-shore and outflow further away from

shore.

5.6 Comparison with CODAR data in 1991

The CANDIE model is run with observed wind stress as of 20 June 1991 for comparisons with CODAR data collected from 2-19 July 1991. As before, the model uses 10 m vertical resolution, 1 km horizontal resolution and a vertical diffusion coefficient of momentum and density set at 10^{-4} m^2 s^{-1}. Figures 5.18 and 5.19 show the surface layer (10 m) model velocities at 12 noon from 2-19 July for Conception Bay using the non-linear version of the code without vertical diffusion of initial density. While only Conception Bay is discussed, the model is run with the Trinity and Conception Bay topography shown in Figure 2.8.

The model results are compared with the observed CODAR velocity fields from Figures 2.19 and 2.20 in Chapter 2. Furthermore, a comparison run with the linear version of the CANDIE code was undertaken and is discussed (but not shown) later in this section.

5.6.1 CODAR Measured Surface Currents and the Ekman Layer

CODAR measures the Doppler shift of the radar backscatter from surface gravity waves to determine surface currents. The effective depth of measurement of the velocity depends on the radar frequency and is roughly 1 m for the 25.4 MHz frequency

system used in Conception Bay. This upper 1 m region of the water column, does not behave like a classic Ekman spiral where surface velocities in steady state are 45° to the right of the wind (Kundu, 1990).

At the surface of the ocean, a kinematic boundary condition applies where a parcel of fluid at the air/sea interface remains on the interface. This condition dampens turbulence at the air/sea interface. A wall layer (Csanady, 1982) with a depth of order 1 m exists below the interface in which currents rotate from a wind parallel direction with a magnitude of 3% of the winds speed in a direction 45° to the right at the top of the Ekman layer (Fernandez et al., 1996). The wall layer can be decomposed into three parts. The first is a viscous region where velocity decays linearly followed by a buffer zone to the 3rd part in which velocity decays exponentially before reaching the top of the Ekman layer (Kundu, 1990).

Near the air-sea interface (top 1 m), Phillips (1977) remarked that viscous effects dominate and the Coriolis force is negligible. Therefore currents near the air-sea interface tend to be parallel to the wind. Near surface currents consist of Stokes drift, geostrophic currents, direct wind induced (wall layer) currents (Fernandez et al., 1996) and currents produced by shear stress from sub-surface flow (Zedel et al., 1999).

Many studies have observed the existence of significant vertical shear in the top 1 m of the ocean (Fernandez et al., 1996; Csanady, 1982). Between 30 and 50 cm from the surface, horizontal currents drop by 5-18% in magnitude and rotate clockwise (in the northern hemisphere) by 13-18° (Fernandez et al., 1996). Observations made using

upward looking ADCP moorings confirm that under certain circumstances surface currents are parallel to the wind (Schott, 1989; Zedel et al., 1996). This phenomenon is more prevalent when currents measured at an arbitrary depth (i.e. 20 m) are subtracted from the observed surface velocities (Zedel et al., 1999). These ADCP based observations contrast with standard Ekman theory and agree with the radar observations of Fernandez et al. (1996) and boundary layer theory (Kundu, 1990; Phillips, 1977).

In brief, the dynamics associated with the top 1 m of the ocean do not follow simple Ekman theory due to the presence of the abrupt density gradient (the air/sea interface) and the associated "wall layer" in which viscous flows dominate. In particular, the Coriolis terms are negligible for currents in the top 1 m of the ocean, since viscous terms dominate. Away from the coast, the top 10 m averaged currents are expected to be weaker (by a factor of 2 (Fernandez et al., 1996)) and rotated clockwise compared to the surface boundary layer currents. Near the coast within a Rossby radius, however, the Coriolis terms in the model are small under shore parallel wind due to no normal flow at the land boundary. One therefore expects agreement of velocity direction between CODAR data and model results close to the western shore of Conception Bay under shore parallel (out of the bay) winds.

5.6.2 Results

From 2-9 July, wind is blowing out of the bay for periods of of 1 or 2 days (Figure 5.18). During these wind events, an outward flowing coastal jet that develops on the west side of the bay in the model spreads around the bay with the coast to the right. As the wind subsides, so does the growth of the outward flowing jet on the west side of the bay, which then recedes out of the bay from 6-8 July (Figure 5.18). On 9 July, a strengthening of the wind increases the coastal jet up to speeds of 20 cm s^{-1}(Figure 5.18).

Chapter 4 demonstrated that the outward flowing coastal jet on the west side of the bay develops into a gyre when a wind stress of 0.05 Pa directed out of the bay is applied over a period of 5 days or more. The time scale for gyre development is shorter for increased wind stress. Wind stress from 8-12 July is directed out of the bay with a strength varying from 0.05 to 0.08 Pa. By 10 July, a cyclonic gyre is visible in the inner half of the bay. The lack of diffusion of the initial stratification (as is applied in the present chapter) promotes the formation of gyres since the horizontal density gradients are enhanced by preserving the stratification. The gyre visible on 10 July weakens on the 12^{th} and is barely perceptible in the velocity field on 13 July when the wind subsides.

On 16 July, a weak anti-cyclonic gyre is present in the centre of the bay with a current amplitude of about 5 cm $s^{-1}$and a radius of 8 km. This gyre appears to be produced during relaxation of the wind stress on 14 July. As identified in Chapter 4,

subsiding out-of-the-bay winds allow for the wind forced upwelling setup in the bay to relax and form gyres.

The model velocity fields show reasonable qualitative agreement with the observed CODAR data during times of moderate to strong wind stress (i.e 0.05 Pa or more), particularly on the west coast of Conception Bay. During these periods of higher wind stress the model reproduces the outflow or inflow coastal jet on the western side of the bay. Furthermore, a separation of the out-flowing coastal jet from the western side of the bay as found in Chapter 4 features in both the observations and the model output. Both velocity fields show strong variability in the coastal jet on the western side of the bay. On the eastern side of the bay, both CODAR data (Figure 2.19) and the CANDIE model exhibit relatively weak flow. While most of the time the CODAR data exhibits no apparent coastal jet on the east side of the bay, a strong out-flowing coastal jet is present on 17 July when winds are strong. On this day however, the CANDIE model shows no sign of coastal intensification of the current on the east side of the bay.

Another feature of the CODAR data is that currents show a more uniform spatial structure than the model results, particularly during periods of strong winds (see 17 July, for example Figure 2.20). As discussed in section 5.6.1, direct frictional drag from the wind dominates the circulation of the top 1 m of the water column which was observed in the CODAR data. Hence horizontal density gradients play a lesser role in driving circulation in the top 1 m compared to the top 10 m of the ocean.

CODAR measured currents (top 1 m of the water column) reach roughly 55 cm s^{-1} in contrast to the model output whose maximum velocities are 25 cm s^{-1}(top 10 m layer). Gyres are present in the CODAR data but circulate mainly in the opposite sense (cyclonically) to that given by the model. a further indication of the different dynamics between the upper layer and the model.

In addition in the CODAR data. the gyres occur near the mouth of the bay (and not inside the bay as seen in the model), suggesting a possible influence by the inshore branch of the Labrador current (Petrie and Anderson, 1983).

5.6.3 Comparisons with the Linear Model

An identical model run was undertaken with the linearized CANDIE code. A comparison between the linearized and non-linearized model runs reveals the effects of the non-linear model terms. The non-linear terms suppress the development of a Kelvin wave generated coastal jet on the east side of the bay while enhancing the generation of Kelvin wave generated coastal jets on the west side of the bay. The non-linear terms allow for the separation of a jet from the western coast and the subsequent transport density gradients into the interior of the bay. These non-linear terms are also responsible for increasing the strength of the alongshore gradients of velocity and density. In addition, the non-linear terms generate gyres in the interior of the bay. The presence of the non-linear terms improves agreement with the CODAR data.

5.6.4 Comparison of the Mean Velocity Fields

Figures 5.20 and 5.21 show the mean and standard deviations of the horizontal velocity components covering 2-19 July, 1991 for the CODAR observations and the non-linear model results respectively.

The mean velocity pattern in the CODAR data features a cyclonic gyre 5-8 km in radius near the west side of the bay's mouth. There is strong outflow (20 cm s^{-1}) near the mouth on the east side of the bay. Inside the bay, mean flow on the west side of the bay is weak (less than 2 cm s^{-1}) and directed across the bay. On the east side of the bay, flow is parallel to the shore flowing outward with speeds of 10 cm s^{-1}.

The modeled mean currents for this period (Figure 5.21), in contrast with the CODAR data, show a strong coastal jet on the west side of the bay with speeds of 10 cm s^{-1}. An anticyclonic circulation is present inside the bay. Near the mouth, mean currents are comparatively weak, with the exception of a small coastal jet around the headland to the east of the bay. The broad cyclonic gyre seen in the time averaged model velocity field (Figure 5.21) is consistent with the mean currents observed by current moorings in 1990 and presented in Figure 2.15.

In the CODAR data, the standard deviations of the u-component of velocity are highest across the mouth, whereas in the CANDIE model the u-component has relatively weak variability everywhere except near the headland on the eastern side of the bay. For the v-component the spatial pattern of the standard deviations are similar inside the bay, with the highest standard deviations found on the western side

of the bay in both observations and the model. Near the mouth of Conception Bay, the standard deviation of the v-component is relatively high in the CODAR data.

5.6.5 Absence of Coriolis Force

In this section the non-linear CANDIE model is run with the Coriolis constant set to 0. Vertical diffusivity and viscosity are increased to 10^{-3} m^2 $s^{-1}$to keep the model stable. This increase in vertical mixing has no effect on the circulation pattern except for a small decrease in circulation strength. All other model parameters remain identical. Figures 5.22 and 5.23 show the surface velocity field from the model over a period of 18 days. Removing the Coriolis force allows velocity magnitudes to increase since they are accelerated in the direction of the wind with only bottom friction and vertical mixing to slow down the surface velocity field down. Maximum surface velocities are around 50 cm s^{-1} which is comparable to those of the CODAR data.

For $f = 0$, velocities increase with wind-fetch as the surface of the water accelerates away from shore. Velocities are relatively uniform with respect to the base case of $f = 10^{-4}$ s^{-1}. There is no visible coastal jet on the western side of Conception Bay. While no gyres occur on the western side of the bay near the mouth as in the CODAR observations, an anti-cyclonic gyre of radius 6 km occurs on the eastern side of the mouth on the occasions when wind stress resumes after one or two days without wind. Another important observation is that the apparent coastal intensification of current on the eastern side of the bay. This is probably caused by wind blowing across the

bay at an angle to the mouth. Pressure builds up on the eastern side of the bay and combined with the wind stress drives a surface coastal jet directed out of the bay (i.e. 18 July).

The mean velocity field from the zero Coriolis force run case is shown in Figure 5.24. Circulation on the western side of the bay is weak and intensifies with distance from the head of the bay and from the western shore. This pattern agrees well with the CODAR data although the model does not represent the gyre on the western side of the mouth, and the mean flow away from the western shore (Figure 5.20). The model reproduces the standard deviation structure of the cross-bay component of velocity. This includes increased variability along the western shore near the head and at the mouth of the bay. For the along-bay component of velocity, the modeled standard deviation exhibits along-bay structure rather than cross-bay structure in agreement with the CODAR data (Figure 5.20).

5.6.6 Summary

The non-linear CANDIE model reproduces some notable features observed by HF radar surface velocity measurements in Conception Bay. These include a relatively strong coastal jet on the western side of the bay, comparatively weak circulation on the eastern side of the bay and an occasional separation of the coastal jet from the west side of the bay.

The model results compare best with observations when the wind stress is above

0.05 Pa. In particular the relative intensity, the along-shore length scales, direction and position of the coastal jets show good agreement. At the mouth of the bay, the model shows the the poorest agreement with the observations. This may be due to remote forcing of the circulation by the inshore branch of the Labrador Current which is not included in the model.

5.7 Comparison with SST images

In this section, the non-linear CANDIE model is run with winds from July and August of 1998 to allow comparison with the SST satellite based images of Figure 2.24 (Chapter 2).

The modeled surface density and velocity fields are shown in Figures 5.25 and 5.26, respectively, for the 4 days featured in the Satellite SST images. The assumption in this section is that the modeled surface density field patterns are representative of surface temperature patterns. However, the model's upstream boundary condition does not include the Labrador Current nor local solar heating over the course of the summer. Solar heating increases the stratification of the water over the summer. Furthermore, it could also dampen observed upwelling since the surface heat flux depends on the air-sea temperature difference. Thus upwelled water would be heated more rapidly than warmer surface waters.

The AVHRR sensor measures the radiance of the skin surface of the ocean. Empirical algorithms convert these data estimates of temperature in the top metre of the

ocean. The surface model layer is however 10 m thick. As in the comparisons with CODAR data, the depth averaged temperature in the top 1 m and the top 10 m of the water column may differ. The CODAR data indicate that surface currents (1 m) are more influenced by winds then the top 10 m of the water column. The surface (top 1 m) distribution of cold upwelled water could be affected by stronger surface currents changing the horizontal distribution of this upwelled water in comparison to the distribution by the top 10 m averaged currents.

On day 204 in 1998, with winds having increased from near zero wind stress to 0.1 Pa directed out of the bay, the model shows upwelling on the west side of both Trinity and Conception Bays (Figure 5.25). In particular in Trinity Bay, denser water on the western side of the bay extends out in two locations; in the middle of the bay and near the mouth. Upwelled water with a density increase greater than 0.5 kg m^{-3} from initial values, extends roughly 10-15 km from the western shore. By contrast in Conception Bay, denser upwelled water is spread more or less uniformly across the western shore line with a density increase from initial values of 0.5 kg m^{-3} spread within 4 km of shore.

A common feature in both bays is a finger of denser water spreading across the mouth of the bay from the western shore. The associated velocity field for day 204 (Figure 5.26) shows that the separation of the coastal jet from the western shore line moves denser water to the interior of the bay.

By day 209, winds are subsiding after blowing out of the bay with magnitudes of

0.1 Pa for 4 days. Upwelled dense water develops into three prongs on the western side of the bay situated near the head, in the middle and near the mouth of the bay. These prongs are associated with gyres and meandering circulation features (Figure 5.26). Compared to day 204, upwelling is more intense at day 209, due to higher wind speeds. Near the western coast of Trinity Bay density is increased by 1 kg m^{-3} (dark red) from initial values.

By day 209 in Conception Bay, there is a separation of the coastal jet visible in the density and velocity fields. Beyond the mouth and the separated jet, currents are weak with little cross-shore density gradients. The separated jet veers into the bay as it reaches the eastern side of the bay. Around the headland between the two bays, a small anti-cyclonic gyre is present with a radius of 5-6 km.

At day 214 in Trinity Bay, the three pronged formation of upwelled dense water is clearly visible. By this time, winds are weak and 5 gyres (anti-cyclonic as well as cyclonic) are present in Trinity Bay. A gyre is present on each side of the 3 prongs of upwelled water with the exception at the mouth of the bay. There, a single gyre inside the bay from the upwelling prong is formed. The gyre at the mouth of Trinity Bay covers the entire mouth of the bay, with a downstream entrainment of current due to the presence of the coast (Nof, 1988) on the south-eastern side of the bay, driving flow around the headland. As at day 209 there is still as small anti-cyclonic gyre present at day 214 just south of Cape Freels (between Trinity and Conception Bays).

By day 214, in Conception Bay, there is convergence of the along-shore component of velocity leading to flow across the mouth transporting dense water across the mouth as at day 209. The extent of upwelling is slightly greater than at day 209.

By day 223, winds are the strongest among the 4 days observed in the SST images. The three prong formation of dense water in Trinity Bay is still highly visible, although the width and the density gradients are greater than in the previous three images. The middle tongue of upwelled water (> 0.5 kg m^{-3}) extends across the width of the bay.

The gyres observed during periods of lighter winds now form meandering currents with strongest velocities across the mouth of the bay. On the east side of Trinity Bay, there is an out flowing jet extending around the headland into Conception Bay.

In brief, the model shows that cold upwelled water appears on the western side of both Trinity and Conception Bays and is related to wind strength. The upwelling in Trinity Bay consists of three prongs, one near the mouth, one in the middle and one at the head. In particular, the strength of the prong in the middle of Trinity Bay seems related to wind stress strength. In Conception Bay, the upwelling pattern features a single prong usually associated with a single gyre observed in the bay. The model shows that upwelling features are always stronger in Trinity Bay than in Conception Bay, in agreement with the satellite sea surface temperature images. The model tends to produce an anti-cyclonic gyre in Conception Bay; however, in Trinity Bay, both cyclonic and anti-cyclonic gyres are produced.

In the CODAR data, the separation of the coastal jet does not produce cyclonic gyres due to the predominant influence of wind stress over geostrophic influences. Consequently the pattern of the spreading of upwelled water as seen by SST observations may differ from the modeled upwelling patterns which are determined in part by the wind and geostrophy.

The greatest contrast between model surface density patterns and observed SST patterns is near the mouth of the bays. In both Trinity Bay and Conception Bay, the model overestimates the cross-shore transport of dense water across the mouth compared to the SST data. This transport across the mouth of the bay is associated with the production of density gradient driven gyres which is not observed in the CODAR data. Near the head of both bays however, the model underestimates the cross-shore extent of upwelled water with respect to the SST data. This may also be related to the formation of density driven gyres present in the model.

A possible reason for underestimating the cross-shore extent of upwelled water near the head and overestimating the extent of upwelled water near the mouth is an alignment difference of wind and model topography compared to wind and actual topography. A model run with winds rotated by 20 degrees (so that mean winds are parallel to the axis of the bay) indicates that the basic upwelling pattern remains generally unchanged for a small change in wind direction, however, the intensity of upwelling near the head does increase slightly while upwelling decreases slightly in intensity near the mouth.

For Trinity Bay, as mentioned in Chapter 4, the upwelling near the mouth of the bay on the western shore is preserved due to the proximity of the upstream open boundary. This boundary allows no Kelvin waves to enter the domain. Extending the model topography further north to include Bonavista Bay (the next bay to the north) would allow Kelvin waves originating from Bonavista Bay to arrest partially the upwelling generated on the western shore of Trinity Bay and in particular near the mouth of the bay. Indeed, as seen in Figure 5.27 for a run done using topography that includes Trinity, Conception and Bonavista Bays, the upwelling intensity at the mouth of Trinity Bay is reduced in intensity and located further inside the bay in keeping with the SST data. Also noticeable in this particular model topography (Figure 5.27) is the absence of the Bellevue Peninsula in Trinity Bay . The absence of this peninsula seems to reduce the amount of upwelling at the head of Trinity Bay and emphasises the importance of the Bellevue Peninsula to upwelling and circulation patterns near the head.

A feature not seen in the model is the presence of small sinuous fingers of cold water 4 km wide seen on day 214 in the SST data (Figure 2.24). Differences between observations and model results may also arise due to differences between the vertical averaged state variables over the top 1 m and the top 10 m of the water column.

Common features of the modeled surface density pattern and the SST data include stronger upwelling in Trinity Bay over Conception Bay, a consistent three pronged upwelling spreading pattern in Trinity Bay and a single patch pattern in Concep-

tion Bay and the fact that upwelling strength and extent is directly related to wind strength. The model suggests that the along-shore scale of upwelling features is related to the along-shore distance over which a coastal jet separates from the head of the bay and the scale of the gyres produced in the bay.

Along-shore variations in the distribution of cold/dense upwelled water are visible in both the modeled output and SST data. In the linear model, only Kelvin waves and coastline shape are responsible for setting up the alongshore gradients of density near the coast. In the non-linear model, the separation of the coastal jet from the western side of the bays as well as the formation of gyres contribute to forming along-shore temperature/density gradients near the coast.

5.8 Summary

In this chapter, the time dependent response of Trinity and Conception bay has been examined using the 3-D non-linear CANDIE model. Model results have been compared to a variety of data observations taken in 1990, 1991, 1994 and 1998. The model only includes wind forcing over the model domain with no prescribed inflow at the model boundaries.

The model reproduces the mean anti-cyclonic circulation pattern observed at 20m in the current mooring data. Observed upwelling is reproduced by the model, with the non-linear model out performing slightly the shallow water model and the linearized CANDIE model. While linear models reproduce most major upwelling events, the

non-linear model represents the slope of isopycnal displacement in time more accurately for upwelling and downwelling events.

The model reproduces only some of the features of the ADCP transects taken at the mouth of the bay. The model mostly shows strong velocities near the surface and near shore. The ADCP data features complex sub-surface flow that includes columnar type flow one to two km in depth. Furthermore. the coastal jet that is seen in the ADCP data, can be distributed over the entire depth of the water column near shore.

The model shows reasonable agreement with CODAR data during periods of strong winds. Inclusion of the Labrador Current inshore branch may be needed to improve agreement at the mouth of the bay. A case study with zero Coriolis force reproduces the intensification of currents with distance from the head of the bay (as observed in the CODAR data) as well as a coastal intensification on the eastern side of the bay.

While most of the observations were made in Conception Bay, comparisons with SST data for both Trinity and Conception Bay have provided fruitful results in understanding the upwelling pattern differences between the two bays. Upwelling is stronger in Trinity Bay and is spread away from the western shore in a 3 pronged pattern. In Conception Bay, upwelling is weaker and shows no along-shore patchiness as in the case for Trinity Bay. Including Bonavista Bay into the model reduces the extend of upwelling at the mouth of Trinity Bay and produces better agreement with

the SST observations.

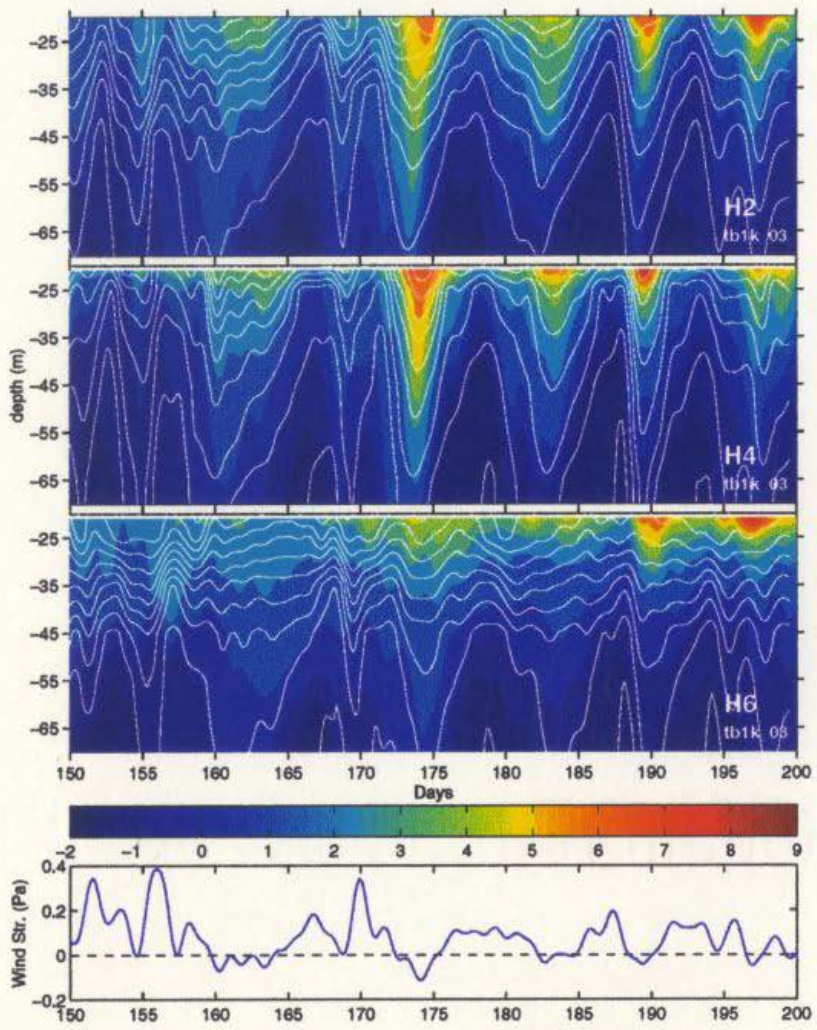

Figure 5.1: Density profile (white lines) output from non-linear CANDIE run and observed temperature profile in 1990 (colour contours) at 3 current mooring locations. From top to bottom, the moorings are H2, H4 and H6 respectively (Figure 2.11). Also shown is the corresponding along-bay wind stress time series. The modeled density profile has been shifted to the left by 0.5 days for better visual correspondence.

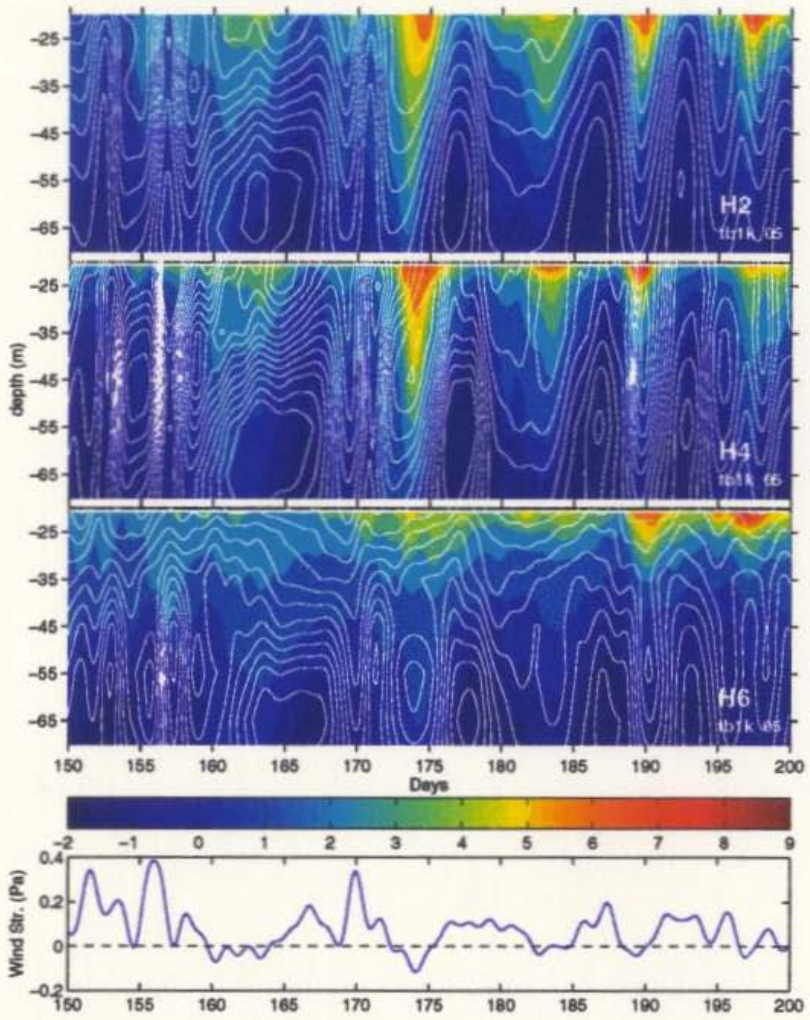

Figure 5.2: As in Figure 5.1 but for the linear model run. Model data are not shifted in time.

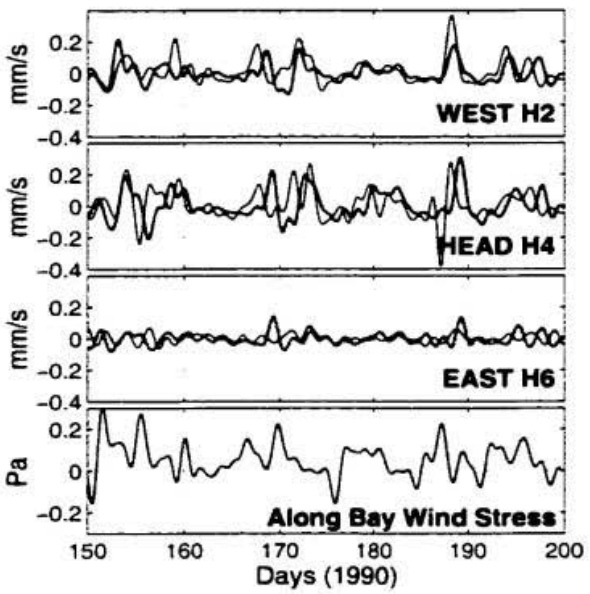

Figure 5.3: Apparent modeled vertical velocities (thick line) from density field of non-linear CANDIE model with realistic bottom topography and apparent observed vertical velocities for 1990 thermocline data (thin line).

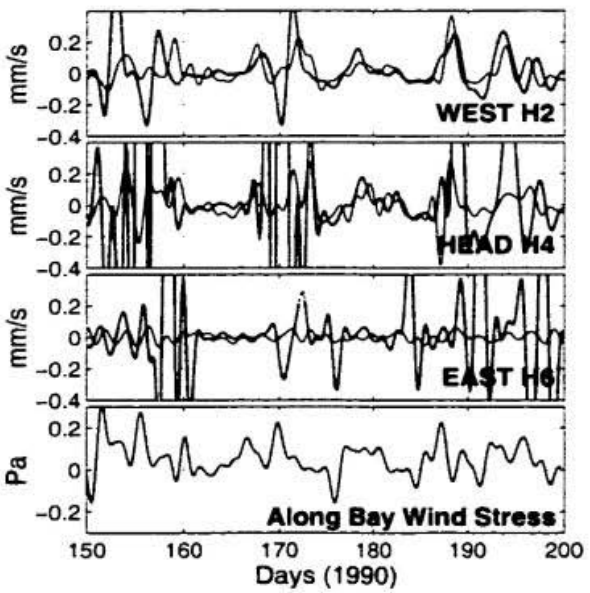

Figure 5.4: As in Figure 5.3, but for linearized CANDIE model.

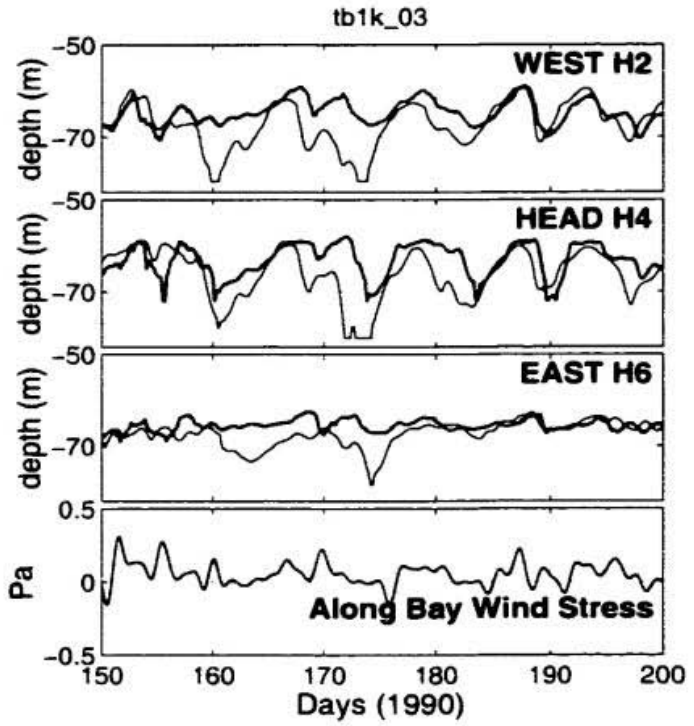

Figure 5.5: Vertical position of the 1025.8 kg m^{-3} isopycnal (thick line) for the non-linear CANDIE model with realistic bottom topography and the observed 1 °C isotherm (thin line) at H2, H4 and H6 mooring locations.

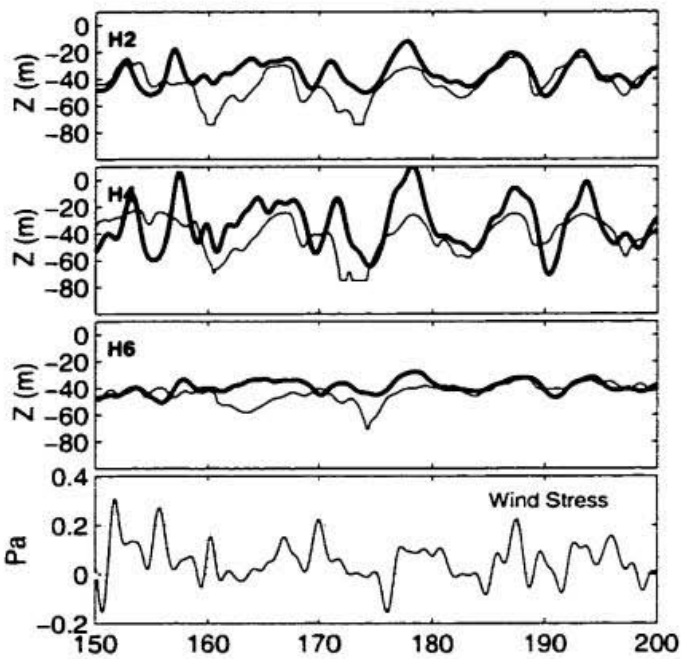

Figure 5.6: Shallow water interface position (thick line) compared to the position of the observed 1 °C isotherm (thin line) at H2, H4 and H6 mooring location.

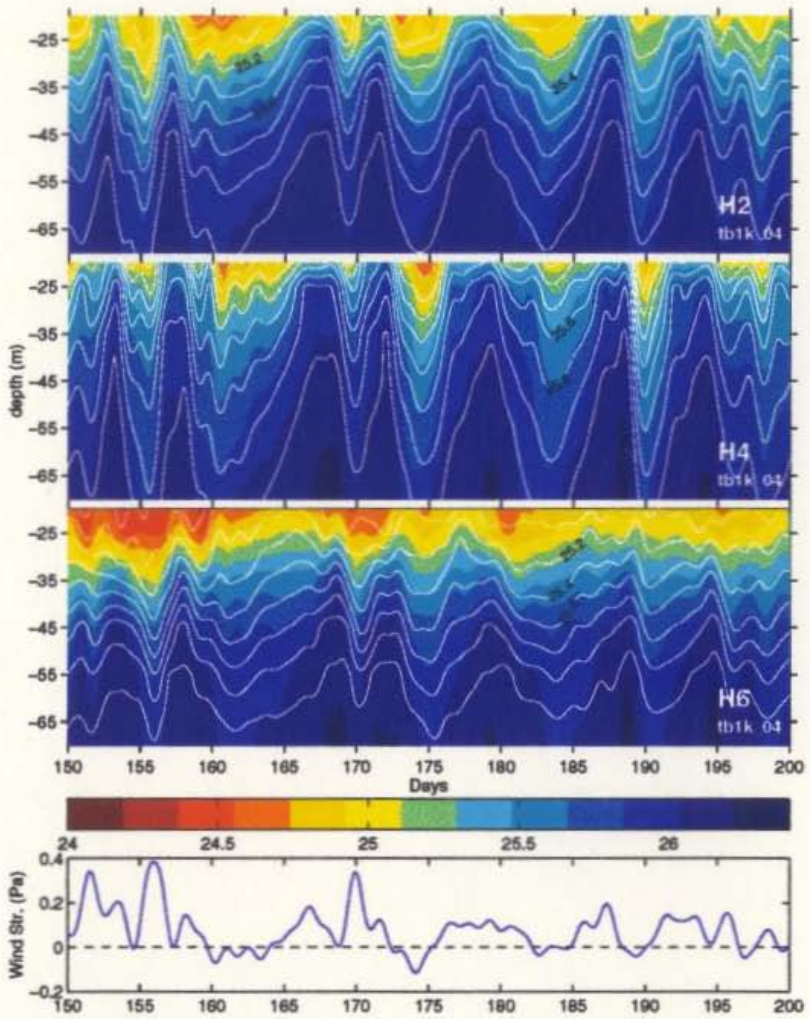

Figure 5.7: Density profile comparison between realistic bottom run (colour contours) and flat bottom run (white contours). Both model runs are non-linear and identical, save for bottom topography.

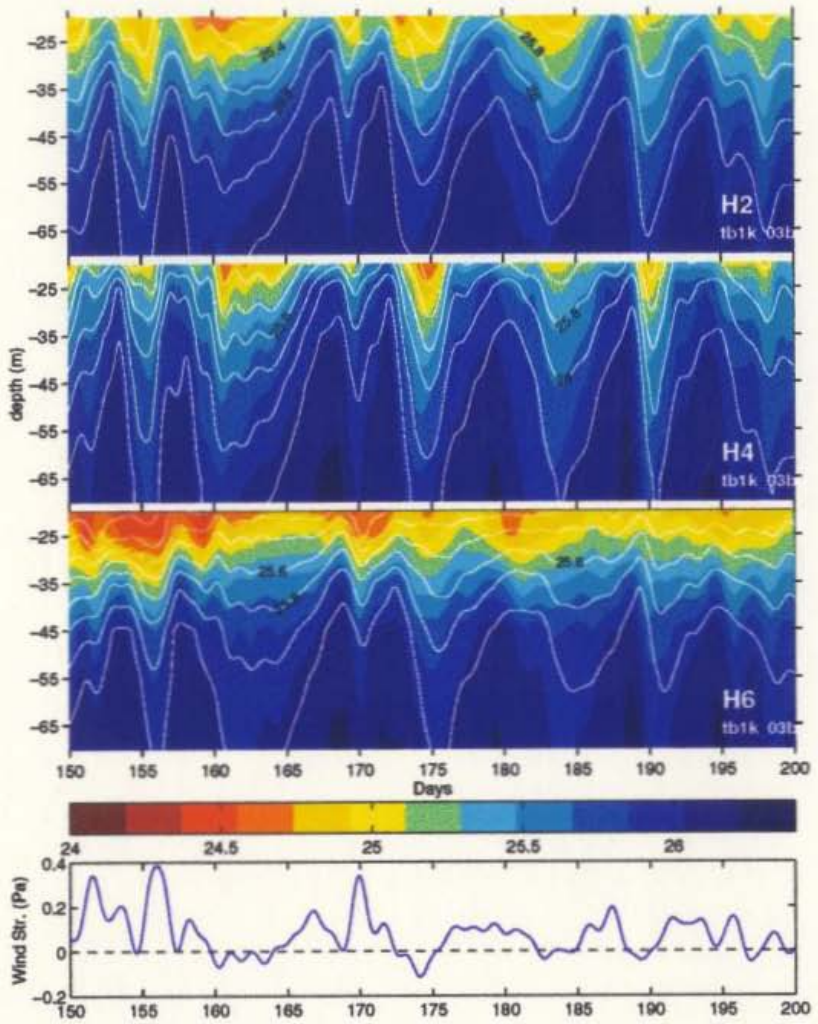

Figure 5.8: Density profile comparison between model run with a Prandtl number of 1 (colour contours) and run with a Prandtl number of 100 (white contours). In the latter case vertical viscosity is set at 10^{-2} m^2 s^{-1}instead of 10^{-4} m^2 s^{-1}.

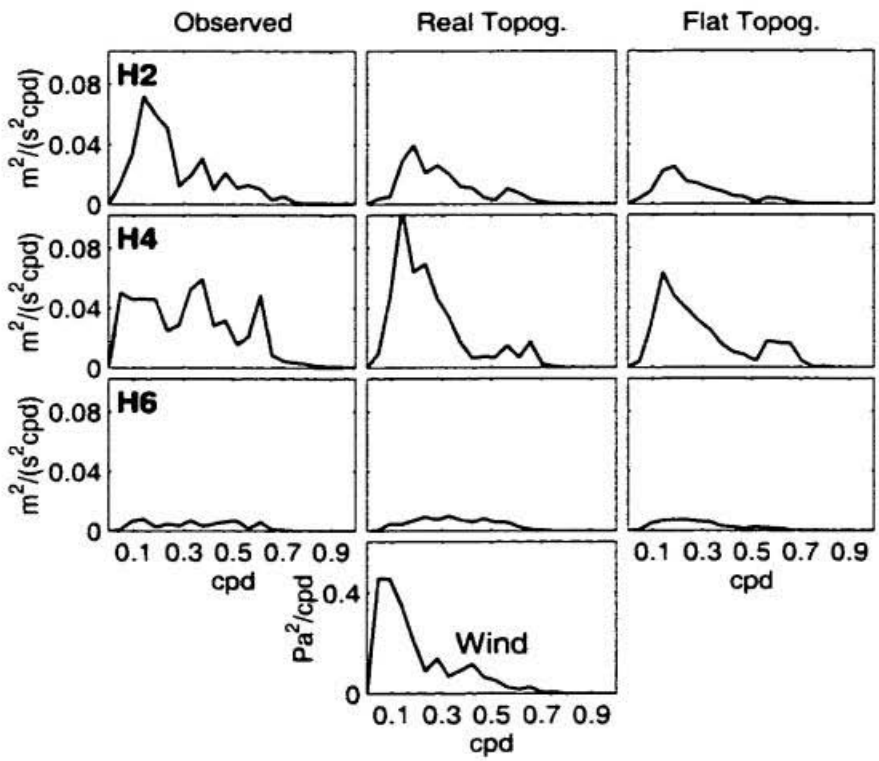

Figure 5.9: Power spectra of apparent vertical velocities from day 150 to 200 in 1990. The left column shows the observations, the centre column represents model output from the non-linear CANDIE model with realistic bottom topography, and the right column features results from the flat bottomed model run. Also shown at the bottom is the power spectrum for the along-bay wind stress time series.

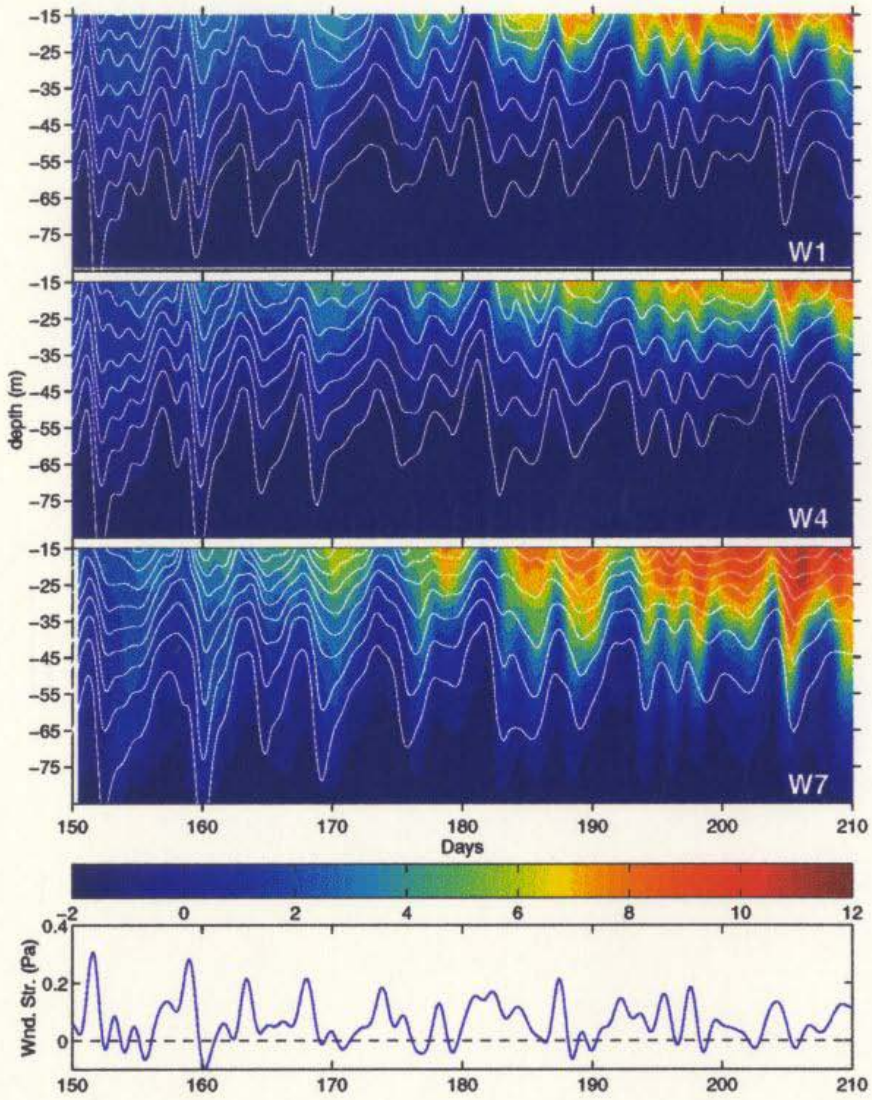

Figure 5.10: Density profile (white lines) output from non-linear CANDIE run and observed temperature profile (colour contours) at 3 current mooring locations in 1994. From top to bottom, the moorings are W1, W4 and W7 and are situated on the western shore of Conception Bay over the 100 m isobath. The corresponding along-bay wind stress time series is shown below. The modeled density profile has been shifted to the left by 1 day.

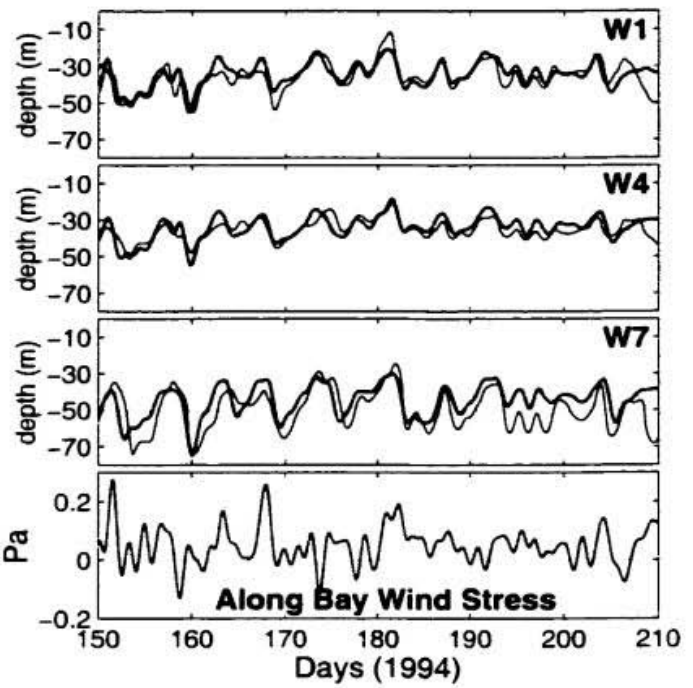

Figure 5.11: Comparison of observed 1 °C isotherm with the 1025.7 kg m^{-3} isopycnal from the non-linear CANDIE model on the western shore of Conception Bay in 1994. At W7, the 1026 kg m^{-3} modeled isopycnal is shown instead since the 1 °C isotherm is deeper at this location (roughly 50 m deep). Lagged correlations with between model and data are 0.70, 0.67 and 0.74 at W1, W4 and W7 moorings, respectively. The model lags the data by roughly 24 hrs at all three locations.

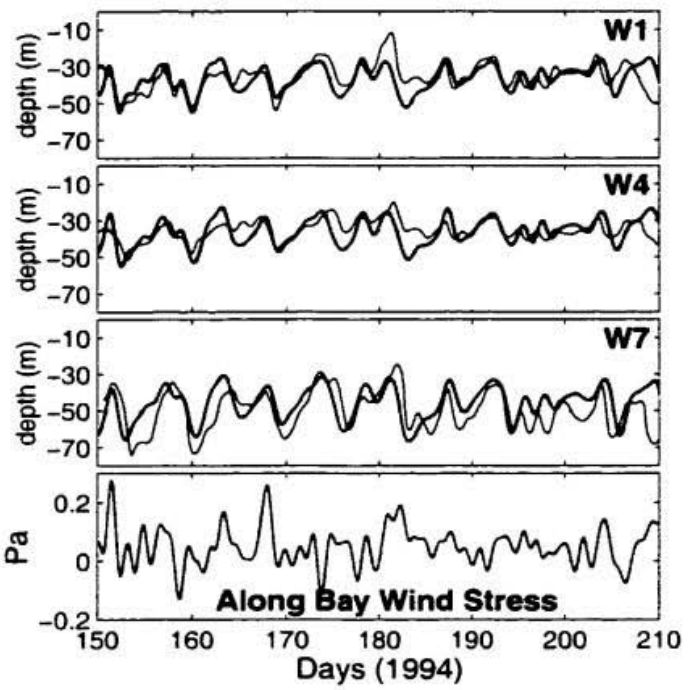

Figure 5.12: As in Figure 5.11 but using the linearized CANDIE model with realistic bottom topography. Lagged correlations with between model and data are 0.52, 0.48 and 0.57 at W1, W4 and W7 moorings, respectively. The model lags the data by roughly 12 hrs in all three locations.

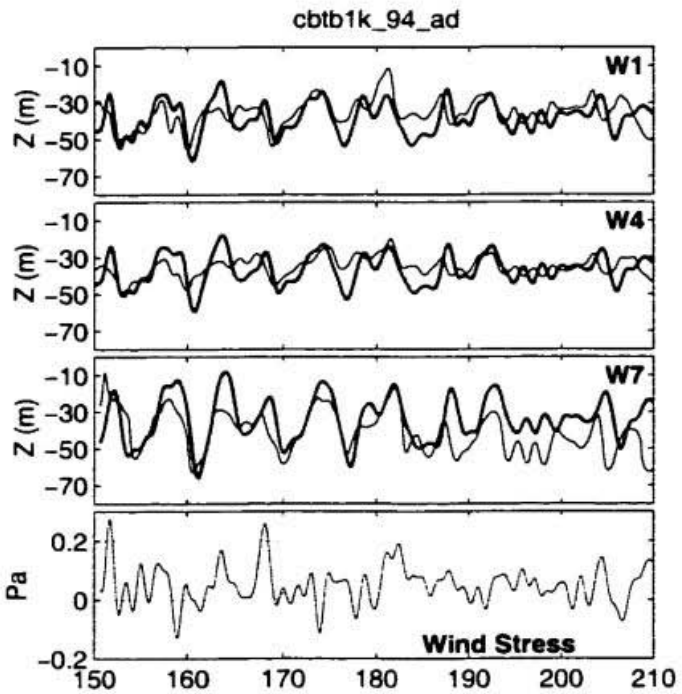

Figure 5.13: Comparison of observed 1 °C isotherm with interface position of shallow water model on the western shore of Conception Bay. Model lags data by 12 hours with correlations of 0.60, 0.56 and 0.67 at moorings W1, W4 and W7, respectively. For W7, the comparison was done with the 2^o thermocline.

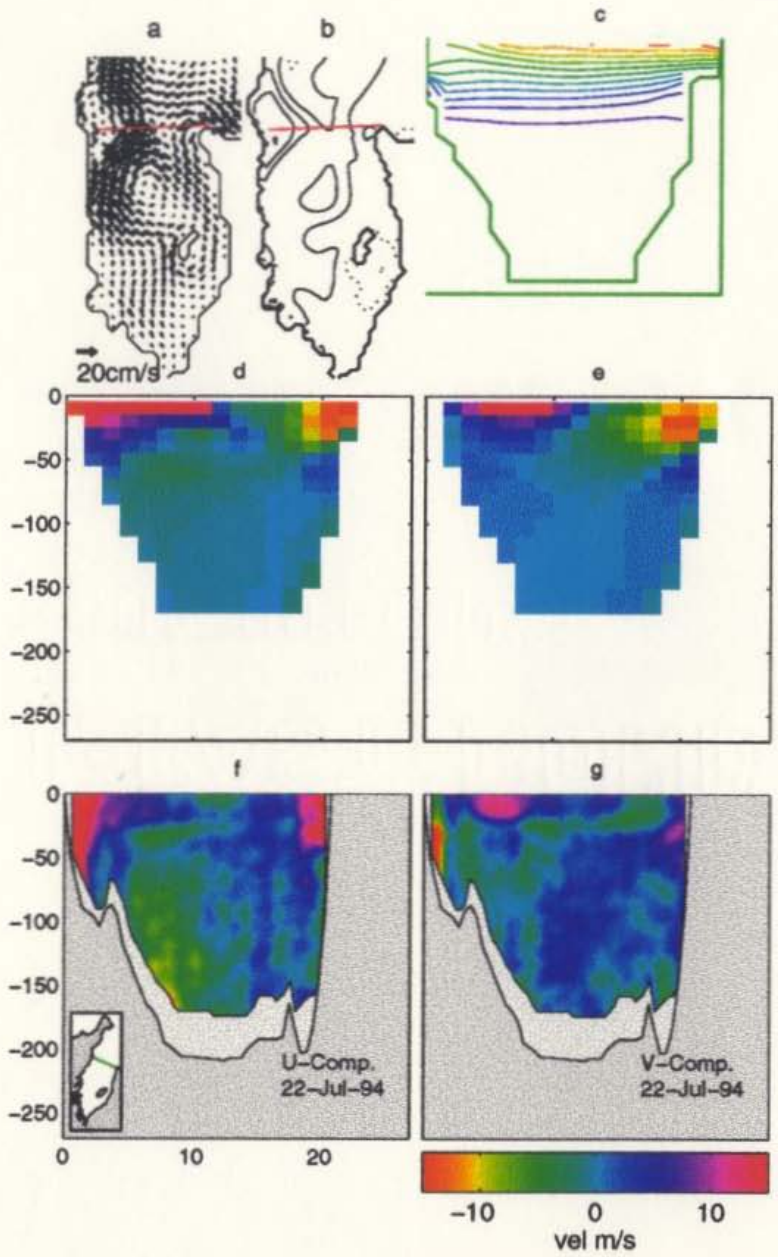

Figure 5.14: Comparison of non-linear CANDIE model and ADCP observations on 22 July (day 203). (a) Surface velocity field from model. (b) Surface density field from model with 0.05 kg m^{-3} contours. (c) Cross section of model density field. The interval between contours is 0.05 kg m^{-3}. (d) Cross section of the modeled U component of velocity (cross-bay). (e) Cross section of the along-bay (V) component of velocity. (f) Observed U component of velocity. (g) Observed V component of velocity.

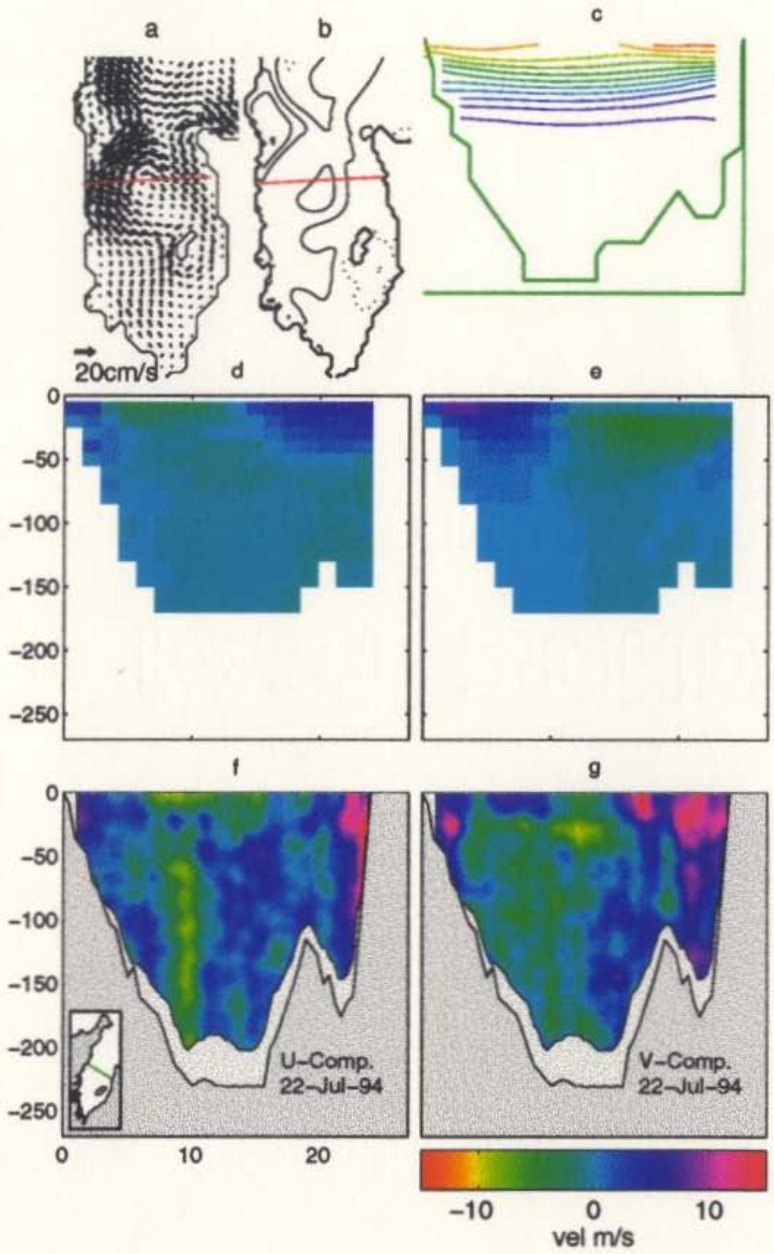

Figure 5.15: As in Figure 5.14 but for a transect located further into the bay by 10 km.

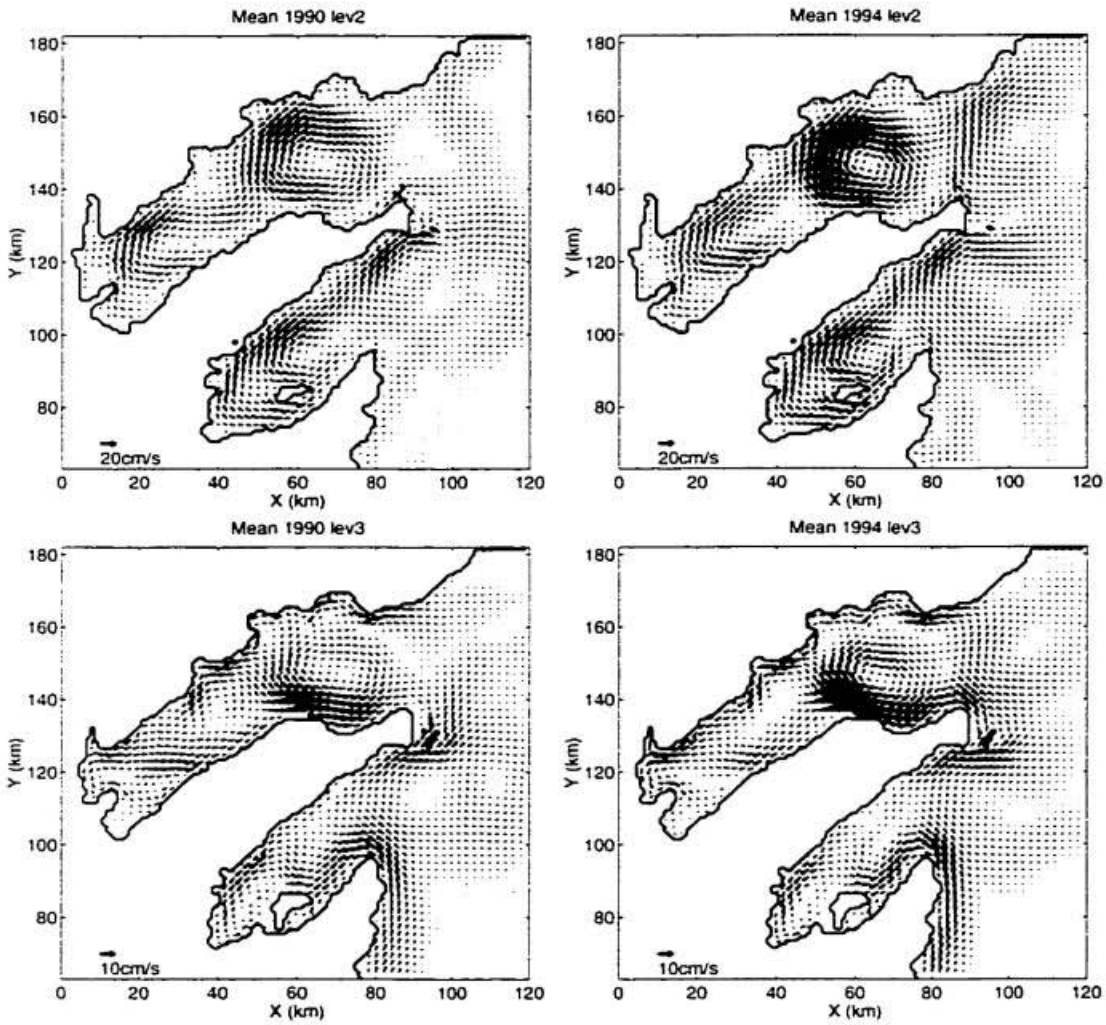

Figure 5.16: Mean currents at 15 m (lev2) and 45 m (lev3) in the 1990 (50 days) and 1994 (60 days) model runs. Every third model velocity vector is plotted (i.e every 3 km). These plots should be compared to observations featured in Figures 2.15 and 2.16.

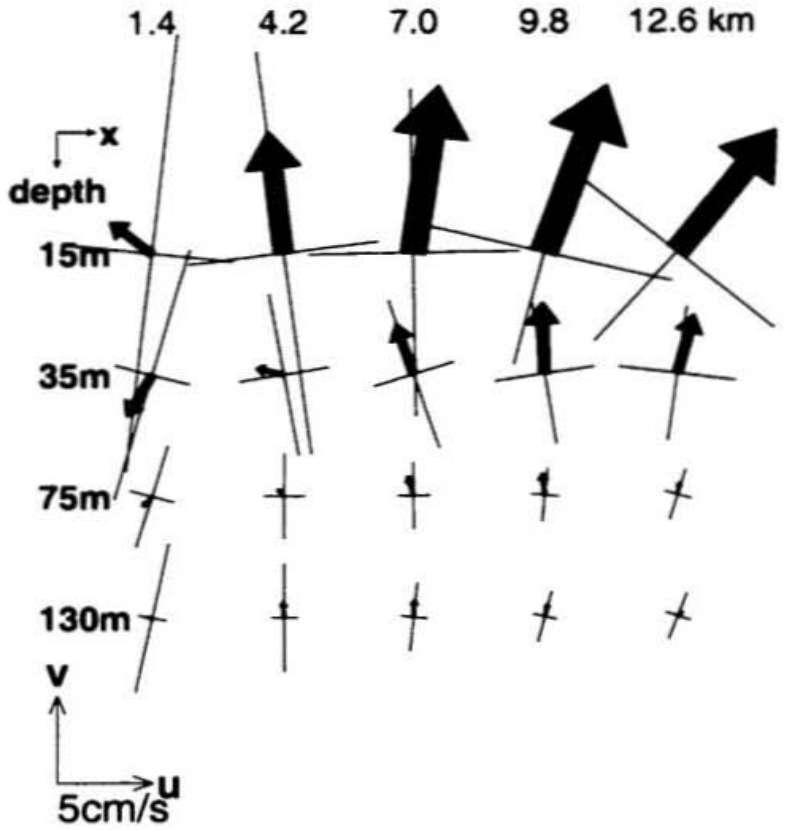

Figure 5.17: Cross-shore vertical transect (as in Figure 2.16) of mean modeled current and the corresponding major and minor axis of standard deviations. Model run is the non-linear CANDIE model with flat 200 m bottom topography.

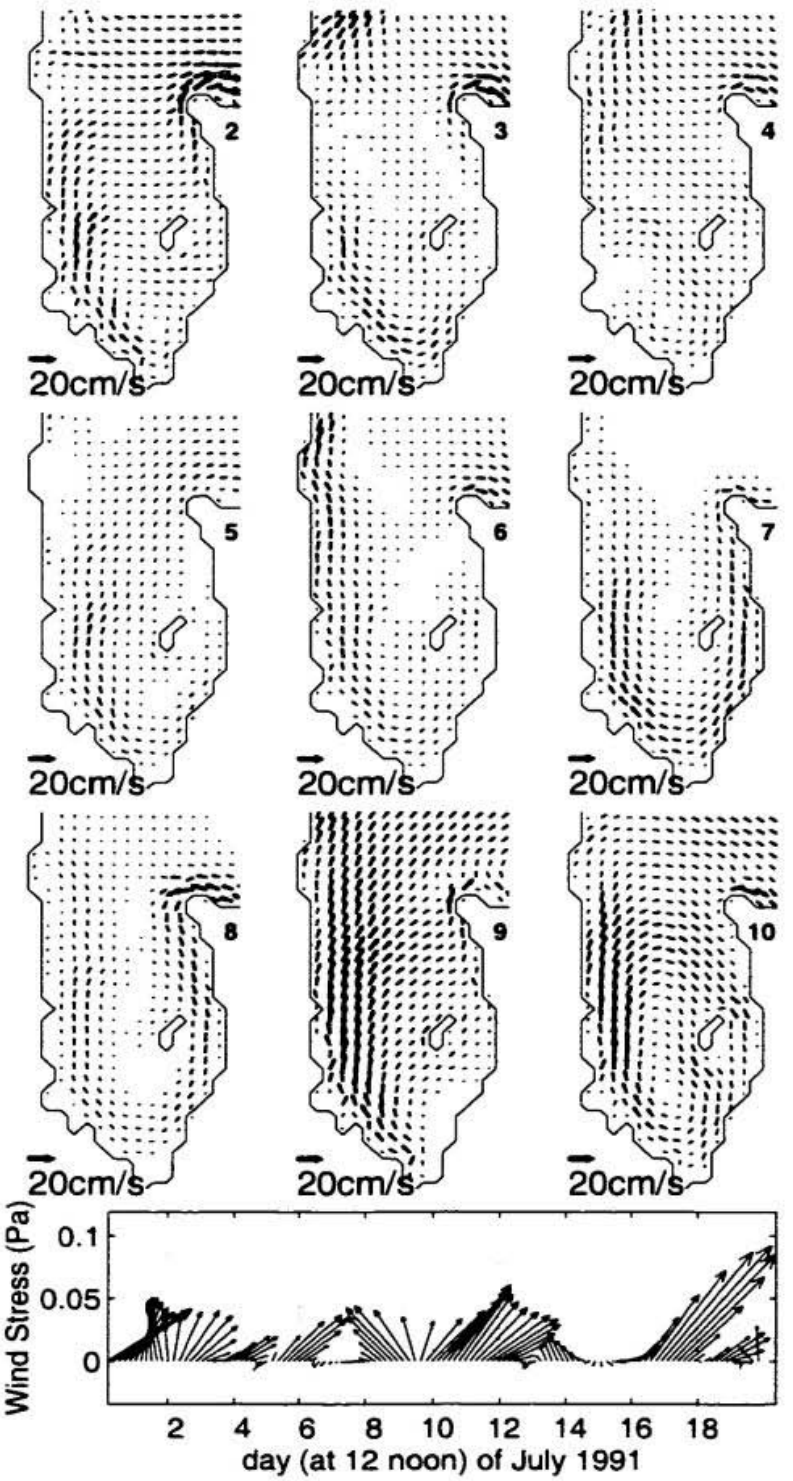

Figure 5.18: Velocities from CANDIE model shown at 12 noon from July 2^{nd} to the 10^{th}. The spacing between vectors is 2 km.

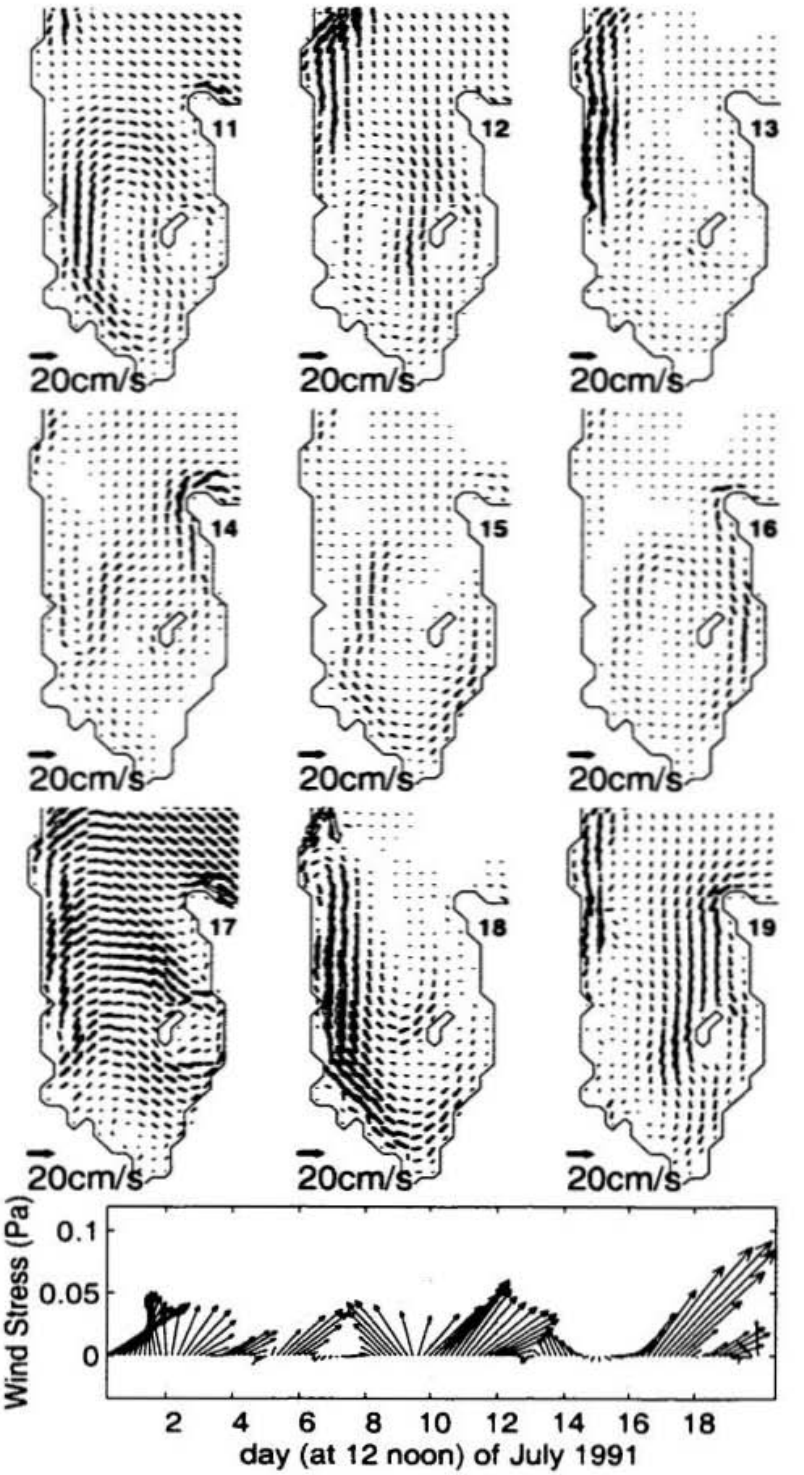

Figure 5.19: As in Figure 5.18, but covering July 11^{th} to the 19^{th}. The spacing between vectors is 2 km.

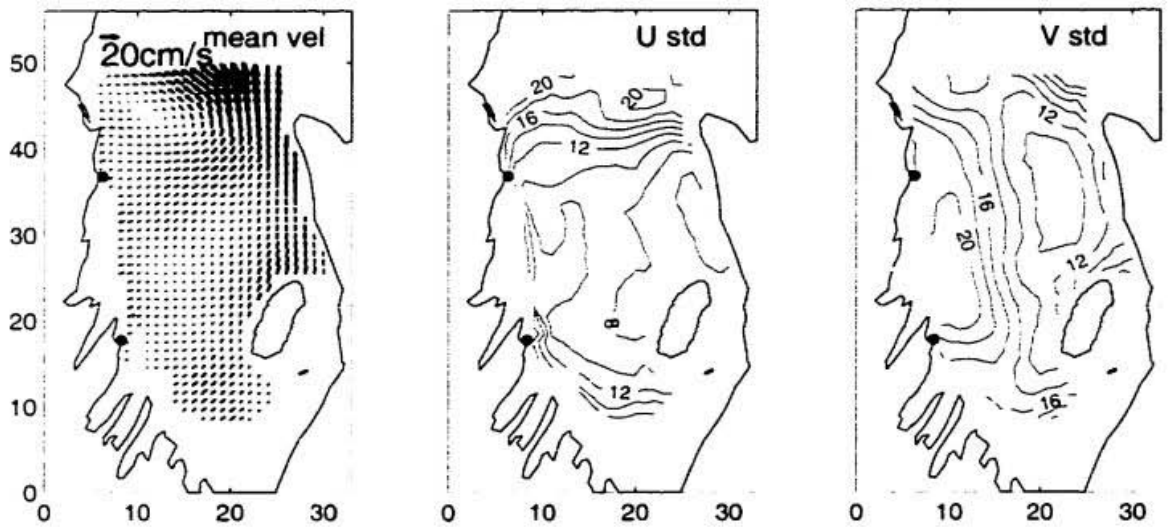

Figure 5.20: Mean surface currents (top 1 m) from hourly CODAR observations from July 2^{nd} to the 19^{th} of 1991. Also shown are the corresponding standard deviation fields of the u and v components of velocity.

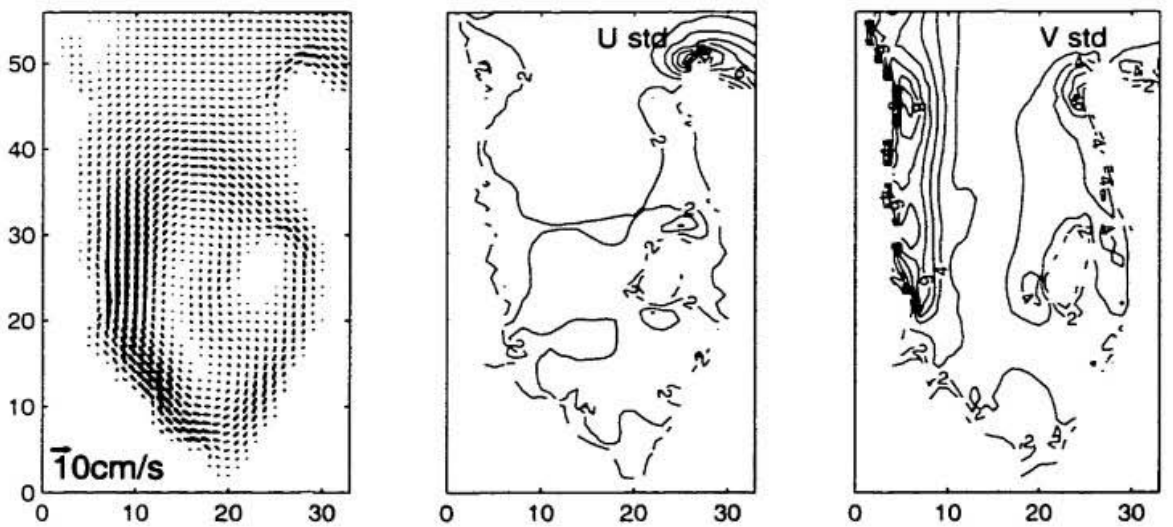

Figure 5.21: Mean surface layer currents (10 m) of non-linear CANDIE model 6 hourly output from July 2^{nd} to the 19^{th} of 1991. Also shown are the corresponding standard deviation fields of the u and v components of velocity.

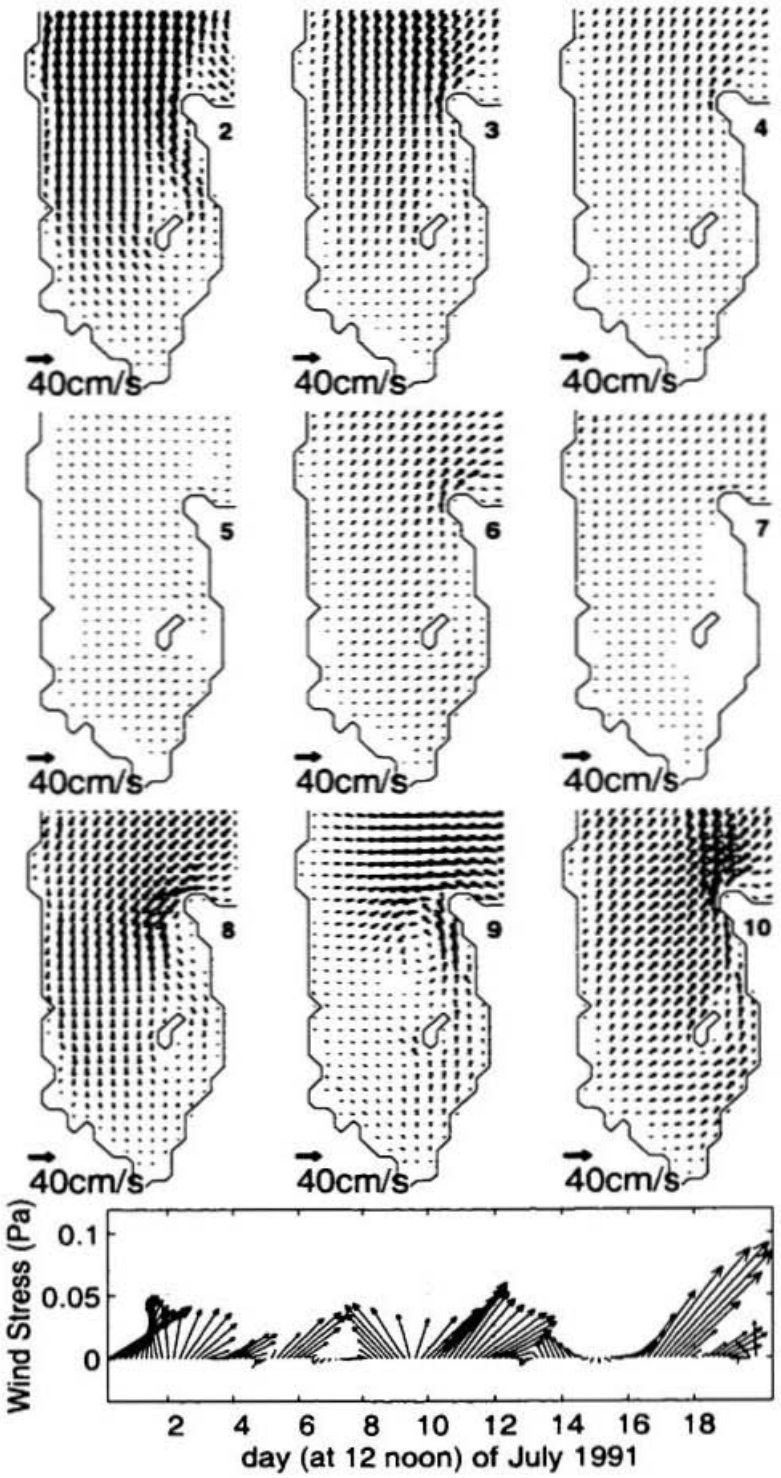

Figure 5.22: Velocities from CANDIE model with $f = 0$ shown at 12 noon from July 2^{nd} to the 10^{th}. The spacing between vectors is 2 km.

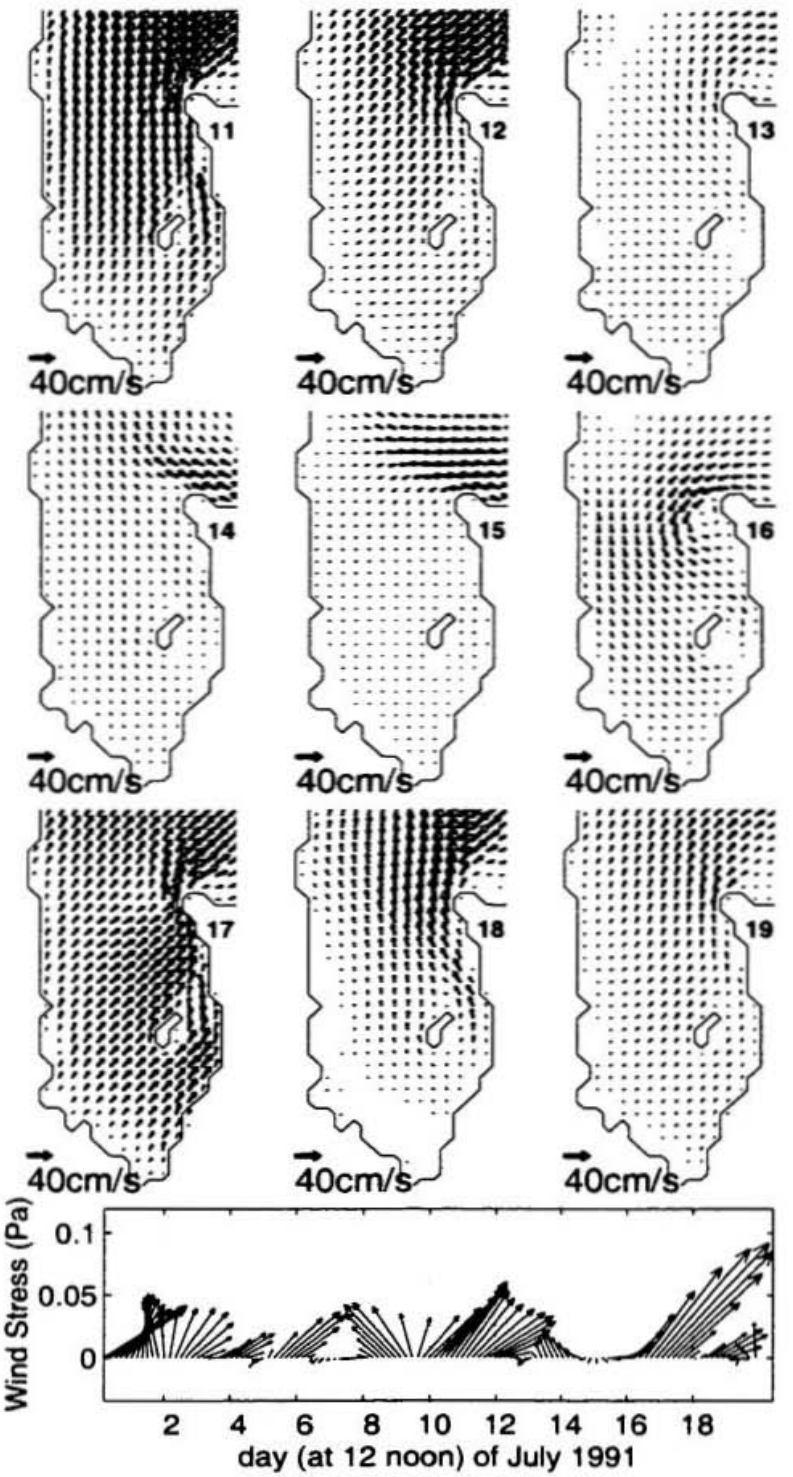

Figure 5.23: As in Figure 5.22, but covering July 11^{th} to the 19^{th}. The spacing between vectors is 2 km.

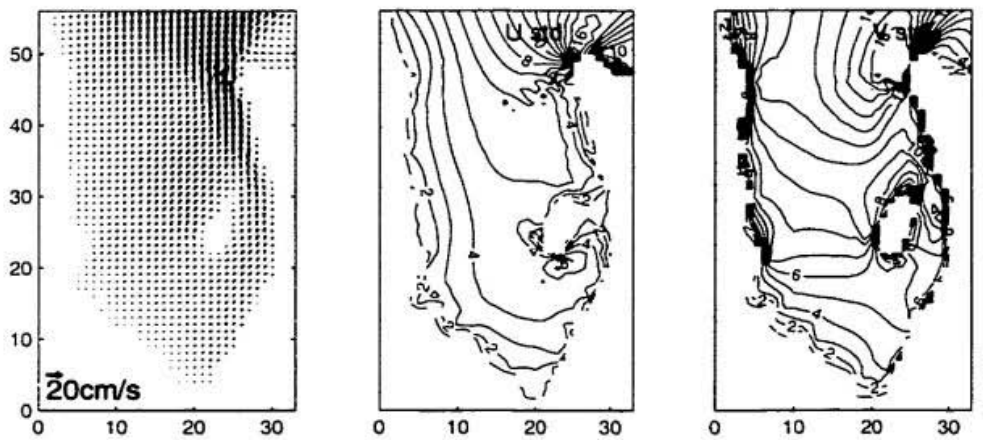

Figure 5.24: Mean surface layer currents (10 m) of non-linear CANDIE model without the Coriolis force (i.e. $f = 0$). Also shown are the corresponding standard deviation fields of the u and v components of velocity.

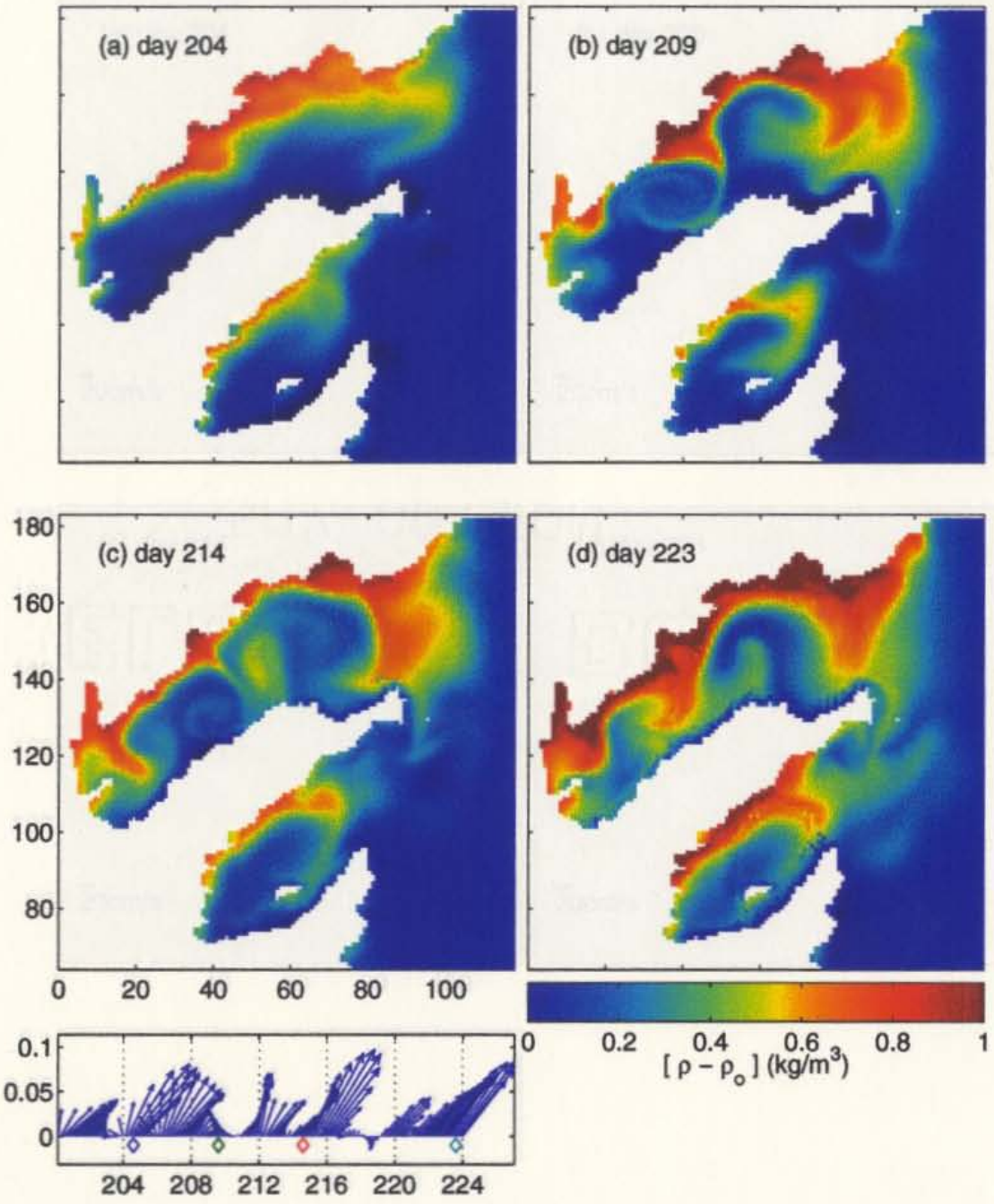

Figure 5.25: Surface density from non-linear CANDIE model using 1998 wind forcing at 12 noon local time. Julian days shown are (a) day 204 (22 Jul), (b) day 209 (27 Jul), (c) day 214 (1 Aug) and (d) day 223 (10 Aug).

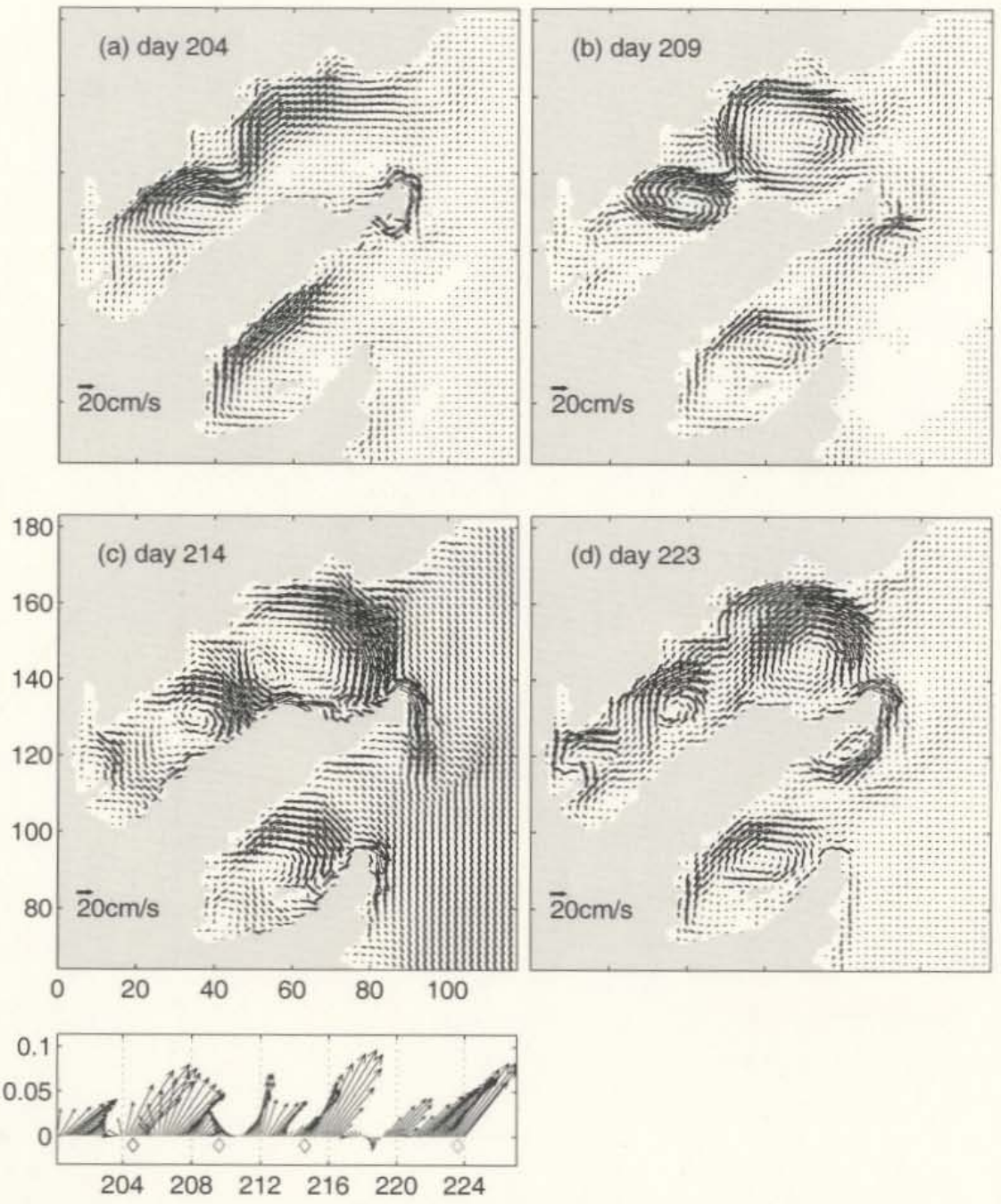

Figure 5.26: Surface velocity from non-linear CANDIE model using 1998 wind forcing. Julian days shown are (a) day 204 (22 Jul), (b) day 209 (27 Jul), (c) day 214 (1 Aug) and (d) day 223 (10 Aug).

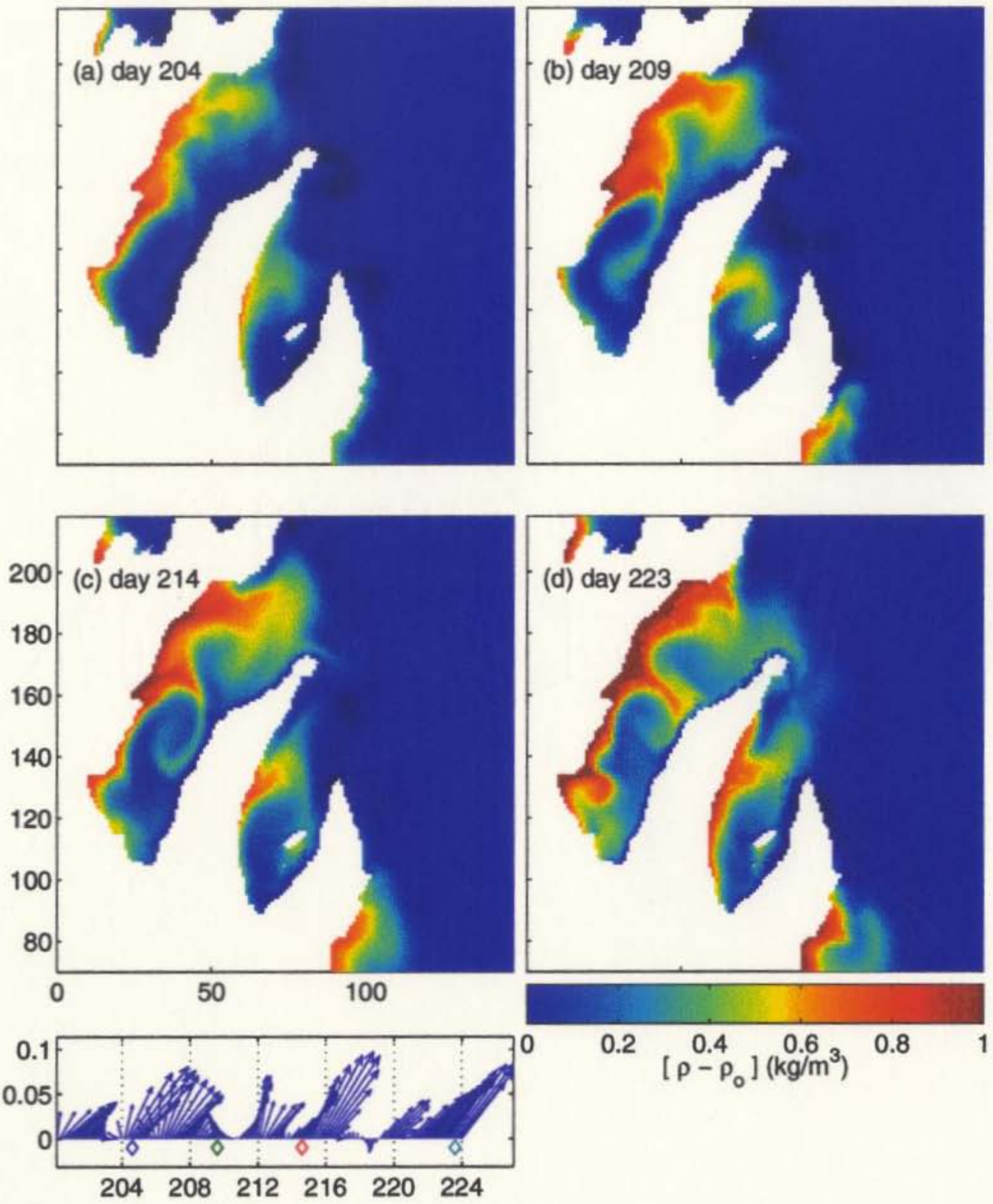

Figure 5.27: As in Figure 5.25 but using an alternate topography file that includes Bonavista Bay. Note that the Bellevue Peninsula at the head of Trinity Bay is not featured in this model run.

Chapter 6

Biological Application

6.1 Introductory Remarks

Trinity and Conception Bays, are spawning grounds for several species of fish (Smedbol and Wroblewski (1997); Frank and Leggett (1982); Laprise and Pepin (1995)). Knowledge of factors that influence survival of fish eggs and larvae is important groundwork towards predicting recruitment of adult fish. Early life stages of fish are particularly sensitive to the physical environment due to their limited mobility and energy reserves. Physical transport and vertical distribution in the water column are the primary determinants in the trajectory of larvae (Werner et al., 1993; Bartsch et al., 1989). The location and timing of spawning with respect to hydrodynamic features can be important in ensuring transport from spawning to nursery grounds (Hjort, 1914; Iles and Sinclair, 1982; Kasai et al., 1992). On the Newfoundland Shelf, Helbig et al. (1992) applied the barotropic velocity field (vertically averaged currents) of Greenberg and Petrie (1988) along with a Pollard-Millard wind driven slab model

to track passive drifters. They demonstrated that appropriate wind forcing such as the passage of a storm, was required to carry larvae into Newfoundland Bays from the Grand Banks and the Northeast Newfoundland shelf. Davidson and de Young (1995) suggested that eggs spawned on the shoreward half of the Newfoundland shelf may have some chance to drift into the eastern bays of Newfoundland. This study applied a diagnostic model, with 16 km resolution. The limited model resolution permitted them to show that larvae could reach the bays, but could not resolve how or if larvae would drift into the bays.

While the physical environment plays an important role, biological processes such as predation and feeding cannot be neglected in providing an explanation of larval survival (Bakun et al., 1982). The concentration of a larval fish population at a particular location depends on the natural production of eggs and larvae, natural mortality, mortality due to predators as well as the efflux and influx of eggs and larvae from different regions. The state of the water, if nutrient poor or rich, cold or warm, affects growth of eggs and larvae and consequently their survival. Several studies have explored the effects of onshore movement of fresh cold shelf water into Conception Bay on emerging capelin larvae (Frank and Leggett, 1982; Leggett et al., 1984; Taggart and Leggett, 1987). These studies document the emergence of capelin larvae into the water column coinciding with the arrival of fresh shelf water. This shelf water is considered a safe site in which capelin larvae find an abundance of food and fewer predators (Frank and Leggett, 1982).

A common problem in inferring larval fish mortality from abundance observations, is the effect of advective losses and gains (Pepin et al., 1995). It is, therefore important to understand larval dispersion before inferring larval mortality from abundance measurements.

In this chapter, I present a simple study of the application of the CANDIE model developed in this thesis to examine the dispersion of particles in Trinity and Conception Bays. I focus on evaluating the properties of drifters released in both the non-linear and linear CANDIE model velocity fields. The circulation model is forced with winds from 1998, starting on day 190 and running for 35 days. This period covers day 201 and 208, which are dates on which Department of Fisheries and Oceans larval surveys in Conception Bay were undertaken (P. Pepin, DFO, St. John's, informal communication). While the larval data is not discussed here, the basic properties of drifter dynamics during this fish larval sampling period will be presented.

As shown in previous chapters, wind forcing creates the development of gyres in both Trinity and Conception Bay. But how do the non-linear terms and the development of these gyres affect the retention of particles in Trinity and Conception Bays?

6.2 Velocity Field Description and Methods

The CANDIE model is applied with the standard parameters discussed in Chapter 2. The model is initiated at day 190 with smoothed St. John's winds introduced over

a 2 day period. Most winds during this period are calm (Figure 6.1 bottom panel) with gusts of 4-5 days reaching up to 1 Pa and blowing out of the bay.

Particles are released on day 201 at 12 am. Figure 6.1 shows the surface currents on day 201 and every 4^{th} day thereafter untill day 213. The surface velocity features weak circulation in Conception Bay on day 201, with circulation strength increasing under stronger wind on day 205. For days 209 and 213, gyres are formed in the centre of Conception Bay. Strong southward flow between the bays appears around the headland with a small gyre of 4 km radius formed just south of the headland. In Trinity Bay, gyre formation is fully developed on day 209 and 213, 8 and 12 days respectively after particle release. These gyres, particularly those in Trinity Bay, will affect particle drift.

As a reference, Figure 6.2 shows the velocities for the linear CANDIE model run. Here strong flow is confined to the coastal wave guide near-shore. The outward flowing coastal jet in Trinity Bay on the western shore is present in all four days in the linear model case (Figure 6.2). Flow is mostly directed inwards to the bay on the eastern side of Trinity with an intensified southward coastal jet flowing around the head land between the two bays. In Conception Bay, flow is at times weak (e.g. day 209) due to the influence of Trinity Bay (as seen in Chapter 4). In Conception Bay, flow is mostly anti-cyclonic around the coast of the bay.

The drifter model implemented is described in Davidson and de Young (1995) and is designed to track particles smoothly through a finite resolution velocity field.

In this implementation, particles are set at a given model level from the CANDIE velocity field output. There is no vertical transport so particles are constrained to a 2-D velocity field. Thus particles will accumulate near the coast where downwelling occurs near to shore in the model. However since vertical velocities in numerical models are inferred from the continuity equation, they are inherently noisy. For simplicity, I describe only particle drift in two dimensions.

On day 201, the bays are seeded with a uniform grid of particles set a kilometer apart for a total of roughly 5000 particles in the two bays. This initial patch of particles is divided into 4 quadrants for each bay (Figure 6.3 (right panel)). Unless otherwise stated, the drifters were given a random walk component to their displacement at every time step equivalent to a diffusion coefficient of 10 $m^2\ s^{-1}$. This allows for particles seeded at the same location in the model, to be dispersed from each other over time. Particles are advected for 20 days for both non-linear and linear model runs in the modeled surface layer.

6.3 Results

6.3.1 General Particle Drift

For the non-linear model run, particle positions after 4 days and 12 days of drift are computed for the 4 quadrants in each bay (Figures 6.3 and 6.4). Particles seeded in quadrant 1 on the western side near the mouth of Trinity Bay are advected southward

from their initial location. The presence of the coastal jet is visible by the lack of drifters near the coastline. Particles seeded at the mouth on the eastern side of Trinity Bay (quadrant 2), are mostly retained in this region due to onshore flow (Figure 6.1). Some particles are advected towards the head of the bay due to the anti-cyclonic gyre circulation in the interior of the bay, and inflow into the bay along the eastern shore.

After 12 days of drift, particles from quadrant 1 are mostly advected outside the bay with particles scattered southward outside the mouth of Conception Bay. Particles from quadrant 2 are distributed in a similar fashion to those of quadrant 1 with the exception of an absence of particles at the mouth of Trinity Bay and the distribution of 2 patches of particles inside Trinity Bay. These patches are a consequence of the gyres developed in Trinity Bay (Figure 6.1).

Particles seeded near the head of the bay on the western side (quadrant 3), are separated into three groups after 4 days of drift. One group is advected along the western side of the bay towards the mouth of the bay, another is advected southward and the remaining group remains in the area of weak flow sheltered by the Bellevue Peninsula at the head of Trinity Bay.

Particle seeded in quadrant 4, are situated in one patch that is spread along the eastern shore near the head of the bay, and in the center of the bay towards the mouth.

After 12 days of drift, particles from quadrant 3, and to a lesser extent particles from quadrant 4 are spread over the entire extent of Trinity Bay. Some particles from

quadrant 4 are trapped near-shore on the eastern side of the bay. For quadrant 4, the presence of the Bellevue Peninsula seems to retain particles between it and the coast due to weak circulation.

In Conception Bay, the results for particle drift are similar to those of Trinity Bay. Particles seeded near the mouth undergo southward out of the bay drift, particularly the particles seeded in quadrant 6 (Figure 6.3 and 6.4). For particles from quadrant 5, these particles are retained near the mouth of the bay with some advective losses past the model boundary at the south. Furthermore these particles may drift into the bay and ground along the coastline. As in Trinity Bay, particles released at the head of Conception Bay (quadrant 7 and quadrant 8), gradually spread out over the entire Bay over the course of 12 days.

Particle drift was also computed using the linear velocity field (Figure 6.2). Most strong flows in the linear case are confined to the coastal wave guide. For the linear case, only the results after 12 days of drift are shown here (Figure 6.6), since the difference of the non-linear terms are most apparent after 12 days of drift then 4 days.

The main influence of the non-linear terms is in the increased scatter of particles (compare Figures 6.6 and 6.4). While the overall distribution pattern remains roughly the same, there are some clear differences. For Trinity Bay in the linear case, quadrant 1 drifters are mostly all situated in a thin 5 km band on the south-eastern shore of the bay and outside the mouth. This contrasts with the non-linear case where most

of the particles are situated outside of the bay. For particles released from quadrant 3 at the head of Trinity Bay, particles are situated in the south eastern half of the bay after 12 dyads of drift. Particles releases from quadrant 4, form a 20 km wide band between the head of the bay and the western side of the bay near the mouth.

The effects of non-linearity are also readily comparable. The most pronounced difference is noticeable for quadrant 5 particles released near the mouth on the western side. In the linearized case a thin band of particles is located across the mouth. However in the non-linear case particles are spread out over a square patch of 40 km in width.

A few sample drifter trajectory plots are shown in Figure 6.7 for the non-linear case and Figure 6.8 for the linear case. In both cases, drifter trajectories include diffusion. On average, the particles driven by the non-linear velocity field travel greater distances and are susceptible to circular motion due to gyres (panel d for example). In the linear case, most of the transport of particles occurs near the coast.

Figures 6.9 and 6.10 show the path integral distance of particle trajectories over 20 days of drift. As seen in the non-linear case, particles caught in the gyres in the middle of Trinity Bay travel the greatest distance. Most of this travel, however, would be circular motion undertaken by the particles due to the eddies. Near the mouth of Trinity Bay and Conception Bay, there is an area of reduced advection with distances traveled less than 40 km. Most of these particles are advected towards land and become "beached" in the model. The area of reduced advection is, however, nearer

to the mouth in the non-linear case runs compared to the linear case.

6.4 Summary

In this chapter I have qualitatively described the basic motions of particle drift in Trinity and Conception Bay for a period of 20 days beginning on day 201 of 1998. Wind during this time is relatively weak. The results suggest that it is unlikely that there is significant exchange of particles between Trinity and Conception Bays during periods of weak out-of-the-bay winds. Furthermore the head of the bay is an ideal place for seeding drifters so that they remain within but dispersed throughout the bay. The effects of non-linearity includes the separation of particles into patches due to the effect of eddies. Non-linearity increases the dispersion of particles and allows for stronger drift in the middle of the bays away from the coastal boundary layer.

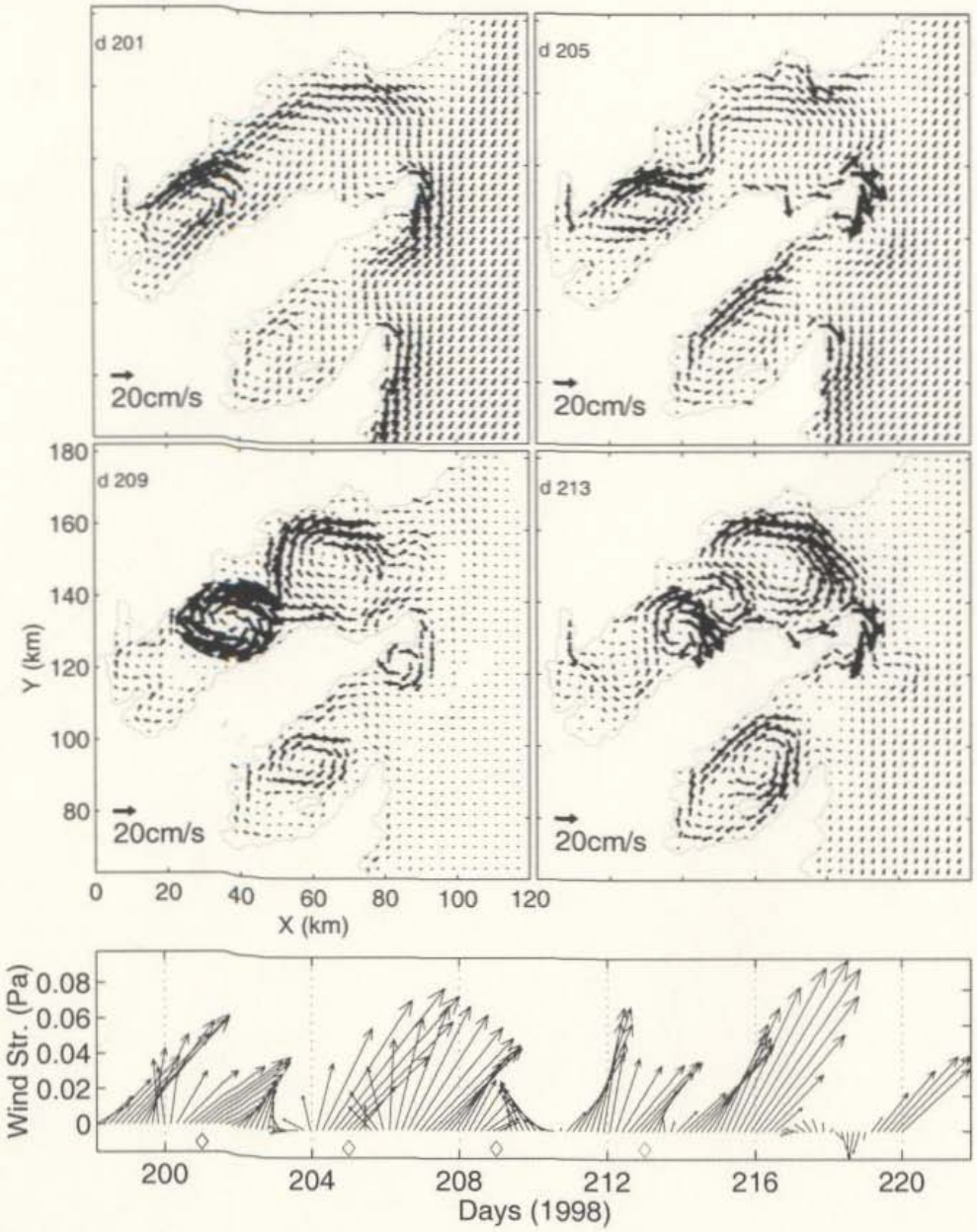

Figure 6.1: Surface velocity field from non-linear CANDIE model shown at day 201 (the start date of the drifter release) and 4, 8 and 12 days later in 1998. Every third velocity vector is plotted, so the distance between the arrows is 3 km. The bottom panel features the wind stress for this period with the diamonds indicating the time at which the velocity snap shots were taken in the model.

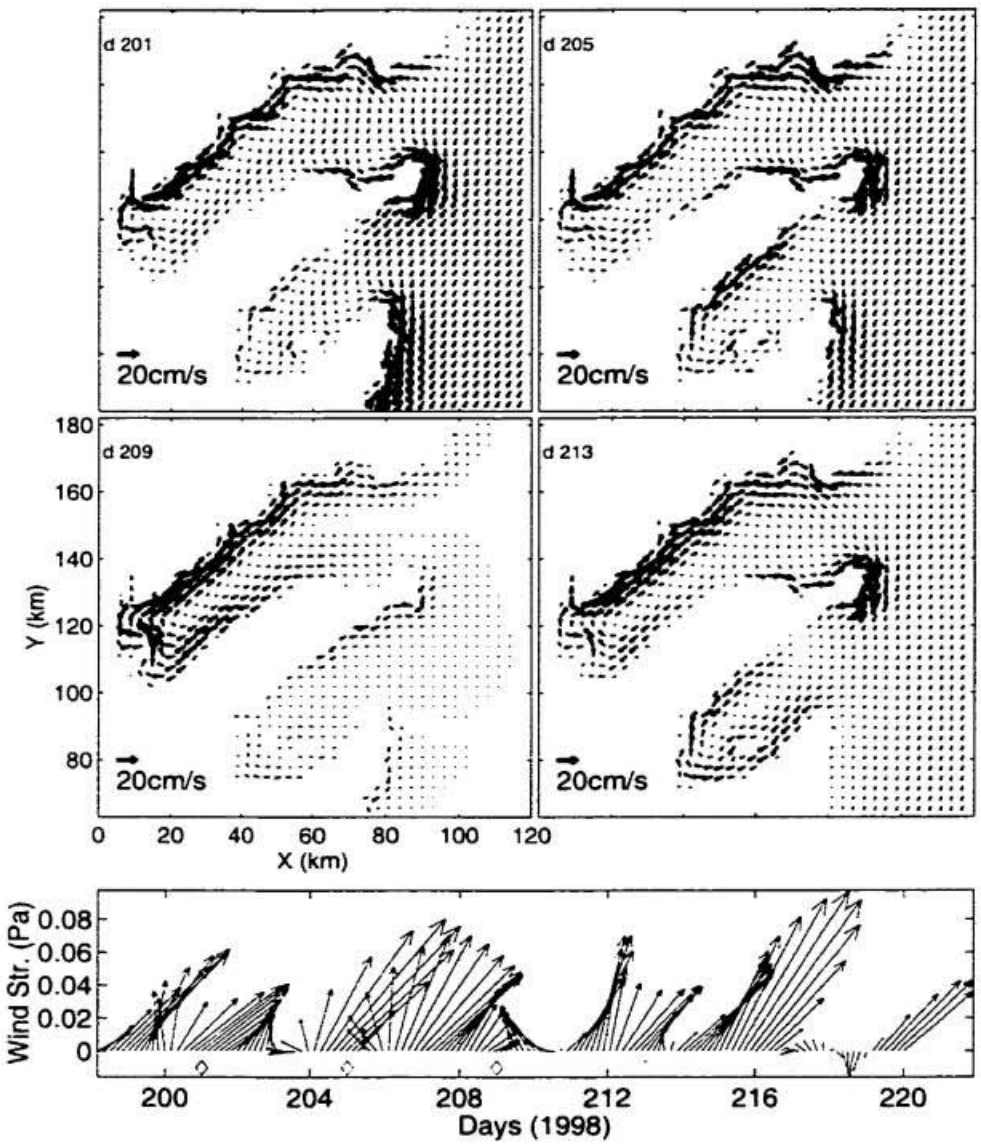

Figure 6.2: Surface velocity field from the linear CANDIE model shown at day 201 (the start date of the drifter release) and 4, 8 and 12 day later in 1998. Every third velocity vector is plotted, so the distance between the arrows is 3 km. The bottom panel features the wind stress for this period with the diamonds indicating the time at which the velocity snap shots were taken in the model.

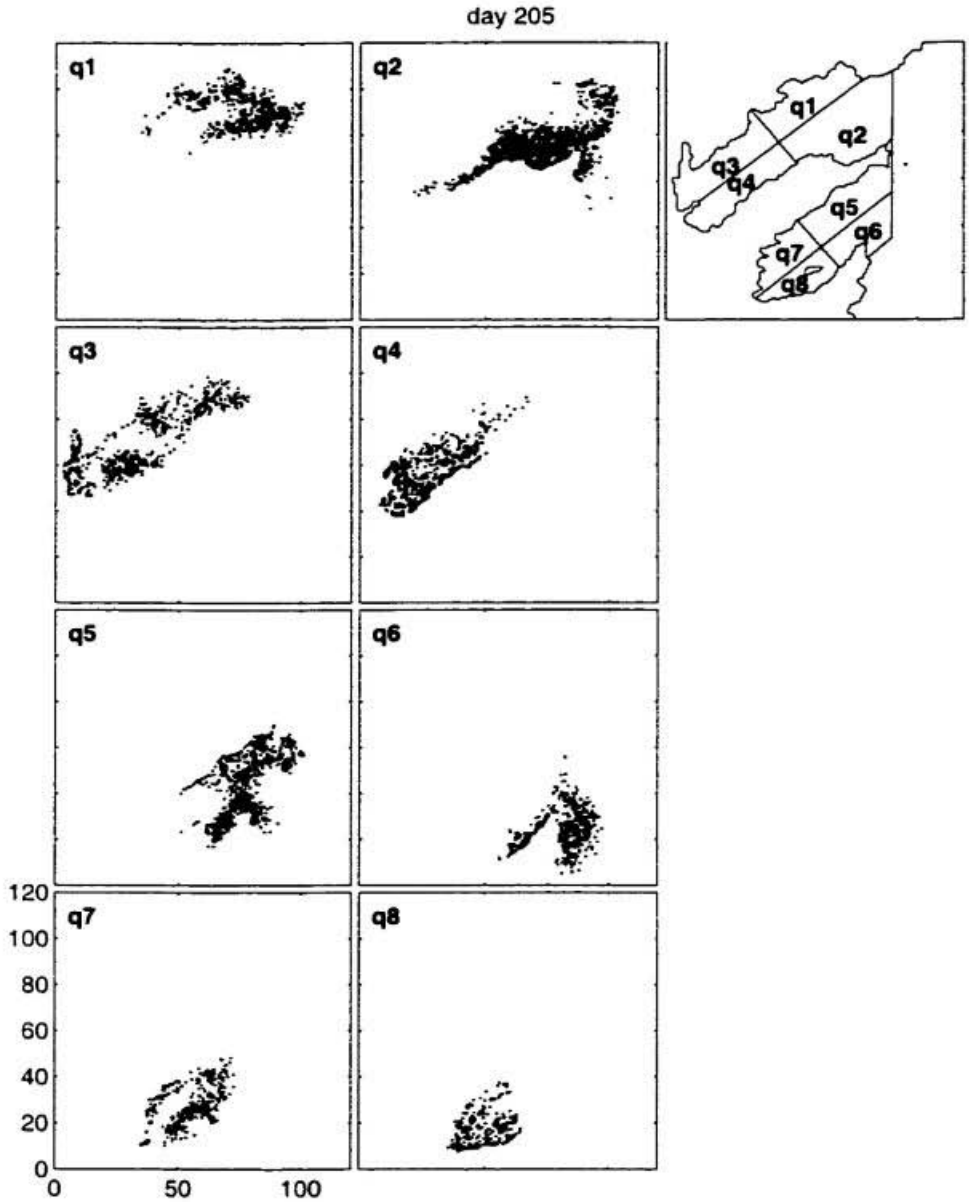

Figure 6.3: Drifter positions 4 days after release (on day 201) in the surface layer of the non-linear velocity field in Trinity and Conception Bay. Drifters are separated into quadrants by their initial start location as indicated at the upper right.

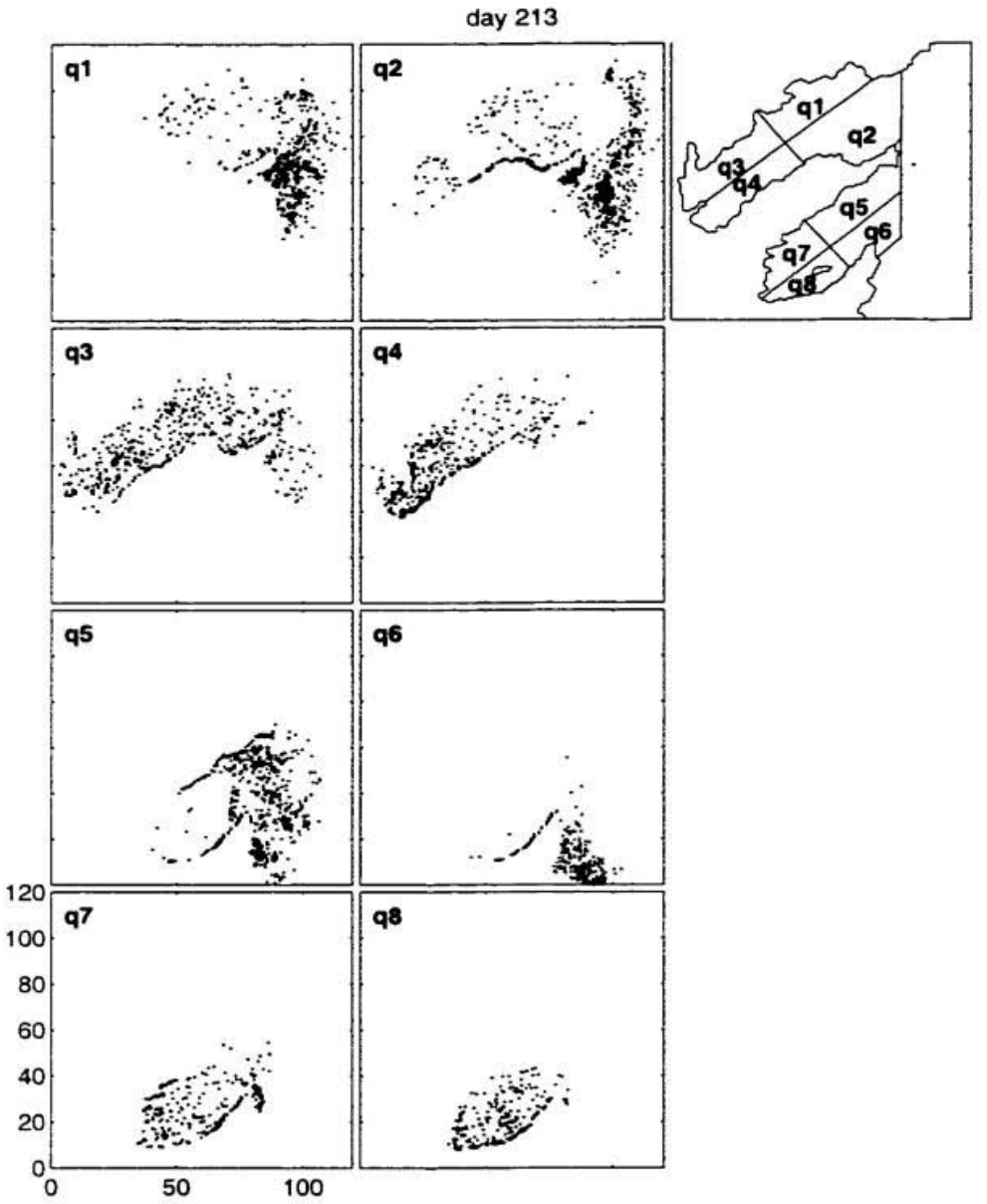

Figure 6.4: Position at day 213 (i.e. 12 days of drift) of drifters released at day 201 in the surface layer of the non-linear velocity field in Trinity and Conception Bay. Drifters are separated into quadrants by their initial start location as indicated at the upper right.

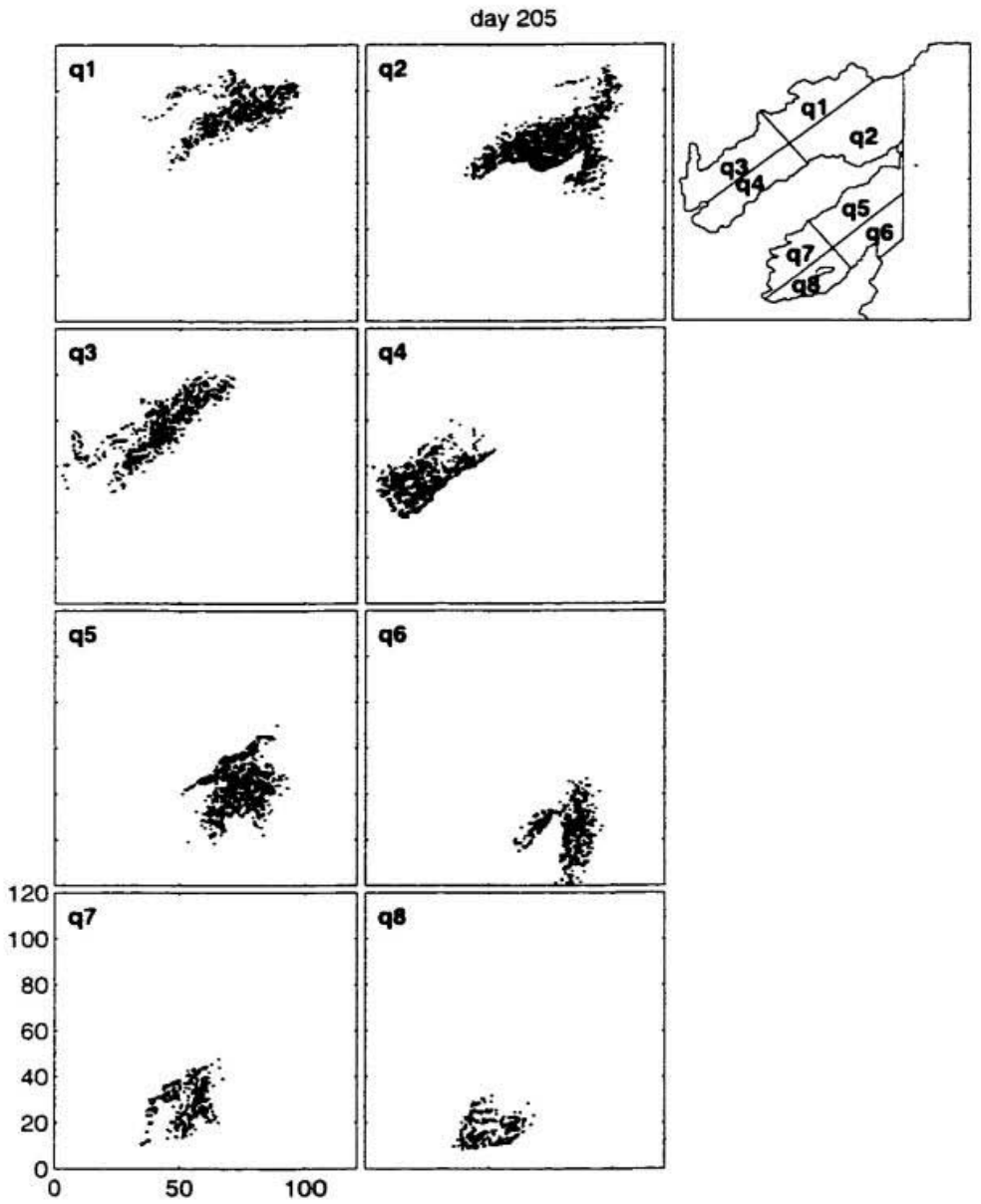

Figure 6.5: Drifter positions 4 days after release (day 201, 1998) for surface velocities from linear model. Drifters are separated into quadrants by their initial start location as indicated at the upper right.

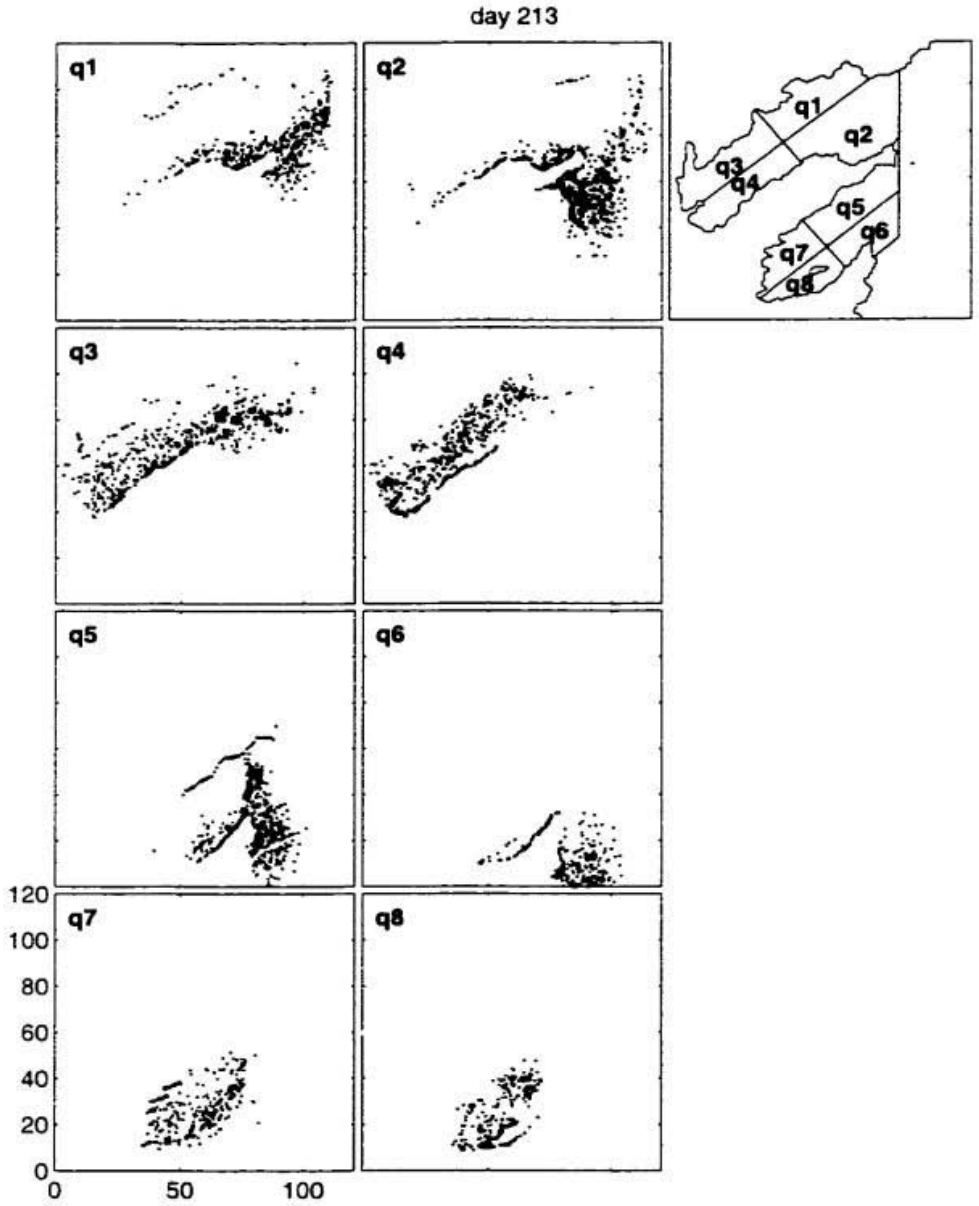

Figure 6.6: Drifter positions 12 days after release (day 201, 1998) for surface velocities from linear model. Drifters are separated into quadrants by their initial start location as indicated at the upper right.

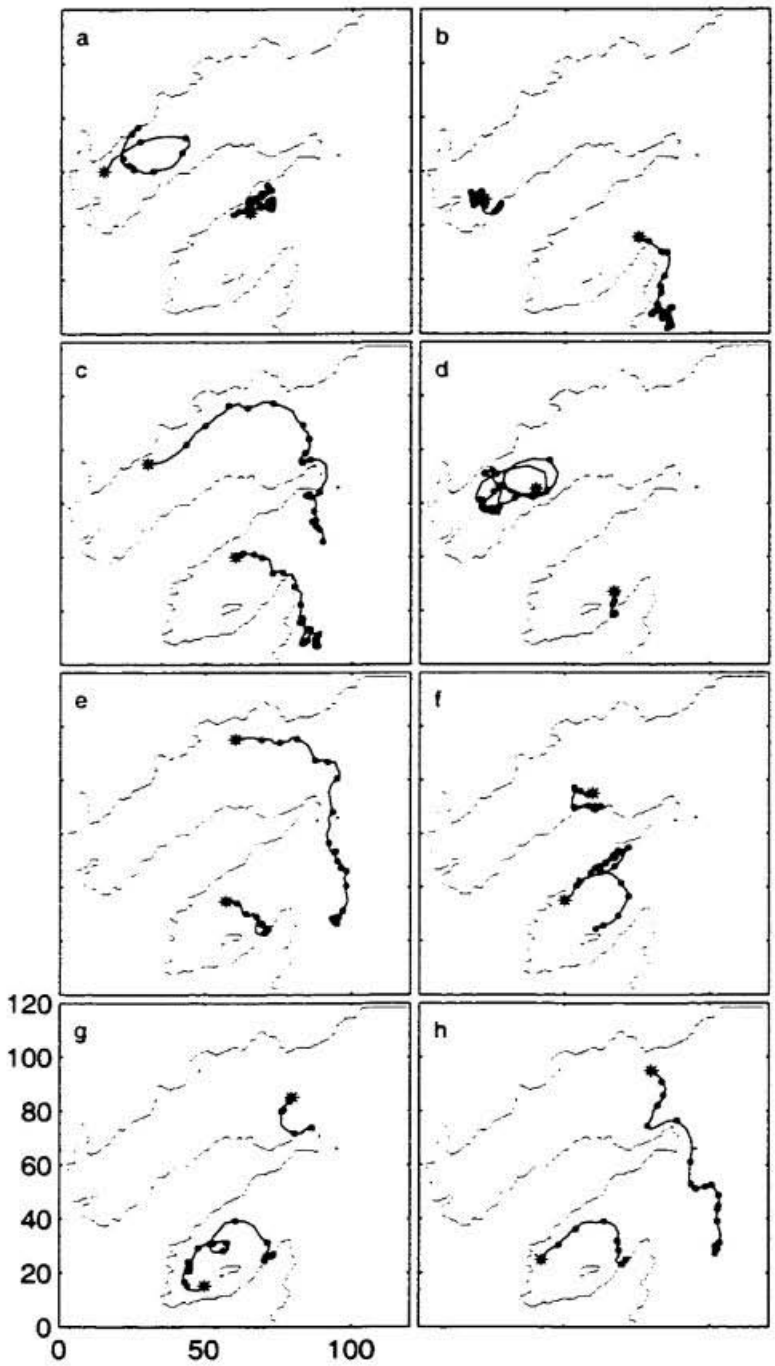

Figure 6.7: Sample of drifter tracks over a period of 20 days starting day 201 1998. The non-linear velocity field is used with particle diffusion set at 10 m^2 s^{-1}. The black dots along the trajectory path indicate the passage of days.

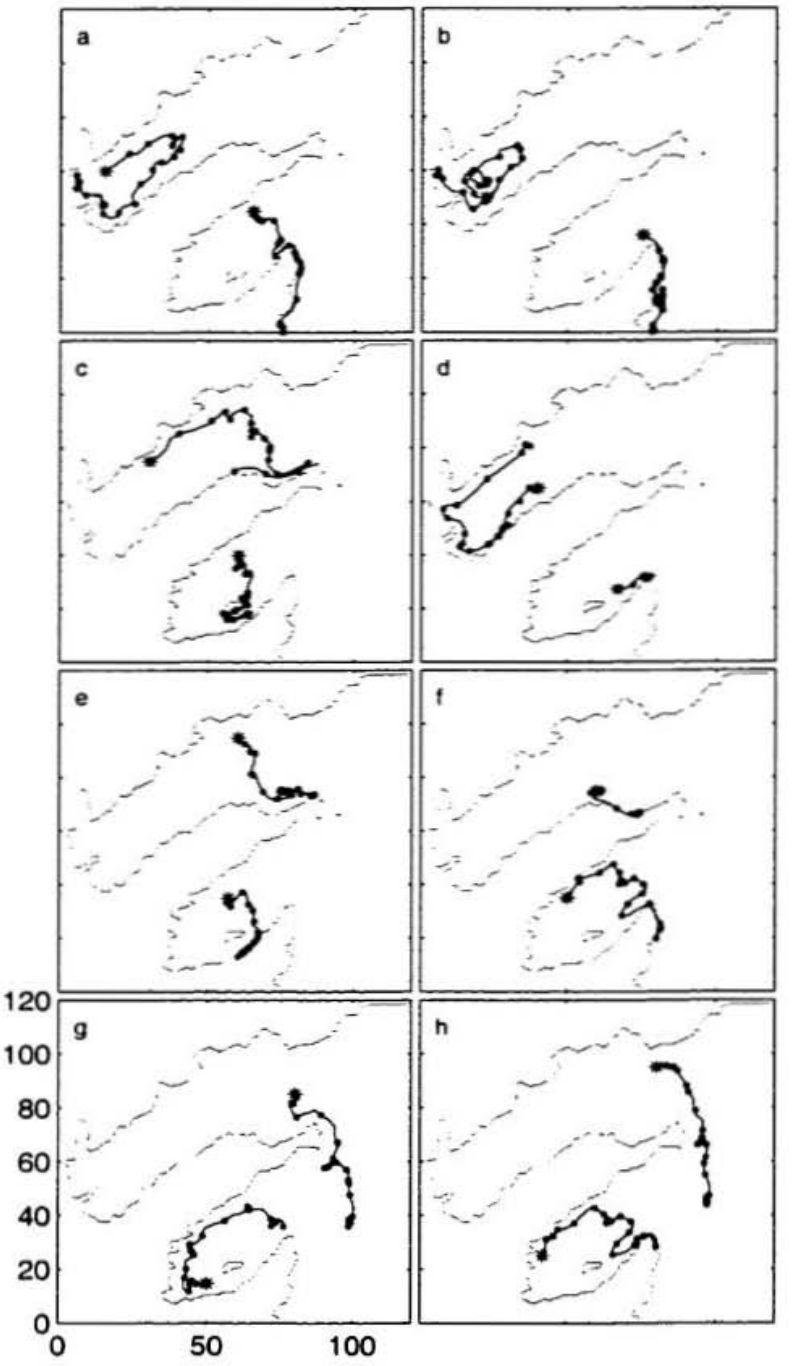

Figure 6.8: Sample of drifter tracks over a period of 20 days starting day 201 1998 using the linear velocity field. Particle diffusion is set at 10 $m^2\ s^{-1}$.

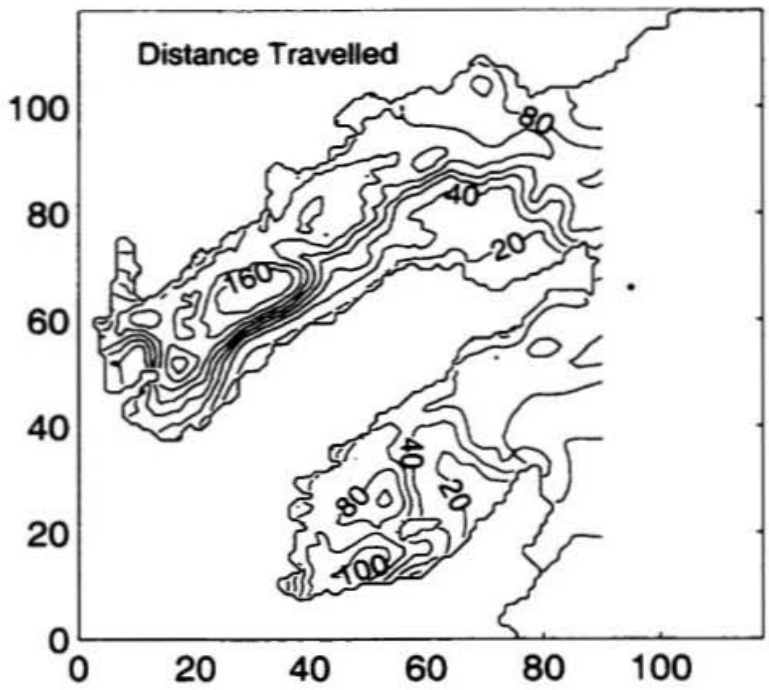

Figure 6.9: Distance travelled over 20 days by particles released in non-linear model on day 201. Particles were initially seeded every 1 km in the bays. The contour shows the path integral distance travelled by a particle from a given location.

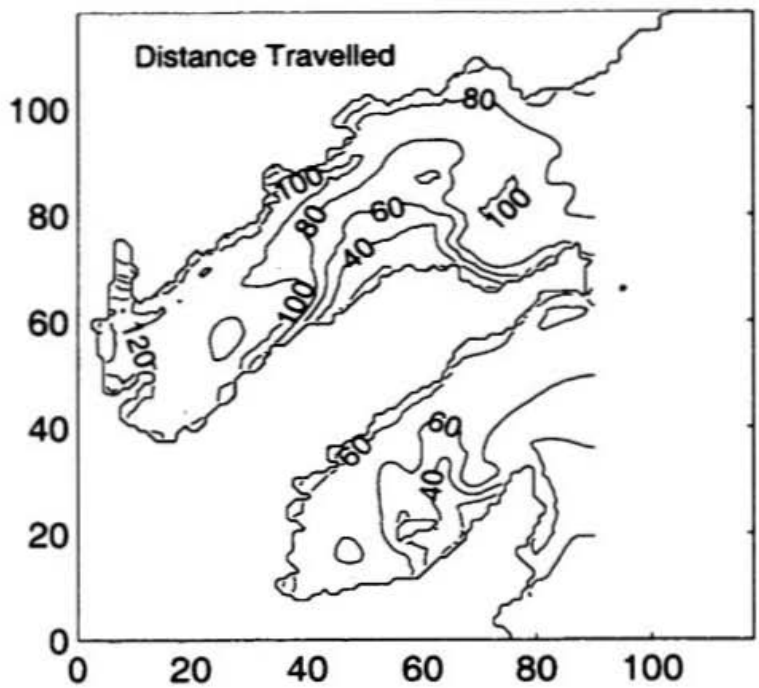

Figure 6.10: Distance travelled over 20 days by particles released in linear model on day 201.

Chapter 7

Conclusion

In this thesis I have undertaken a study of the wind-driven response of Trinity and Conception Bays. I have described the response to steady and time varying wind and have investigated the influence of stratification and non-linearity.

To relate this modeling effort to previous modeling studies in this region (de Young et al., 1993a,b), I have implemented a single-layer, shallow-water model for reference. Such a model has simple dynamics and its results are readily understood. I have developed a continuously stratified, shallow-water model and contributed heavily to the development of Memorial University's version of the fully prognostic CANDIE model. This model was run in both linear and non-linear mode to provide additional insight into the dynamics of wind driven circulation in embayments.

Since no modeling effort to represent an aspect of circulation is complete without reference to the real world, I have assembled available oceanographic data (published and unpublished) from several sources for Trinity and Conception Bays. These data

include current and temperature observations from moorings deployed in 1990 and 1994, Coastal Ocean Dynamics Application Radar (CODAR) observations of surface velocities in 1991 for Conception Bay, sea surface temperature images of the Avalon Peninsula for 1997 and 1998 and Acoustic Doppler Current Profiler (ADCP) observations at the mouth of Conception Bay in 1994. These data were presented and analysed in Chapter 2. Comparisons with these data were made in Chapter 5.

A test of the numerical model applied to a parabolic lake was presented in Chapter 3. I have shown that the combination of vertical mixing, the surface and bottom boundary conditions and variable bottom topography, can together produce a cyclonic circulation in an embayment or lake (or anti-cyclonic circulation around a sea-mount) in the northern hemisphere in the absence of any explicit forcing. Of these three factors, the combination of vertical mixing and variable bottom depth appears to be the key factor, contrary to Schwab et al. (1995) who claim that the adiabatic boundary condition alone produces such flow. These results relate well to the long term flow pattern in Lake Ontario for the summer months (Simons and Schertzer, 1989). For Conception Bay however, mixing of the thermocline in combination with bottom topography produces only mean flows that are less than 1 cm s^{-1} in strength with anti-cyclonic flow in the bay. This contrasts with the observed cyclonic mean flow in Conception Bay and the wind driven circulation pattern for a mean wind stress directed out of the bay (the principle wind direction during the summer). I conclude that vertical diffusion over variable topography is not an important factor

in driving mean flow in Trinity and Conception Bay (as it may be in Lake Ontario or other large stratified lakes).

A major contribution of this work is in defining the effect of the non-linear density transport terms on the separation of the coastal wind driven jet on the upwelling side of the bay under steady out-of-the-bay wind conditions. I have concluded that this separation is a corner effect. It is initially generated by the narrowing of the coastal jet on the western side of the bay near the head due to transport of water into the corner at the head of the bay. As the coastal jet narrows near the head of the bay, it generates an along-shore pressure and density gradient that drives cross-shore flow. This separation appears to be unstable with wave-like disturbances associated with the separated coastal jet propagating towards the mouth of the bay, with an apparent phase speed equivalent to that of the first baroclinic mode.

Another important contribution of the work is in identifying the importance of upwelling in Trinity Bay versus Conception Bay. In fact, observations around the entire Avalon Peninsula presented here, identify the western shore of Trinity Bay as the strongest upwelling centre with upwelling occurring in 24 of 27 clear day SST images. The second strongest upwelling region is on the southern shore of the Avalon Peninsula near Cape Race with upwelling observed on 21 of 27 clear SST image days.

Satellite images show an along-bay patchiness of cold upwelled water on the western shore of Trinity Bay that is reflected in the non-linear model results. The model suggests that this patchiness is due to the separation of the coastal jet on the western

side of the bay and the subsequent formation of gyres. The model shows the formation of three upwelling patches in Trinity Bay and one in Conception Bay, consistent with satellite observed upwelling patterns.

The CODAR data used provides the velocity for the top 1 m layer of Conception Bay. In the top 1 m of the water column, Phillips (1977) notes that the Coriolis force is negligible and direct acceleration of the water by the wind stress is apparent. The dynamical difference between the CANDIE model and CODAR data dynamics can be determined with the vertical Ekman number ($E_z = \frac{K}{fz^2}$) which is the ratio of the vertical viscosity term over the coriolis term in the horizontal momentum equations. Here K is the coefficient of vertical viscosity, f is the coriolis parameter and z is the vertical length-scale/model-resolution. For the CODAR data, E_z has a value of 1 for a value of 10^{-4} m^2 $s^{-1}$for K and 1m for z. However E_z is probably lower since vertical diffusivity diminishes near the surface (Fernandez et al., 1996). In the CANDIE model however, vertical resolution is 10m and the corresponding vertical Ekman number E_v is 0.01. Therefor in the CANDIE model runs, the Coriolis force dominates this term balance while in the CODAR data the Coriolis and vertical viscosity terms are equal.

As a check, the non-linear CANDIE model was run with the Coriolis parameter (f) set to a near zero value of f giving an Ekman number of 0.05. Many aspects of observed CODAR flow were reproduced by the "zero-Coriolis" run. These include stronger outflow on the eastern side of Conception Bay, an overall roughly two-fold increase in velocity strength and an increase of surface velocity throughout the bay

with distance from the head (due to increased fetch). The zero-Coriolis runs do not produce the coastal jet on the western side of the bay as observed in the data. This intensified jet on the western coast is reproduced in runs that include the Coriolis force. Thus it appears that some aspects of CODAR data are reproduced by the zero-Coriolis model run, but other features do require rotational dynamics.

There are many further steps that may be undertaken with the currently developed model for Trinity and Conception Bay. The most needed improvement would be in providing for the seasonal variation in stratification. This would allow the wave speed to vary over time, providing better representation in the coastal wave guide. The second improvement would be in the inclusion of the inshore branch of the Labrador Current in both the density and velocity fields of the model. From the mooring data collected on the western side of Conception Bay, it is apparent that near the mouth stratification changes from that in the interior of the bay. I speculate that this an influence of the circulation and water mass on the shelf.

One motivation for this modeling work was for the application to larval drift problems and identification of wind driven upwelling areas on the Avalon. Particle tracking studies show that for a period of time with light summer winds from the southwest, particles seeded near the head of the bays, are dispersed over the entire bay within 6-10 days. Particles seeded near the mouth on the eastern side of Conception Bay have the greatest likelihood of being advected out of the bay in agreement with de Young et al. (1993a). A finding in this thesis, is that in the surface layer (top

10 m), it is unlikely that there is significant exchange of larvae between the bays during periods of light winds less than 0.08 Pa in strength, except at the mouth of Conception Bay. When larvae from Trinity Bay drift out of the bay, they tend to be advected around the headland and flow past the mouth of Conception Bay without entering into the bay. Studies of drift during periods of strong wind (0.2-0.3 Pa) need to be undertaken to determine if exchange of larvae between the bays may occur during those times.

Finally, in conclusion I would like to identify some possible directions for future investigation for coastal ocean modelling in this region. Wind stress over Conception Bay does vary spatially due to orographic effects (i.e. wind influenced by the presence of coastal land topography). However, without a wind observation field program, this study was limited to using wind stress based from St. John's airport. The use of CODAR derived surface velocity observations may be a useful tool for providing spatially and time varying surface stress to the model instead of using wind observations. This would bypass assumptions about the transfer of momentum from the atmosphere to the ocean. A question remains, how the CODAR measured velocity relates to underlying flow. A two wavelength CODAR system could provide input for the vertical shear into the water column and give a value for shear stress at the surface of the water column. Simple improvements to the model are also needed, for example using a 1-D mixed layer model (Mathieu and de Young, 1995; Price et al., 1978) and parameterization of the Labrador Current in the model.

Bibliography

Anderson, C. (1986). *Motions driven by buoyancy forces and atmospheric stresses in the Avalon Channel, Newfoundland, Canada.* Ph.d. thesis, Institute of Oceanography, McGill University.

Bakun, A., Beyer, J., Pauly, D., Pope, J. G., and Sharp, G. D. (1982). Ocean sciences in relation to living resources. *Can. J. Fish. Aquat. Sci.*, 39:1059–1070.

Barrick, D. E., Lipa, B. J., and Crissman, R. D. (1985). Mapping surface currents with CODAR. *Sea Tech.*, 26(Oct.):43–48.

Bartsch, J., Brander, K., Heath, M., Munk, P., Richardson, K., and Svendsen, E. (1989). Modeling the advection of herring larvae in the North Sea. *Nature*, 340:632–636.

Bennett, A. F. and Kloeden, P. (1978). Bounded conditions for limited forecasts. *J. Atmos. Sci.*, 35:990–998.

Blumberg, A. L. and Mellor, G. L. (1987). A description of a three dimensional coastal ocean circulation model. three-dimensional coastal ocean models, coastal and estuarine sciences. *Ed. Amer. Geophys. Union*, 4:1–16.

Chapman, D. C. (1985). Numerical treatment of cross-shelf open boundaries in a barotropic coastal ocean model. *J. Phys. Oceanogr.*, 15:1060–1075.

Chapman, D. C. and Beardsley, R. C. (1989). On the origin of shelf water in the Middle Atlantic Bight. *J. Phys. Oceanogr.*, 19:384–391.

Colbourne, E., de Young, B., Narayanan, S., and Helbig, J. A. (1996). Comparison of hydrography and circulation on the Newfoundland Shelf 1990-1993. *Can. J. Fish. Aquat. Sci.*, 54 (suppl. 1):68–80.

Cornillion, P., Gilman, C., Stramma, L., Brown, O., Evans, R., and Brown, J. (1987). Processing and analysis of large volumes of satellite-derived thermal infrared data. *J. Geophys. Res.*, 92:12993–13002.

Crombie, D. D. (1955). Doppler spectrum of sea echo at 13.56 Mc./s. *Nature*, 175:681–682.

Csanady, G. T. (1982). *Circulation in the Coastal Ocean*. D. Reidel Publishing, Dordrecht, Holland.

Davidson, F. J. M. and de Young, B. (1995). Modeling advection of cod eggs and larvae on the Newfoundland Shelf. *Fish. Oceanogr.*, 4:33–51.

de Young, B., Anderson, J., Greatbatch, R. J., and Fardy, P. (1994). Advection-diffusion modeling of capelin larvae in Conception Bay, Newfoundland. *Can. J. Fish. Aquat. Sci.*, 51:1297–1307.

de Young, B., Greatbatch, R. J., and Forward, K. B. (1993a). A diagnostic coastal circulation model with application to Conception Bay, Newfoundland. *J. Phys. Oceanogr.*, 23:2617–2635.

de Young, B., Otterson, T., and Greatbatch, R. J. (1993b). The local and nonlocal response of Conception Bay to wind forcing. *J. Phys. Oceanogr.*, 23:2636–2649.

de Young, B. and Sanderson, B. (1995). The circulation and hydrography of Conception Bay, Newfoundland. *Atmos. Ocean*, 33:135–162.

Dietrich, D. E., Marietta, M. G., and Roache, B. D. (1987). An ocean modeling system with turbulent boundary layers and topography: Numerical description. *Int. J. Num. Meth. Fluids*, 7:833–855.

Dower, J. F., Pepin, P., and Leggett, W. C. (1998). Enhanced gut fullness and an apparent shift in size-selectivity by radiated Shanny (*Ulvaria-subbufurcata*) larvae in reponse to increased turbulence. *Can. J. Fish. Aquat. Sci.*, 55:128–142.

Emery, K. O. and Csanady, G. (1973). Surface circulation of lakes and nearly land-locked seas. *Proc. Natl. Acad. Sci. U.S.A.*, 70:93–97.

Fernandez, D. M., Vesecky, J. F., and Teague, C. C. (1996). Measurements of upper ocean surface current shear with high-frequency radar. *J. Geophys. Res.*, 101:28615–28625.

Frank, K. T. and Leggett, W. (1982). Coastal water mass replaement: its effect on zooplankton dynamics and the predator-prey complex associated with larval capelin *Mallotus villosus*. *Can. J. Fish. Aquat. Sci.*, 39:991–1003.

Gill, A. E. (1982). *Atmosphere-Ocean Dynamics*. Academic Press, San Diego.

Greatbatch, R. J. and Otterson, T. (1991). On the formulation of open boundary conditions at the mouth of a bay. *J. Geophys. Res.*, 96:18431–18445.

Greenberg, D. A. and Petrie, B. D. (1988). The mean barotropic circulation on the Newfoundland shelf and slope. *J. Geophys. Res.*, 93:15541–15550.

Heaps, N. S. (1971). On the numerical solution of the three-dimensional hydrodynamical equations for tides and storm surges. *Mem. Soc. R. Sci. Liège*, 4:143–180.

Helbig, J. A., Mertz, G., and Pepin, P. (1992). Environmental influences on the recruitment of Newfoundland/Labrador cod. *Fish. Oceanogr.*, 1:39–56.

Helbig, J. A. and Pepin, P. (1998a). Partitioning the influence of physical processes on the estimation of ichtyoplankton mortality rates. I. Theory. *Can. J. Fish. Aquat. Sci.*, 55:2189–2205.

Helbig, J. A. and Pepin, P. (1998b). Partitioning the influence of physical processes on the estimation of ichtyoplankton mortality rates. II. Application to simulated and field data. *Can. J. Fish. Aquat. Sci.*, 55:2206–2220.

Hickey, K. J., Gill, E. W., Helbig, J. A., and Walsh, J. (1994). Measurement of ocean surface currents using a long-range, high-frequency ground wave radar. *IEEE J. Oceanic Eng.*, 19:549–553.

Hjort, J. (1914). Fluctuations in the great fisheries of northern europe. *Rapp. P.-v. Réun. Cons. Int. Explor. Mer.*, 20:1–228.

Hsieh, W. W., Davey, M. K., and Wajsowicz, R. C. (1983). The free Kelvin wave in finite-difference numerical models. *J. Phys. Oceanogr.*, 13:1383–1397.

Huthnance, J. M. (1976). On coastal trapped waves: Analysis and numerical calculation by reverse iteration. *J. Phys. Oceanogr.*, 8:74–92.

Iles, T. D. and Sinclair, M. (1982). Atlantic herring: Stock discreteness and abundance. *Science*, 215:627–633.

Ings, D. W., Horne, J. K., and Schneider, D. C. (1997). Influence of episodic upwelling on capelin, *Mallotus villosus*, and Atlantic Cod, *Gadus morhua*, in Newfoundland coastal waters. *Fish. Oceanogr.*, 6:41–48.

Jeans, P. K. and Donnelly, R. (1986). Four-element CODAR beam forming. *IEEE J. Oceanic Eng.*, 11:296–303.

Kasai, A., Kishi, M. J., and Sugimoto, T. (1992). Modeling the transport and survival of japanese sardine larvae in and around the Kuroshio Current. *Fish. Oceanogr.*, 1:1–10.

Kollmeyer, R. C., McGill, D. A., and Corwin, N. (1967). Oceanography of the Labrador Sea in the vicinity of Hudson Strait in 1965. *Bull. U.S. Coast. Guard*, 19:1–34.

Kundu, P. K. (1990). *Fluid Mechanics*. Academic Press, San Diego.

Laprise, R. and Pepin, P. (1995). Factors influencing the spatio-temporal occurence of fish eggs and larvae in a nothern, physically-dynamic coastal environment. *Mar. Ecol. Prog. Ser.*, 122:73–92.

Large, W. G. and Pond, S. (1981). Open ocean momentum flux measurements in moderate to strong winds. *J. Phys. Oceanogr.*, 11:324–336.

Lazier, J. R. N. and Wright, D. G. (1993). Annual velocity variations in the Labrador Current. *J. Phys. Oceanogr.*, 23:659–678.

Leggett, W. C., Frank, K. T., and Carscadden, J. E. (1984). Meteorological and hydrographic regulation of year class strength in capelin (*Mallotus villosus*). *Can. J. Fish. Aquat. Sci.*, 41:1193–1201.

Mathieu, T. and de Young, B. (1995). Application of a mixed layer model to the inner Newfoundland Shelf. *J. Geophys. Res.*, 100:921–936.

McCreary, J. P. (1981). A linear stratified ocean model of the equatorial undercurrent. *Phil. Trans. Roy. Soc. London A*, 298:603–635.

Mellor, G. L. (1992). User's guide for a three-dimensional, primitive equation, numerical ocean model. Technical Report 35, Princeton University, Princeton,N.J.

Mellor, G. L. and Yamada, T. (1974). A hierarchy of turbulence closure models for planetary boundary layers. *J. Atmos. Sci.*, 31:1791–1806.

Mertz, G., Narayanan, S., and Helbig, J. A. (1993). The freshwater transport of the Labrador Current. *Atmos. Ocean*, 31:281–295.

Myers, R. A. and Akenhead, S. A. (1990). The influence of Hudson Bay runoff and ice-melt on the salinity of the inner Newfoundland Shelf. *Atmos. Ocean*, 28:241–256.

Mysak, L. (1980). Topographically trapped waves. *Ann. Rev. Fluid Mech.*, 12:45–76.

Nof, D. (1988). Eddy-wall interactions. *J. Mar. Res.*, 46:527–555.

Otterson, T. (1992). An analysis of the wind-forced response of Conception Bay using a reduced-gravity numerical model. M.Sc. thesis, Memorial University, St. John's, Newfoundland, Canada.

Paradis, A., Pepin, P., and Brown, J. A. (1996). Vulnerability of fish eggs and larvae to predation - review of the influence of the relative size of prey and predator. *Can. J. Fish. Aquat. Sci.*, 53:1226–1235.

Pepin, P. (1991). The effect of temperature and size on development, mortality, and survival rates of the pelagic early life history stages of marine fish. *Can. J. Fish. Aquat. Sci.*, 48:503–518.

Pepin, P., Helbig, J. A., Laprise, R., Colbourne, E., and Shears, T. H. (1995). Variations in the contribution of transport to changes in planktonic animal abundance: a study of the flux of fish larvae in Conception Bay, Newfoundland. *Can. J. Fish. Aquat. Sci.*, 52:1475–1486.

Petrie, B. and Anderson, C. (1983). Circulation on the Newfoundland Continental Shelf. *Atmos. Ocean*, 21:207–226.

Petrie, B., Loder, J. W., Akenhead, S., and Lazier, J. (1992a). Temperature and salinity variations on the eastern Newfoundland shelf: the annual harmonic. *Atmos. Ocean*, 30:120–139.

Petrie, B., Topliss, B. J., and Wright, D. G. (1992b). Coastal upwelling and eddy development off Nova Scotia. *J. Geophys. Res.*, 12:12979–12991.

Phillips, O. M. (1977). *On the Dynamics of the Upper Ocean*. Cambridge University Press, New York.

Pollard, R. T. and Millard, R. C. (1970). Comparison between observed and simulated wind-generated inertial oscillations. *Deep Sea Res.*, 17:813–821.

Price, J. F., Weller, R. A., and Pinkel, R. (1978). Observations and models of the upper ocean response to diurnal heating, cooling and wind mixing. *J. Geophys. Res.*, 91:8411–8427.

Prinsenberg, S. J., Peterson, I. K., Narayanan, S., and Umoh, J. U. (1997). Interaction between atmosphere, ice cover, and ocean off Labrador and Newfoundland from 1962-1992. *Can. J. Fish. Aquat. Sci.*, 54(Suppl.1):30–29.

Robinson, A. R. (1964). Continental shelf waves and the response of the sea leavel to weather systems. *J. Geophys. Res.*, 69:367–367.

Robinson, I. S. (1995). *Satellite Oceanography*. John Wiley & Sons, Chichester.

Rose, G. A. and Leggett, W. C. (1988). Atmosphere-ocean coupling in the northern Gulf of St. Lawrence: effects of wind forced variation in sea temperatures on currents and nearshore distributions and catch rates of *Gadus mohua*. *Atmos. Ocean*, 45:1234–1243.

Ruzzante, D. E., Taggart, C. T., Cook, C., and Goddard, S. (1996). Genetic differentiation between inshore and offshore Atlantic Cod *Gadus morhua* off Newfoundland. *Can. J. Fish. Aquat. Sci.*, 53:634–645.

Schneider, D. C. (1994). Distribution of capelin *Mallotus villosus* in relation to coastal upwelling in the Avalon Channel. *J. Northw. Atl. Fish. Sci.*, 17:23–31.

Schneider, D. C. and Methven, D. A. (1988). Response of Capelin to wind-induced thermal events in the Southern Labrador Current. *J. Mar. Res.*, 46:105–118.

Schott, F. (1989). Measuring winds from underneath the ocean surface by Upward Looking Acoustic Doppler Current Profilers. *J. Geophys. Res.*, 94:8313–8321.

Schwab, D. J., O'Connor, W. P., and Mellor, G. L. (1995). On the net cyclonic circulation in large stratified lakes. *J. Phys. Oceanogr.*, 25:1516–1520.

Sheng, J. (1999). Dynamics of the buoyancy-driven coastal jet: the Gaspé Current. *J. Phys. Oceanogr.*, submitted.

Sheng, J., Wright, D. G., Greatbatch, R. J., and Dietrich, D. E. (1998). CANDIE: A new version of the DieCAST ocean circulation model. *J. Atmos. Oceanic Technol.*, 15:1414–1432.

Simons, T. J. and Schertzer, W. M. (1989). The circulation of Lake Ontario during the summer of 1982 and the winter of 1982/1983. Technical Report 171, Environment Canada Scientific Series.

Smedbol, R. K. and Wroblewski, J. S. (1997). Evidence for inshore spawning of northern atlantic cod (*Gadus morhua*) in Trinity Bay, Newfoundland, 1991-1993. *Can. J. Fish. Aquat. Sci.*, 54 Suppl. 1:177–186.

Smith, E. H., Soule, F. M., and Mosby, O. (1937). The Marion and General Greene expeditions to Davis Straight and Labrador Sea. *Bull. Coast Guard*, 19:259.

Smith, P. C. and MacPherson, J. I. (1987). Cross-shore variations of near-surface wind velocities and atmospheric turbulence at the land-sea boundary during CASP. *Atmos. Ocean*, 25:279–303.

Spiegel, E. A. and Veronis, G. (1960). On the Boussinesq approximation for a compressible fluid. *Astrophys. J.*, 131:442—447.

Stewart, R. H. and Joy, J. W. (1974). HF radio measurements of surface currents. *Deep Sea Res.*, 21:1039–1049.

Taggart, C. T. and Leggett, W. C. (1987). Wind-forced hydrodynamics and their interaction with larval fish and plankton abundance: a time-series analysis of physical-biological data. *Can. J. Fish. Aquat. Sci.*, 44:438–451.

Templeman, W. (1966). *Marine Resources of Newfoundland*, volume 154. Bull. Fish. Res. Bd. Can.

Ullmann, D., Brown, J., Cornillion, P., and Mavor, T. (1998). Surface temperature fronts in the Great Lakes. *J. Great. Lakes Res.*, 24:753–775.

Wang, D. P. and Mooers, C. N. K. (1976). Coastal-trapped waves in a continuously stratified ocean. *J. Phys. Oceanogr.*, 6:853–863.

Werner, F. E., Page, F. H., Lynch, D. R., Loder, J. W., Lough, R. G., Perry, R. I., Greeberg, D. A., and Sinclair, M. M. (1993). Influences of mean advection and simple behaviour of cod and haddock early life stages on Georges Bank. *Fisheries Oceanography*, 2:43–64.

Wunsch, C. (1970). On oceanic boundary mixing. *Deep Sea Res.*, 17:293–301.

Yamagata, T. and Philander, S. G. H. (1985). The role of damped equatorial waves in the oceanic response to winds. *J. Oceanographical Soc. Japan*, 41:345–357.

Yao, T. (1986). The response of currents in Trinity Bay, Newfoundland, to local wind forcing. *Atmos. Ocean*, 24:235–252.

Zedel, L., Crawford, G. B., and Gordon, L. R. (1996). On the determination of wind direction using an upward looking acoustic Doppler current profiler. *J. Geophys. Res.*, 101:12163–12176.

Zedel, L., Gordon, L. R., and Osterhus, S. (1999). Ocean ambient sound instrument system: Acoustic estimation of wind speed and direction from a sub-surface package. *J. Atmos. Ocean Tech.* In Press.